Fall 12-2022

Effectiveness of Suspended Lead Dampers in Steel Buildings Under Localized Lateral Impact and Vertical Pulsating Load

Herish Abdullah Hussein
Old Dominion University, herishkung@yahoo.com

EFFECTIVENESS OF SUSPENDED LEAD DAMPERS IN STEEL BUILDINGS UNDER LOCALIZED LATERAL IMPACT AND VERTICAL PULSATING LOAD

by

Herish Abdullah Hussein
B.S. July 2009, Koya University, Iraq
M.S. December 2014, Old Dominion University

A Dissertation Submitted to the Faculty of
Old Dominion University in Partial Fulfillment of the
Requirements for the Degree of

DOCTOR OF PHILOSOPHY

CIVIL AND ENVIRONMENTAL ENGINEERING

OLD DOMINION UNIVERSITY
December 2022

Approved by:

Zia Razzaq (Director)

Shahin N. Ameri (Member)

Julie Hao (Member)

Mojtaba B. Sirjani (Member)

ABSTRACT

EFFECTIVENESS OF SUSPENDED LEAD DAMPERS IN STEEL BUILDINGS UNDER LOCALIZED LATERAL IMPACT AND VERTICAL PULSATING LOAD

Herish Abdullah Hussein
Old Dominion University, 2022
Director: Dr. Zia Razzaq

Presented herein is a study of the effectiveness of suspended lead dampers for use in steel buildings under a localized impact load and a vertical pulsating load. A series of lead spheres mounted on a string are suspended inside the building columns or damping panels to absorb the energy of vibration through a collision between the lead dampers and internal surfaces of the members. Experiments are conducted on a three-story steel building model and a cantilever member with suspended lead dampers and subjected to localized impact loading. The cantilever under impact load is analyzed with a partial differential equation of dynamic equilibrium using a central finite-difference scheme. The numerical scheme is also used to unveil the dynamic stability characteristics of a typical building column under lateral impact and vertical pulsating load. The building model and a full-scale building frame with damping characteristics of the suspended lead dampers are then analyzed using SAP-2000 program with localized impact and a vertical pulsating load. The study shows a substantial reduction in building vibration when suspended lead dampers are used. The elastic-plastic transient dynamic analysis of the full-scale steel building reveals that the impacted column does not develop a plastic hinge at its top when bolted panels with suspended lead dampers are used. In the absence of such damping

panels, the impacted column develops three plastic hinges thereby turning into a collapse mechanism.

ACKNOWLEDGMENTS

First, I acknowledge the Creator who has given me an interest in learning and the ability to deal with the challenges of life, including the pursuit of a Ph.D. degree program. Big thanks and love are due to my parents who were always there for me throughout my life. Deep appreciation and love are also due to my wife who persuaded me to pursue the doctoral degree program. I thank and appreciate my adviser, Dr. Zia Razzaq, who provided guidance in many different ways. I will also never forget his advice and encouragement to make it a habit to read books. I also wish to thank my colleague Ramani Ayakannu for his help in issues related to SAP-2000 and data processing.

NOMENCLATURE

a	Acceleration
b	Width of column
c	Damping Coefficient
c_c	Critical Damping Coefficient
d	Cross-sectional depth of column
E	Modulus of elasticity
ϵ	Strain
e	Distance from neutral axis
f	Natural Frequency
F(t)	Forcing Function
h	Segment length
I	Moment of Inertia of the hollow section member
K	Stiffness
L	Length of Column
M	Moment [Do you mean bending moment? If so, please call say so].
m	Member mass per unit length
n_i	Segment number
T	Time Period
t	Time
Δt	Time Interval

$\ddot{U}_{i,j}$	Acceleration at time i, j
v	Displacement
W	Effective weight of the hollow section member
ω_n	Natural Circular Frequency
ω_D	Damped Circular Frequency
$\omega_{e_{exp.}}$	Effective Experimental Natural Circular Frequency
Z	Member longitudinal axis
ζ	Damping Ratio
x	Shape Function
σ_y	Yielding Strength
$\sigma_{ult.}$	Ultimate Strength
δ	Truncation error
Š	Shear Factor

TABLE OF CONTENTS

Page

Page

LIST OF TABLES

LIST OF FIGURES

Figure Page

Figure Page

Figure Page

Figure Page

Figure Page

Figure Page

CHAPTER I

1. INTRODUCTION

1.1 Background

The events of the past few decades resulting in collapse of buildings caused by a sudden loss of one or more column support at the ground level have made the need for investigating building structural response under such conditions an important research area. The 1995 terrorist attack on Murrah Federal building in Oklahoma resulted in building collapse due to the loss of support at the ground level, and several other similar events in the USA such as those of 9/11 and around the world are well-documented. Such events can also be caused by a vehicle hitting a building, or due to a gas explosion. A fundamental problem is that of the challenge of absorbing energy of impact on a typical column at the ground level of a building to circumvent the collapse of the structure. A majority of the existing energy-absorbing devices include passive and active dampers developed primarily for applications in earthquake engineering.

In an exploratory study related to passively damping the vibration of NASA's space station structural members, Razzaq et al. [13-21] developed a damping system consisting of a series of lead dampers mounted on a string and suspended inside the hollow spaces of the structural members. The vibration was shown to be significantly damped due to the lead dampers colliding with the internal surfaces of the structural members. Although the study involved both natural vibrations as well as those induced by harmonic forcing functions, the effectiveness of the suspended lead dampers under impact loading conditions was not studied in the presence or absence of pulsating axial loading.

The research evaluates the effectiveness of the suspended lead dampers when installed in a steel building structure subjected to lateral impact loading combined with an axial pulsating load. Experimental investigations on a laboratory model steel building are conducted and the results are compared with theoretical predictions well as prototype structures.

1.2 Literature Review

The published literature related to the use of passive damping devices mostly for applications in earthquake engineering is vast. Presented here is a brief overview of some of the important developments.

The metallic-yielding damper is one of the most common passive damping systems. This system is a buckling restrained brace (BRB). This type is used in tall and intermediate buildings in locations where an earthquake is a threat [1]. This type is high in ductility and gives stable energy dissipation in the bracing members. By incorporating supplemental energy-dissipating devices, BRB reduces plastic formation in the structural members.

Benavent [2] has researched a brace-type damping system on hollow structural sections. He used tube-in-tube assemblage, then he cut slits from the outer tube to weld the strips to the inner tube section, the cut-strips are used diagonally to dissipate energy through flexural and shear yielding. The results of this experimental study show that strength is increased by 1.25 times the yield strength, and this system shows stable hysteric response by 30 to 60 times yield displacement. However, the results do not show a significant difference between the proposed bracing system and the conventional steel-plate system in dissipating energy.

Ghabraie et al. [3] in their research on shape optimization of metallic yielding devices (slit damper) for passive mitigation of seismic energy have used bi-directional evolutionary structural optimization to optimize energy dissipation in structural steel buildings for earthquake risk mitigation. The results of their study show an increase in

energy dissipation and better-distributing stress during an earthquake. In their four different models, various tapered bars are used to optimize their results. They were able to record improvements in energy absorption capacity between 58% to 96%. Chan and Albermani [4] conducted an experimental study on steel slit dampers with different slit lengths cut from steel plates for passive energy dissipation, they ran nine tests subjecting the different slit dampers to inelastic cyclic deformation. The devices yielded a small angular distortion to dissipate energy during earthquake events. The results of their practical tests showed that the slit passive damping systems performed stable hysteretic behavior with significant capacity of dissipating energy up to 10.3 KJ. Part of their increase in energy dissipation was from strain-hardening that led the specimens' ultimate strength to be higher than their yielding strength by a factor of 2. The results showed that the longer and wider slits performed higher flexibility, on the other hand, the shorter and the narrower slits showed more stiffness and more capability in dissipating energy.

For reinforced concrete buildings, damping braces are used to retrofit RC buildings against earthquake shaking. Mazza and Vulcano [5] used a displacement-based design procedure to retrofit their six-story RC plane frame under seismic loads. The numerical results show that the stiffness ratio is based on the reduction in ductility in the RC frame. Also, damage in the frame is more in artificially generated ground motion rather than recorded ground motions.

The friction damping system is among the most common passive damping systems for tall buildings. This system relies on utilizing a solid friction mechanism to dissipate energy [1]. Friction dampers provide both damping and stiffness. Compared to the viscus and metallic damping system, friction damper has the most effective in

dissipating energy. Both velocity and temperature are the two most effective factors in the efficiency and capacity of friction dampers. Low cost, high performance, no maintenance, and consistency of friction dampers have made the designers and builders show interest in using them in both strengthening and stiffening their buildings.

Xu and Ng [6] ran an experimental study on using friction dampers in a 12-story building to strengthen it against seismic loads. They used a piezoelectric actuator to make three friction-damping controllers: a Viscous and Reid Friction controller, Modulated Homogenous Friction controller, and a Non-sticking Friction controller. The results show a 15-17% reduction in inter-story drift in the building and a 16-20% reduction in peak acceleration. The maximum root-mean-square reductions in both drift and accelerations reached 31-54% and 35-53%, respectively.

Perez et al. [7] in their research on reliability-based optimum design of passive friction dampers in buildings in seismic regions used a novel optimization technique to decrease the probability of failure in seismic regions buildings. The results show a significant decrease in failure probability in the 6-story reinforced concrete building model in 50 years the structure equipped with the optimal design of friction dampers by 91% with a reduction in peak displacement by 50%.

Friction dampers are widely used in different businesses; Ramaiah and Krishnaiah [8] have used friction dampers to control vibration in a gas-turbine blade. They have confirmed their theoretical results by doing experimental tests. They concluded that increasing energy dissipation in friction damping strongly depends on the coefficient of friction, normal load, damper stiffness, the elasticity of damper material, and force at the

damper end. In-band brake technology, Downey et al. [9] used friction dampers to mitigate the natural hazard. They showed that large damping forces can be obtained at lower applied forces. Their rotary friction device was able to amplify friction force by 125-150 times the applied force.

Due to the impacts of dynamic loads on building structures, a variety of damping systems have been invented. Viscoelastic dampers are among the developed damping systems used in tall and intermediate buildings to dissipate energy during impact loads and seismic loads. The rubbers/polymers used in viscoelastic dampers have both viscous and elastic characteristics [1]. This type of damping system has consisted of two steel plates and rubber between the two steel plates. The dampers are usually located in locations that experience relative motion during dynamic loads. Viscoelastic characteristics of the rubbers change with respect to the temperature that affects the deformation of the rubbers during dynamic loads. At higher temperatures, the rubbers dissipate energy less.

Montgomery and Christopoulos [10] did an experimental study on using viscoelastic coupling dampers in high-rise buildings. They replaced coupling beams with viscoelastic dampers at certain locations, therefore, do not occupy any unstable architectural space. They tested five small scales and six full-scale viscoelastic dampers. The small-scale test results showed that ISD111H materials properties do not change, while viscoelastic materials properties change with respect to excitation frequency and temperature. The full-scale test results showed that temperature did not change in the rubbers drastically, i.e., no effect of temperature change on the rubber properties. During harmonic tests, no material properties were observed.

Gong et al. [11] used 112 viscoelastic dampers in Nanjing Dabaoen Temple, which is a tall irregular steel structure. They ran the model of the temple in SAP-2000 for both moderate and major earthquakes. The installed dampers improved both capacity and displacement in the temple structure. The results showed a decrease in drift by 9% and 34% under moderate earthquakes and major earthquakes, respectively.

Both Yang and Lam, and Tebaldi [12, 13] used viscoelastic dampers in connecting adjacent buildings to observe dynamic behaviors. Yang and Lam connected three buildings, a 16-story, a 10-story, and a short building. They used three different mass eccentricities; 0, 10%, and -10% with respect to the dimensions of the buildings. Both top displacement and base shear were notably reduced in the symmetric buildings. In contrast, top displacement in asymmetric buildings is increased. Also, the dampers caused increasing base shear by 9%. In addition, bidirectional excitations caused an increase in base shear by up to 29%. Tebaldi used only two buildings in his study, a short and a tall building. The viscoelastic dampers were installed to connect the two buildings at the top of the short building. The maximum attained damping ratio depends on the mass ratio. In this study, the maximum damping ratio obtained was 0.14. Also, the study showed that the performance of the connected buildings did not change due to using viscoelastic or viscous dampers.

In the industry of passive damping systems, fluid, such as viscous fluid, has been broadly used in dissipating energy and it is gaining worldwide acceptance. Through a piston, the generated dynamic load pushes the fluid in a cylinder orifice to produce a damping pressure to dissipate energy [1]. Since the damping force is 90 degrees out of

phase with the displacement response, the viscous fluid damping system does not add any stiffness to the building.

Salvia et al. [14] used a viscous fluid damping system in a 39-story high-rise building to decrease the effects of wind on the building structure. In their study, they focused on the cost-effect approach as well. The results of dissipating energy compared to the total cost; it is shown that the viscous fluid damping system is among the most cost-effective approach in reducing the dynamic impact of wind on high-rise buildings. The total cost for this 39-story building was less than one million dollars even including the installation fee.

Since concrete buildings are the most brittle structures, the researchers shed light on the most influential damping systems to be used in dissipating energy in RC buildings. Rofooei and Mohammadzadeh [15] have done research on using a viscous fluid damping system in a 3x4-bay 1-story concrete frame to decrease dynamic load impact on torsional behavior by focusing on the moment-resisting behavior of the building. For this purpose, they have considered different one-way stiffness and strength eccentricities. It is determined that in the linear range; stiffness eccentricity has a major role in finding the optimal center of the damping constant. On the other hand, it is found that in the nonlinear range, strength eccentricity has a major role in determining the optimal center of the damping constant. Despite the effects of the viscous fluid damping system on decreasing displacement and acceleration in the building, viscous fluid damping system is found that it is very effective in controlling torsional behavior.

Wang and Mahin [16] used a viscous fluid damping system in a 35-story high-rise steel moment-resisting frame to retrofit is against a seismic load. They did a two-level retrofit approach for the building that was designed in the early 1970s. The purpose of their study was to achieve a collapse prevention limit state under major earthquake events. The results showed that by using the viscous fluid damping system, they were able to achieve the retrofitting goals and decrease both collapse and economic losses by 90% by improving the structural behavior of the building such as decreasing the top floor's drift by 30%.

Ras and Boumechra [17], in their research paper, have focused on seismic energy dissipation in a 12-story steel building using a viscous fluid damping system. They used Boumerdes earthquake data to study the building's nonlinear time history analysis using SAP-2000. The results showed that they were able to achieve effective energy dissipation without increasing rigidity in the structure. Also, due to using the viscous fluid damping system, they needed much less steel to achieve stability as compared to the same frame without the damping system. The analysis results showed that they were able to decrease the fundamental period by 220%, maximum displacement by 32%, maximum acceleration by 37%, and both moment and base shear by 40%, and the difference between the floors' accelerations is minimized.

The Tuned-mass damping system (TMD) is one of the most common damping systems for both tall buildings and bridge structures. This system has different forms depending upon the application. Among the most common types of TMD, mass and coil spring, mass and flexure, and pendulum are used widely. TMD through its resonance out of phase absorbs energy and decreases vibration. The decay of motion in TMD is

considerably higher than decreasing acceleration. It is very effective in reducing wind excitations and impact loads on tall buildings. Depending on the structure's dominant mode, damping factor, mass, and spring stiffness must be tuned [1].

Lucchini et al. [18] did research on the robust design of tuned damper systems for seismic protection of multistory buildings. They have used robustness as a multi-objective optimization formula in designing the damping system to account for uncertainties. Their study concluded that the performance of the damping system is directly related to the total mass of the TMD system; with increasing total mass, there is an increase in performance. Also, the robustness of the damping system increases when uncertainty in the properties of the ground excitation reduces. However, with increasing uncertainty levels, the damping system's period and damping increase.

As mentioned before, the TMD system is also widely used in retrofitting bridges as well. Latifi and Razani [19] showed a reduction in the vibration of a railway bridge located in Iran by installing a TMD system in it. They also studied a seismic behavior of a 10-story building structure after installing TMD in it. After severe damage in the longest span of the bridge (72 meters), this span was replaced with a steel deck. Because the railway is curved and the replacing deck is straight, the bridge has excessive vibration due to the eccentricity issue in the deck. After using TMD in the bridge, they found that with the damping system with an optimum parameter, an excessive reduction in vibration can be achieved. They also found that the bridge's natural modes are close to the resonant speed of the train at speeds of 32 and 40 kilometers per hour. For the high-rise building, they conclude that for telecom towers, TMD seems to have the best effect on reducing

vibrations caused by both earthquake and wind loads, especially for those towers where their concentrated mass is located at a high altitude.

Johnson et al. [20] used a nonlinear tuned mass damper coupled with a buckling restrained brace in retrofitting a three-story existing building structure after installing the damping system on the top roof of the building. The results showed excessive energy dissipation in the building after installing TMD and buckling restrained bracing in the building. The numerical results showed that a 40% reduction in spectral acceleration in the period of the first second of excitation and a 13% reduction in top roof displacement can be obtained. It is also mentioned that the building is improved in self-centering ability after being retrofitted against seismic loads.

In retrofitting lightweight superstructures, Erdle et al. [21] have studied the effectiveness of base isolation TMD in decreasing lateral motion during earthquake and wind loads. The TMD system they used in testing their model-scale structure added only 1.3 and 2% to the gravitational mass of the building. The results showed a considerably large reduction in lateral motion and acceleration in the model building. Also, broad-spectrum damping was achieved without adding considerable load to the structure.

The summary of the above and other studies shows that both passive and active damping systems have a big role in dissipating energy during dynamic loads and decreasing both vibration and lateral displacement in the structures. Also, they reduce the construction limitations of high-rise buildings [22]. In this study, the pendulum TMD damper is focused on. The main focus of the study is to decrease vibration in tall buildings during wind load, low earthquake, or impact load. A sample of using the

pendulum TMD system is used in Tapyh Tower (101-story) in Taiwan. This pendulum damper is the largest and heaviest damper ever installed in buildings [23]. This pendulum's steel damper with a diameter of 18-foot weighing 1605-pound is installed at the top stories of the building at an elevation of 1640-foot. This pendulum system reduces vibration in the building by 30 to 40% [23].

Arsava et al. [24] have developed numerical models to investigate the response of a beam model against impact load. They have installed magnetorheological dampers in the models to decrease the influence of impact load on building structures. They have proposed a time-delayed adaptive neuro-fuzzy inference system (TANFIS) used to predict the nonlinear behavior of the models. The results showed that TANFIS is very effective in investigating structural members under effective impact loads.

Zhang et al. [25] presented a study on the control system of magnetorheological dampers under impact load with and without a PI control system. The results showed that to control the optimum damping force in a magnetorheological damping system, PI control helps decrease the damping force in the system by 21.7%. decreasing the damping force in the damping system helps the structures to resist bigger impact loads.

Uzair Magbool [26] in his thesis, has focused on the effectiveness of passive dampers in decreasing the impacts of quasi-static and impact loading on steel structures. This study showed the response of the dissipative joints to accidental conditions. His developed comprehensive model shows that using slip resistance connections helps the joint fasteners during impact loads and decreases the chance of collapse in buildings.

In 1982, Robinson [27] reported that a total of 92 lead-rubber bearings had been used in New Zealand to base-isolate one building and three bridges. In 1994, he summarized [28] the characteristics of the lead devices and applications of hysteretic dampers to seismic isolation in Italy, the USA, Japan, and New Zealand. In 1995, he published a summary [29] of research and applications of seismic isolation in New Zealand. In that paper, he reported that out of the ten hospitals affected by the 1994 Northridge earthquake in Los Angeles, only the hospital seismically isolated by a lead-rubber bearing system was able to continue to operate. He also referred to the excellent behavior of two isolated buildings in the 1995 Hyogo Ken-Nanbu earthquake. In 1998, Robinson summarized [30] New Zealand's experience in passive control of structures including sliding bearings or flexible piles with steel or dead dampers providing the damping and the lead rubber bearing which, in one unit, provides both the isolation and the damping. He reported that more than fifty bridges and ten buildings have been isolated with most structures being isolated with lead rubber bearing systems.

Ribakov and Gluck [31] presented a design method for a passive control system for multistory structures using optimal Adding Damping and Stiffness (ADAS) dampers. Since Optimal Control Theory (OCT) is commonly used to obtain the levels of viscous damping at each story, the optimization itself leads to different levels of damping at each story. Therefore, a solution with viscous dampers is inconvenient and can be expensive. The authors proposed a method that enables the use of relatively less expensive optimal ADAS devices dissipating energy that is equivalent to that of viscous dampers. The method is examined in a numerical analysis of a seven-story shear-framed structure.

Significant improvement was obtained in the behavior of the ADAS-damped structure compared to the uncontrolled one.

Jankowski, Kujawa, and Czeslawszymczak [32] investigated the effectiveness of a pendulum damper in reducing wind-induced vibrations of a steel chimney. A two-degree-of-freedom non-linear model is used to simulate the behavior of the structure equipped with a damper. The results showed that the use of a pendulum with tuned frequency leads to a significant reduction in structural response

Nakashima, Pan, Zamfirescu, and Weitzmannl [33] summarized design and construction statistical data with respect to the common usage of base-isolated buildings in Japan since the 1995 Hyogoken-Nanbu (Kobe) earthquake including new developments and refinements made in the material, device, design, and construction of these structures.

Curadelli and Riera [34] summarized the development of efficient, low-cost, and reliable structural dampers, suitable for use in structures subjected to wind, seismic, and other dynamic excitations. Different from similar dampers described in the literature, the energy dissipation device described works by plastic shear deformation of a set of lead rings. On account of its almost perfectly rigid-plastic behavior, with little rate dependence, the device proved in laboratory tests to be able to absorb a large amount of energy during 103 cycles with no sign of shakedown. This article presented the basic design of the damper and the experimental determination of its mechanical characteristics by means of a set of cyclic tests, for frequencies ranging between 0.1 and 3 Hz and

displacement amplitudes ranging from 1 to 12 mm. They also presented a simplified design procedure using a finite-element model.

Sajjadi, Keyhani, and Pourmohammadl [35] investigated the behavior and performance of steel structures equipped with Added Damping and Stiffness (ADAS) and Triangular Added Damping and Stiffness (TADAS) metallic dampers and compared them with conventional earthquake-resisting steel structures such as CBF, CHEVRON and EBF systems. In this study, ground acceleration records of the El Centro, Hachinohe, San Fernando, and Taft earthquakes were used as the disturbing ground motion in a series of numerical simulations of a multi-story steel building. The numerical simulations were carried out by using the DRAIN-2DX program and the nonlinear dynamical behavior of the different systems was compared with each other. Results showed suitable behavior of systems equipped with ADAS and TADAS metallic dampers in that the main damage occurred in dampers while keeping the main structure safe.

Bayat and Abdollahzade [36] have presented a study of the seismic behavior of structures with metallic dampers in the so-called ADAS (Added Damping and Stiffness) category. The paper compared the ratio of the hysteretic energy to input energy for five, ten, and fifteen-story three-bay Concentric Braced Frames (CBF) with and without ADAS. The PERFORM 3D.V4 software along with three earthquake records (Northridge, Imperial Valley, and Tabas) is used for nonlinear time history analysis and the conclusions are drawn upon energy criterion. It was found that with a higher earthquake energy absorption capacity and a larger ratio of the plastic energy to input energy, the ADAS system has generally a superior vibration performance compared to that of the CBF structural system. The authors have also presented a fairly comprehensive

summary world-wide application of various types of passive damping methodologies including bituminous rubber viscoelastic and other types of viscoelastic dampers, friction dampers, bending type honeycomb dampers, slit dampers and shear panel type dampers.

Warn and Ryan [37] summarized seismic isolation practices including widely used hardware and chronicled the history and development of modern seismic isolation through shake table testing of isolated buildings including past efforts to achieve three-dimensional seismic isolation. The review of current practices and past research are synthesized with recent developments from full-scale shake table testing to highlight areas where research is needed to achieve full seismic damage protection of buildings. The emphasis of this paper is on the application of passive seismic isolation for buildings primarily as practiced in the United States, though systems used in other countries are also discussed.

Soydan Yuksel, and Irtem [38] studied the seismic behavior of a steel connection equipped with the lead extrusion damper (LED) with a spherical type bulge and without a lubricant layer. Cyclic force-displacement relations of the connections *with* and *without* LED were recorded. Measures of dissipated energy, equivalent damping ratio, and effective stiffness are obtained from the experimental study. The total energy dissipated by the connection with the LED was found to be about 175% greater than the total energy dissipated by the bare connection. Nonlinear dynamic time history analyses performed for the selected earthquakes and mass conditions using the analytical models for the connections with LED showed a 50% reduction in maximum top displacement compared with that without it for the considered earthquakes.

Razzaq et al. [39-45] developed various types of passive damping devices in exploratory studies related to NASA's space station applications. These included suspended dampers filled with viscous oil, brush friction dampers, and suspended lead dampers. The studies were focused on reducing structural natural vibrations as well as those caused by harmonic flexural forcing functions in the presence of constant axial loads.

To the best of the author's knowledge, the proposed research has not previously been published in the literature.

1.3 Problem Statement

This dissertation studies the effectiveness of suspended lead dampers when used in rectangular steel buildings subjected to localized lateral impact load in the presence of a pulsating vertical load as shown in Figure 1(a). The focus of this study is to determine the effectiveness of the suspended lead dampers when used inside existing building columns, and/or use of bolted or welded damping panels constructed from a series of hollow steel tubes containing suspended lead dampers. Figure 1(b) shows a typical damping panel. The problem also includes first validating the transient dynamic analysis process by a comparison to the experimental behavior of a model building frame, and then applying the analysis to determine the performance of a full-scale steel building. In addition, impact tests and analysis are conducted on a full-scale isolated steel cantilever member to determine the effectiveness of the suspended lead dampers. Figure 2 shows the cantilever member with suspended lead dampers. Both dynamic stability phenomenon as well as sequential plastic hinge formation in a ground-level building column under impact are investigated.

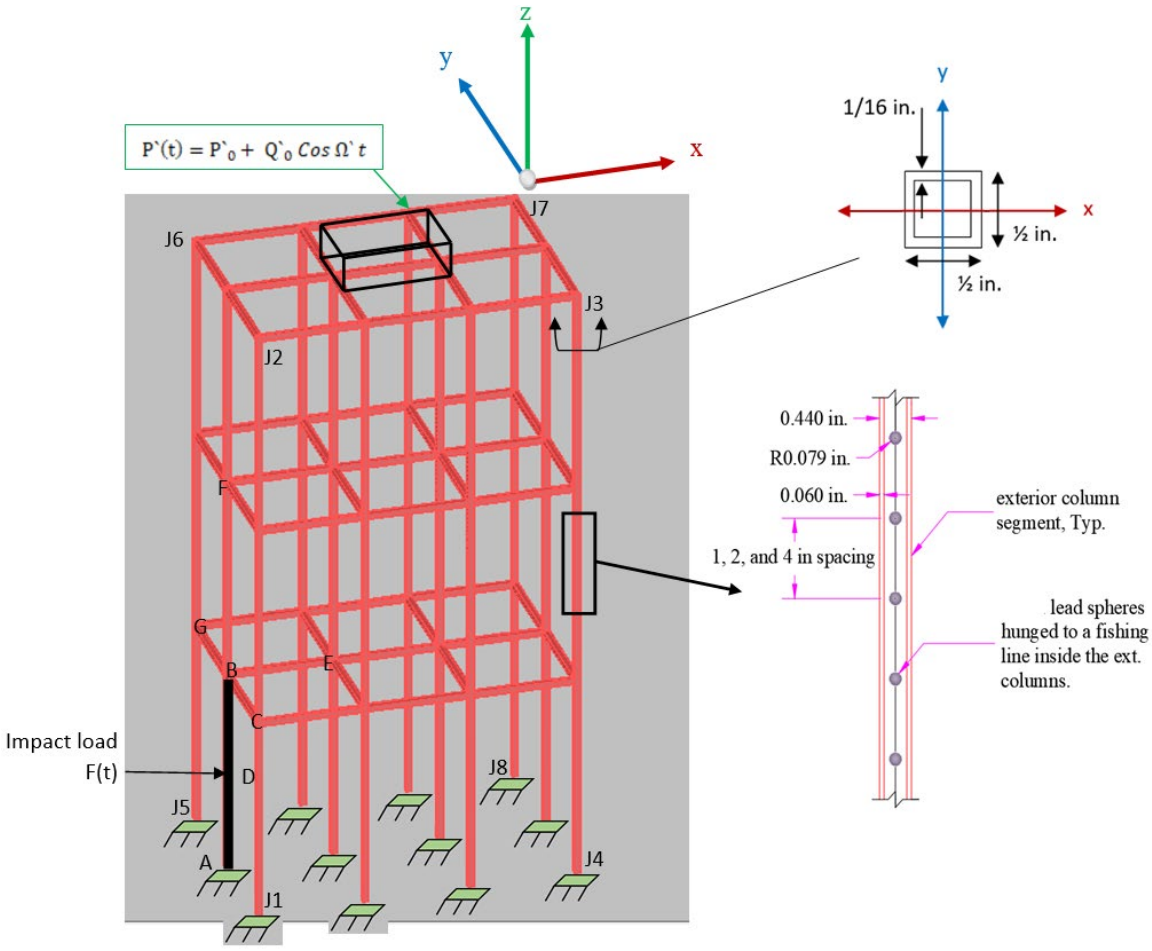

(a) Building frame with HVAC system and impact load

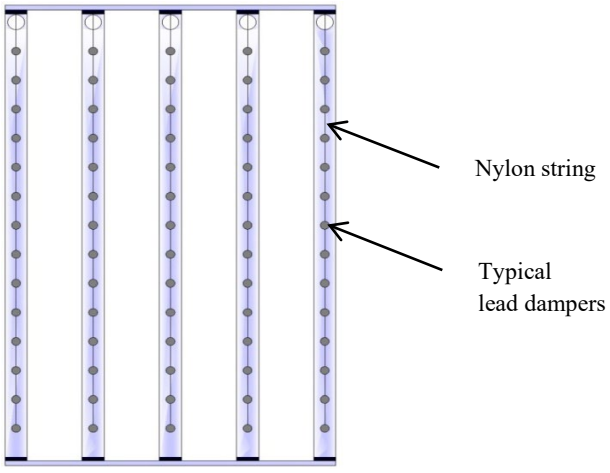

(b) Typical damping panel with suspended lead dampers

Figure 1. Building frame and typical damping panel

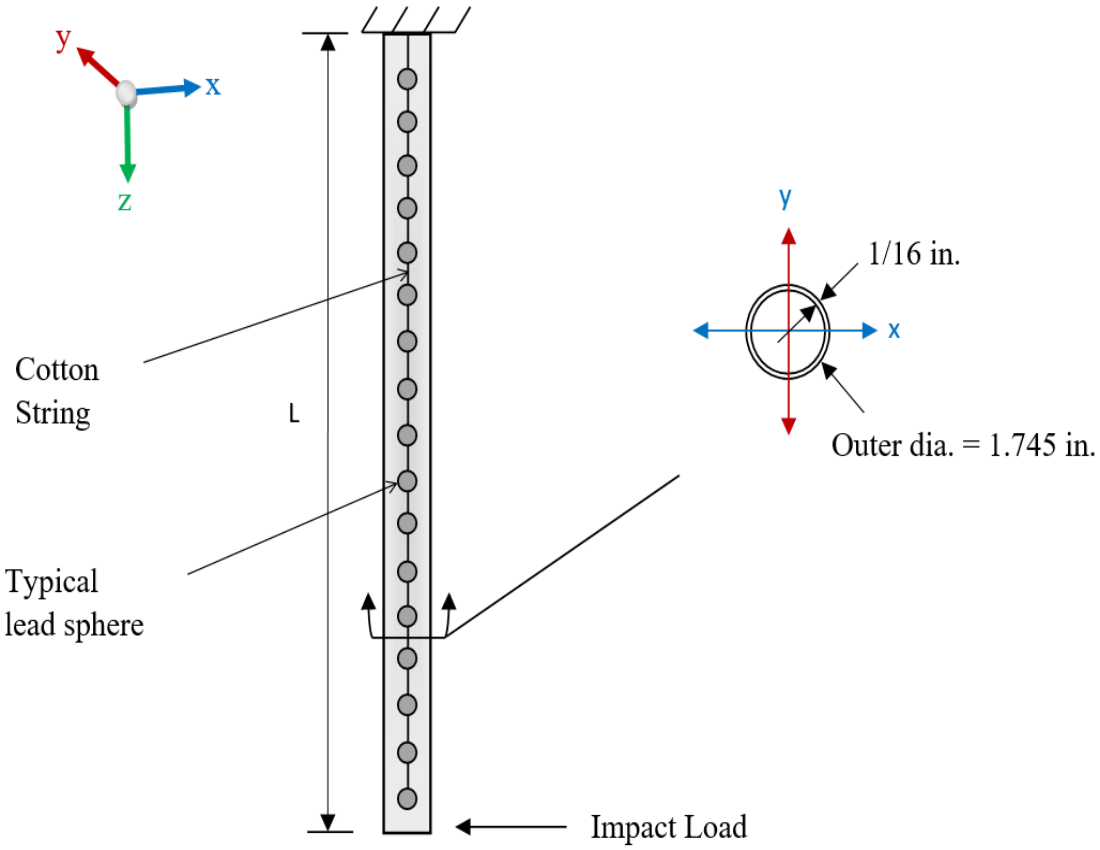

Figure 2. Full-scale damping member modeled as a cantilever under impact load

Figure 3 shows a schematic of the ground-level column AB with the bottom end A initially fixed, and the top end B partially restrained. At joint B, k is rotational stiffness and K is lateral stiffness. The column shown in Figure 3 has an axial constant load, P_0, combined with a pulsating load, $Q_0\ Cos\Omega t$, induced by an air compressor system installed on the top of the building as shown in Figure 1(a).

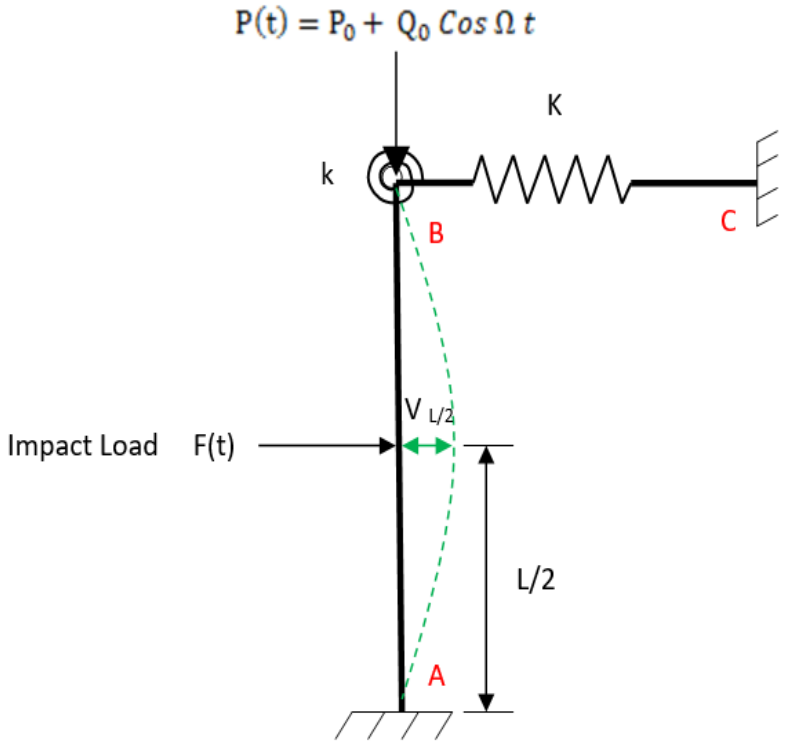

Figure 3. Schematic of ground-level column

1.4 Objectives and Scope

The specific objectives and scope of the study are:

1. Build a three-story steel building laboratory model and an apparatus for applying a localized impact load at the mid-height of one ground-level column, and a separate full-scale cantilever test setup, for experimental studies both with and without suspended lead dampers.
2. Conduct an experimental study of the influence of suspended lead dampers on the building model and the isolated cantilever under natural vibration condition, and when subjected to a localized impact in the absence of an axial pulsating load.

3. Develop a finite-difference algorithm to solve the governing partial differential equation of dynamic equilibrium for the individual member studies including the effect of suspended lead dampers.
4. Investigate the theoretical dynamic stability characteristics of a typical ground-level column including the influence of lateral impact load both with and without lead dampers.
5. Predict the effectiveness of the degree of damping provided by suspended lead dampers for the building laboratory model as well as a prototype three-story steel building under localized impact load both with and without a vertical pulsating load and vertical service loads.

Use is made of wireless accelerometers to establish the forcing function generated by the impact load, and the dynamic response of the test specimens.

The primary goal of the experimental and theoretical study is to determine the effectiveness of suspended lead dampers for use in building frame subjected to a localized impact load.

1.5 Assumptions and Conditions

1. The normal stress-strain relationship for steel members is elastic-perfectly-plastic.
2. Shear deformations and axial shortening are negligible.
3. Small deflection theory is adopted.
4. Structural members do not develop any local buckling.
5. The impact load is applied at only a single location.

6. The axial loads are of such magnitude that the vertical traveling waves are considered negligible.

CHAPTER II

2. EXPERIMENTAL STUDY

The outcome of the experimental part of the study is presented in this chapter. In addition to characterization of material properties, results are documented for impact tests on a three-story steel building model, and a full-scale cantilever specimen with and without suspended lead dampers.

2.1 Material Properties

The material of the structural member and frames tested is steel. The mechanical steel properties are determined following the ASTM procedure [46]. The specimens are cut following the standard dimensions required by ASTM as shown in Figure 4.

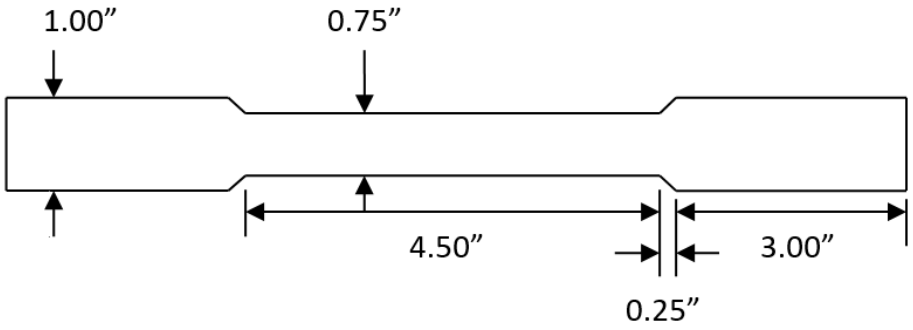

Figure 4. Tension test specimen dimensions

2.1.1 Steel Mechanical Properties

The model steel frame shown in Figure 1(a) was fabricated using 0.5x0.5x0.0625 in. hollow steel sections. The tension test result for this material is shown in Figure 5(a). The stress-strain relationship is slightly curved beyond the elastic range and exhibits a

small amount of strain-hardening. Using a 0.1 percent strain offset method, the yield stress, σ_y, is found to be 62.0 ksi. Based on this yield stress and to the Young's modulus, E, of 28,000 ksi, the idealized elastic-perfectly-plastic stress-strain (σ-ϵ) relationship is shown in Figure 5(b), and is used in this study. Both E and σ_y are needed for the transient dynamic analysis portion of the study.

Figure 6 shows stress-strain relationship for the hollow circular section steel used in the cantilever specimen shown in Figure 3. Only the Young's modulus, E = 28,261 ksi, is needed for the cantilever study for determining the effectiveness of the suspended lead dampers.

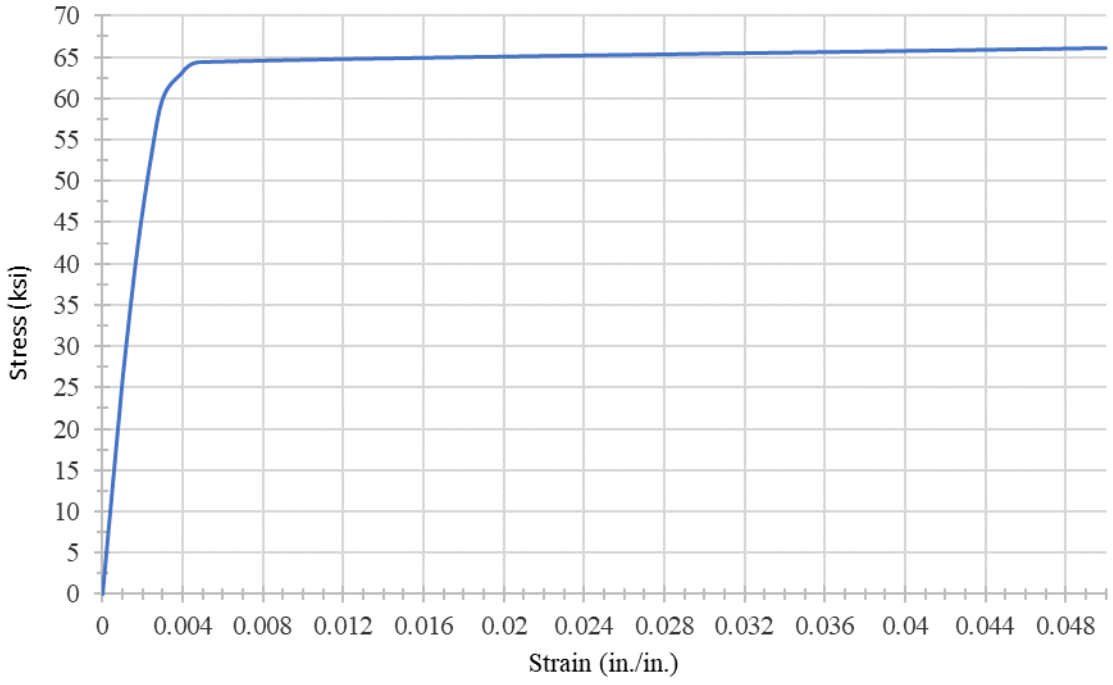

(a) Experimental stress-strain relationship

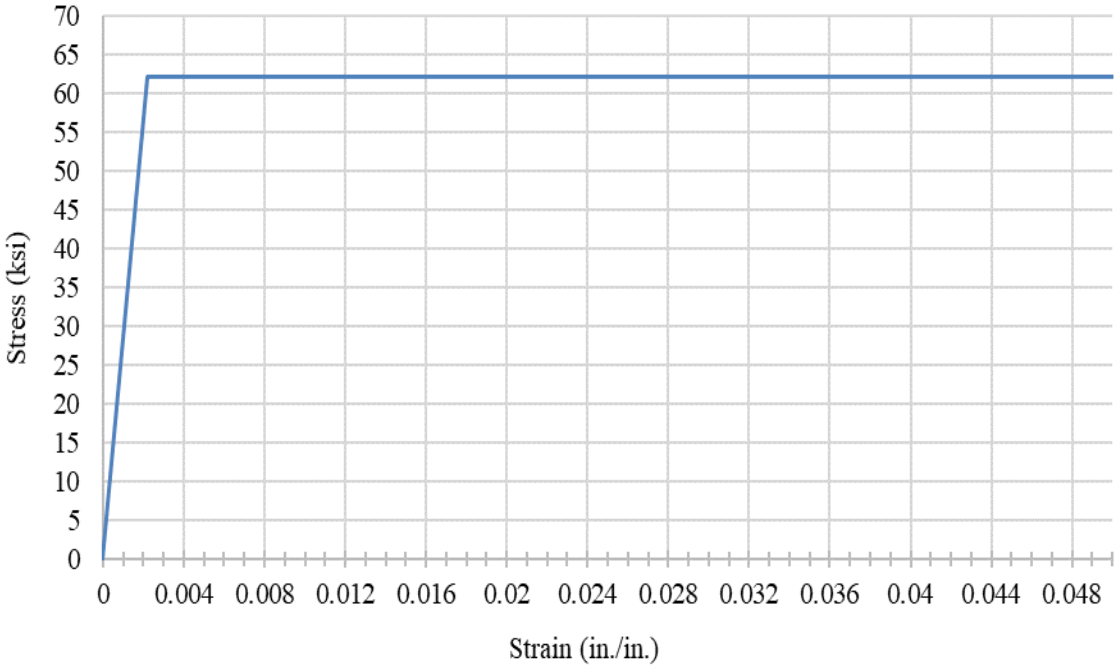

(b) Idealized stress-strain relationship

Figure 5. Stress-strain relationships

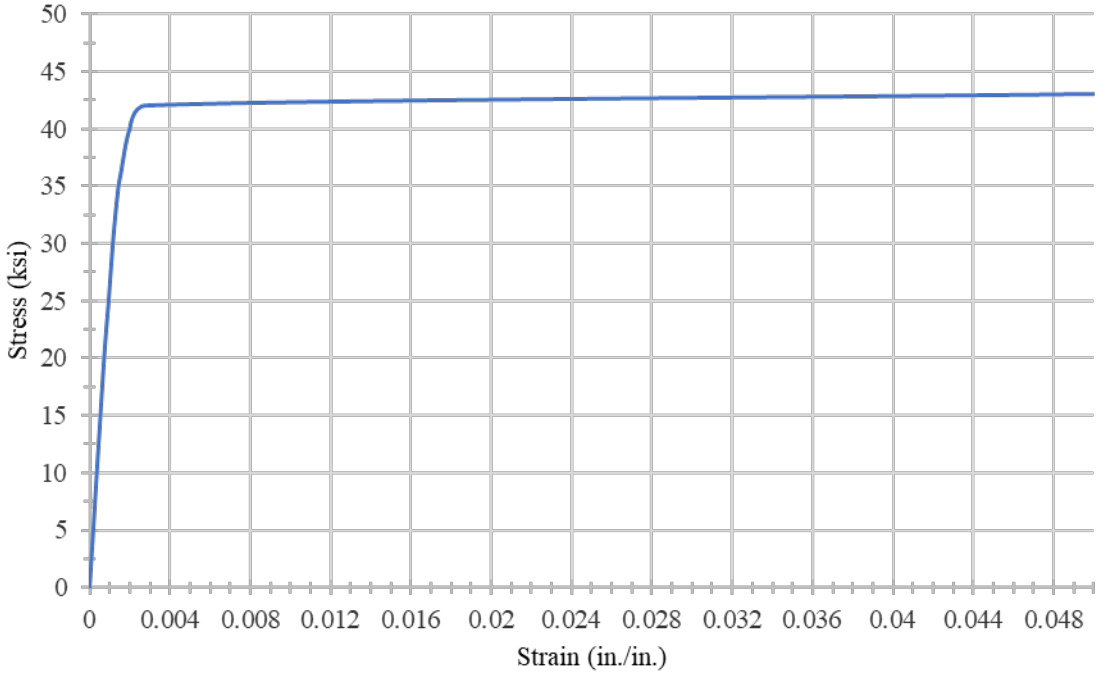

Figure 6. Stress-strain relationship for steel used in cantilever specimen

2.1.2 Lead Dampers

Figure 7 shows the dimensions of the lead dampers used for the cantilever tests and are spherical in shape with a narrow slot used for attachment to a string. The string with the lead dampers is then suspended inside the steel member. The lead dampers used in the model test frame had diameters of 0.15-in. for the exterior columns, and 0.20-in. for the damping panels in the model frame.

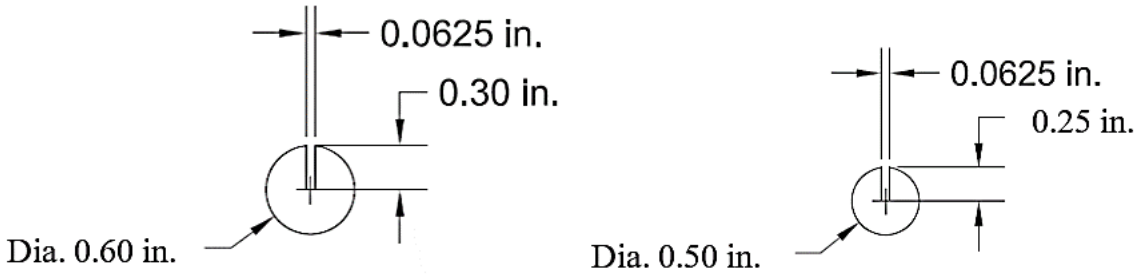

Figure 7. Dimension of lead dampers used for cantilever tests

2.2 Test Specimens

Two different structural models are studied in this research. The first model is a three-dimensional 3-story 3x2-bay steel building frame. As shown and mentioned before, this frame is made of hollow square section steel members. The second model is a 107-in. long, 1.745-in. diameter, hollow circular section steel cantilever. Each of the two models and the testing procedures are explained in the following sections.

2.2.1 Steel Building Frame Model

A three-story three-bay by two-bay frame is used for both natural vibration and impact tests. The columns and the beams have the same cross-section and are made of

hollow square 0.5x0.5x0.0625 in. tubes. A shown in Figure 8(a), the impact load is applied at the mid-height of the ground-level column by means of a swinging steel pendulum from distance of q from the tip of the hammer head to the mid-height of the ground-column. The weight of the ‘hammer head’ is 38-lb and its stem weighing 24-lb.

As shown in Figure 8(a), Six accelerometers numbered 1 through 6 are installed on the frame to measure acceleration versus time relations on the three floors as shown. Accelerometers are mounted on the steel pendulum; one on the hammer head and the other one at the mid-height of the stem. These accelerometers provided acceleration-time relations later used to generate the forcing function F(L/2,t). It was found that the acceleration on the hammer head gave the same acceleration-time relation as that on the stem. Thus, it was decided to use the output from the accelerometer on the hammer head to generate F(L/2,t).

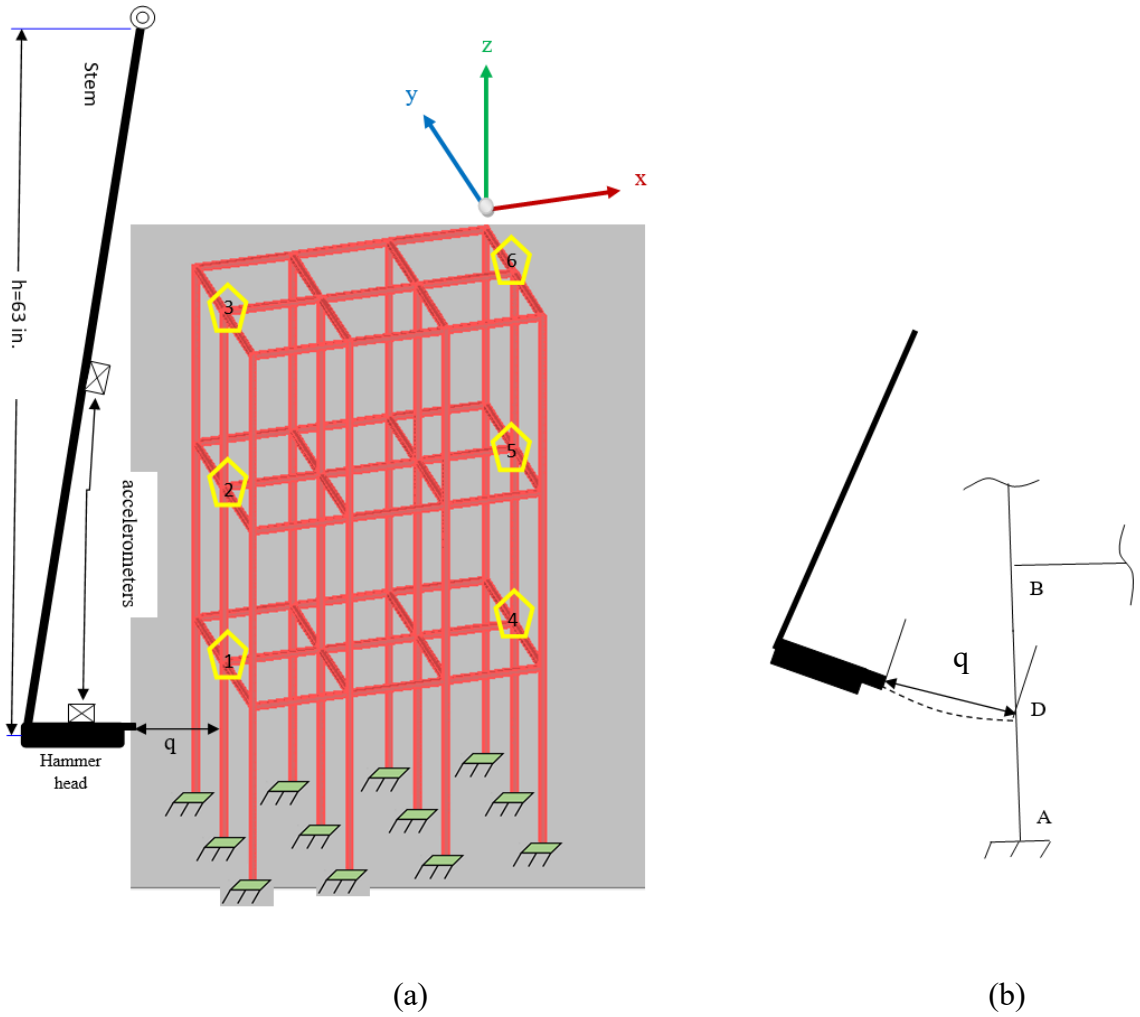

(a) (b)

Figure 8. (a) Steel frame subjected to impact load, (b) Schematic of column AB at a distance q from pendulum hammer head

2.2.1.1 Lead dampers in all exterior columns

The following three different lead damper configurations were used for the frame model tests on the x-axis direction:

1. Twelve 0.15-in. diameter lead dampers with a center-to-center spacing of 4.0-in.
2. Twenty-four 0.15-in. diameter lead dampers with a center-to-center spacing of 2.0-in.
3. Forty-eight 0.15-in. diameter lead dampers with a center-to-center spacing of 1.0-in.

The building frame model is tested again, but this time on the y-axis for the same impact load intensity hitting the two middle ground-columns simultaneously to observe the impact of suspended lead dampers on the y-axis as shown in Figure 9.

2.2.1.2 Panels with welded or bolted damping panels

Figure 10 shows the welded cold-formed steel panels mounted in frame bents J1-J2-J3-J4 and J5-J6-J7-J8 identified in Figure 1(a). Each panel is made of five thin-wall (0.05 in. thick) pipes with an inner diameter of 0.60 in., the pipes have 0.38 in. hole sizes at the top part as shown in Figure 11. The holes are to insert the 0.2 in. diameter lead dampers into the damping panel members. The frame is tested once when the exterior columns have the 1-inch spaced 0.15 in. lead dampers (48 lead dampers in each exterior column) and the empty welded steel damping panels are installed (tac-welded) to the frame. Then, the frame is tested again to the same impact load when 15 0.2 in. lead dampers with one-inch spacing are inserted into the welded panel pipes, the 15 lead dampers are attached to the strings and tightened to the top and freed at the bottom. The same procedure is repeated with the same sets of panels with the only difference of instead of welding the 15 in. pipes to the top and bottom of the panel flange, they are bolted as shown in Figure 12 and each panel member has fourteen lead dampers each with a diameter of 0.2 in.

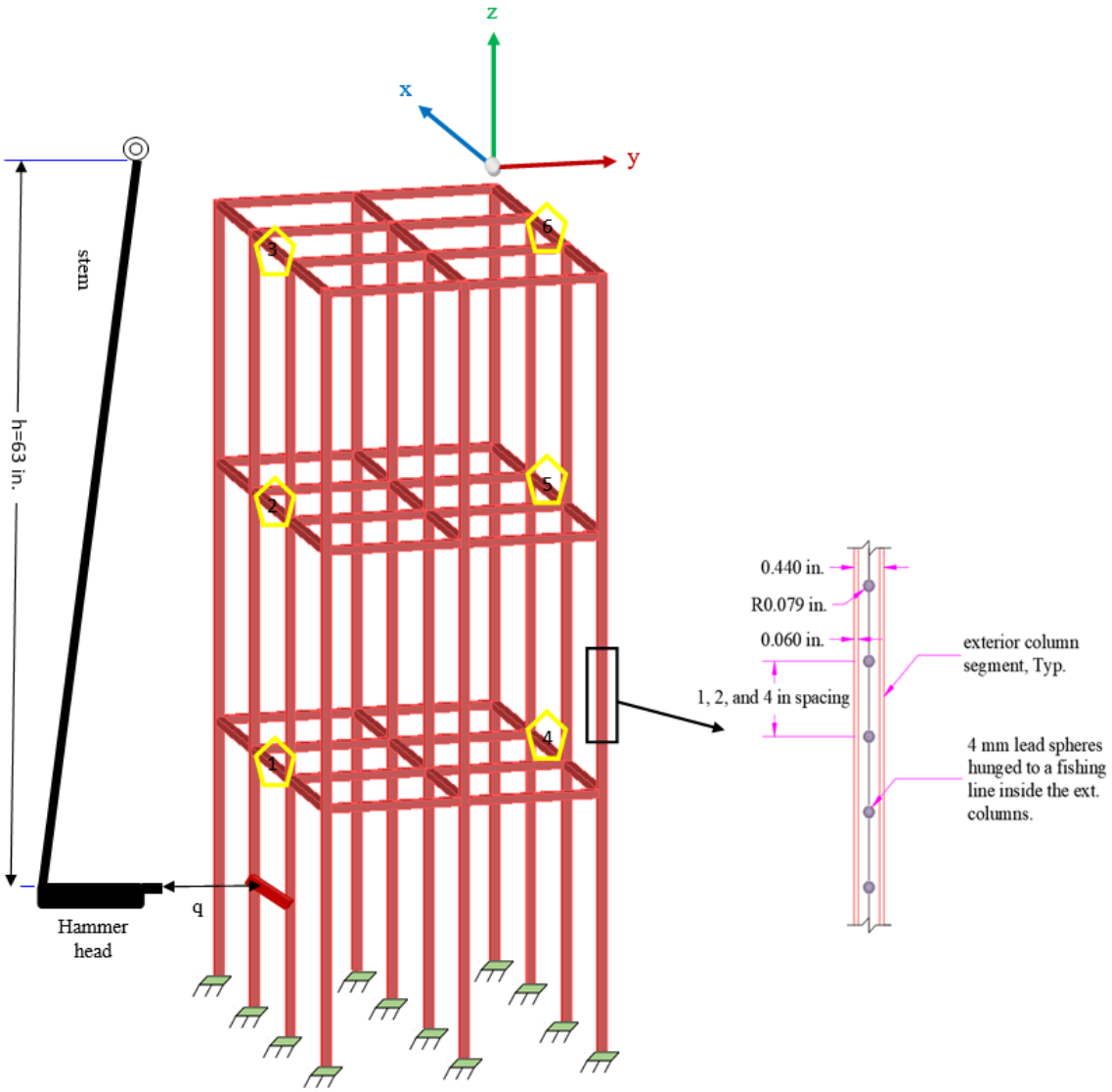

Figure 9. Steel frame subjected to impact load along y-axis

Figure 10. Frame with welded damping panels in bents J1-J2-J3-J4 and J5-J6-J7-J8

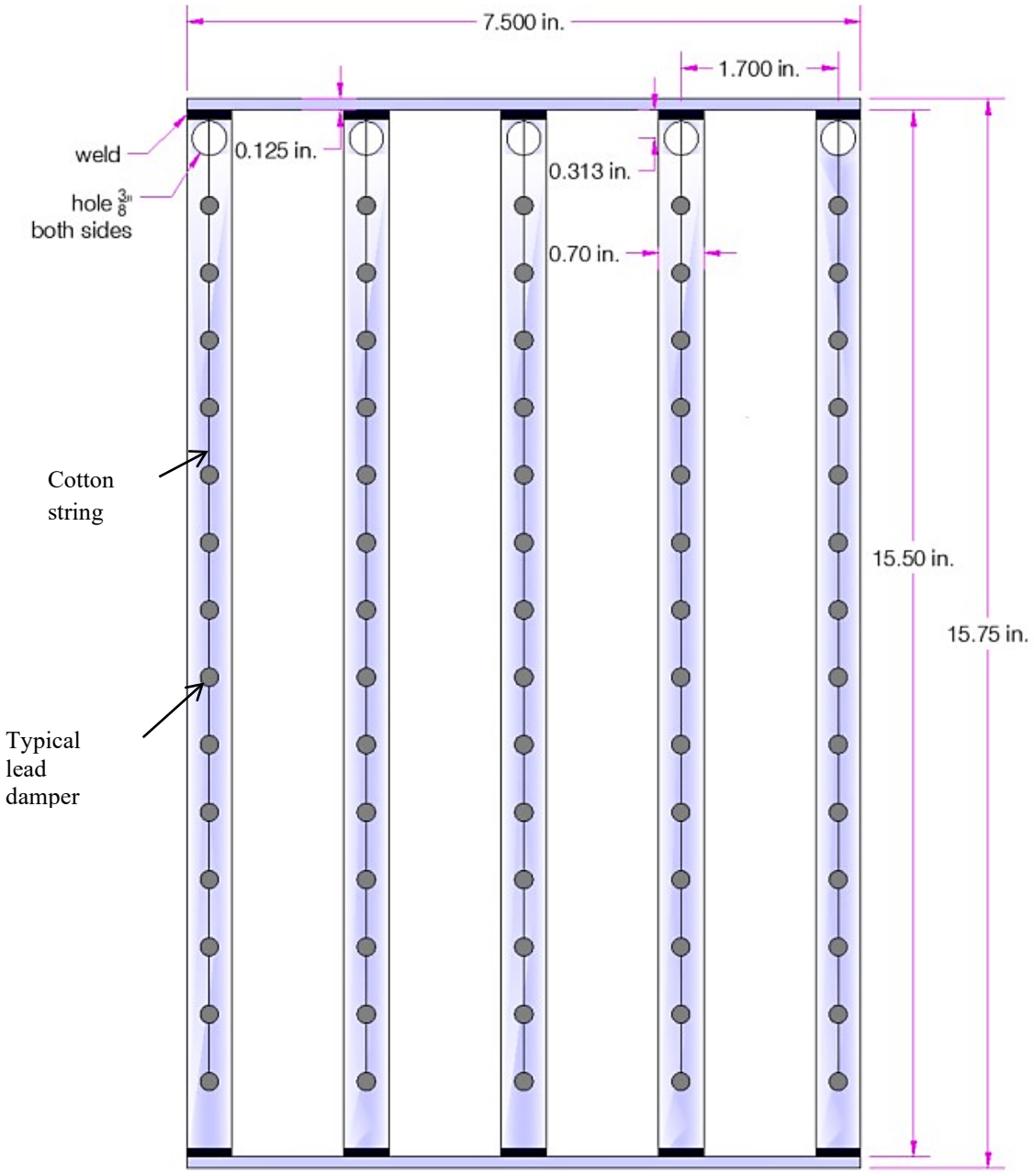

Figure 11. Details of a typical welded steel damping panel

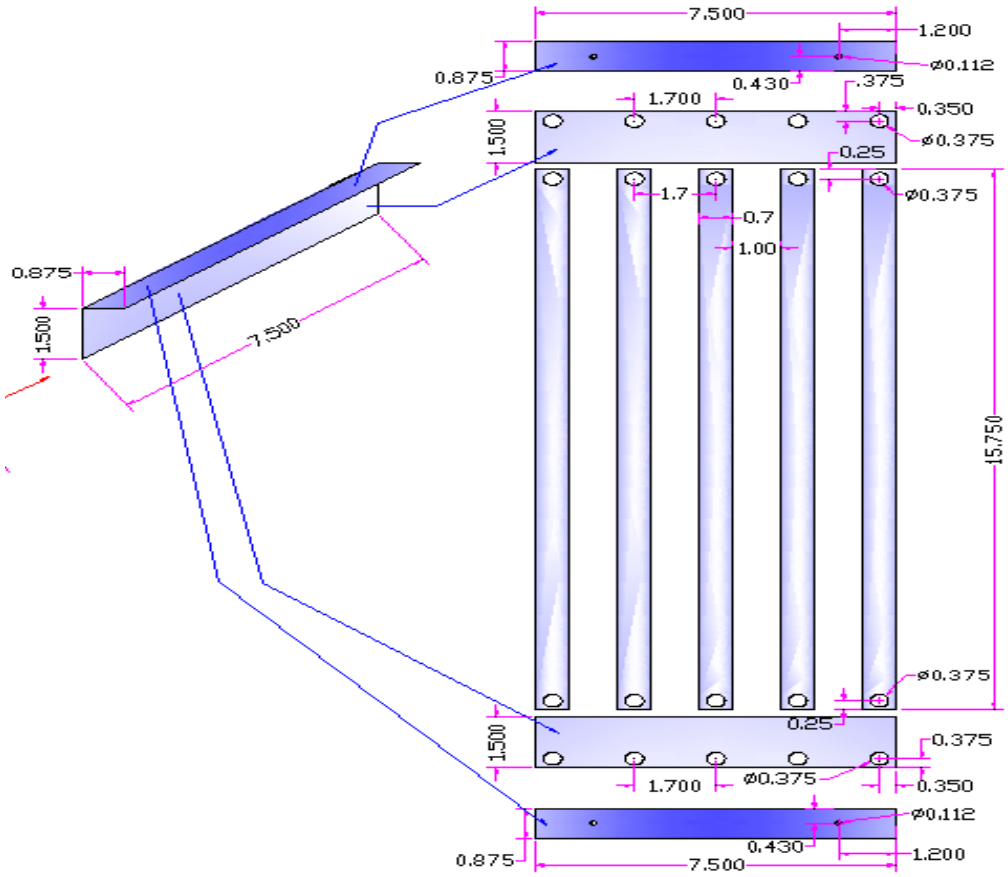

Figure 12. Details of a typical bolted steel damping panel

2.2.2 Steel Cantilever with Lead Dampers

Figure 13 shows a full-scale steel cantilever made of a 107-in. long hollow circular member with an outer diameter of 1.745 in. and a wall thickness is 0.0625 in. The cantilever is welded at the top and free at the bottom. Three wireless accelerometers are installed at 1/5L, 1/2L, and at L (free end). The cantilever is excited by a pendulum weighing 10.5 lb. The pendulum is installed to a 50 inches long cotton robe and released 19 inches away from the free end of the cantilever.

For the cantilever, two different lead damper sizes are used, separately, 0.5 in. diameter and 0.6 in. diameter lead dampers. The first case is attaching the 0.5 in. diameter

lead dampers to a cotton string every 4 inches (27 lead dampers in total) along the 107-in. long cantilever, then changing the lead damper spacings to 2 in. (53 lead dampers), respectively. For each case, the cantilever is excited by the pendulum shown in Figure 14. The same procedure is repeated to the 0.6 in. diameter lead dampers, the same distribution, and the same applied impact load.

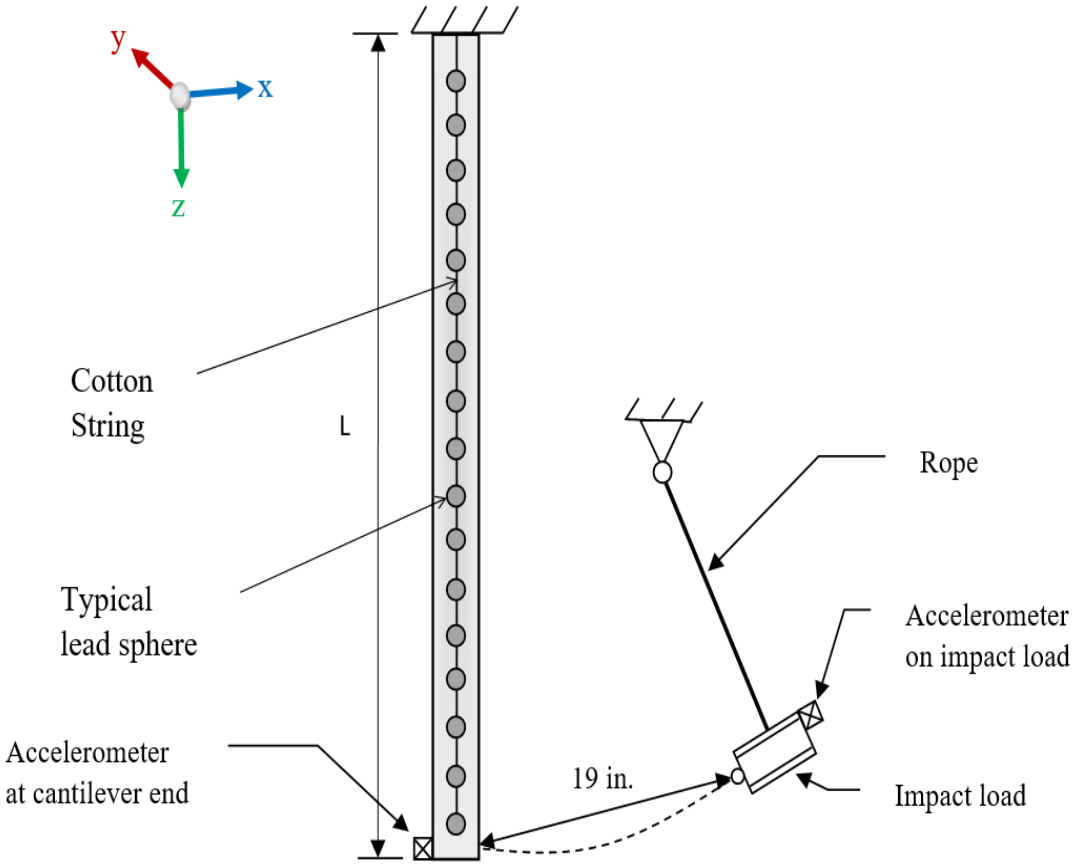

Figure 13. Schematic of cantilever test setup

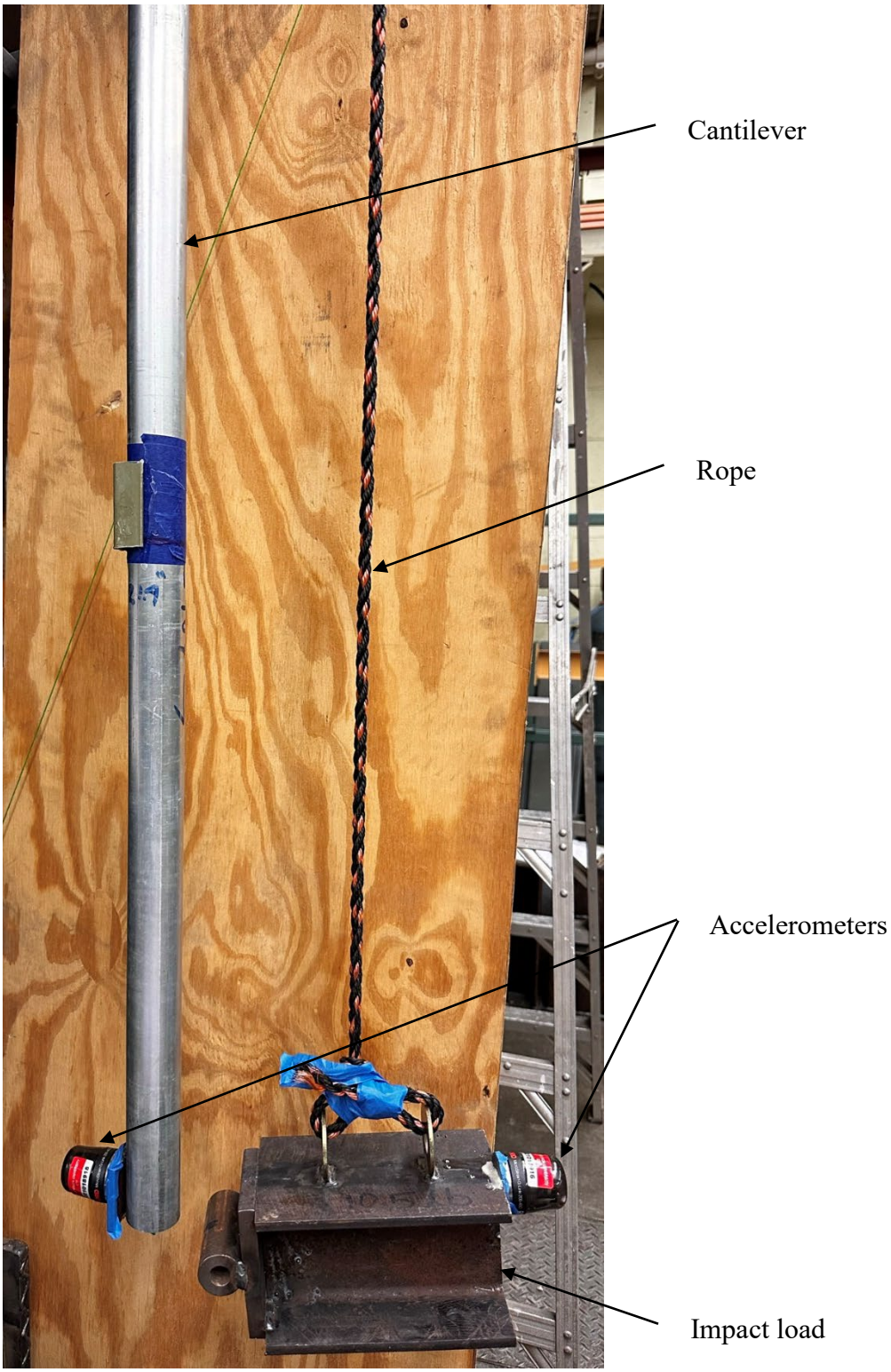

Figure 14. Apparatus for cantilever test

2.3 Test Setups and Procedures

The three-story steel building frame model and the fixed-end steel cantilever are tested under impact loads generated by pendulum dynamic loads. The test setups and the procedures are explained in the following:

2.3.1 Steel Building Frame Model

The steel building frame model is subjected to a dynamic load generated by a 38-pound pendulum released seven inches away from the frame, also, the stem has a weight of 24 lb. The generated dynamic force hits the ground-level middle ground-column of the frontside of the frame. The generated impact load from the pendulum is calculated after investigating the acceleration of the pendulum from the installed accelerometers on the weight and the lever arm. It is observed that the weight and stem of the cantilever had the same excitement response (acceleration vs time) when the pendulum hit the frame. In the forcing function calculations, both weights, the main weight and the steel elver arm's weight, are summed and included. The acceleration versus time graph of the pendulum weight is shown in Figure 15. Using the MS Excel program, the acceleration-time data is curve fitted to the second-order to define the forcing function $f(t)$ for each pendulum impact load. For the building frame, it is determined that the impact load duration is 0.02122 seconds from initial time, t_i = 0.24959 sec. to time, t_d = 0.27028 sec. the applied dynamic forcing function curve is shown in the load-time Figure 16. The applied forcing function given in Equation 1 is shifted to start at t = 0 sec. to t = 0.02069 sec.

$$F\left(\frac{L}{2}, t\right) = (-45300t^2 + 937.2t) \times 62 \quad (1)$$

For t = 0.01 sec., this equation gives the applied force amplitude, F_{max}, as F_{max} = 300 lb.

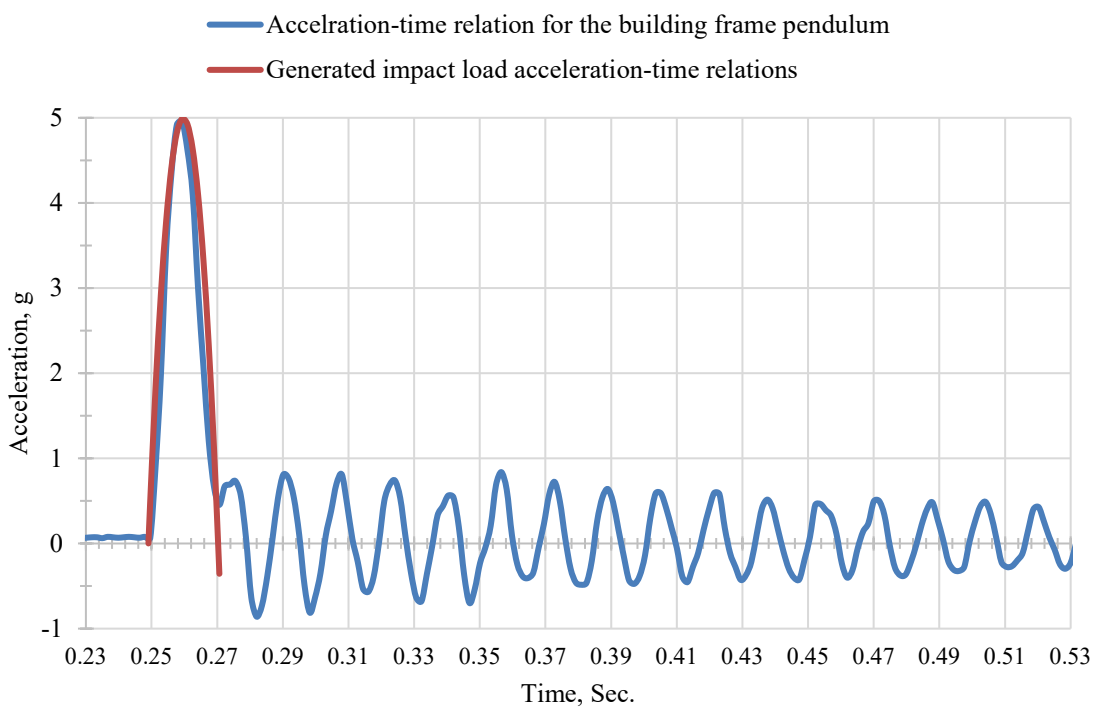

Figure 15. Hammer head accelerometer output for frame model test with q = 7.0-in.

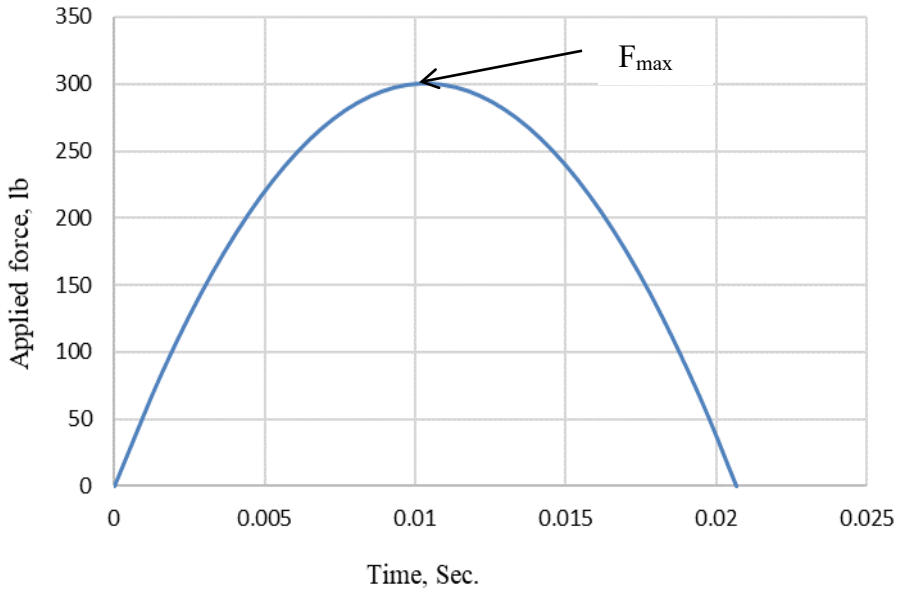

Figure 16. Impact forcing function for frame model with q = 7.0-in.

2.3.2 Steel Cantilever

For the steel cantilever, the pendulum shown in Figure 14 is used, the pendulum has a weight of 10.5 lb. The weight is released from 19 inches away from the free end of the cantilever. The generated acceleration versus time after hitting the end tip of the cantilever is shown in Figure 17 for two trials, the generated acceleration versus time relations is simplified to fit both trials. The impact force curve is shown in Figure 18, where t_i = 0.00 second and t_d = 0.03 second. The applied forcing function is given by:

$$F(L,t) = 100 \times Q \times t_d \times \left(\sin\frac{\pi t}{t_d}\right) \quad (2)$$

In this equation, Q is the impact load shown in Figure 13, and is equal to 10.5 lb, t_d = 0.03 sec. from Figure 17.

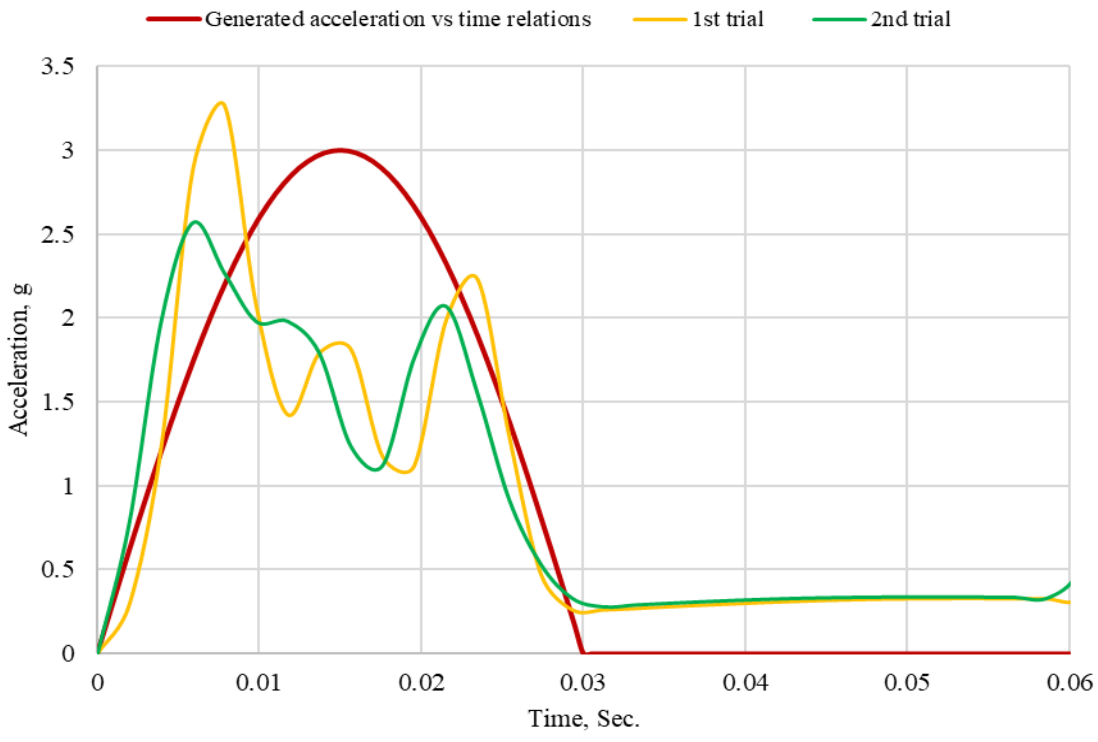

Figure 17. Impact load acceleration-time relations for cantilever

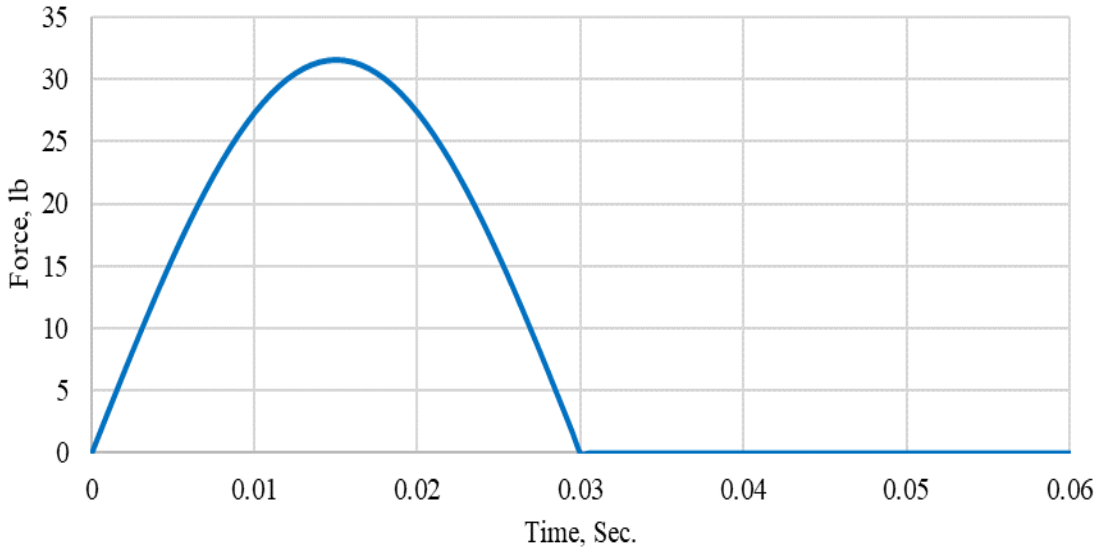

Figure 18. Impact forcing function for cantilever

2.4 Measurement of Acceleration

Wireless accelerometers used in the research are manufactured by "Parker Lord". The wireless accelerometers are 10G and 40G range [47]. Both accelerometers run on the same computer program, Node Commander. The adjustable ranges are 2/4/8/10/20/40G. They are extremely low noise, 25-80 $\mu g/\sqrt{Hz}$. They can be set up on various frequencies. The accelerometers are triaxial, they have the capability of collecting data on three different axes, simultaneously. The 40G accelerometer has a wireless range as far as 6600 ft. Operating temperature range is -40 to +185 F°. The sensitivity range is ±0.01%/°C. The accelerometers are wirelessly connected to a base station, model WSDA-Base, the base station is connected to the computer to transfer received data to the computer program. The base station can receive up to four data from four different accelerometers at the same time.

For the building frame, six wireless accelerometers are installed, at each floor, two wireless accelerometers are installed; one on the front side of the building, and another one on the back of the building. The wireless accelerometers are named node 1 through node 6 as shown in Figure 9. The steel cantilever has three wireless accelerometers each at locations 1/5L, 1/2L, and at the free end (L).

2.5 Natural Frequency Tests

For each of the testing models, natural frequency of each model is calculated after pulling the model and releasing it for free vibration. The natural frequency results obtained from the lab are also compared with the natural frequencies obtained from the theoretical analysis of FDM and SAP-2000.

2.5.1 Steel Building Frame Model

The building frame is pulled at two different locations at different times to check for vibration at the first and top floor. First, the top floor is pulled by 0.25 inches on the x-axis direction and then released to obtain the acceleration vs time of the model. Figure 19 and 20 show free vibration of the top floor (Node 3) and the first floor (Node 1), respectively. Using the collected data shown in Figure 19 the natural frequency is calculated as the following:

From Figures 19, it is found that at the top floor (Node 3), and the first floor (Node 1), the Time Period, T_n, is 0.0464 seconds, and the natural frequency, $f = \frac{1}{T} = \frac{1}{0.0464} = 21.57$ Hz.

The natural frequency of the model is found using the computer program SAP-2000 on the x-axis which is 21.08 Hz on the x-axis, and it is 20.62 Hz on the y-axis. The

x-axis natural frequency found on the SAP-2000 is very close to the natural frequency calculated from the collected data on the x-axis direction.

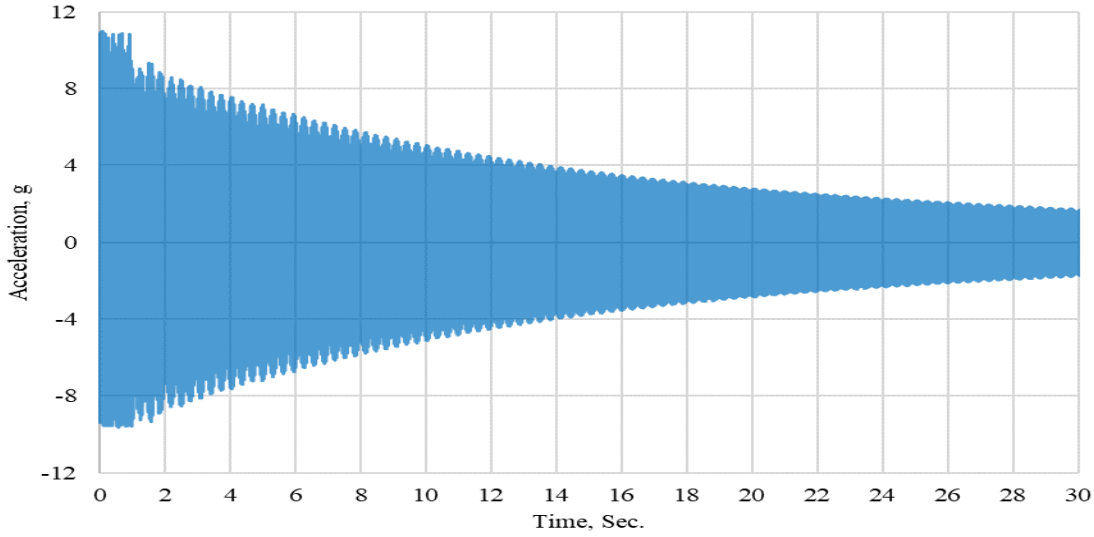

Figure 19. Node 3 acceleration-time relation at top floor for natural vibration test

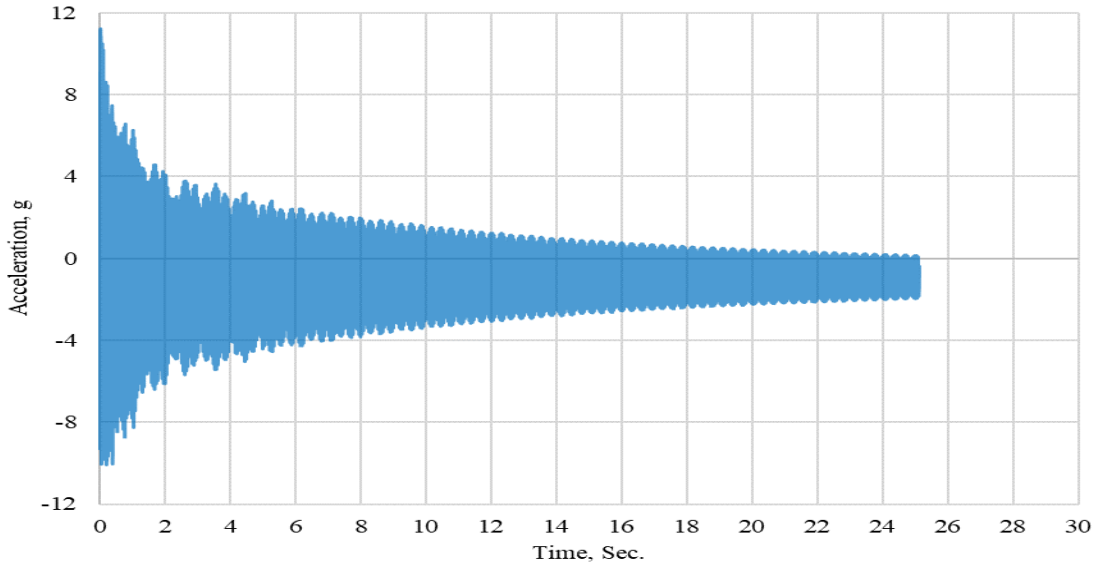

Figure 20. Node 1 acceleration-time relation at first floor for natural vibration test

The second set of natural vibration is observed when the first floor of the building frame (Node 1) is pulled by 0.039 inch (1mm) and released for free vibration. Figure 21

shows data collected on the first floor (Node 1). From Figure 21, it is found that the Time Period, T_n, is 0.0145175 seconds, and the natural frequency is f = 68.88 Hz.

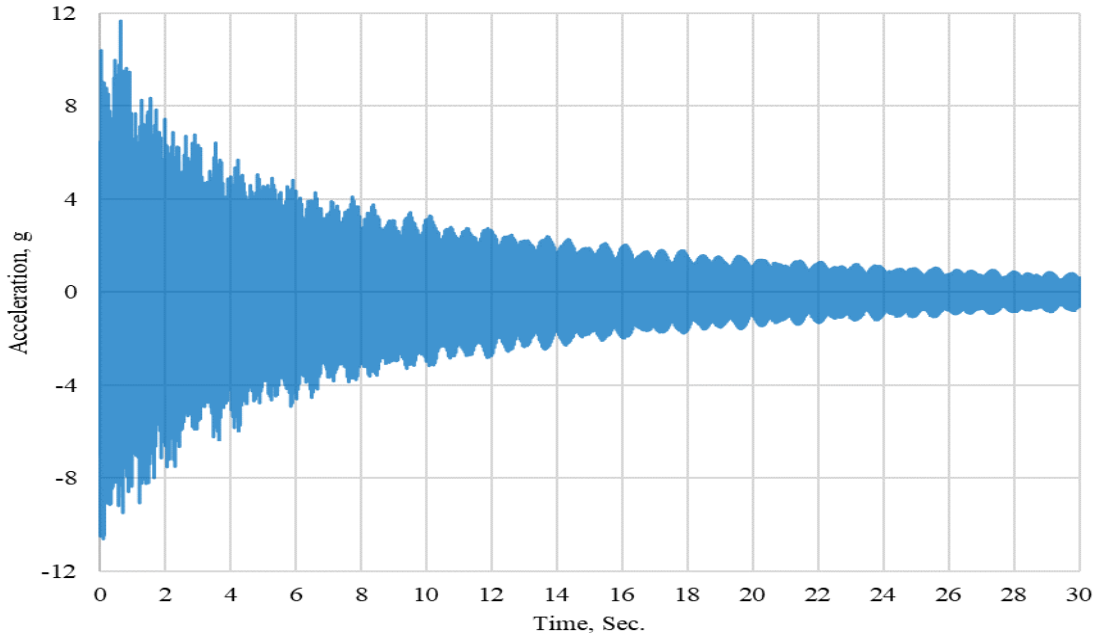

Figure 21 Node 1 acceleration-time relation at top floor for natural vibration test

Figures 19 and 21 show the difference in the building's vibration when the building is pulled at different locations. In the theoretical analysis, the building is excited on the first floor. The natural frequency calculated from Figure 19 is compared to the natural frequency obtained from SAP-2000 and used in the analysis calculations of the building frame, and the natural frequency calculated from Figure 21 is compared to the natural frequencies obtained from both the theoretical analysis of FDM and SAP-2000 for the isolated ground-column AB.

2.5.2 Steel Cantilever

The free end of the cantilever is pulled by 0.25 inches and then released. From the attached three wireless accelerometers along with the member, acceleration vs time data is obtained. The collected data at 1/5L, 1/2L, and at the free end (L) is shown in Figures 22, 23, and 24, respectively. From the following graphs, it is found that the Time Period, T, is 0.199 seconds, and the natural frequency is 5.03 Hz. Using the computer program, SAP-2000, the Time period is 0.187 seconds, and the natural frequency is 5.34 Hz.

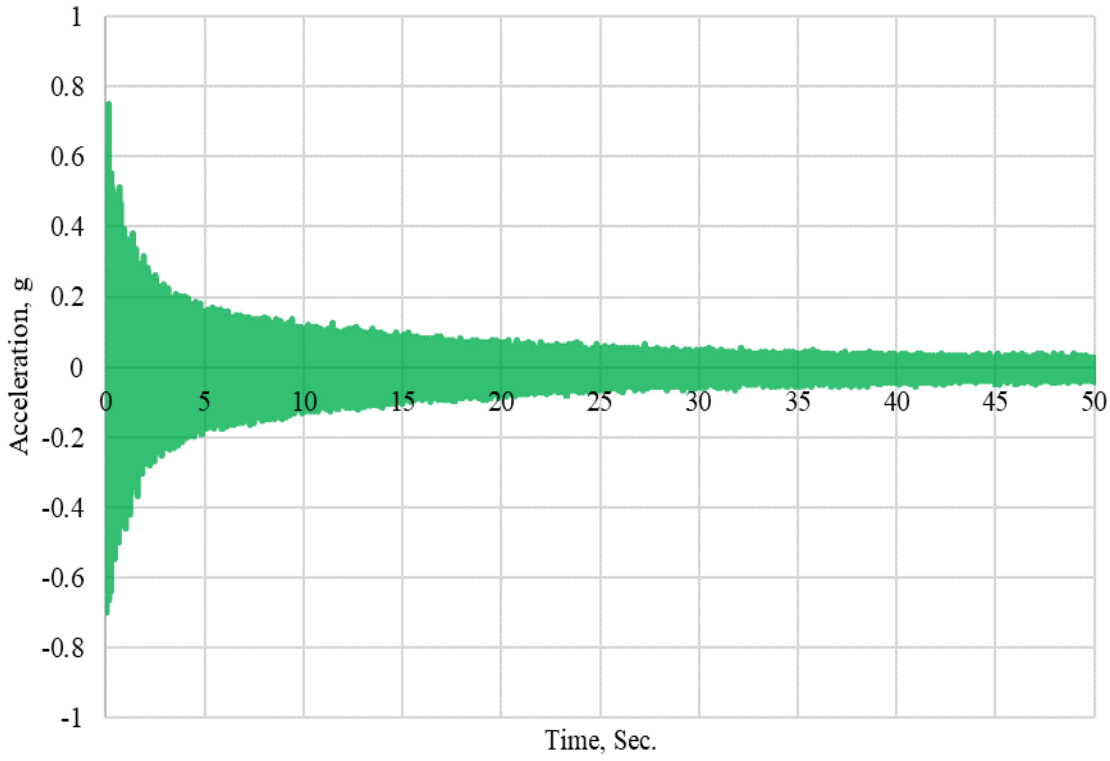

Figure 22. Acceleration-time relation of cantilever at 1/5L

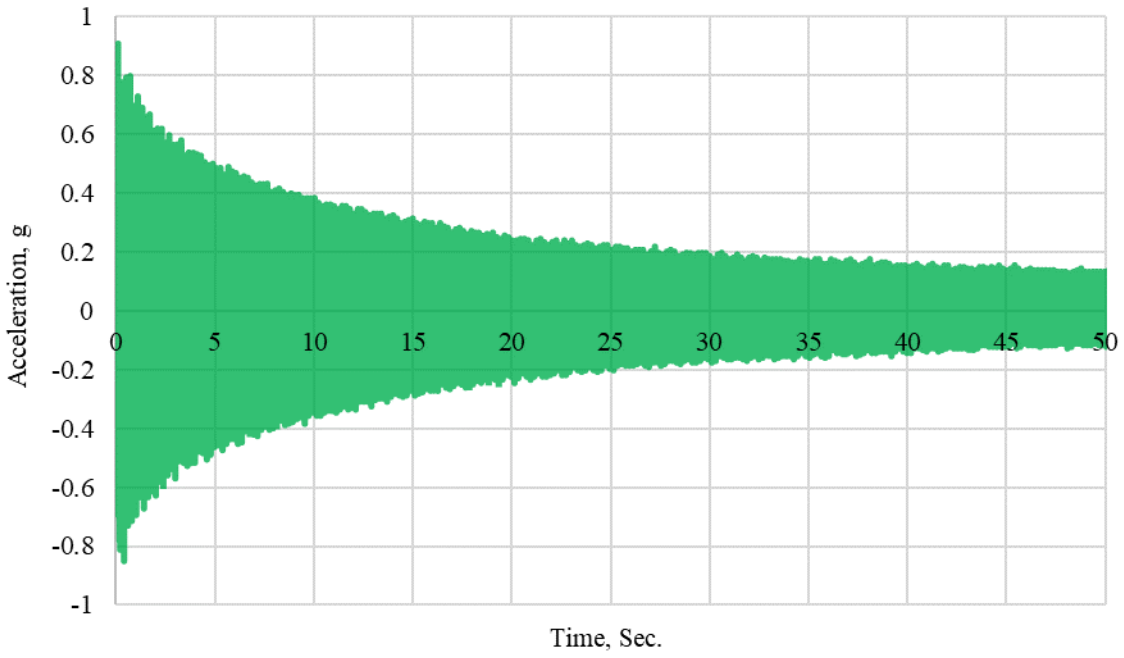

Figure 23. Acceleration-time relation of cantilever at 1/2L

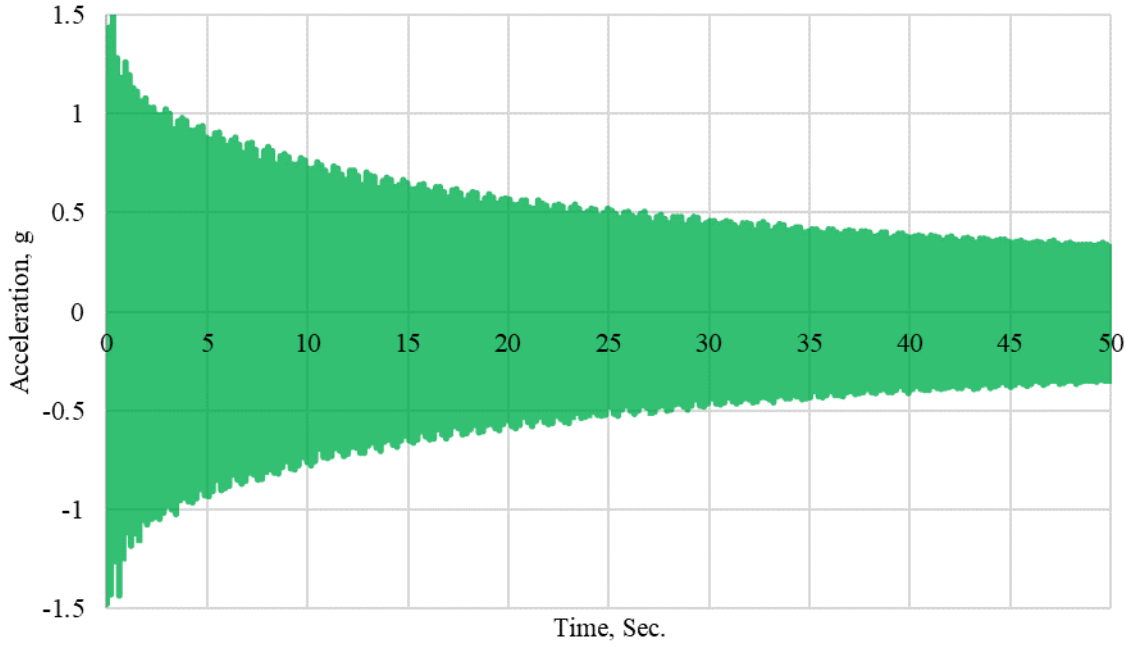

Figure 24. Acceleration-time relation of cantilever at L

2.6 Impact Tests

After the building frame model is excited by the impact load, the data is collected for each of the various lead dampers' schemes through the wireless accelerometers installed at various locations. Then, the frame is rotated 90 degrees to repeat the same procedure on the y-axis.

The steel cantilever is also excited by an impact load at the free end. Excitation of the member is observed at the free end.

2.6.1 Steel Building Frame

The building frame is tested on both x-axis and y-axis with and without the presence of various lead dampers in the exterior columns. At each set of the tests, it is obvious that the top floor was vibrating the most. Because of that, for both axes, the focus is on Node 3 which is located at the top floor of the frame. The building frame is also tested on both directions when the welded or bolted damping panels are installed.

The second test is hitting the middle column on the x-axis with an impact load to form three plastic hinges in the column at the supports and the middle of the column. An approximate estimation is used to estimate the failure impact load by relying on various impact loads and both bending moment and maximum generated force from each impact load at the three locations.

2.6.1.1 Lead dampers in all exterior columns

The building frame is first impacted at the absence of the lead dampers to use the collected data as a reference, Figures 25 and 26 show the building's response at the top floor, Node 3, that are used as reference data for each x-axis and y-axis, respectively. The

same intensity of impact load is applied to the frame for each of the various schemes when lead dampers are installed in the building. Figures 27, 28, and 29 show the building's response when 12, 24, or 48 lead dampers are installed in each of the exterior columns and the building is excited on the x-axis direction, respectively. Figure 30 shows the building response when 48 lead dampers are installed in each of the exterior columns and the building frame is excited on the y-axis.

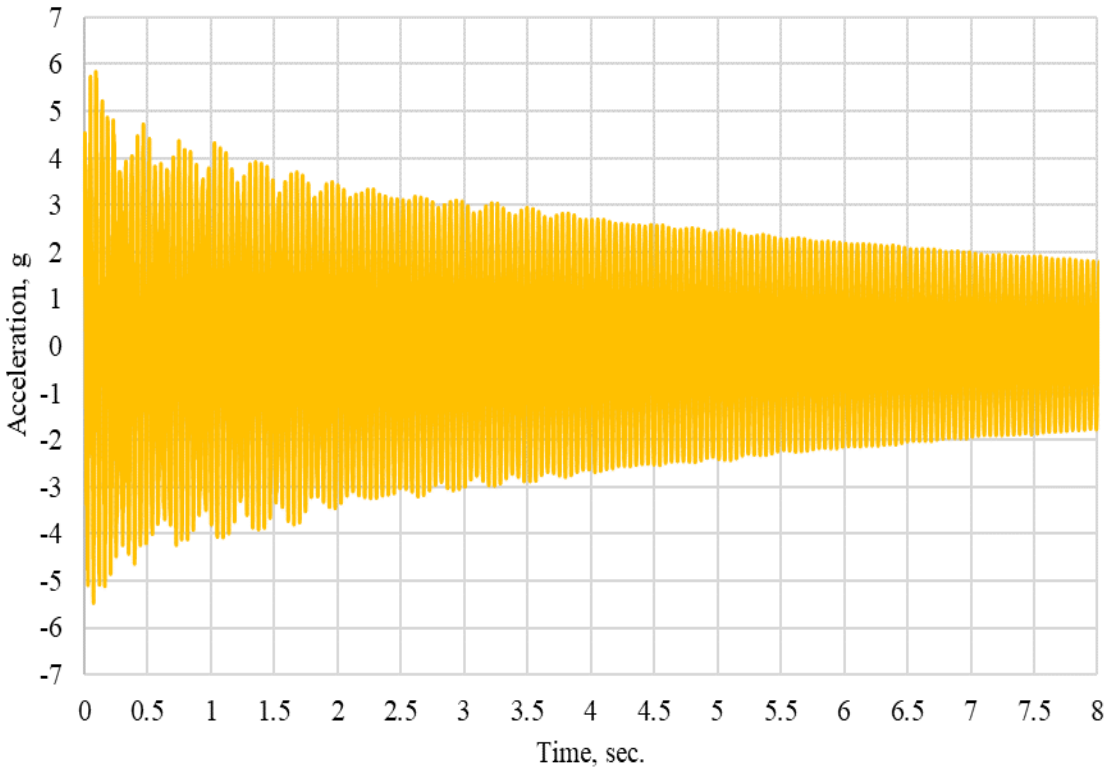

Figure 25. Node 3 acceleration-time relation of frame model along x-axis without lead dampers

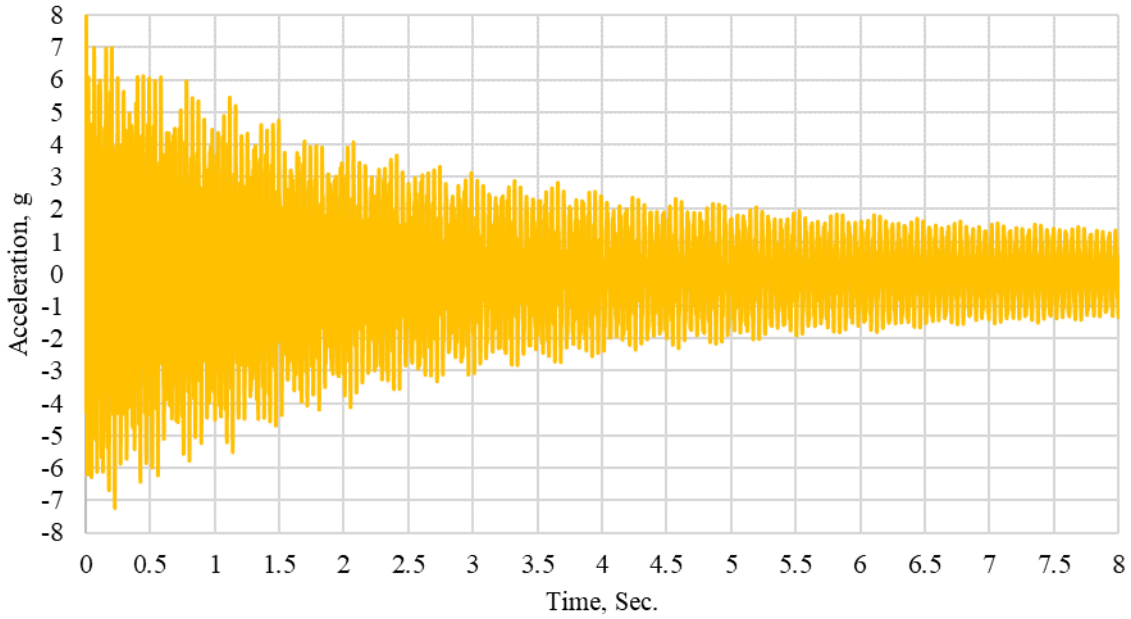

Figure 26. Node 3 acceleration-time relation of frame model along y-axis without lead dampers

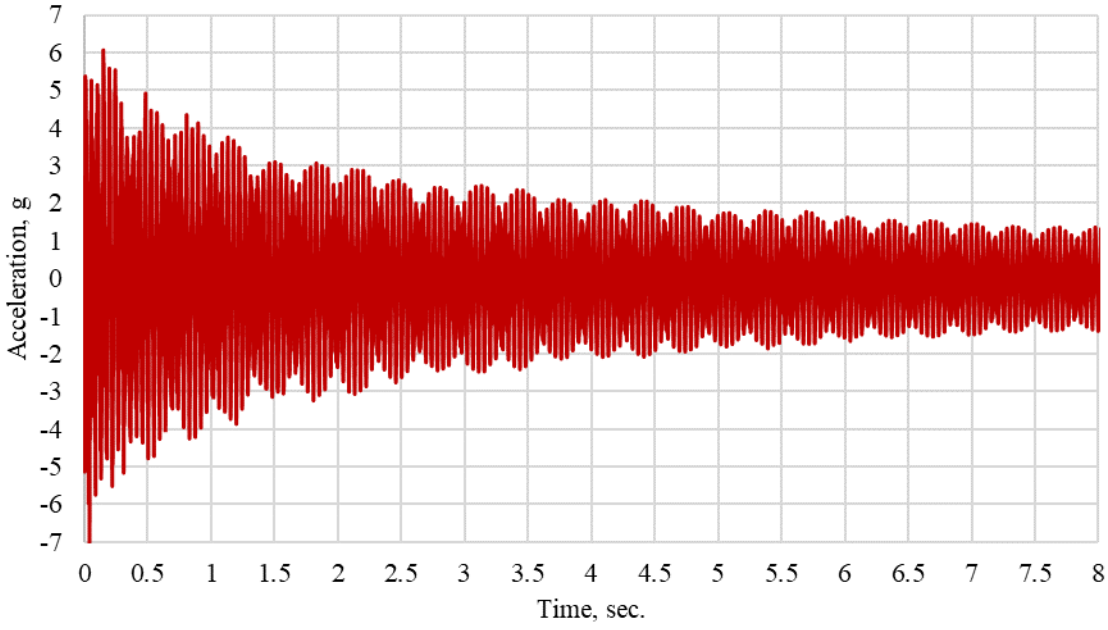

Figure 27. Node 3 acceleration-time relation of frame model along x-axis with 12 lead dampers

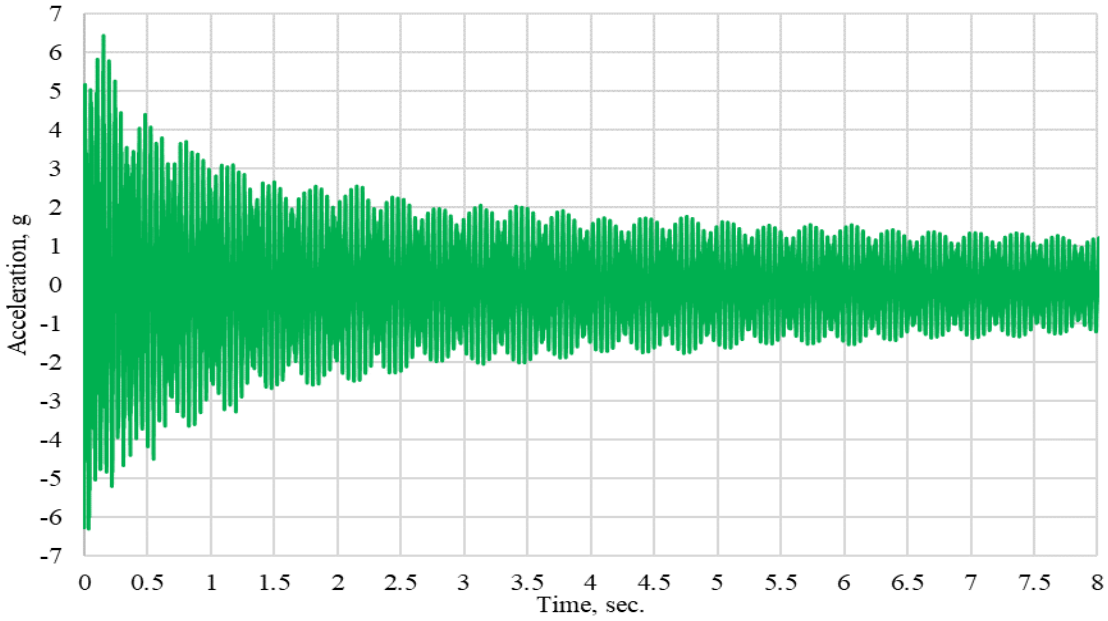

Figure 28. Node 3 acceleration-time relation of frame model along x-axis with 24 lead dampers

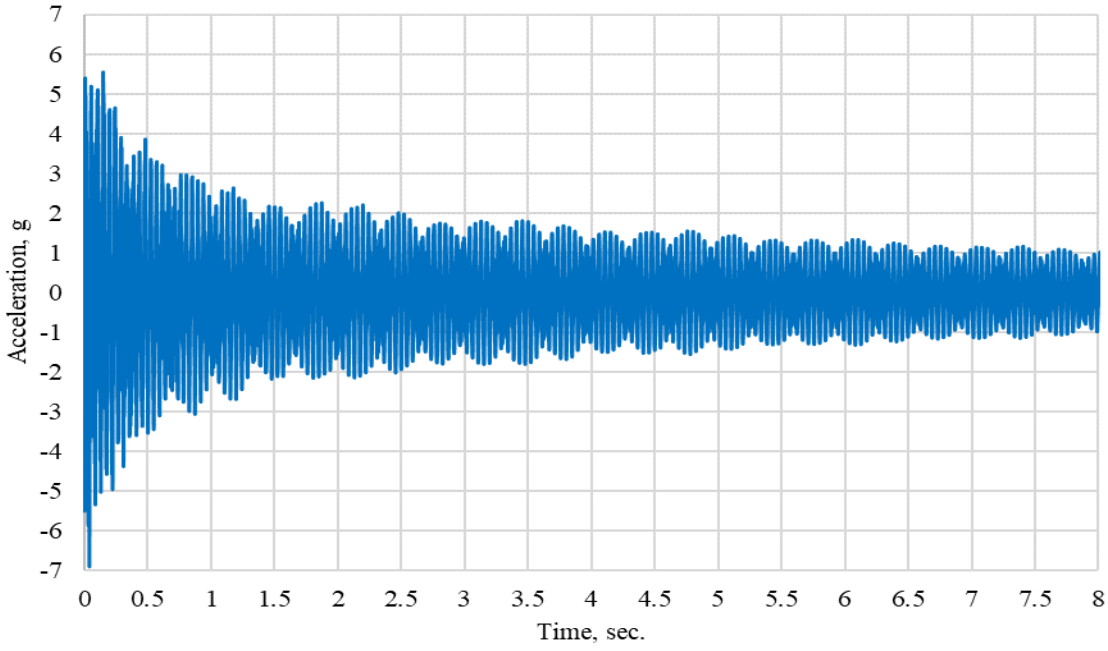

Figure 29. Node 3 acceleration-time relation of frame model along x-axis with 48 lead dampers

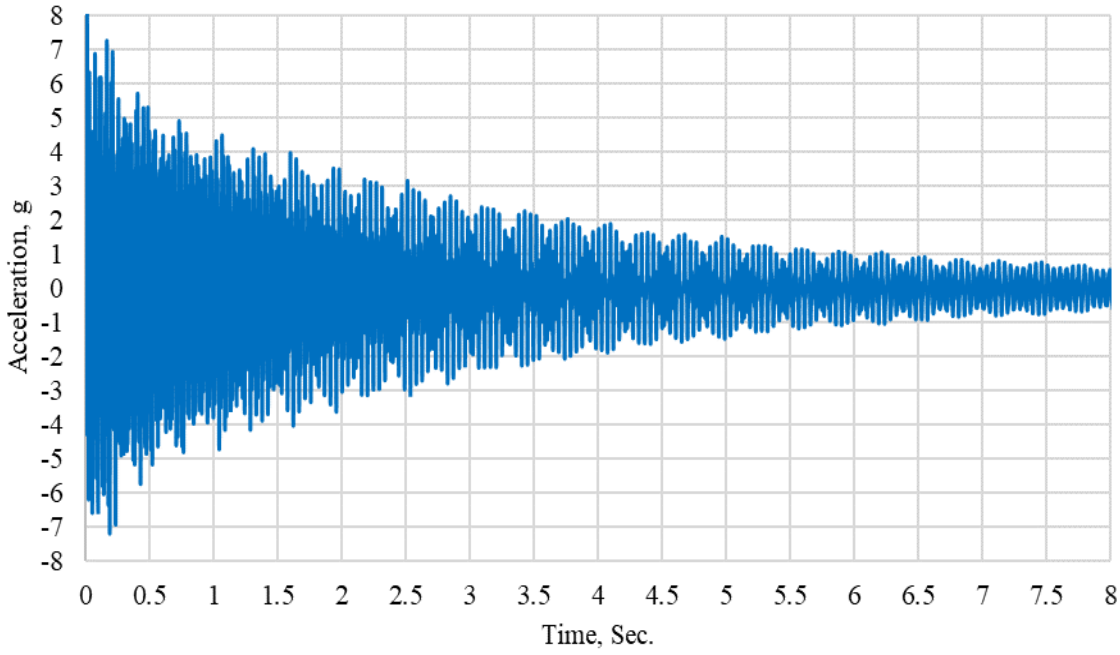

Figure 30. Node 3 acceleration-time relation of frame model along y-axis with 48 lead dampers

2.6.1.2 Welded damping panel along x-axis

The second scheme is installing tac-welded steel panels mounted in frame bents J1-J2-J3-J4 and J5-J6-J7-J8 with the 48 lead dampers in each of the exterior columns. The frame is tested before and after installing 15 lead dampers of diameter 0.2-in. to nylon strings and tightened to the top and freed at the bottom. Figures 31 show the building's response when the empty panels are added, and Figure 32 show the building's response when the lead dampers are added to the damping panels.

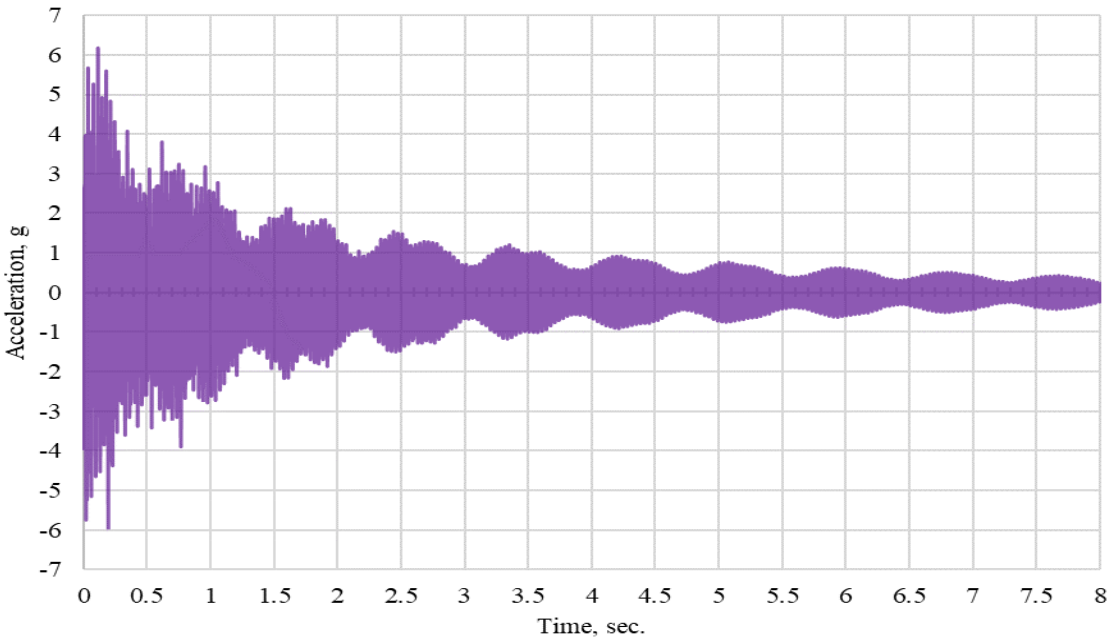

Figure 31. Node 3 acceleration-time relation of frame model along x-axis with empty welded panels and 48 lead dampers in the exterior columns

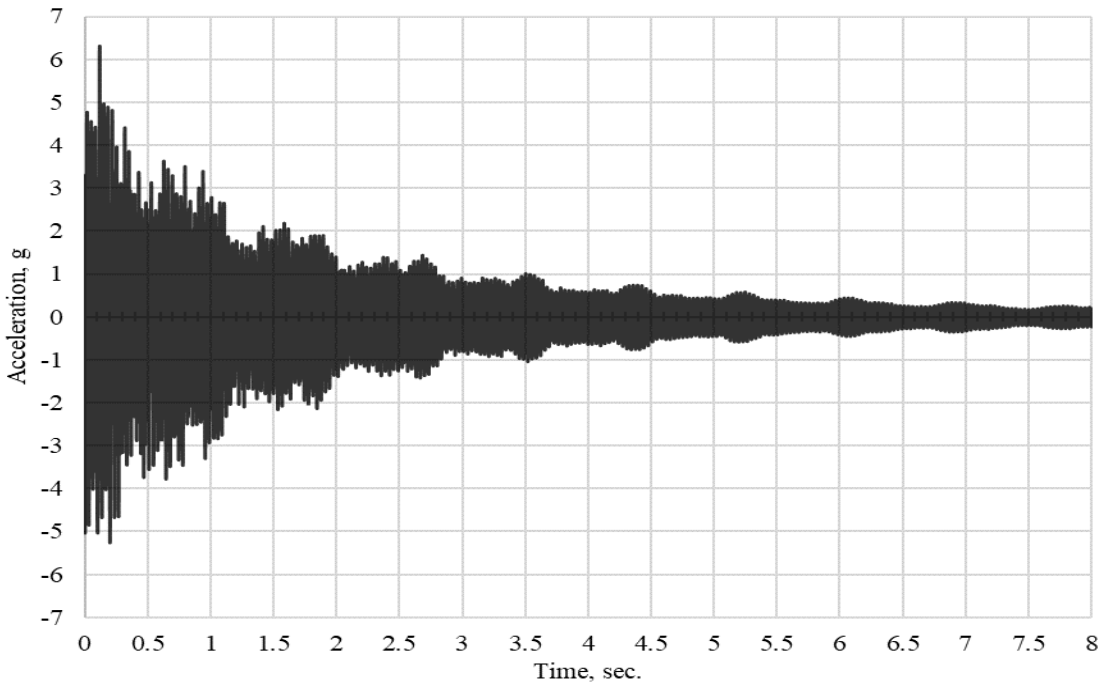

Figure 32. Node 3 acceleration-time relation of frame model along x-axis with welded panels including 15 lead dampers in each and 48 lead dampers in the exterior columns

2.6.1.3 Bolted damping panel along x-axis

The same procedure explained in the previous section, section 26.1.2, is repeated in this section, except, this time, the panels are bolted, instead. Details of the bolted panels are shown in Figure 14. Figures 33 and 34 show the impact of both the empty bolted panels and the bolted panels with 14 0.2-in diameter lead dampers in each panel column, respectively, on decreasing vibration in the frame significantly.

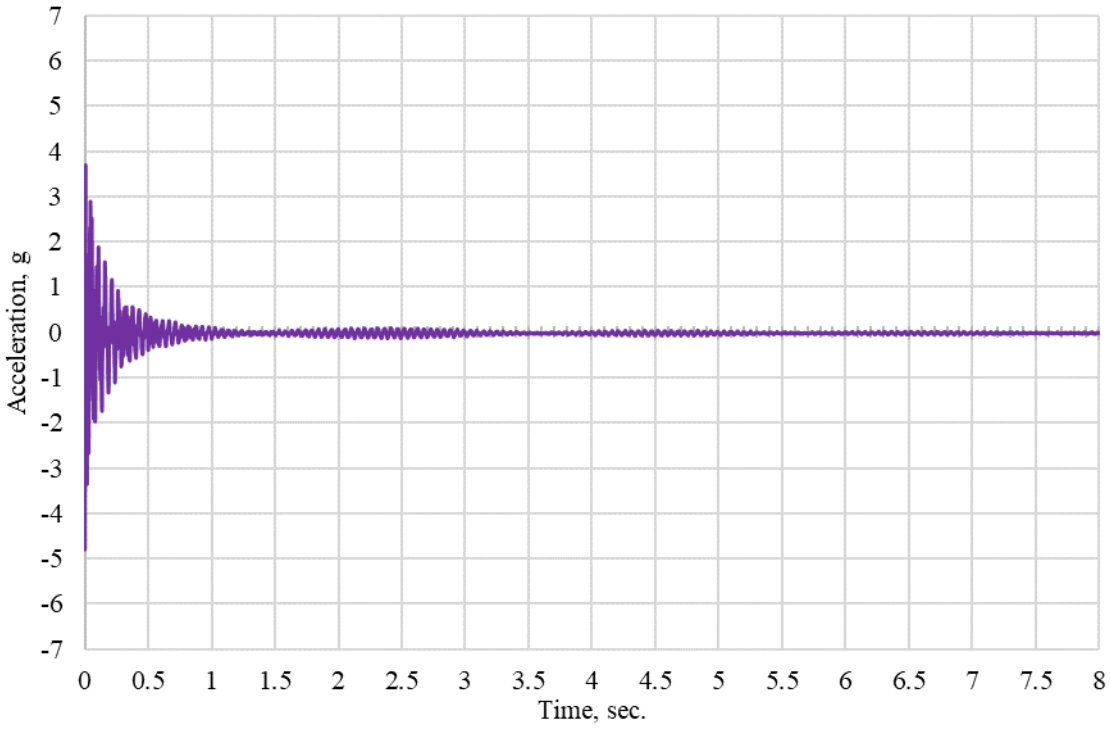

Figure 33. Node 3 acceleration-time relation of frame model along x-axis with empty bolted panels and 48 lead dampers in the exterior columns

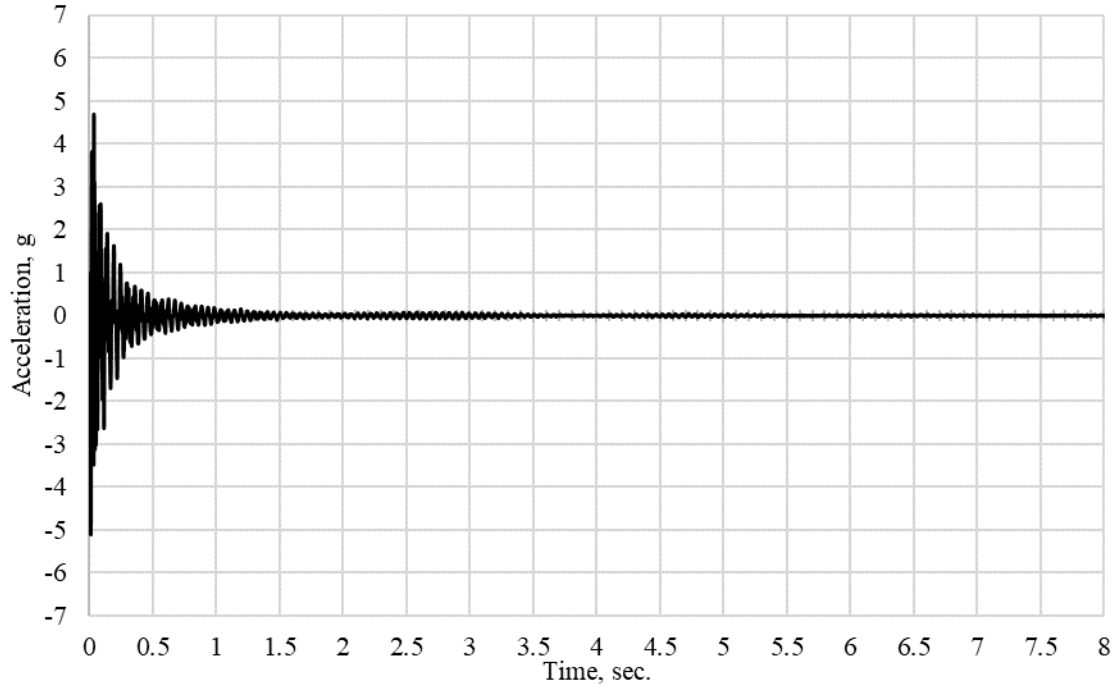

Figure 34. Node 3 acceleration-time relation of frame model along x-axis with bolted panels including 14 lead dampers in each and 48 lead dampers in the exterior columns

2.6.1.4 Bolted damping panel along y-axis

On the y-axis, steel panels mounted in frame bents J1-J2-J6-J5 and J4-J3-J7-J8 with the 48 lead dampers in each of the exterior columns. The same panel size and number of lead dampers are used on the y-axis. Figures 35 and 36 show the impact of both the empty bolted panels and the bolted panels with 14 0.2-in diameter lead dampers in each panel column, respectively.

2.6.2 Steel Cantilever Test with Lead Dampers

Two different lead damper sizes, 0.5 in.-diameter and 0.6 in. diameter lead dampers, are installed in the steel cantilever. The first scheme is attaching the 0.5 in. diameter lead dampers to a string at every 4 inches (27 lead dampers in total) along the 107-in. long cantilever, then changing the lead damper spacings to 2 in. (53 lead

dampers). For each case, the cantilever is excited by the pendulum's generated forcing function shown in Figure 15. The same procedure is repeated with the second lead damper, 0.6 in. diameter.

The cantilever is first impacted by the 10.5-lb pendulum to collect data at the free end to use it as a reference, then, the same intensity of impact load is applied to the cantilever for each of the various schemes. Figures 37 and 38 show the cantilevers response when 27 or 53 0.5 inches dead dampers are installed, respectively. Furthermore, Figures 39 and 40 show the cantilevers response when 27 or 53 0.6 inches dead dampers are installed in the cantilever.

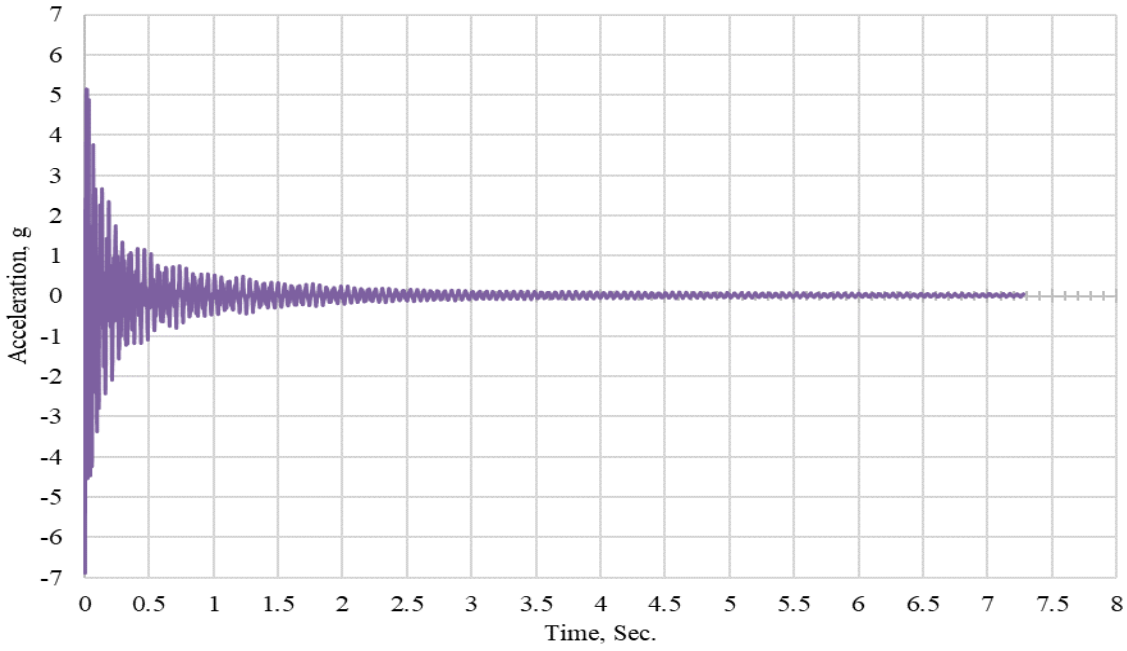

Figure 35. Node 3 acceleration-time relation of frame model along y-axis with empty bolted panels and 48 lead dampers in the exterior columns

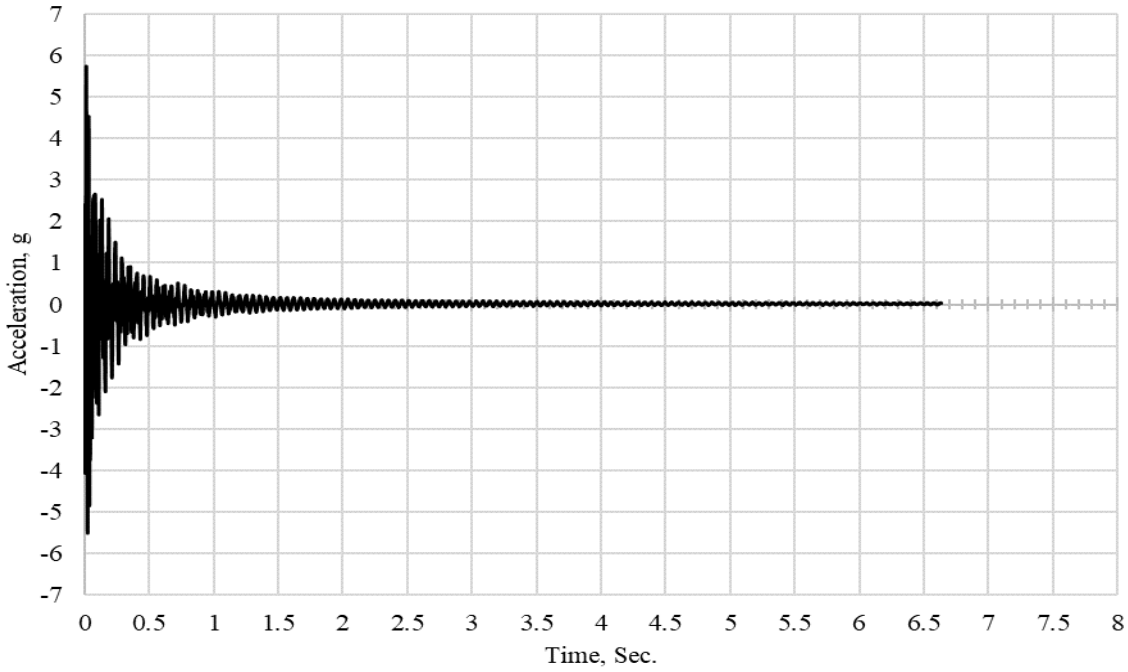

Figure 36. Node 3 acceleration-time relation of frame model along y-axis with bolted panels with 14 lead dampers in each and 48 lead dampers in exterior columns

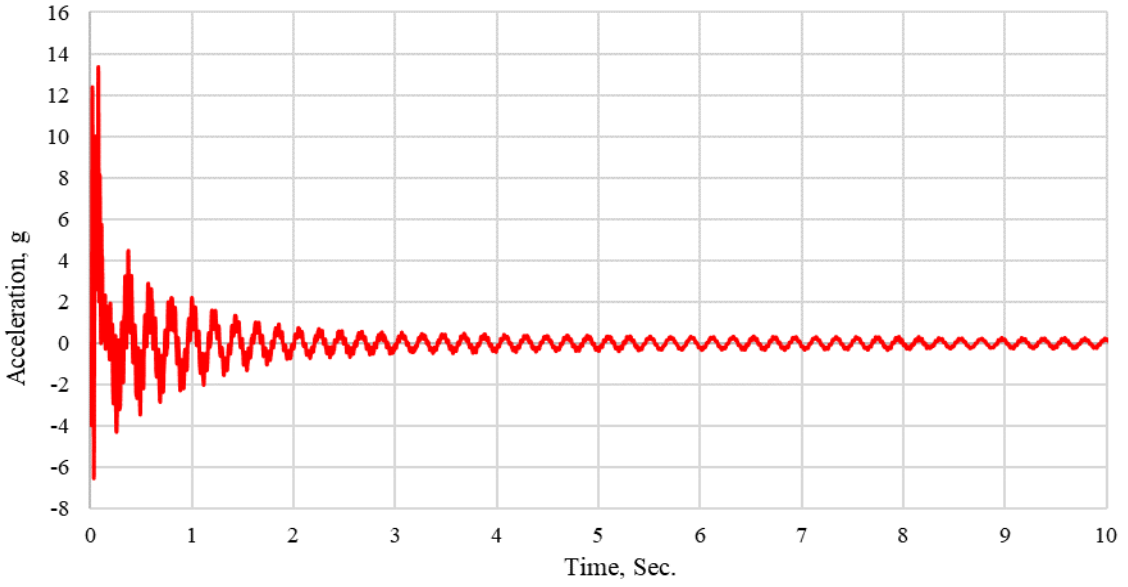

Figure 37. Cantilever acceleration-time relations with 27 lead dampers each of 0.5-in. dia.

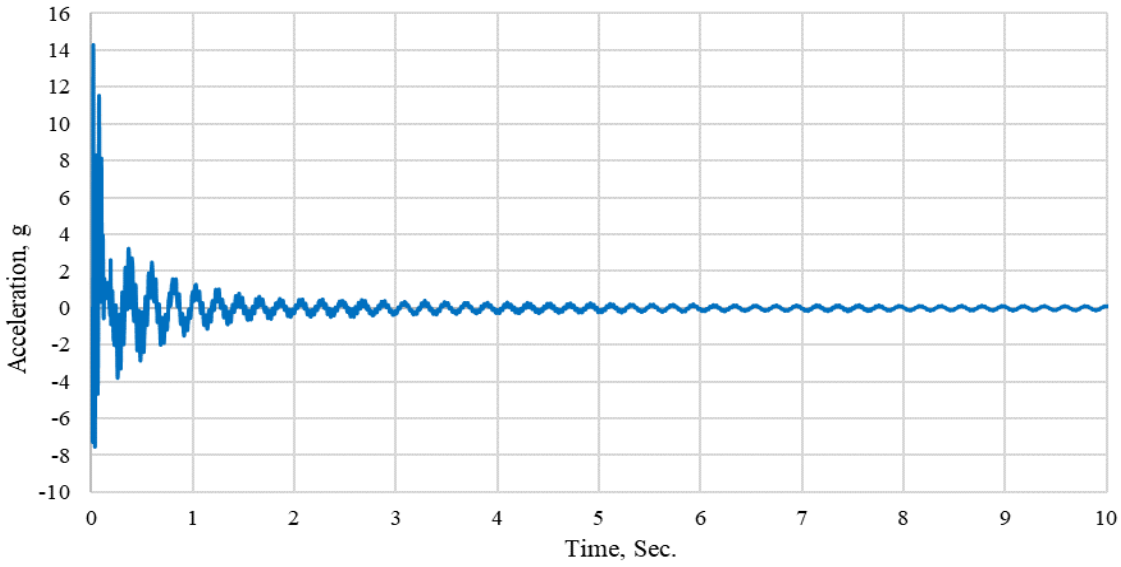

Figure 38. Cantilever acceleration-time relations with 53 lead dampers each of 0.5-in. dia.

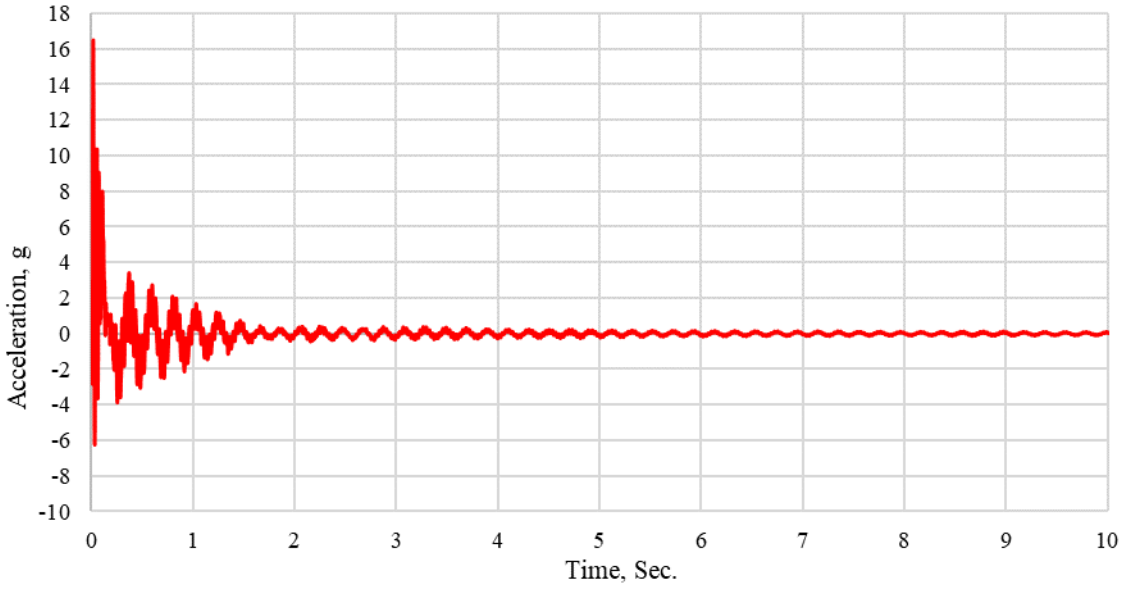

Figure 39. Cantilever acceleration-time relations with 27 lead dampers each of 0.6-in. dia.

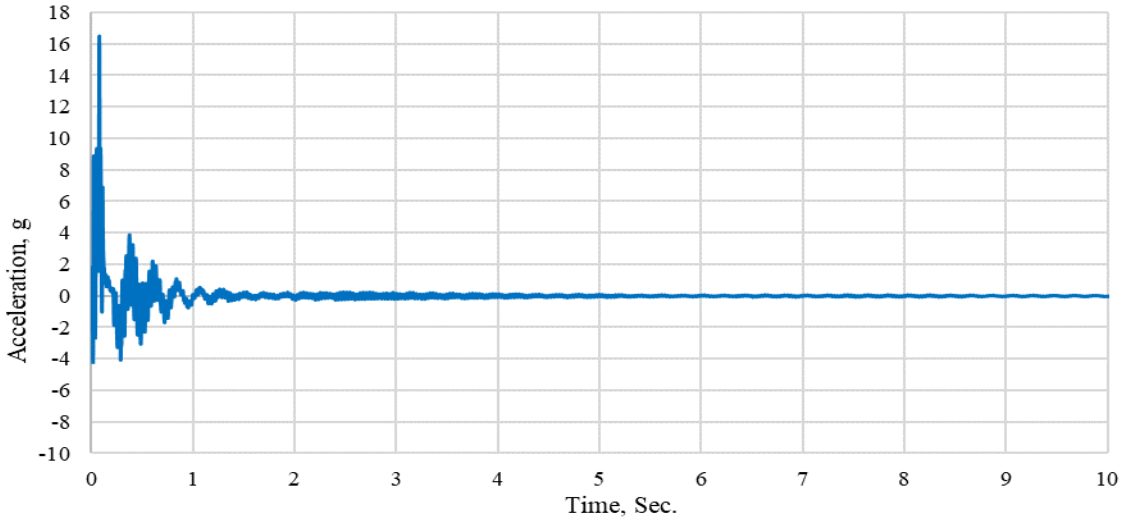

Figure 40. Cantilever acceleration-time relations with 53 lead dampers each of 0.6-in. dia.

2.6.3 Steel Building Frame Plastic Hinges

Ground-column AB of the steel building frame model is impacted under multiple impact loads shown in Figure 41 to predict the required impact load that forms three plastic hinges in the building column. First, three impact loads are applied to the ground-column's mid-height by swinging the pendulum from different distances, q = 5, 7, and 9 inches. The first predicted impact load at q = 16 inches is subjected to the ground-column, but no plastic hinges predicted in the column. Then, the column is impacted again at q = 18 inches, this time, the column had 0.1 inches permanent deformation with two plastic hinges at the ground joint and the mid-height. Then the column is impacted again at q = 25 inches, this time, three plastic hinges were formed at the ground joint, top joint, ant the middle of the column with 0.44 inches of permanent deformation. Figures 42 and 43 show acceleration versus time at the top floor at Node 3 when the ground-column is impacted by the pendulum at q = 18 inches and 25 inches.

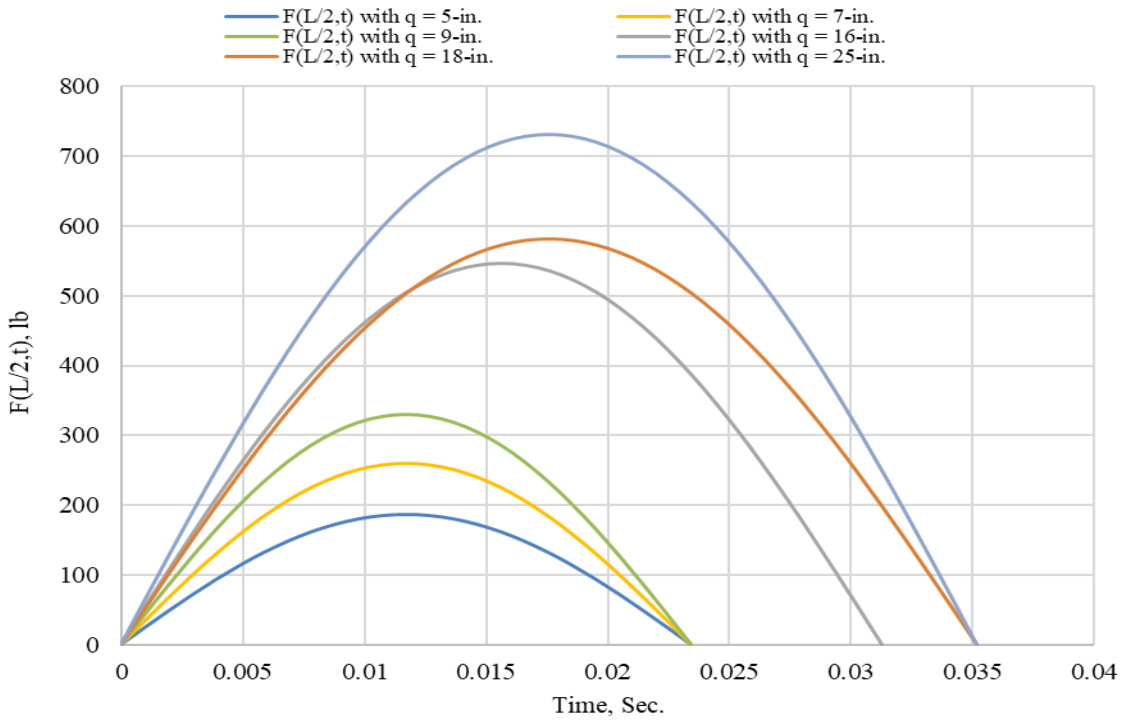

Figure 41. Applied impact forcing functions

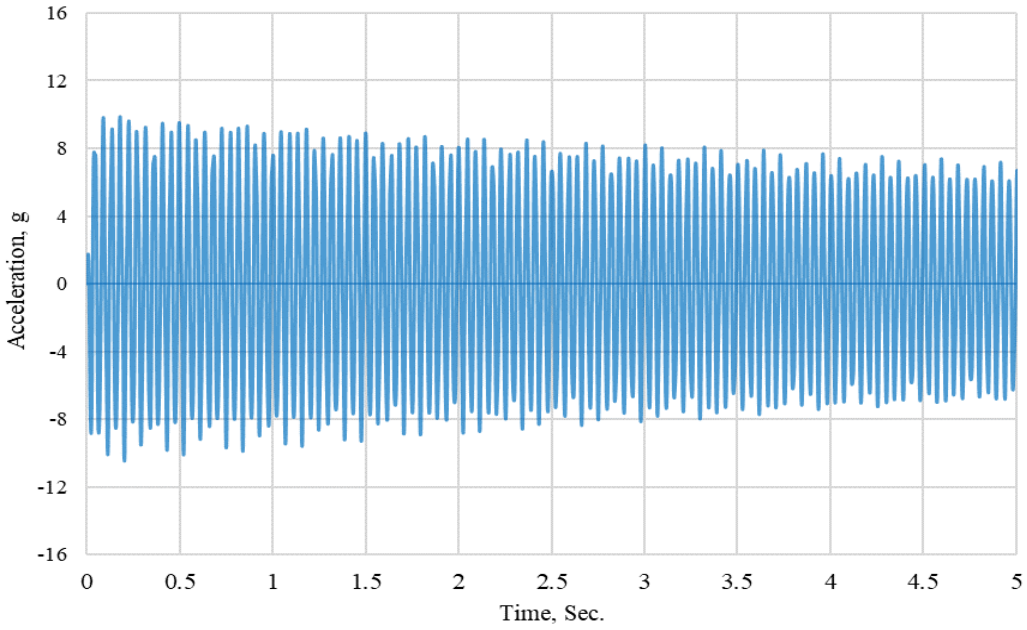

Figure 42. Node 3 acceleration-time relation of frame model along x-axis with q = 18-in.

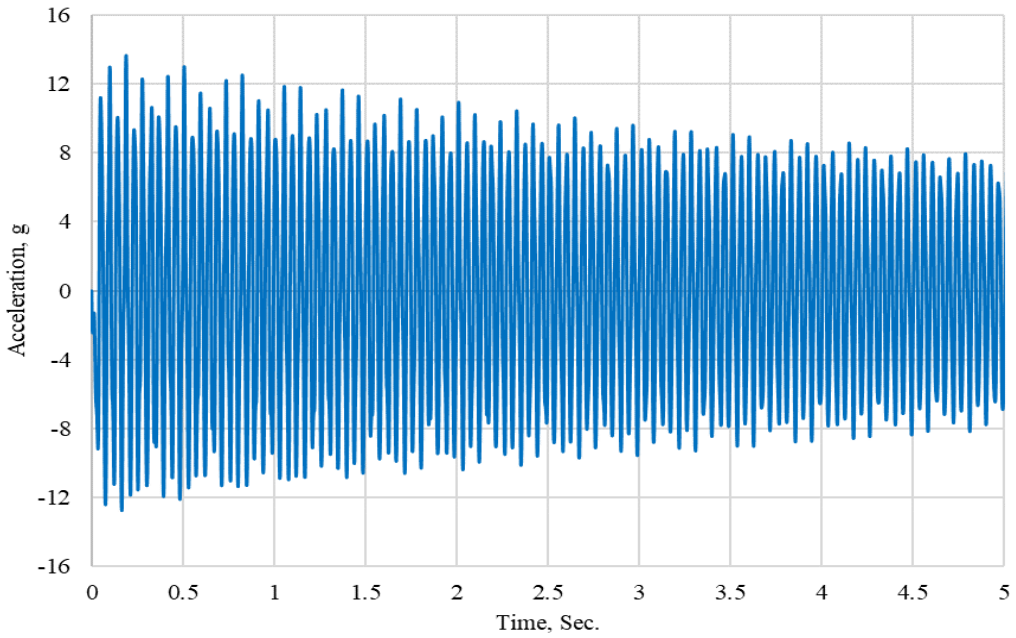

Figure 43. Node 3 acceleration-time relation of frame model along x-axis with q = 25-in.

2.7 Damping Properties

In this section, the damping properties for the model frame and the cantilever are presented both without and with lead dampers.

2.7.1 Model Frame Damping Properties without Lead Dampers

For the steel frame model, damping coefficient is calculated from Figure 19 which shows acceleration vs time at the top floor when the building is pulled by 0.25-in. at the top floor and released for free vibration. Also, using SAP-2000, the frame is pushed by a lateral point load at the top floor by a 150 lb, the lateral displacement was 0.227 inches. From that, lateral stiffness is calculated to be 660.8 lb/in.

From Figure 19, it is found that the time period, T_n, for the building at Node 3 is 0.0464 seconds and frequency is 21.57 Hz. From the figure; from acceleration

$\ddot{U}_i$=1.76118g to $\ddot{U}_j$=1.75123g, number of complete periods, j, is 15. Damping ratio, ζ, is calculated using the logarithmic decrement method [48].

$$\zeta = \frac{\ln \frac{\ddot{U}_i}{\ddot{U}_{i+j}}}{2\pi j} \tag{3}$$

in Equation 3, $\ddot{U}_i$ is the acceleration at time i, and $\ddot{U}_j$ is the acceleration at time j.

$$\zeta = \frac{ln\frac{1.76118g}{1.75123g}}{2\pi \times 15} = 0.00006 = 0.006\%$$

Then, natural circular frequency, ω_n, and damping natural circular frequency, ω_D, of the frame is calculated as follows:

$$\omega_n = \frac{2\pi}{T_n} \tag{4}$$

$$\omega_n = \frac{2\pi}{0.0464} = 135.55 \text{ rads/sec.}$$

Also, the damping natural circular frequency, ω_D, is found as the following:

$$\omega_D = \omega_n\sqrt{1 - \zeta^2} \tag{5}$$

$$\omega_D = 135.55\sqrt{1 - 0.00006^2} = 135.55 \text{ rads/sec.}$$

Because the damping ratio is small, the experimental natural circular frequency found in equation 4 is the same as the damping natural circular frequency, ω_D, found in equation 5.

Using the experimentally found natural circular frequency, $\omega_{e_{exp.}}$, and the calculated stiffness, the experimental effective mass, $m_{e_{exp.}}$, of the cantilever is calculated as the following:

$$\omega_{e_{exp.}} = \sqrt{\frac{K}{m_{e_{exp.}}}} \tag{6}$$

$$135.55 = \sqrt{\frac{660.8}{m_{e_{exp.}}}}$$

$m_{e_{exp.}}$ = 0.03596 lb-Sec^2/in.

The critical damping coefficient, c_c and damping coefficient, c, are calculated as the following:

$$c_c = 2\ m\ \omega_n \tag{7}$$

$$c_c = 2 \times 0.03596 \times 135.55 = 9.75$$

From damping ratio, one gets:

$$\zeta = \frac{c}{c_c} \tag{8}$$

$$0.00006 = \frac{c}{9.75}$$

c = 0.000586 lb-sec./in.

The above calculated damping coefficient is used in the theoretical analysis of the steel frame model in Chapter 3.

2.7.2 Ground-Level Column Damping Properties without Lead Dampers

From Figure 21, it is found that the time period, T_n, for the building at Node 1 is 0.0145175 seconds and frequency is 68.88 Hz. From the figure, from acceleration $\ddot{U}_i$=0.4456g to $\ddot{U}_j$=0.4348g, number of complete periods, j, is 47. Damping ratio, ζ, is calculated using the logarithmic decrement method used in the above section:

$$\zeta = \frac{ln\frac{0.4456g}{0.4348g}}{2\pi \times 34} = 0.000083 = 0.0083\%$$

$$\omega_n = \frac{2\pi}{0.0145175} = 432.80 \text{ ads/sec.}$$

Based on the experimental studies, ω_n = 432.80 rad/sec. This frequency value embodies the influence of the mass of the entire building model and is used to estimate an effective mass per unit length, m_{ef}, needed for isolated ground-level column. Using an iterative process, m_{ef} is found to be 0.0016311 lb-sec2/in./in.

The critical damping coefficient, c_c and damping coefficient, c, are calculated using Equations 7 and 8:

$$c_c = 2 \text{ m } \omega_n$$

$$c_c = 2 \times 0.0016311 \times 16.25 \times 66 = 3.50$$

$$\zeta = \frac{c}{c_c}$$

$$0.000083 = \frac{c}{3.50}$$

c = 0.00029 lb-sec./in.

The above calculated damping coefficient is used in the theoretical analysis of ground-level Column AB in Chapter 3.

2.7.3 Cantilever Damping Properties without Lead Dampers

From Figure 24, it is calculated that using the logarithmic decrement method, the T_n = 0.199 Sec., f = 5.03 Hz, $\zeta_{avg.}$ = 0.0825%, $\omega_{e_{exp.}}$ = 31.57 rads/sec. From the computer program, SAP-2000; T_n = 0.187 Sec., f_{SAP} = 5.34 Hz, ω_n = 33.55 rads/sec. Meaning; there is around 6% difference between the SAP-2000 model and the experimental natural frequency.

To calculate the effective mass of the cantilever, the stiffness of the material needs to be calculated. For that, the material properties of the cantilever are needed. The moment of inertia, I is found to be 0.1155 $in.^4$, and from the stress-strain material properties of the cantilever, yielding stress, σ_y, is 42,000 psi, and Young`s Modulus, E, 28,261,000 psi. First, stiffness of the cantilever is calculated,

$$K = \frac{3EI}{L^3} \tag{9}$$

$$K = \frac{3 \times 28261000 \times 0.1155}{107^3} = 7.9935 \text{ lb/in.}$$

In Equation 9, L is the total length of the cantilever.

Using the experimentally found natural circular frequency, $\omega_{e_{exp.}}$, and the calculated stiffness, the experimental effective mass, $m_{e_{exp.}}$, of the cantilever is calculated using Equation 6:

$$\omega_{e_{exp.}} = \sqrt{\frac{K}{m_{e_{exp.}}}}$$

$$31.57 = \sqrt{\frac{7.9935}{m_{e_{exp.}}}}$$

$m_{e_{exp.}}$ = 0.00802 lb-Sec^2/in.

The critical damping coefficient, c_c and damping coefficient, c, are calculated from Equations 7 and 8:

$c_c = 2\ m\ \omega_n$

$c_c = 2 \times 0.00802 \times 31.57 = 0.5064$

$\zeta = \frac{c}{c_c}$

$0.000825 = \frac{c}{0.5064}$

c = 0.000418 lb-sec./in.

The above camping coefficient is the damping coefficient and damping ratio for the cantilever.

Using the Figures 22, 23, and 24, damping coefficient for the cantilever is found along the member with time. the generated damping coefficients at each node for each time increment are shown in Figure 44 and Table 1. The following damping coefficient values are used in the analytical calculations of the cantilever in Chapter 3.

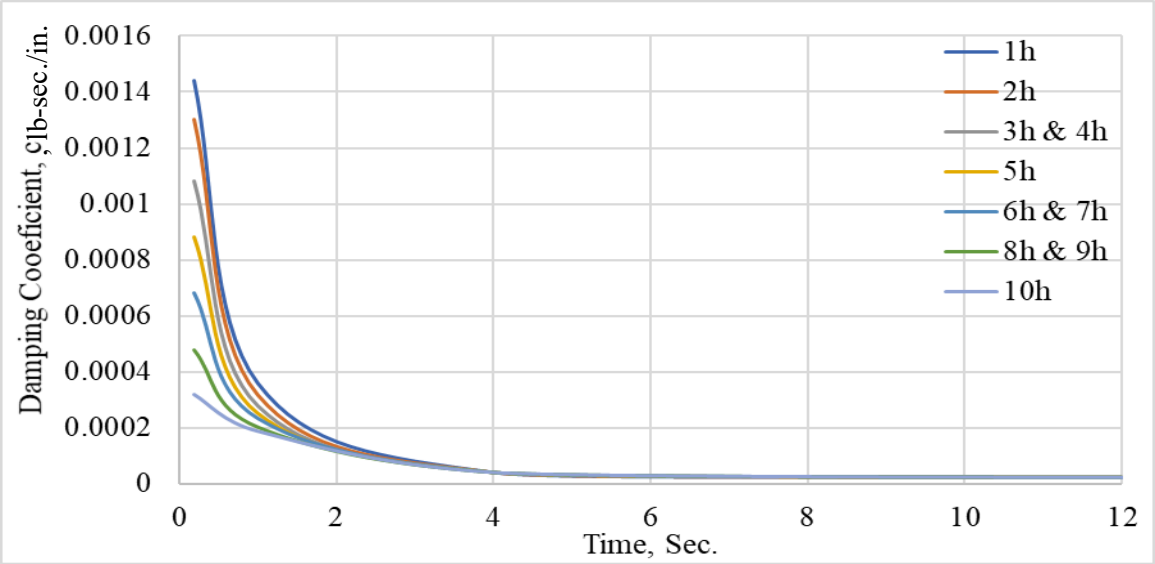

Figure 44. Damping coefficient versus time at each node of cantilever

Table 1. Damping coefficient values along cantilever length

Node No. / Time, sec.	2	3	4 and 5	6	7 and 8	9 and 10	11
0 -0.188	0.00144	0.0013	0.00108	0.00088	0.00068	0.00048	0.00032
0.188 -1	0.00036	0.000318	0.000279	0.000252	0.000234	0.000204	0.000189
1 - 4	0.000042	0.000042	0.000042	0.000042	0.000042	0.000042	0.000042
4 - 10	0.0000252	0.0000252	0.0000252	0.0000252	0.0000252	0.0000252	0.0000252
10 - 50	0.0000105	0.0000105	0.0000105	0.0000105	0.0000105	0.0000105	0.0000105

2.7.4 Summary of Damping Properties

In this section, damping coefficient, c, for each of the experimental tests are calculated as shown in the following Table 2. Percentage of increase in damping

coefficient for each system is calculated based on the reference damping value of the specimens at the same time slot.

Table 2. Damping coefficients for model frame

Event	Time (sec.)	c (lb-sec./in.)	c increase (%)
No Lead Dampers	29.0-29.8	0.000586	-
	1-1.5	0.019	-
12 Lead Dampers		0.044	56.59
24 Lead Dampers		0.045	57.56
48 Lead Dampers		0.050	61.80
No Lead Dampers	0-0.5	0.034	-
Empty Welded Damping Panels, x-axis		0.069	50.72
Welded Damping Panels with 15 0.2-in. Lead Dampers, x-axis		0.093	63.44
Empty Bolted Damping Panels, x-axis		0.500	93.20
Bolted Damping Panels with 14 0.2-in. Lead Dampers, x-axis		0.586	94.20
No Lead Dampers		0.032	
48 Lead Dampers, y-axis		0.047	31.91
Empty Bolted Damping Panels, y-axis		0.348	90.80
Bolted Damping Panels with 14 0.2-in. Lead Dampers, y-axis		0.438	92.69

Table 3. Damping coefficients for cantilever

Event	Time (sec.)	c (lb-sec./in.)	c increase (%)
	18.0-20.0	0.000418	-
No Lead Dampers	0.0-2.0	0.012	-
27 0.5-in. Lead Dampers		0.032	62.50
53 0.5-in. Lead Dampers		0.043	72.09
27 0.6-in. Lead Dampers		0.042	71.43
53 0.6-in. Lead Dampers		0.052	76.92

Tables 2 and 3 show that with increasing the number of lead dampers, damping coefficient value increases in the structure. It is found that for the frame model, the most effective damping system is the bolted system.

CHAPTER III

3. THEORETICAL ANALYSIS

3.1 Introduction

This chapter presents the outcome of a rigorous transient dynamic analysis of the cantilever, isolated ground-level column, the building model frame, and a full-scale building. Both vertical pulsating and lateral impact loads are considered. For the full-scale building, both service dead and live loads are included in addition to the vertical pulsating load and the vertical impact load on the ground-level column. The dynamic stability characteristics for both the isolated ground-level column, the model frame, and the full-scale building are also investigated. These studies utilized damping characteristics based on the experimental data from Chapter 2.

3.2 Finite-Difference Solution for Cantilever Under Impact

Including the influence of the damping coefficient c and localized impact forcing function F(L, t), the governing differential equation for the dynamic equilibrium of the cantilever becomes:

$$\mathrm{EI}\frac{\partial^4 v}{\partial z^4} + m\frac{\partial^2 v}{\partial t^2} + c\frac{\partial v}{\partial t} = \mathrm{F(L,t)} \tag{10}$$

Finite-difference-method is used to calculate the above equation of motion, Equation 10. The following approximations of the finite-difference-method [52] are used:

$$\left(\frac{dv}{dz}\right)_{\mathrm{i}} = \frac{V_{i+1}^k - V_{i-1}^k}{2h} + \delta \tag{11}$$

$$\frac{d^2 v}{dz^2} \approx \frac{V_{i-1}^k - 2V_i^k + V_{i+1}^k}{h^2} + \delta \tag{12}$$

$$\frac{d^3v}{dz^3} \approx \frac{-V_{i-2}^k+2V_{i-1}^k-2V_{i+1}^k+V_{i+2}^k}{2\times h^3} + \delta \quad (13)$$

$$\frac{d^4v}{dz^4} \approx \frac{V_{i-2}^k- 4V_{i-1}^k+ 6V_i^k- 4V_{i+1}^k+V_{i+2}^k}{h^4} + \delta \quad (14)$$

$$\frac{dv}{dt} = \frac{V_i^{k+1} - V_i^{k-1}}{2\Delta t} + \delta \quad (15)$$

$$\frac{d^2v}{dt^2} = \frac{V_i^{k-1} - 2V_i^k + V_i^{k+1}}{\Delta t^2} + \delta \quad (16)$$

δ = truncation error ≈ 0

where:

v = Displacement at any point

h = Length of each segment

t = time

Δt = time increment

From Figure 45, it is shown that the tangent of the displacement curve for three points (two segments) can be used to find the slope of the curve by taking derivation to the tangent line as shown in Equation 11. After taking the second derivation of the tangent line, the curvature of the displacement curve can be obtained as expressed in Equation 12. The cantilever should be divided into equal segments (h). With increasing segment numbers, the accuracy of finding displacement to the beam increases.

Since the FDM is used for the equation of motion, the FDM is used for a two-domain region. For the fixed end steel pipe cantilever, the length is 107 inches along Z-axis. The total length is divided into ten segments, each segment is h = 10.7 inches.

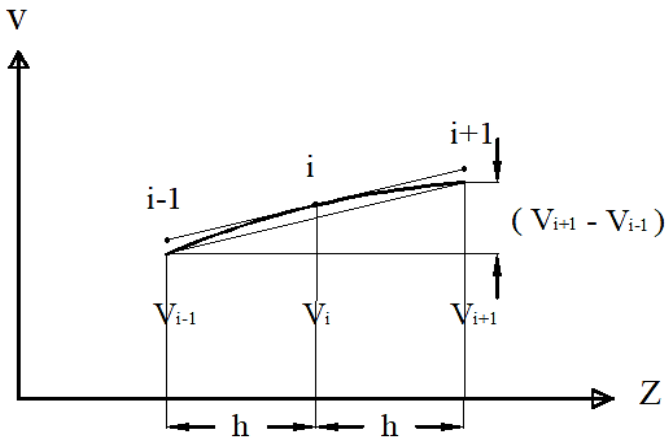

Figure 45. Finite-Difference nodes and nodal displacements

Equations 15 and 16 are applied to solve for velocity and acceleration in the partial differential equation of motion. As shown in Figure 46, the cantilever is divided into ten segments, eleven nodes, with three extra nodal points which are out of the boundary of the beam called the Phantom points or Imaginary points. For this case, eleven equations are needed. Then the matrix equation will be generated, having forcing function, $f(L,t)$, segment length, h, mass per unit length, m, damping coefficient, c, time increment, Δt, and displacement, v. The generated matrix equation is solved for each time increment, $t + \Delta t$, starting from $t = 0$ second to $t = 50$ seconds. Time increment, Δt is 0.0005 seconds per run. In order to have a stable calculation, the time increment must be equal to or smaller than 0.0005 seconds, $\Delta t \leq$ 0.0005 seconds. From the

boundary condition, it is found that displacement at the support is zero (v_1^k= 0). After specifying segment length and time, the displacement of each segment can be found [49-53]. In this study, only the free end displacement (v_{11}^k) has been taken into consideration. Finally, repeat this procedure for each time interval, Δt, the cantilever's time history, displacement vs time, velocity vs time, and acceleration vs time can be found. The boundary conditions are:

$v_1^k = 0$

$(\frac{dv}{dz})_1 = \frac{v_2^k - v_0^k}{2h} = 0$, $v_2^k = v_0^k$

Also, based on symmetry, $v_3^k = v_{-1}^k$

Also, at the free end, the bending moment and shear are zero [39]. Thus, at Node 11:

$EI\ (\frac{d^2v}{dz^2})_{11} \approx EI\ (\frac{v_{10}^k - 2v_{11}^k + v_{12}^k}{h^2})_{11}$

$EI\ (\frac{d^3v}{dz^3})_{11} \approx EI\ (\frac{-v_9^k + 2v_{10}^k - 2v_{12}^k + v_{13}^k}{2 \times h^3})_{11}$

The above two expressions resulted in:

$$v_{12}^k = -v_{10}^k + 2v_{11}^k \quad (17)$$

$$v_{13}^k = v_9^k - 2v_{10}^k + 2v_{12}^k \quad (18)$$

From Equations 17 and 18:

$$v_{13}^k = v_9^k - 4v_{10}^k + 4v_{11}^k \quad (19)$$

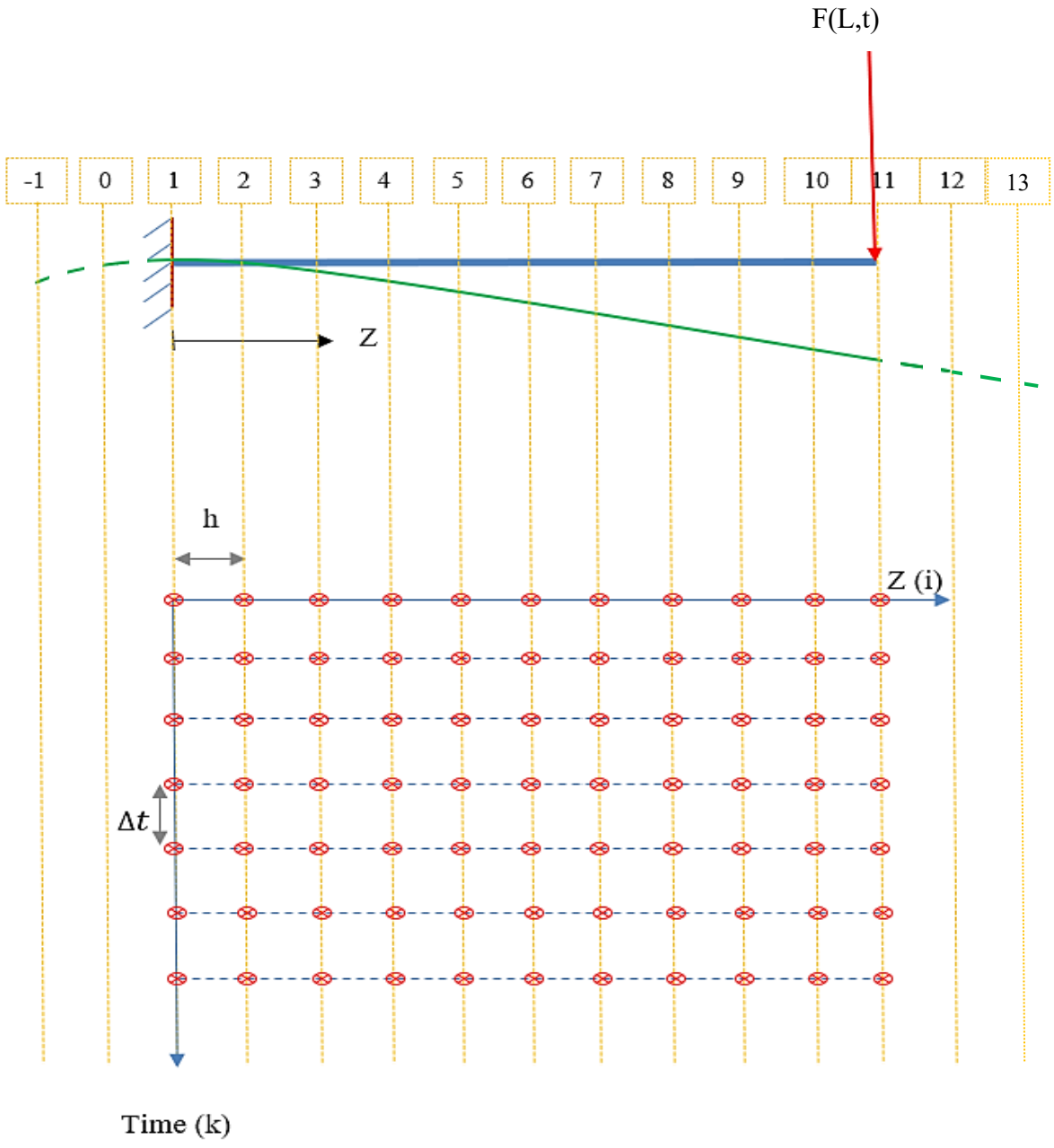

Figure 46. Finite-Difference nodal scheme for cantilever

Applying the finite-difference method to Equation 16, one gets:

$$\mathrm{EI}\frac{v_{i-2}^{k}-4v_{i-1}^{k}+6v_{i}^{k}-4v_{i+1}^{k}+v_{i+2}^{k}}{h^{4}}+m\frac{v_{i}^{k-1}-2v_{i}^{k}+V_{i}^{k+1}}{\Delta t^{2}}+c_{i}^{k}\frac{v_{i}^{k+1}-v_{i}^{k-1}}{2\Delta t}=F(L,t) \qquad (20)$$

Equation 20 is rearranged to calculate displacement at time $t+\Delta t$, i.e. at time $k+1$:

$$v_i^{k+1} = \{[-(\gamma)v_{i-2}^k + (4\gamma)v_{i-1}^k - (6\gamma - 2\beta)v_i^k + (4\gamma)v_{i+1}^k - (\gamma)v_{i+2}^k - (\beta - \alpha)v_i^{k-1}] + F(L,t)\}/(\beta + \alpha) \quad (21)$$

Where

$\gamma = \frac{EI}{h^4}$,

$\beta = \frac{m}{\Delta t^2}$, and

$\alpha = \frac{c_i^k}{2\,\Delta t}$

In Equation 21, the subscript i represents nodal place along the cantilever, and subscript k represents the time increment.

3.2.1 Steel Cantilever Natural Frequency Using FDM

To solve Equation 21 for the natural frequency of the cantilever, the forcing function is eliminated from the equation. Furthermore, to predict lateral displacement at each node, v_i^{k+1}, it is needed to know/pre-find displacement in time k-1 for each node.

For the first time interval solution, shape function ($\varkappa$) is merged with the first time interval for forwarding difference approximation, as shown in the following [54]:

$$\varkappa = \frac{PZ^2}{6EI} \quad (3L - Z) \quad (22)$$

$$\frac{v_i^{k=1} - v_i^{k=0}}{\Delta t} = \frac{\partial v}{\partial t}\,(Z_i, 0) + \frac{\Delta t}{2}\,\frac{\partial^2 v}{\partial t^2}\,(Z_i, 0) \quad (23)$$

Where P is an imaginary applied load (2.038 lb) at the free end of the cantilever to displace it by 0.255 inches.

Then, Equation 23, is substituted into equation 10,

$$\frac{\partial^2 v}{\partial t^2} = -\frac{EI}{m}\frac{\partial^4 v}{\partial x^4} - \frac{c_i^k}{m}\frac{\partial v}{\partial t}$$

$$\frac{\partial^2 v}{\partial t^2}(Z_i, 0) = -\frac{EI}{m}\frac{\partial^4 v}{\partial x^4}(Z_i, 0) - \frac{c_i^k}{m}\frac{\partial v}{\partial t}(Z_i, 0)$$

$$\frac{\partial^2 v}{\partial t^2}(Z_i, 0) = -\frac{EI}{m}\frac{d^4}{dx^4}\Phi(Z_i) - \frac{c_i^k}{m}\frac{d}{dt}\Phi(Z_i) \quad (24)$$

Finite-Difference method is applied to Equation 24 to get the following equation:

$$\frac{\partial^2 v}{\partial t^2}(Z_i, 0) = -\frac{EI}{mh^4}(\varkappa_{i-2} - 4\varkappa_{i-1} + 6\varkappa_i - 4\varkappa_{i+1} + \varkappa_{i+2}) - \frac{c_i^k}{m}\frac{\partial v}{\partial t}(Z_i, 0) \quad (25)$$

Finally, Equation 25 is substituted in Equation 23. From boundary conditions, velocity is zero, $\frac{\partial v}{\partial t}(Z_i, 0) = 0$, at time = 0 seconds, just before releasing the cantilever to vibrate freely.

$$\frac{v_i^{k=1} - v_i^{k=0}}{\Delta t} = \frac{\partial v}{\partial t}(Z_i, 0) + \frac{\Delta t}{2}\left(-\frac{EI}{mh^4}(\varkappa_{i-2} - 4\varkappa_{i-1} + 6\varkappa_i - 4\varkappa_{i+1} + \varkappa_{i+2}) - \frac{c_i^k}{m}\frac{\partial v}{\partial t}(Z_i, 0)\right) \quad (26)$$

$$v_i^1 = v_i^0 + \frac{\Delta t^2}{2}\left(-\frac{EI}{mh^4}(\varkappa_{i-2} - 4\varkappa_{i-1} + 6\varkappa_i - 4\varkappa_{i+1} + \varkappa_{i+2})\right)$$

$$v_i^1 = \varkappa_i + \frac{\Delta t^2}{2}\left(-\frac{EI}{mh^4}(\varkappa_{i-2} - 4\varkappa_{i-1} + 6\varkappa_i - 4\varkappa_{i+1} + \varkappa_{i+2})\right) \quad (27)$$

In order to solve for Equation 27, the shape function is applied to each node at time 0, the values are given in the following; also, Young's modulus, E, Moment of Inertia, I, mass per unit length, m, and node displacement, h, is needed.

E = 28,261,000 psi

I = 0.1155 $in.^4$

m $= \frac{9.92 \div 386.0886}{107}$ = 0.00024 (lb-Sec^2/in.)/in.

h = 10.7 in., and

After solving for the first time-interval, $t+\Delta t$, the following equations are applied to each node. The boundary equations are embedded in the following nodal equations. The following nodal equations are run for each time interval, Δt. In order to have a stable calculation, Δt, must not be bigger than 0.0005 seconds. Also, the damping coefficient values, c_i^k, shown in Table 1 is used.

Equation 21 is applied at each node to calculate displacement versus time for each node as the following:

1 $v_1^{k+1} = \{-(\gamma)v_{-1}^k + (4\gamma)v_0^k - (6\gamma - 2\beta)v_1^k + (4\gamma)v_2^k - (\gamma)v_3^k - (\beta - \alpha)v_1^{k-1}\}/(\beta + \alpha)$

$(8\gamma)v_2^k - (2\gamma)v_3^k = 0$ (28-a)

2 $v_2^{k+1} = \{-(\gamma)v_0^k + (4\gamma)v_1^k - (6\gamma - 2\beta)v_2^k + (4\gamma)v_3^k - (\gamma)v_4^k - (\beta - \alpha)v_2^{k-1}\}/(\beta + \alpha)$

$v_2^{k+1} = \{-(7\gamma - 2\beta)v_2^k + (4\gamma)v_3^k - (\gamma)v_4^k - (\beta - \alpha)v_2^{k-1}\}/(\beta + \alpha)$ (28-b)

3 $v_3^{k+1} = \{-(\gamma)v_1^k + (4\gamma)v_2^k - (6\gamma - 2\beta)v_3^k + (4\gamma)v_4^k - (\gamma)v_5^k - (\beta - \alpha)v_3^{k-1}\}/(\beta + \alpha)$ (28-c)

4 $$v_4^{k+1} = \{-(\gamma)v_2^k + (4\gamma)v_3^k - (6\gamma - 2\beta)v_4^k + (4\gamma)v_5^k - (\gamma)v_6^k - (\beta - \alpha)v_4^{k-1}\}/(\beta + \alpha) \quad (28\text{-d})$$

5 $$v_5^{k+1} = \{-(\gamma)v_3^k + (4\gamma)v_4^k - (6\gamma - 2\beta)v_5^k + (4\gamma)v_6^k - (\gamma)v_7^k - (\beta - \alpha)v_5^{k-1}\}/(\beta + \alpha) \quad (28\text{-e})$$

6 $$v_6^{k+1} = \{-(\gamma)v_4^k + (4\gamma)v_5^k - (6\gamma - 2\beta)v_6^k + (4\gamma)v_7^k - (\gamma)v_8^k - (\beta - \alpha)v_6^{k-1}\}/(\beta + \alpha) \quad (28\text{-f})$$

7 $$v_7^{k+1} = \{-(\gamma)v_5^k + (4\gamma)v_6^k - (6\gamma - 2\beta)v_7^k + (4\gamma)v_8^k - (\gamma)v_9^k - (\beta - \alpha)v_7^{k-1}\}/(\beta + \alpha) \quad (28\text{-g})$$

8 $$v_8^{k+1} = \{-(\gamma)v_6^k + (4\gamma)v_7^k - (6\gamma - 2\beta)v_8^k + (4\gamma)v_9^k - (\gamma)v_{10}^k - (\beta - \alpha)v_8^{k-1}\}/(\beta + \alpha) \quad (28\text{-h})$$

9 $$v_9^{k+1} = \{-(\gamma)v_7^k + (4\gamma)v_8^k - (6\gamma - 2\beta)v_9^k + (4\gamma)v_{10}^k - (\gamma)v_{11}^k - (\beta - \alpha)v_9^{k-1}\}/(\beta + \alpha) \quad (28\text{-i})$$

10 $$v_{10}^{k+1} = \{-(\gamma)v_8^k + (4\gamma)v_9^k - (6\gamma - 2\beta)v_{10}^k + (4\gamma)v_{11}^k - (\gamma)v_{12}^k - (\beta - \alpha)v_{10}^{k-1}\}/(\beta + \alpha)$$

$$v_{10}^{k+1} = \{-(\gamma)v_8^k + (4\gamma)v_9^k - (5\gamma - 2\beta)v_{10}^k + (2\gamma)v_{11}^k - (\beta - \alpha)v_{10}^{k-1}\}/(\beta + \alpha) \quad (28\text{-j})$$

11 $$v_{11}^{k+1} = \{[-(\gamma)v_9^k + (4\gamma)v_{10}^k - (6\gamma - 2\beta)v_{11}^k + (4\gamma)v_{12}^k - (\gamma)v_{13}^k - (\beta - \alpha)v_{11}^{k-1}]\}/(\beta + \alpha)$$

$$v_{11}^{k+1} = \{[-(2\gamma)v_9^k + (4\gamma)v_{10}^k - (2\gamma - 2\beta)v_{11}^k - (\beta - \alpha)v_{11}^{k-1}]\}/(\beta + \alpha) \quad (28\text{-k})$$

For each Δt, starting from 0 seconds, v_{11} is calculated to generate displacement-time relations, shown in Figure 47, velocity-time relations, shown in Figure 48, and acceleration-time relations, shown in Figure 49 for the cantilever at free vibration when the free end is pulled by 0.255 inches and released to vibrate freely. Figure 50 is a comparison between the experimental and theoretical acceleration-time data. The figure shows that the experimental response is in a good agreement with the theory.

Velocity and acceleration at Node 11 are calculated at each time increment using Equations 15 and 16.

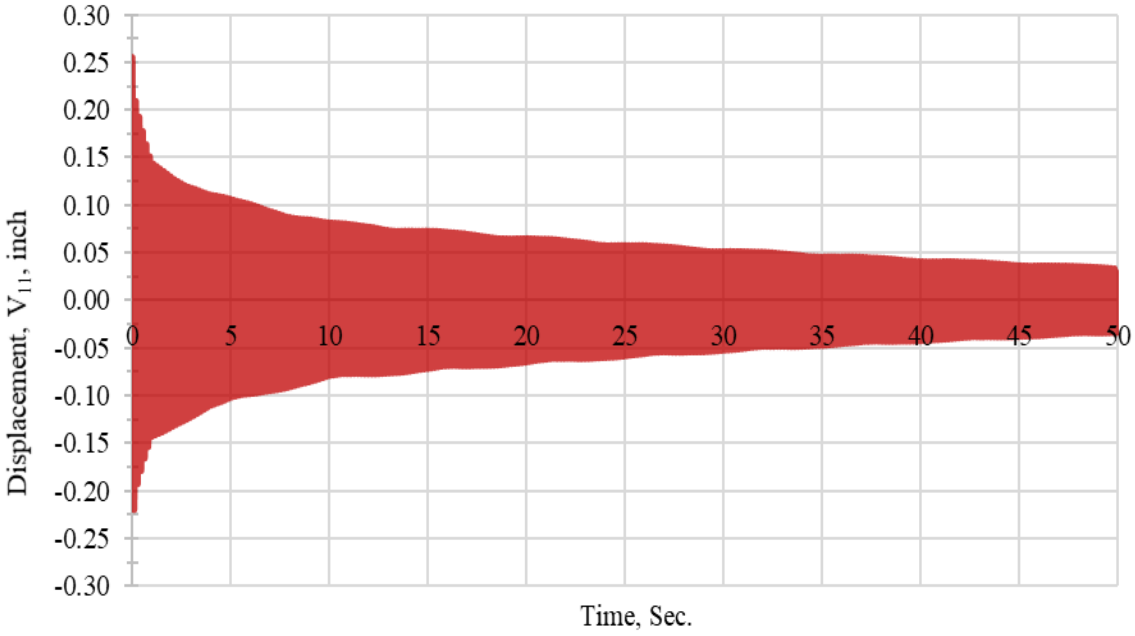

Figure 47. Displacement-time relation at cantilever free end

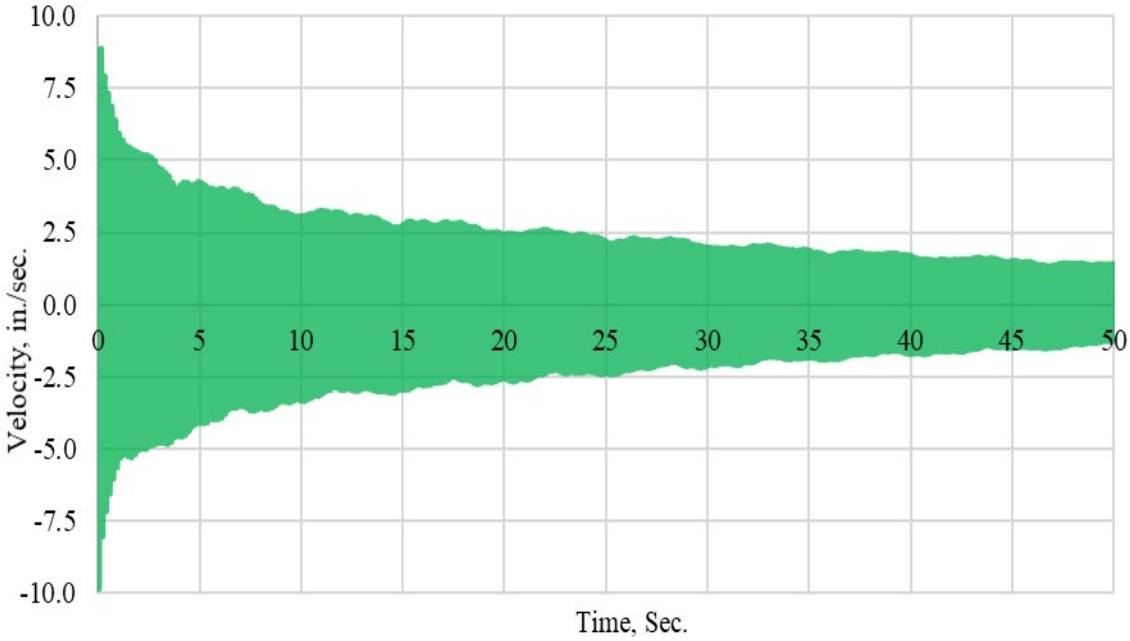

Figure 48. Velocity-time relation at cantilever free end

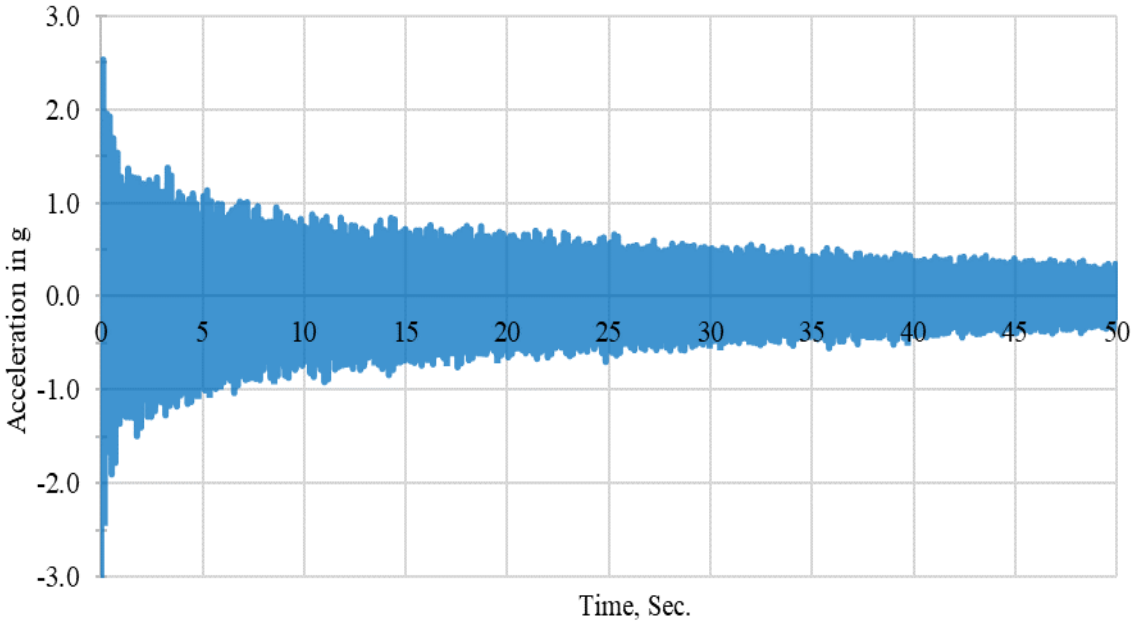

Figure 49. Acceleration-time relation at cantilever free end

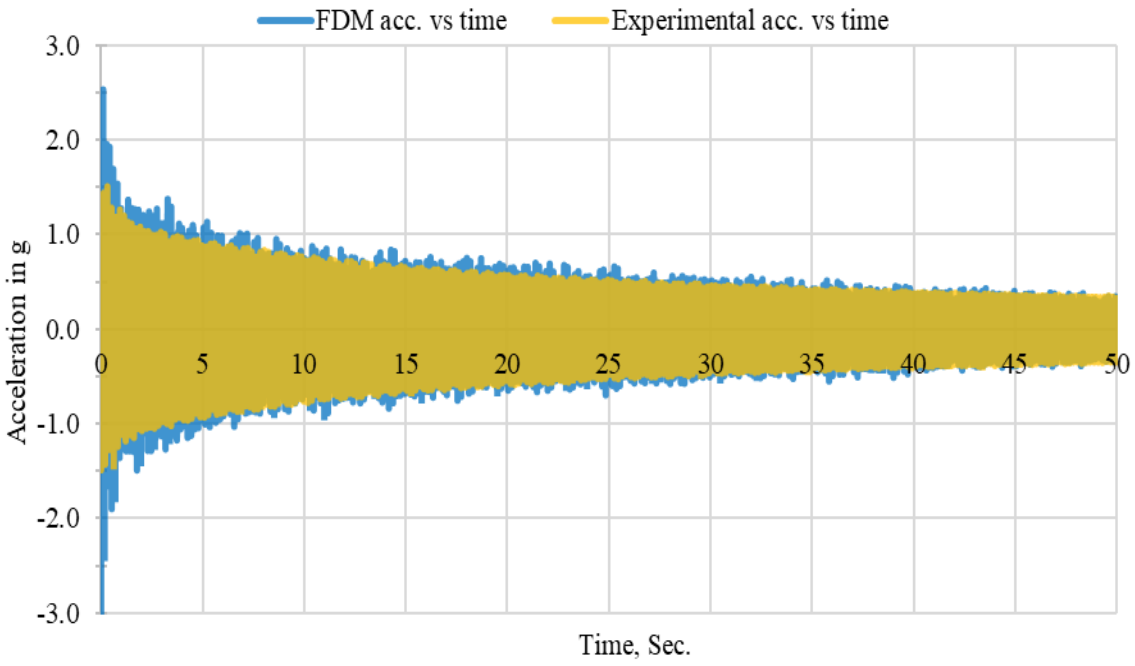

Figure 50. Experimental and FDM acceleration-time relations at cantilever free end

3.2.2 Steel Cantilever Under Impact Load

The Cantilever is subjected to a 10.5-lb impact load at its free end. This resulted in the forcing function shown in Figure 18.

Equation 16 can be expressed in the following finite-difference form:

$$v_i^1 = \varkappa_i + \frac{\Delta t^2}{2}\left(\left(-\frac{EI}{mh^4}\left(\varkappa_{i-2} - 4\varkappa_{i-1} + 6\varkappa_i - 4\varkappa_{i+1} + \varkappa_{i+2}\right)\right) + \frac{1}{m}F(L,t)\right) \quad (29)$$

In this equation, F(L,t) is given by Equation 2.

It is assumed that the cantilever has an imperfection at the free end by 0.005 in. In order to solve for Equation 29, the initial condition for each node is found using Equation 28 with an applied load of 0.0396 lb. Also, Young's modulus, E, Moment of Inertia, I, mass per unit length, m, and node displacement, h, are used like the following:

E = 28,261,000 psi

I = 0.1155 $in.^4$

m $= \frac{9.92 \div 386.0886}{107}$ = 0.00024 (lb-Sec^2/in.)/in.

h = 10.7 in.

After solving for the first time-interval, $t + \Delta t$, the following equations are applied to each node. The boundary equations are embedded in the following nodal equations. The following nodal equations are run for each time interval, Δt. In order to have a stable calculation, Δt, must be equal or smaller than 0.0005 seconds.

1 $v_1^{k+1} = \{-(\gamma)v_{-1}^k + (4\gamma)v_0^k - (6\gamma - 2\beta)v_1^k + (4\gamma)v_2^k - (\gamma)v_3^k - (\beta - \alpha)v_1^{k-1}\}/(\beta + \alpha)$

$$(8\gamma)v_2^k - (2\gamma)v_3^k = 0 \quad \text{(30-a)}$$

2 $v_2^{k+1} = \{-(\gamma)v_0^k + (4\gamma)v_1^k - (6\gamma - 2\beta)v_2^k + (4\gamma)v_3^k - (\gamma)v_4^k - (\beta - \alpha)v_2^{k-1}\}/(\beta + \alpha)$

$$v_2^{k+1} = \{-(7\gamma - 2\beta)v_2^k + (4\gamma)v_3^k - (\gamma)v_4^k - (\beta - \alpha)v_2^{k-1}\}/(\beta + \alpha) \quad \text{(30-b)}$$

3 $$v_3^{k+1} = \{-(\gamma)v_1^k + (4\gamma)v_2^k - (6\gamma - 2\beta)v_3^k + (4\gamma)v_4^k - (\gamma)v_5^k - (\beta - \alpha)v_3^{k-1}\}/(\beta + \alpha) \quad \text{(30-c)}$$

4 $$v_4^{k+1} = \{-(\gamma)v_2^k + (4\gamma)v_3^k - (6\gamma - 2\beta)v_4^k + (4\gamma)v_5^k - (\gamma)v_6^k - (\beta - \alpha)v_4^{k-1}\}/(\beta + \alpha) \quad \text{(30-d)}$$

5 $$v_5^{k+1} = \{-(\gamma)v_3^k + (4\gamma)v_4^k - (6\gamma - 2\beta)v_5^k + (4\gamma)v_6^k - (\gamma)v_7^k - (\beta - \alpha)v_5^{k-1}\}/(\beta + \alpha) \quad \text{(30-e)}$$

6 $$v_6^{k+1} = \{-(\gamma)v_4^k + (4\gamma)v_5^k - (6\gamma - 2\beta)v_6^k + (4\gamma)v_7^k - (\gamma)v_8^k - (\beta - \alpha)v_6^{k-1}\}/(\beta + \alpha) \quad \text{(30-f)}$$

7 $$v_7^{k+1} = \{-(\gamma)v_5^k + (4\gamma)v_6^k - (6\gamma - 2\beta)v_7^k + (4\gamma)v_8^k - (\gamma)v_9^k - (\beta - \alpha)v_7^{k-1}\}/(\beta + \alpha) \quad \text{(30-g)}$$

8 $$v_8^{k+1} = \{-(\gamma)v_6^k + (4\gamma)v_7^k - (6\gamma - 2\beta)v_8^k + (4\gamma)v_9^k - (\gamma)v_{10}^k - (\beta - \alpha)v_8^{k-1}\}/(\beta + \alpha) \quad \text{(30-h)}$$

9 $$v_9^{k+1} = \{-(\gamma)v_7^k + (4\gamma)v_8^k - (6\gamma - 2\beta)v_9^k + (4\gamma)v_{10}^k - (\gamma)v_{11}^k - (\beta - \alpha)v_9^{k-1}\}/(\beta + \alpha) \quad \text{(30-i)}$$

10 $$v_{10}^{k+1} = \{-(\gamma)v_8^k + (4\gamma)v_9^k - (6\gamma - 2\beta)v_{10}^k + (4\gamma)v_{11}^k - (\gamma)v_{12}^k - (\beta - \alpha)v_{10}^{k-1}\}/(\beta + \alpha)$$

$$v_{10}^{k+1} = \{-(\gamma)v_8^k + (4\gamma)v_9^k - (5\gamma - 2\beta)v_{10}^k + (2\gamma)v_{11}^k - (\beta - \alpha)v_{10}^{k-1}\}/(\beta + \alpha) \quad \text{(30-j)}$$

11 $$v_{11}^{k+1} = \{[-(\gamma)v_9^k + (4\gamma)v_{10}^k - (6\gamma - 2\beta)v_{11}^k + (4\gamma)v_{12}^k - (\gamma)v_{13}^k - (\beta - \alpha)v_{11}^{k-1}] + F(L,t)\}/(\beta + \alpha)$$

$$v_{11}^{k+1} = \{[-(2\gamma)v_9^k + (4\gamma)v_{10}^k - (2\gamma - 2\beta)v_{11}^k - (\beta - \alpha)v_{11}^{k-1}] + F(L,t)\}/(\beta + \alpha) \quad \text{(30-k)}$$

For each Δt, starting from 0 seconds, v_{11} is calculated to generate displacement-time relations, shown in Figure 51, velocity-time relations, shown in Figure 52, and acceleration-time relations, shown in Figure 53 for the cantilever. Figure 54 is a comparison between the experimental and theoretical acceleration-time data. The graph shows that both the experimental and theoretical results are acceptably similar and the difference is negligible.

Velocity and acceleration at Node 11 (the free end) are calculated at each time increment using equations 15 and 16.

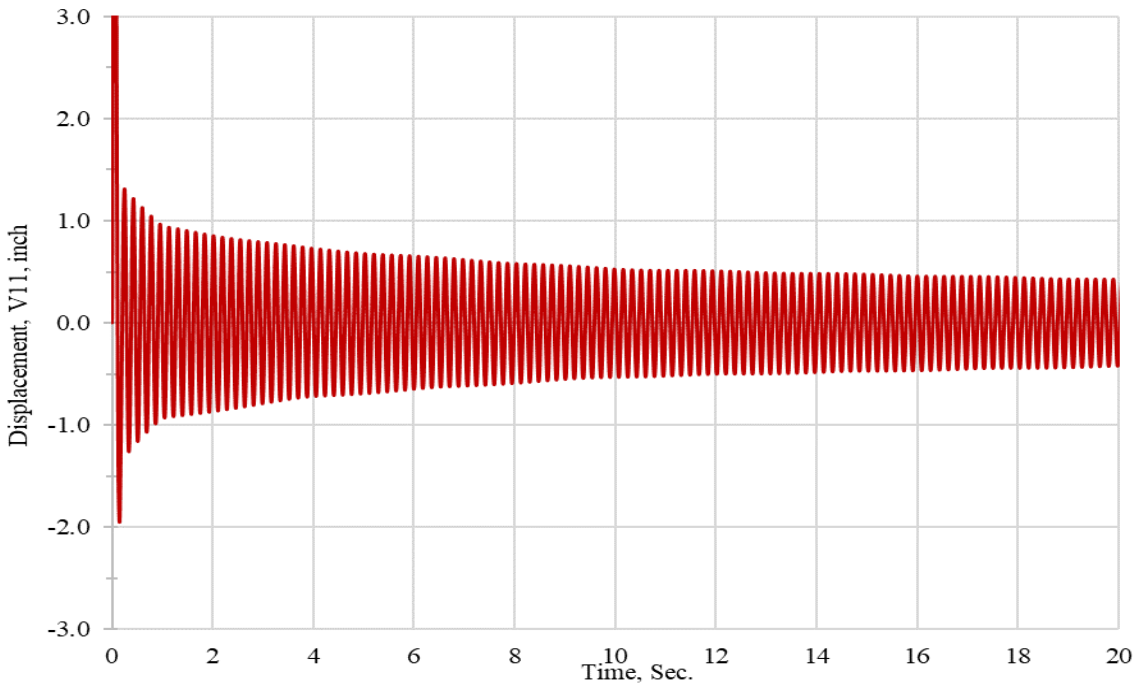

Figure 51. Displacement-time relation at cantilever free end

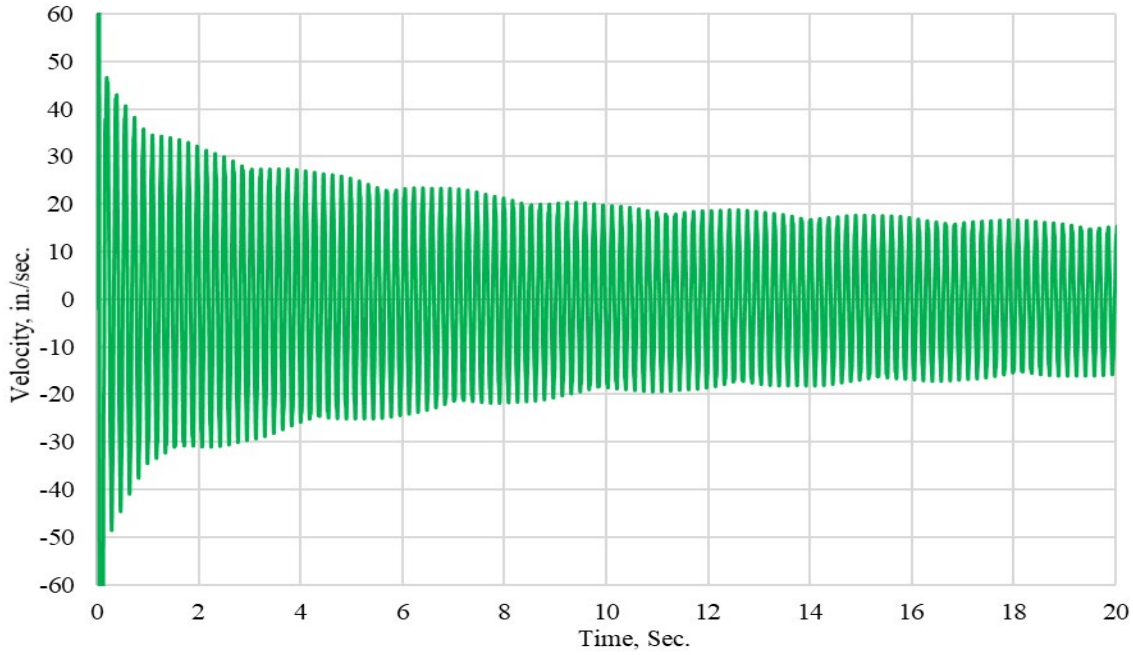

Figure 52. Velocity-time relations at cantilever free end

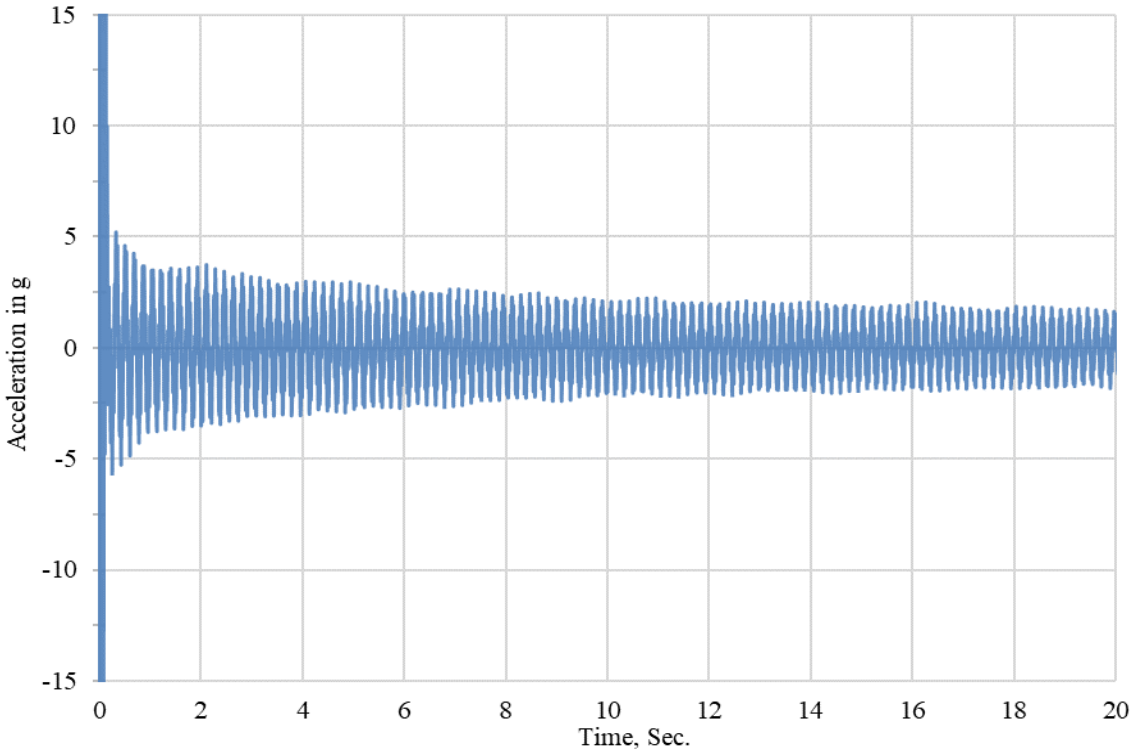

Figure 53. Acceleration-time relations at cantilever free end

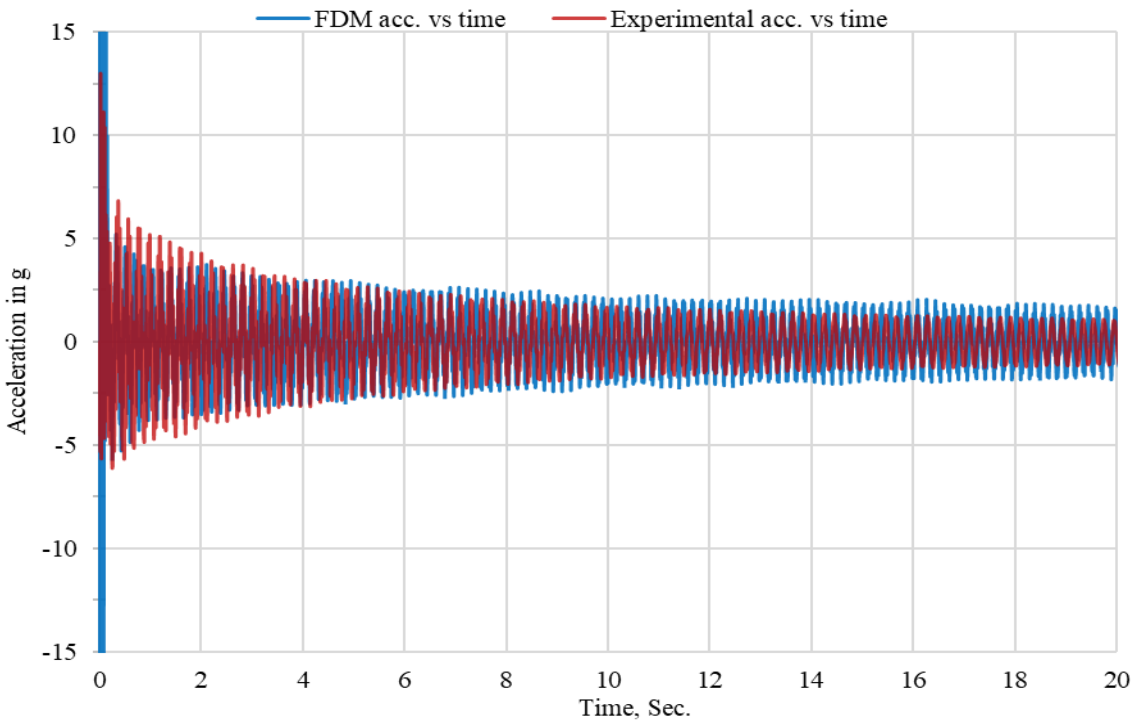

Figure 54. Experimental and FDM acceleration-time relations at free end

3.2.3 Ground-Level Column Natural Vibration Analysis Using FDM

Natural frequency of the ground-column A-B is obtained from the equation of motion when the column is initially displaced by laterally by an amount of a 1 mm or 0.039 inches at the top and then released to vibrate freely.

$$\mathrm{EI}\frac{\partial^4 v}{\partial z^4} + m\frac{\partial^2 v}{\partial t^2} + c\frac{\partial v}{\partial t} = 0 \qquad (31)$$

After applying the finite-difference method to Equation 31, the dynamic equation of motion becomes;

$$\mathrm{EI}\frac{v_{i-2}^k - 4v_{i-1}^k + 6v_i^k - 4v_{i+1}^k + v_{i+2}^k}{h^4} + m\frac{v_i^{k-1} - 2v_i^k + V_i^{k+1}}{\Delta t^2} + c\frac{v_i^{k+1} - v_i^{k-1}}{2\Delta t} = 0 \qquad (32)$$

Equation 32 is rearranged to calculate displacement at time $t+\Delta t$, i.e. at time $k+1$:

$$v_i^{k+1} = \left\{-\gamma v_{i-2}^k + 4\gamma v_{i-1}^k - (6\gamma - 2\beta)v_i^k + 4\gamma v_{i+1}^k - \gamma v_{i+2}^k - (\beta - \alpha)v_i^{k-1}\right\}/(\beta + \alpha) \qquad (33)$$

Where

$\gamma = \frac{EI}{h^4}$,

$\beta = \frac{m}{\Delta t^2}$, and

$\alpha = \frac{c}{2\,\Delta t}$,

In Equation 33, the subscript i represents nodal place along the column, and subscript k represents the time increment.

Both, rotational, k, and lateral stiffness, K, as shown in Figure 55, are determined for the structural members. The rotational stiffness, k=M/Θ, is determined after applying multiple unit moments (50 lb.in., 200 lb.in.) at joint B, and rotations, Θ = 0.00051 Rad, and 0.00205 Rad, respectively, are obtained using SAP-2000. The lateral stiffness, K=P/v, determined after applying multiple lateral unit loads (100 lb, 150 lb) at joint B and then lateral displacements, v = 0.0391 in., 0.0587 in., are obtained using SAP-2000.

Rotational stiffness, k = M/Θ = $\frac{200-50}{0.00205-0.00051}$ = 97,402 Rad/lb.in.

Lateral stiffness, K = P/ v = $\frac{150-100}{0.0587-0.0391}$ = 2,551 lb/in.

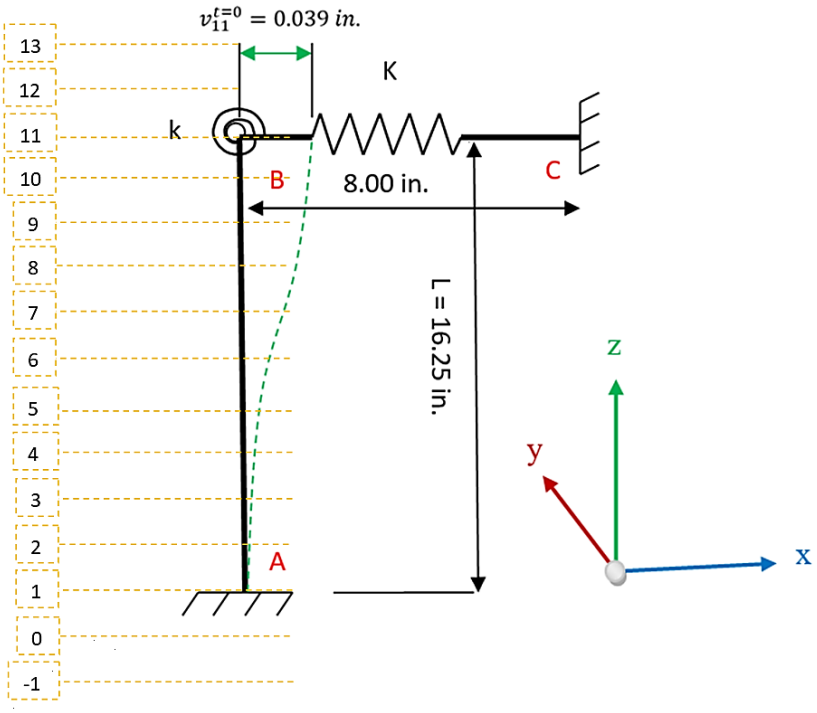

Figure 55. Model used for ground-level column AB

The moment of inertia of the column- section is, I = 0.00356 in4. The boundary conditions are as follows:

$v_1^k = 0$

$$(\frac{dv}{dz})_1 = \frac{v_2^k - v_0^k}{2h} = 0 \quad (33)$$

Joint A is at the ground level and is fixed to the ground, displacement at the imaginary nodes 0 and -1 are zero, but, since FDM is based on sloped/curved line, it is assumed that v_0^k has an imaginary value.

$v_0^k = v_2^k$

Also, from bending moment [39], M=kΘ, and shear [55], P=K v at joint B (Node 11), one gets:

$$EI\left(\frac{d^2v}{dz^2}\right)_{11} \approx -(\mathrm{k}\Theta)_{11} \tag{34}$$

$$\mathrm{EI}\ \frac{v_{10}^k - 2v_{11}^k + v_{12}^k}{h^2} = -\mathrm{k}\ \frac{v_{12}^k - v_{10}^k}{2h} \tag{35}$$

$$EI\ \frac{d^3v}{dz^3} \approx \mathrm{K}v_{11}^k \tag{36}$$

$$\mathrm{EI}\ \frac{-v_9^k + 2v_{10}^k - 2v_{12}^k + v_{13}^k}{2 \times h^3} = \mathrm{K}\ v_{11}^k \tag{37}$$

The above expressions result in:

$$v_{12}^k = \frac{-(\psi+\varphi)v_{10}^k + 2\psi v_{11}^k}{\psi - \varphi}$$

$$v_{13}^k = v_9^k - (2 + \frac{2(\psi+\varphi)}{(\psi-\varphi)})v_{10}^k + (\frac{4\psi}{(\psi-\varphi)} + \varphi`)v_{11}^k$$

where;

$$\psi = \frac{EI}{h^2}$$

$$\varphi = \frac{-k}{2h}$$

$$\varphi` = \frac{2h^3K}{EI}$$

From the initial conditions, For the first time interval solution, shape function ($\varkappa$) is merged with the first time interval for forwarding difference approximation, as shown in the following [54]:

$$\varkappa = (\left(0.5\ (1 + \cos\frac{\pi z}{L}\right)\text{)-1)}\times\text{(-}v_{11}) \tag{38}$$

where in Equation 42, v_{11} = 0.039 in., and,

$$\frac{v_i^{k=1} - v_i^{k=0}}{\Delta t} = \frac{\partial v}{\partial t}\ (\ Z_i, 0) + \frac{\Delta t}{2}\ \frac{\partial^2 v}{\partial t^2}\ (\ Z_i, 0) \tag{39}$$

Shape function, ($\varkappa$), is merged into the equation of motion as the following:

$$\text{EI}\frac{\partial^4 v}{\partial z^4} + m\frac{\partial^2 v}{\partial t^2} + c\frac{\partial v}{\partial t} = 0$$

$$\frac{\partial^2 v}{\partial t^2} = -\frac{EI}{m}\frac{\partial^4 v}{\partial z^4} - \frac{c_i^k}{m}\frac{\partial v}{\partial t}$$

$$\frac{\partial^2 v}{\partial t^2}(\ Z_i, 0) = -\frac{EI}{m}\frac{\partial^4 v}{\partial x^4}(\ Z_i, 0) - \frac{c_i^k}{m}\frac{\partial v}{\partial t}(\ Z_i, 0)$$

$$\frac{\partial^2 v}{\partial t^2}(\ Z_i, 0) = -\frac{EI}{m}\frac{d^4}{dx^4}\varkappa(Z_i) - \frac{c_i^k}{m}\frac{d}{dt}\varkappa(Z_i) \tag{40}$$

Finite-Difference method is applied to Equation 40 to get the following equation:

$$\frac{\partial^2 v}{\partial t^2}(\ Z_i, 0) = -\frac{EI}{mh^4}(\varkappa_{i-2} - 4\varkappa_{i-1} + 6\varkappa_i - 4\varkappa_{i+1} + \varkappa_{i+2}) - \frac{c_i^k}{m}\frac{\partial v}{\partial t}(\ Z_i, 0) \tag{41}$$

Finally, Equation 41 is substituted in Equation 39. From boundary conditions, velocity is zero, $\frac{\partial v}{\partial t}\ (\ Z_i, 0) = 0$, at time = 0 seconds.

$$\frac{v_i^{k=1} - v_i^{k=0}}{\Delta t} = \frac{\partial v}{\partial t}\ (\ Z_i, 0) + \frac{\Delta t}{2}\ (-\frac{EI}{mh^4}(\varkappa_{i-2} - 4\varkappa_{i-1} + 6\varkappa_i - 4\varkappa_{i+1} + \varkappa_{i+2}) -$$

$$\frac{c_i^k}{m}\frac{\partial v}{\partial t}(\ Z_i, 0))$$

$$v_i^1 = v_i^0 + \frac{\Delta t^2}{2}\left(-\frac{EI}{mh^4}(\varkappa_{i-2} - 4\varkappa_{i-1} + 6\varkappa_i - 4\varkappa_{i+1} + \varkappa_{i+2})\right)$$

$$v_i^1 = \varkappa_i + \frac{\Delta t^2}{2}\left(-\frac{EI}{mh^4}(\varkappa_{i-2} - 4\varkappa_{i-1} + 6\varkappa_i - 4\varkappa_{i+1} + \varkappa_{i+2})\right) \quad (42)$$

In order to solve for Equation 42, the shape function is applied to each node at time 0, also, Youngs Modulus, E, Moment of Inertia, I, mass per unit length, m, and node displacement, h= 1.625 in., is needed. Then, the initial displacement at each node is found using Equation 42.

After solving for the first time-interval, $t+\Delta t$, the following equations are applied to each node. The boundary equations are embedded in the following nodal equations. The following nodal equations are run for each time interval, Δt. To have a stable calculation, Δt, must not be bigger than 0.0005 seconds. Also, the damping coefficient value, c_i^k= 0.00029.

1 $v_1^{k+1} = \{[-\gamma v_{-1}^k + 4\gamma v_0^k - (6\gamma - 2\beta)v_1^k + 4\gamma v_2^k - \gamma v_3^k - (\beta - \alpha)v_1^{k-1}]\}/(\beta + \alpha)$ (43-a)

2 $v_2^{k+1} = \{[-\gamma v_0^k + 4\gamma v_1^k - (6\gamma - 2\beta)v_2^k 4\gamma v_3^k - \gamma v_4^k - (\beta - \alpha)v_2^{k-1}]\}/(\beta + \alpha)$

$v_2^{k+1} = \{[-(7\gamma - 2\beta)v_2^k + 4\gamma v_3^k - \gamma v_4^k - (\beta - \alpha)v_2^{k-1}]\}/(\beta + \alpha)$ (43-b)

3 $v_3^{k+1} = \{[-\gamma v_1^k + 4\gamma v_2^k - (6\gamma - 2\beta)v_3^k + 4\gamma v_4^k - \gamma v_5^k - (\beta - \alpha)v_3^{k-1}]\}/(\beta + \alpha)$

$v_3^{k+1} = \{[4\gamma v_2^k - (6\gamma - 2\beta)v_3^k + 4\gamma v_4^k - \gamma v_5^k - (\beta - \alpha)v_3^{k-1}]\}/(\beta + \alpha)$ (43-c)

4 $v_4^{k+1} = \{[-\gamma v_2^k + 4\gamma v_3^k - (6\gamma - 2\beta)v_4^k + 4\gamma v_5^k - \gamma v_6^k - (\beta - \alpha)v_4^{k-1}]\}/(\beta + \alpha)$ (43-d)

5 $v_5^{k+1} = \{[-\gamma v_3^k + 4\gamma v_4^k - (6\gamma - 2\beta)v_5^k + 4\gamma v_6^k - \gamma v_7^k - (\beta - \alpha)v_5^{k-1}]\}/(\beta +$

$\alpha)$ (43-e)

6 $v_6^{k+1} = \{[-\gamma v_4^k + 4\gamma v_5^k - (6\gamma - 2\beta)v_6^k + 4\gamma v_7^k - \gamma v_8^k - (\beta - \alpha)v_6^{k-1}]\}/(\beta + \alpha)$ (43-f)

7 $v_7^{k+1} = \{[-\gamma v_5^k + 4\gamma v_6^k - (6\gamma - 2\beta)v_7^k + 4\gamma v_8^k - \gamma v_9^k - (\beta - \alpha)v_7^{k-1}]\}/(\beta + \alpha)$ (43-g)

8 $v_8^{k+1} = \{[-\gamma v_6^k + 4\gamma v_7^k - (6\gamma - 2\beta)v_8^k + 4\gamma v_9^k - \gamma v_{10}^k - (\beta - \alpha)v_8^{k-1}]\}/(\beta + \alpha)$ (43-h)

9 $v_9^{k+1} = \{[-\gamma v_7^k + 4\gamma v_8^k - (6\gamma - 2\beta)v_9^k + 4\gamma v_{10}^k - \gamma v_{11}^k - (\beta - \alpha)v_9^{k-1}]\}/(\beta + \alpha)$ (43-i)

10 $v_{10}^{k+1} = \{[-\gamma v_8^k + 4\gamma v_9^k - (6\gamma - 2\beta)v_{10}^k + 4\gamma v_{11}^k - \gamma v_{12}^k - (\beta - \alpha)v_{10}^{k-1}]\}/(\beta + \alpha)$

$$v_{10}^{k+1} = \left\{\left[-\gamma v_8^k + 4\gamma v_9^k - ((6\gamma - 2\beta) - \gamma(\tfrac{(\psi+\varphi)}{(\psi-\varphi)}))v_{10}^k - (-4\gamma + 2\gamma(\tfrac{\psi}{(\psi-\varphi)}))v_{11}^k - (\beta - \alpha)v_{10}^{k-1}\right]\right\}/(\beta + \alpha) \quad (43\text{-j})$$

11 $v_{11}^{k+1} = \{[-\gamma v_9^k + 4\gamma v_{10}^k - (6\gamma - 2\beta)v_{11}^k + 4\gamma v_{12}^k - \gamma v_{13}^k - (\beta - \alpha)v_{11}^{k-1}]\}/(\beta + \alpha)$

$$v_{11}^{k+1} = \left\{-2\gamma v_9^k + \left(6\gamma + \left((-2\gamma)\tfrac{(\psi+\varphi)}{(\psi-\varphi)}\right)\right)v_{10}^k + ((-6\gamma + 2\beta - \gamma\varphi') + \left((4\gamma)\tfrac{(\psi)}{(\psi-\varphi)}\right))v_{11}^k - (\beta - \alpha)v_{11}^{k-1}\right\}/(\beta + \alpha) \quad (43\text{-k})$$

For each Δt, starting from 0 seconds, displacement-time relation, v_{11} (top of the column), is calculated as shown in Figures 56 and 57.

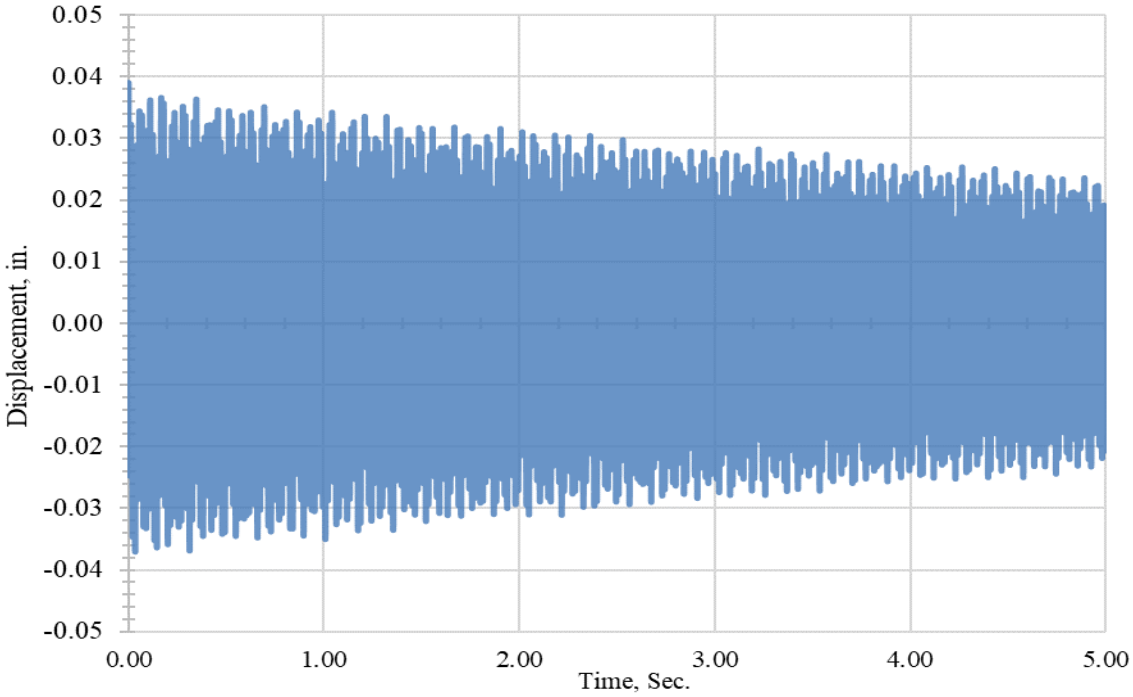

Figure 56. Displacement-time relation for ground-column AB at top

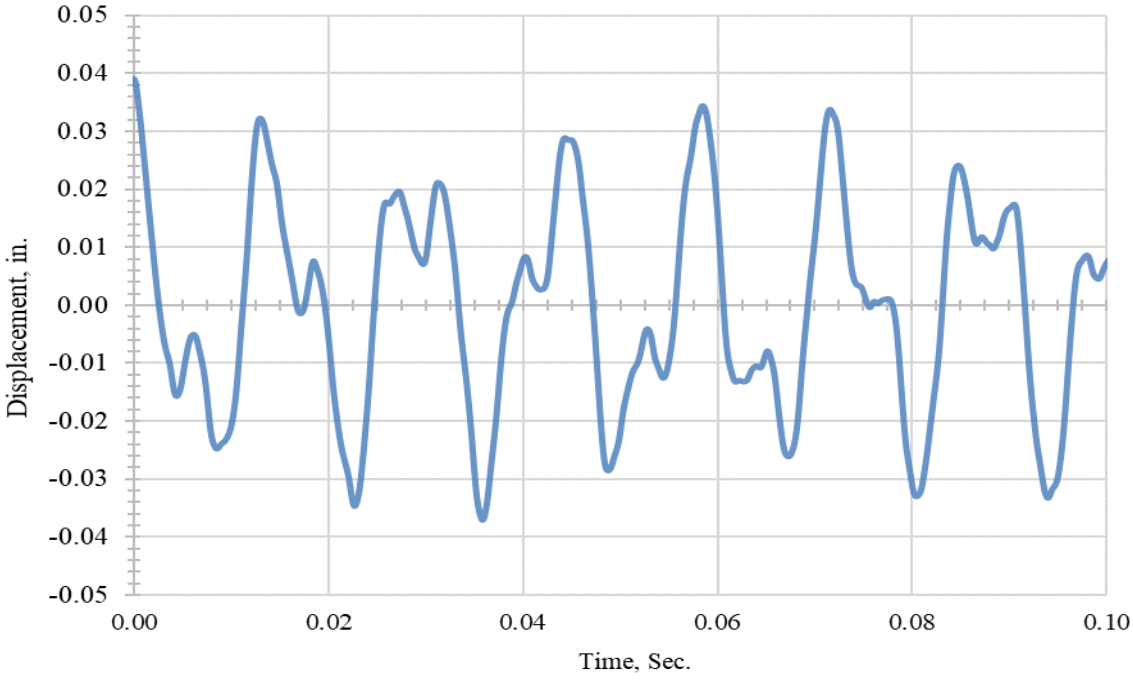

Figure 57. Displacement-time relation for ground-column AB at top, 0<t<0.1 sec.

3.2.4 Ground-Level Column Dynamic Response without Impact Load

In this section, the building frame is analyzed to observe the dynamic stability of the ground floor's middle column, Column AB. The column shown in Figure 58, is analyzed with and without the presence of lead dampers in the member while the structural member has only the time-dependent pulsating axial load, P(t), from the HVAC system. The equation of motion has the pulsating axial load with a specific frequency to add the second-order effect to the equation of motion. The pulsating axial load's frequency is changed incrementally until resonance phenomena are formed to find the frequency causing dynamic instability in the column. Then, the lead dampers are installed in the member to decrease the possibility of failure due to structural instability in the member.

$$\mathrm{EI}\frac{\partial^4 v}{\partial z^4} + m\frac{\partial^2 v}{\partial t^2} + c\frac{\partial v}{\partial t} + \mathrm{P(t)}\frac{\partial^2 v^*}{\partial z^2} = 0 \tag{44}$$

$$\mathrm{P(t)} = \mathrm{P_0} + \mathrm{Q_0}\, Cos\, \Omega\, t \tag{45}$$

$$\mathrm{P`(t)} = \mathrm{P`_0} + \mathrm{Q`_0}\, Cos\, \Omega`\, t \tag{46}$$

Where Equation 44 is the equation of motion to the column, and in Equations 45 and 46, P_0 is the axial dead and live load on the column, and Q_0, is a pulsating axial load on the column from the HVAC system with a frequency of Ω. Also, $P`_0$ is the axial dead and live load on the building, and $Q`_0$, is a pulsating axial load on the building coming from the HVAC system with a frequency of Ω`. Total operating load, $Q`_0$, of one unit of a cooling tower of HVAC system is 7780 lb (operating weight) for a 29-Ton capacity unit (model: FXV-0806A-12D-G) manufactured by Baltimore Inc. [56]. For this study, it is assumed that one closed circuit cooling tower (Length=7.50 ft, Width=8.50 ft,

height=12.50 ft) is installed on the full-scale building with RPM = 505, or frequency = 505/60=8.416 Hz, Ω = 8.416 × 2Π =52.88 Rad/Sec.

Time displacement for the mid-point of column AB is plotted for various frequencies, Ω, until resonance phenomena happens. Then the results are compared to the same results with the installation of lead dampers in the column.

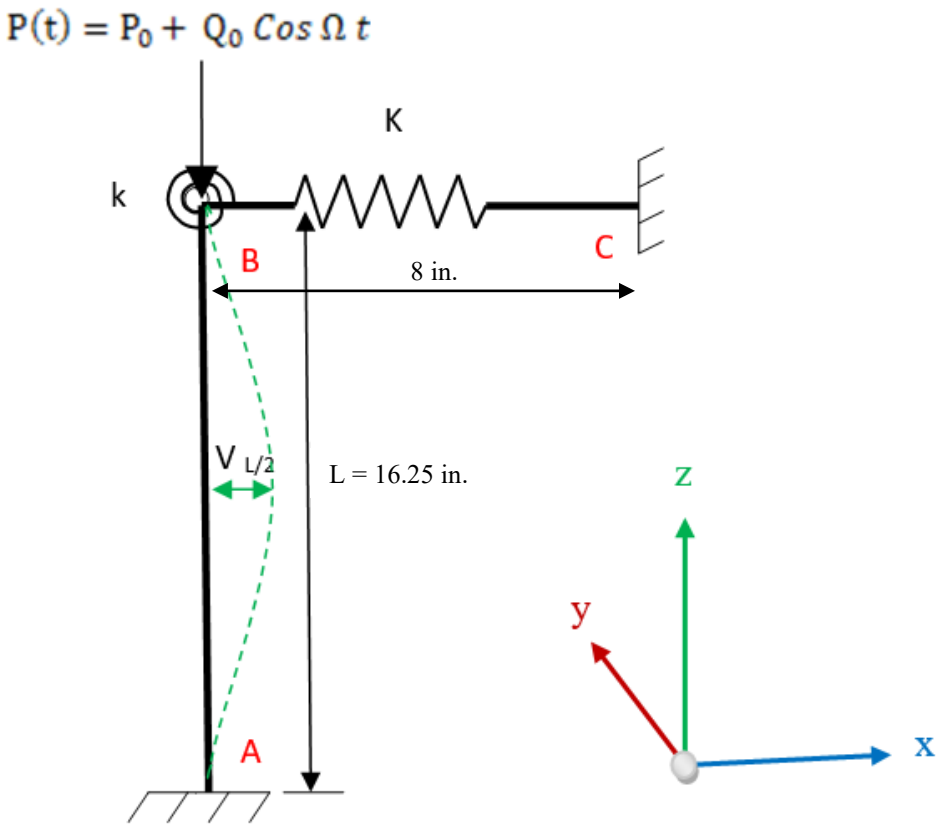

Figure 58. Applied pulsating axial load on Column AB

Since the right side of Equation 44 is equal to zero, this equation becomes an Eigenvalue problem. In order to solve for Equation 36, it is assumed that member AB has an imperfection of L/10,000 at joint B.

Meaning; v^* is the summation of initial imperfection, v_i, and actual deflection, v.

Equation 44 becomes;

$$\mathrm{EI}\frac{\partial^4 v}{\partial z^4} + m\frac{\partial^2 v}{\partial t^2} + c\frac{\partial v}{\partial t} + \mathrm{P(t)}\frac{\partial^2 v}{\partial z^2} = -\mathrm{P(t)}\frac{\partial^2 v_i}{\partial z^2} \quad (47)$$

Equation 47 which represents Equation 44 is not an Eigenvalue problem equation anymore. SAP-2000 is used to calculate the static load of the building frame (P_0) and the static load from the HVAC system (Q_0) at the top of column AB when 10% of the total load of the cooling tower is applied to the top of the lab frame model, the results are; P_0 = 2.49 lb, and Q_0 = 11.00 lb, respectively.

As mentioned before, it is assumed that the column has an initial imperfection, v_i, equal to L/10,000. It is assumed that the column has maximum imperfection value of 0.001625 in. at L (joint B or Node 11).

$$v_i = \varkappa = \frac{L}{10{,}000} Sin\left(\frac{\pi Z}{L}\right) \quad (48)$$

Equation 48 is inserted into equation 47 after being differentiated twice:

$$\mathrm{EI}\frac{\partial^4 v}{\partial z^4} + m\frac{\partial^2 v}{\partial t^2} + c\frac{\partial v}{\partial t} + \mathrm{P(t)}\frac{\partial^2 v}{\partial z^2} = -\mathrm{P(t)}\left(-\left(\frac{\pi^2}{10{,}000\,L} Sin\left(\frac{\pi Z}{L}\right)\right)\right) \quad (49)$$

where in Equation 49, E = 28,000,000 psi, I = 0.00356 in^4, $m_{per\ in.} = \frac{\mathrm{W}}{\mathrm{L}\times\mathrm{g}} = \frac{0.504}{16.25 \times 386.0886}$ = 0.00008 lb-Sec^2/in./in., and c = 0.001.

After applying the finite-difference method to Equation 49, the equation of motion, one gets:

$$\mathrm{EI}\frac{v_{i-2}^{k}-4v_{i-1}^{k}+6v_{i}^{k}-4v_{i+1}^{k}+v_{i+2}^{k}}{h^{4}}+m\frac{v_{i}^{k-1}-2v_{i}^{k}+V_{i}^{k+1}}{\Delta t^{2}}+c\frac{v_{i}^{k+1}-v_{i}^{k-1}}{2\Delta t}+\mathrm{P(t)}\frac{v_{i-1}^{k}-2v_{i}^{k}+v_{i+1}^{k}}{h^{2}}=\mathrm{P(t)}\left(\frac{\pi^{2}}{10{,}000\,L}Sin\left(\frac{\pi Z}{L}\right)\right) \quad (50)$$

Equation 50 is rearranged to calculate displacement at time $t+\Delta t$, i.e. at time $k+1$:

$$v_{i}^{k+1}=\left\{\left[-\gamma \mathrm{v}_{\mathrm{i-2}}^{\mathrm{k}}-(-4\gamma+\lambda)\mathrm{v}_{\mathrm{i-1}}^{\mathrm{k}}-(6\gamma-2\beta-2\lambda)\mathrm{v}_{\mathrm{i}}^{\mathrm{k}}-(-4\gamma+\lambda)\mathrm{v}_{\mathrm{i+1}}^{\mathrm{k}}-\gamma \mathrm{v}_{\mathrm{i+2}}^{\mathrm{k}}-(\beta-\alpha)\mathrm{v}_{\mathrm{i}}^{\mathrm{k-1}}\right]+\mathrm{P(t)}\left(\frac{\pi^{2}}{10{,}000\,L}Sin\left(\frac{\pi Z}{L}\right)\right)\right\}/(\beta+\alpha) \quad (51)$$

where:

$\gamma=\frac{EI}{h^{4}}$,

$\beta=\frac{m}{\Delta t^{2}}$,

$\alpha=\frac{c}{2\,\Delta t}$, and

$\lambda=\frac{\mathrm{P(t)}}{h^{2}}$

In Equation 51, the subscript i represents nodal place along the column, and, subscript k represents the time increment.

Boundary conditions:

From the previous section, sec. 3.4.3, the following boundary conditions are found for Column AB shown in Figure 59:

$v_1^k = 0$

$v_0^k = v_2^k$

$v_{12}^k = \frac{-(\psi+\varphi)v_{10}^k + 2\psi v_{11}^k}{\psi-\varphi}$

Including shear due to P(t) and the top being inclined [55], P=Kv - P(t) Θ at joint B (Node 11), v_{13}^k is found as the following:

and, $EI\,\frac{d^3v}{dz^3} \approx \mathrm{K}v_{11}^k$ - P(t) Θ (52)

EI $\frac{-v_9^k + 2v_{10}^k - 2v_{12}^k + v_{13}^k}{2 \times h^3}$ = K v_{11}^k - P(t) $\frac{v_{12}^k - v_{10}^k}{2h}$ (53)

From Equations 52 and 53, displacement at Node 13 is found as shown below:

$$v_{13}^k = v_9^k - (2 + \frac{2(\psi+\varphi)}{(\psi-\varphi)} - \frac{P(t)}{\psi} - \frac{P(t)(\psi+\varphi)}{\psi(\psi-\varphi)})v_{10}^k + (\frac{4\psi}{(\psi-\varphi)} + \varphi` - \frac{2P(t)\psi}{\psi(\psi-\varphi)})v_{11}^k$$

$$v_{13}^k = v_9^k - (2 + \frac{2(\psi+\varphi)}{(\psi-\varphi)} - \check{\mathrm{S}} - \check{\mathrm{S}}\frac{(\psi+\varphi)}{(\psi-\varphi)})v_{10}^k + (\frac{4\psi}{(\psi-\varphi)} + \varphi` - \check{\mathrm{S}}\frac{2\psi}{(\psi-\varphi)})v_{11}^k$$

Where

$\psi = \frac{EI}{h^2}$

$\varphi = \frac{-k}{2h}$

$\varphi` = \frac{2h^3K}{EI}$

$\check{\mathrm{S}} = \frac{P(t)}{\psi}$

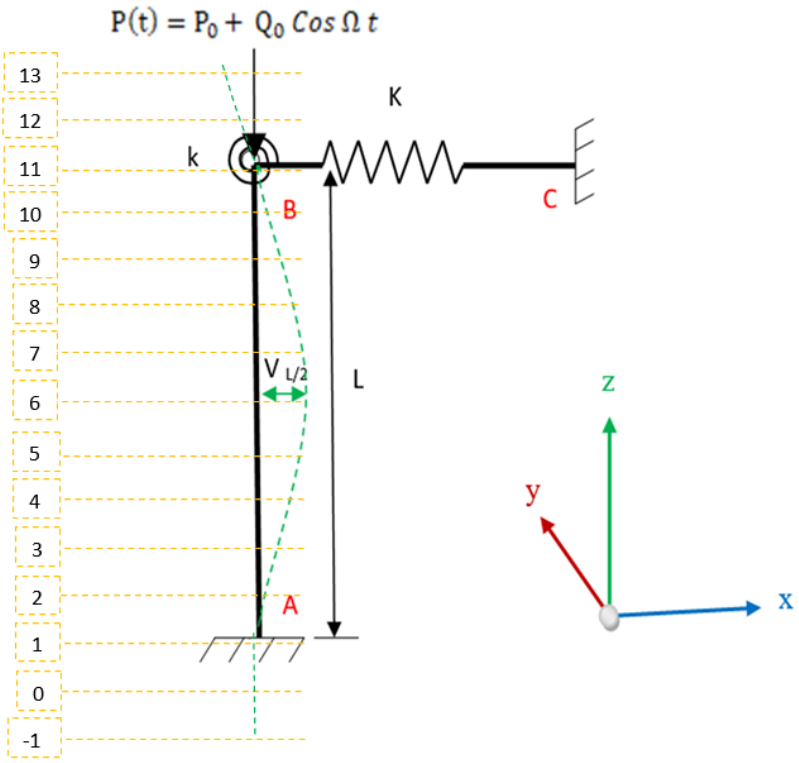

Figure 59. Column AB with FDM nodes and pulsating vertical load

For the first time interval solution, shape function ($\varkappa$), Equation is merged with the first time interval for forwarding difference approximation, as shown in the following [54]:

$$\frac{v_i^{k=1} - v_i^{k=0}}{\Delta t} = \frac{\partial v}{\partial t}\left(Z_i, 0\right) + \frac{\Delta t}{2}\frac{\partial^2 v}{\partial t^2}\left(Z_i, 0\right) \tag{54}$$

Equation 54 is the equation of velocity for the column, and the equation of motion is;

$$\mathrm{EI}\frac{\partial^4 v}{\partial z^4} + m\frac{\partial^2 v}{\partial t^2} + c\frac{\partial v}{\partial t} + \mathrm{P(t)}\frac{\partial^2 v}{\partial z^2} = 0$$

$$\frac{\partial^2 v}{\partial t^2} = -\frac{EI}{m}\frac{\partial^4 v}{\partial z^4} - \frac{c_i^k}{m}\frac{\partial v}{\partial t} - \frac{1}{m}\mathrm{P(t)}\frac{\partial^2 v}{\partial z^2} \tag{55}$$

$$\frac{\partial^2 v}{\partial t^2}(Z_i, 0) = -\frac{EI}{m}\frac{\partial^4 v}{\partial x^4}(Z_i, 0) - \frac{c_i^k}{m}\frac{\partial v}{\partial t}(Z_i, 0) - \frac{\mathrm{P(t)}}{m}\frac{\partial^2 v}{\partial z^2}$$

The shape function is merged into the equation of motion (Equation 55),

$$\frac{\partial^2 v}{\partial t^2}(Z_i, 0) = -\frac{EI}{m}\frac{d^4}{dx^4}\varkappa(Z_i) - \frac{c_i^k}{m}\frac{d}{dt}\varkappa(Z_i) - \frac{\mathrm{P(t)}}{m}\frac{\partial^2 v}{\partial z^2} \quad (56)$$

The finite-difference method is applied to Equation 56 to get the following equation:

$$\frac{\partial^2 v}{\partial t^2}(Z_i, 0) = -\frac{EI}{mh^4}(\varkappa_{i-2} - 4\varkappa_{i-1} + 6\varkappa_i - 4\varkappa_{i+1} + \varkappa_{i+2}) - \frac{c_i^k}{m}\frac{\partial v}{\partial t}(Z_i, 0) - \frac{\mathrm{P(t)}}{m}\frac{\partial^2 v}{\partial z^2} \quad (57)$$

Equation 57 is substituted in Equation 54, to get.

$$\frac{v_i^{k=1} - v_i^{k=0}}{\Delta t} = \frac{\partial v}{\partial t}(Z_i, 0) + \frac{\Delta t}{2}\left(-\frac{EI}{mh^4}(\varkappa_{i-2} - 4\varkappa_{i-1} + 6\varkappa_i - 4\varkappa_{i+1} + \varkappa_{i+2}) - \frac{c_i^k}{m}\frac{\partial v}{\partial t}(Z_i, 0) - \frac{\mathrm{P(t)}}{mh^2}(\varkappa_{i-1} - 2\varkappa_i + \varkappa_{i+1})\right)$$

From boundary conditions, velocity is zero, $\frac{\partial v}{\partial t}(Z_i, 0) = 0$, at time = 0 seconds.

$$v_i^1 = v_i^0 + \frac{\Delta t^2}{2}\left(-\frac{EI}{mh^4}(\varkappa_{i-2} - 4\varkappa_{i-1} + 6\varkappa_i - 4\varkappa_{i+1} + \varkappa_{i+2}) - \frac{\mathrm{P(t)}}{mh^2}(\varkappa_{i-1} - 2\varkappa_i + \varkappa_{i+1})\right)$$

$$v_i^1 = \varkappa_i + \frac{\Delta t^2}{2}\left(-\frac{EI}{mh^4}(\varkappa_{i-2} - 4\varkappa_{i-1} + 6\varkappa_i - 4\varkappa_{i+1} + \varkappa_{i+2}) - \frac{\mathrm{P(t)}}{mh^2}(\varkappa_{i-1} - 2\varkappa_i + \varkappa_{i+1})\right) \quad (58)$$

In order to solve for Equation 58, the shape function is applied to each node at time 0, also, Youngs Modulus, E, Moment of Inertia, I, mass per unit length, m, and node

displacement, h= 1.625 in., is needed. Then, the initial displacement at each node is found using Equation 58.

After solving for the first time-interval, $t+\Delta t$, the following equations are applied to each node. The boundary equations are embedded in the following nodal equations. The following nodal equations are run for each time interval, Δt. In order to have a stable calculation, Δt, must not be bigger than 0.0005 seconds.

1 $$v_1^{k+1} = \left\{\left[-\gamma v_{-1}^k - (-4\gamma+\lambda)v_0^k - (6\gamma-2\beta-2\lambda)v_1^k - (-4\gamma+\lambda)v_2^k - \gamma v_3^k - (\beta-\alpha)v_1^{k-1}\right] + \mathrm{P(t)}\left(\frac{\pi^2}{10{,}000\,L} Sin\left(\frac{\pi Z}{L}\right)\right)\right\}/(\beta+\alpha) \quad (59\text{-a})$$

2 $$v_2^{k+1} = \left\{\left[-\gamma v_0^k - (-4\gamma+\lambda)v_1^k - (6\gamma-2\beta-2\lambda)v_2^k - (-4\gamma+\lambda)v_3^k - \gamma v_4^k - (\beta-\alpha)v_2^{k-1}\right] + \mathrm{P(t)}\left(\frac{\pi^2}{10{,}000\,L} Sin\left(\frac{\pi Z}{L}\right)\right)\right\}/(\beta+\alpha)$$

$$v_2^{k+1} = \left\{\left[-(7\gamma-2\beta-2\lambda)v_2^k - (-4\gamma+\lambda)v_3^k - \gamma v_4^k - (\beta-\alpha)v_2^{k-1}\right] + \mathrm{P(t)}\left(\frac{\pi^2}{10{,}000\,L} Sin\left(\frac{\pi Z}{L}\right)\right)\right\}/(\beta+\alpha) \quad (59\text{-b})$$

3 $$v_3^{k+1} = \left\{\left[-\gamma v_1^k - (-4\gamma+\lambda)v_2^k - (6\gamma-2\beta-2\lambda)v_3^k - (-4\gamma+\lambda)v_4^k - \gamma v_5^k - (\beta-\alpha)v_3^{k-1}\right] + \mathrm{P(t)}\left(\frac{\pi^2}{10{,}000\,L} Sin\left(\frac{\pi Z}{L}\right)\right)\right\}/(\beta+\alpha)$$

$$v_3^{k+1} = \left\{\left[-(-4\gamma+\lambda)v_2^k - (6\gamma-2\beta-2\lambda)v_3^k - (-4\gamma+\lambda)v_4^k - \gamma v_5^k - (\beta-\alpha)v_3^{k-1}\right] + \mathrm{P(t)}\left(\frac{\pi^2}{10{,}000\,L} Sin\left(\frac{\pi Z}{L}\right)\right)\right\}/(\beta+\alpha) \quad (59\text{-c})$$

4 $$v_4^{k+1} = \left\{\left[-\gamma v_2^k - (-4\gamma+\lambda)v_3^k - (6\gamma-2\beta-2\lambda)v_4^k - (-4\gamma+\lambda)v_5^k - \gamma v_6^k - (\beta-\alpha)v_4^{k-1}\right] + \mathrm{P(t)}\left(\frac{\pi^2}{10{,}000\,L} Sin\left(\frac{\pi Z}{L}\right)\right)\right\}/(\beta+\alpha) \quad (59\text{-d})$$

5 $$v_5^{k+1} = \left\{\left[-\gamma v_3^k - (-4\gamma+\lambda)v_4^k - (6\gamma-2\beta-2\lambda)v_5^k - (-4\gamma+\lambda)v_6^k - \gamma v_7^k - (\beta-\alpha)v_5^{k-1}\right] + \mathrm{P(t)}\left(\frac{\pi^2}{10{,}000\,L} Sin\left(\frac{\pi Z}{L}\right)\right)\right\}/(\beta+\alpha) \quad (59\text{-e})$$

6 $$v_6^{k+1} = \left\{\left[-\gamma v_4^k - (-4\gamma+\lambda)v_5^k - (6\gamma-2\beta-2\lambda)v_6^k - (-4\gamma+\lambda)v_7^k - \gamma v_8^k - (\beta-\alpha)v_6^{k-1}\right] + \mathrm{P(t)}\left(\frac{\pi^2}{10{,}000\,L} Sin\left(\frac{\pi Z}{L}\right)\right)\right\}/(\beta+\alpha) \quad (59\text{-f})$$

7 $$v_7^{k+1} = \left\{\left[-\gamma v_5^k - (-4\gamma+\lambda)v_6^k - (6\gamma-2\beta-2\lambda)v_7^k - (-4\gamma+\lambda)v_8^k - \gamma v_9^k - (\beta-\alpha)v_7^{k-1}\right] + \mathrm{P(t)}\left(\frac{\pi^2}{10{,}000\,L} Sin\left(\frac{\pi Z}{L}\right)\right)\right\}/(\beta+\alpha) \quad (59\text{-g})$$

8 $$v_8^{k+1} = \left\{\left[-\gamma v_6^k - (-4\gamma+\lambda)v_7^k - (6\gamma-2\beta-2\lambda)v_8^k - (-4\gamma+\lambda)v_9^k - \gamma v_{10}^k - (\beta-\alpha)v_8^{k-1}\right] + \mathrm{P(t)}\left(\frac{\pi^2}{10{,}000\,L} Sin\left(\frac{\pi Z}{L}\right)\right)\right\}/(\beta+\alpha) \quad (59\text{-h})$$

9 $$v_9^{k+1} = \left\{\left[-\gamma v_7^k - (-4\gamma+\lambda)v_8^k - (6\gamma-2\beta-2\lambda)v_9^k - (-4\gamma+\lambda)v_{10}^k - \gamma v_{11}^k - (\beta-\alpha)v_9^{k-1}\right] + \mathrm{P(t)}\left(\frac{\pi^2}{10{,}000\,L} Sin\left(\frac{\pi Z}{L}\right)\right)\right\}/(\beta+\alpha) \quad (59\text{-i})$$

10 $$v_{10}^{k+1} = \left\{\left[-\gamma v_8^k - (-4\gamma+\lambda)v_9^k - (6\gamma-2\beta-2\lambda)v_{10}^k - (-4\gamma+\lambda)v_{11}^k - \gamma v_{12}^k - (\beta-\alpha)v_{10}^{k-1}\right] + \mathrm{P(t)}\left(\frac{\pi^2}{10{,}000\,L} Sin\left(\frac{\pi Z}{L}\right)\right)\right\}/(\beta+\alpha)$$

$$v_{10}^{k+1} = \left\{\left[-\gamma v_8^k - (-4\gamma+\lambda)v_9^k - ((6\gamma-2\beta-2\lambda) - \gamma(\tfrac{(\psi+\varphi)}{(\psi-\varphi)}))v_{10}^k - ((-4\gamma+\lambda)+2\gamma(\tfrac{\psi}{(\psi-\varphi)}))v_{11}^k - (\beta-\alpha)v_{10}^{k-1}\right] + \mathrm{P(t)}\left(\frac{\pi^2}{10{,}000\,L} Sin\left(\frac{\pi Z}{L}\right)\right)\right\}/(\beta+\alpha) \quad (59\text{-j})$$

11 $$v_{11}^{k+1} = \left\{\left[-\gamma v_9^k - (-4\gamma+\lambda)v_{10}^k - (6\gamma-2\beta-2\lambda)v_{11}^k - (-4\gamma+\lambda)v_{12}^k - \gamma v_{13}^k - (\beta-\alpha)v_{11}^{k-1}\right] + \mathrm{P(t)}\left(\frac{\pi^2}{10{,}000\,L} Sin\left(\frac{\pi Z}{L}\right)\right)\right\}/(\beta+\alpha)$$

$$v_{11}^{k+1} = \left\{-2\gamma v_9^k + \left(6\gamma - \lambda - \gamma\check{S} + \left(\left(\lambda - 2\gamma - \gamma\check{S}\right)\frac{(\psi+\varphi)}{(\psi-\varphi)}\right)\right)v_{10}^k + ((-6\gamma + 2\beta + 2\lambda - \gamma\varphi') + \left(\left(4\gamma - 2\lambda + 2\gamma\check{S}\right)\frac{(\psi)}{(\psi-\varphi)}\right))v_{11}^k - (\beta - \alpha)v_{11}^{k-1} + \mathrm{P(t)}\left(\frac{\pi^2}{10{,}000\,L} Sin\left(\frac{\pi Z}{L}\right)\right)\right\} / (\beta + \alpha) \quad (59\text{-k})$$

For each Δt, starting from 0 seconds, mid-point displacement, v_6, is calculated to generate displacement-time relations for column AB.

Figures 60 and 61 show lateral displacement on the x-axis at the middle of the column, v_6, and at the top of the column, v_{11}, simultaneously, when the actual natural circular frequency of the cooling tower is included in the pulsating axial load equation, Ω =52.88 Rad/Sec. The damping coefficient for the following figures is 0.00029. The figures, also, show the difference in the calculation results obtained in both FDM and SAP-2000. The differences are from the initial condition difference in the FDM and the SAP2000 as well as the different approaches that are used in both sets of calculations; consistent mass is used for the FDM, while SAP-2000 is based on lumped mass.

The Figures 62 and 63 show that the column response when the natural frequency of the pulsating axial load, Ω, is the same as the natural frequency of the column, ω_n=432.80 Rad/Sec with a damping coefficient of 0.00029. Figure 64 shows the resonant response of the column at the top end, v_{11}, for zero damping, and the column's response at various damping ratios. The damping coefficient, c = 0.000586 is calculated from the frame model as explained in Chapter 2, the damping increase ratios 61.8% and 94.2% are also calculated in Chapter 2. This figure shows the significance of installing lead dampers and damping panels in the frame model in reducing vibration.

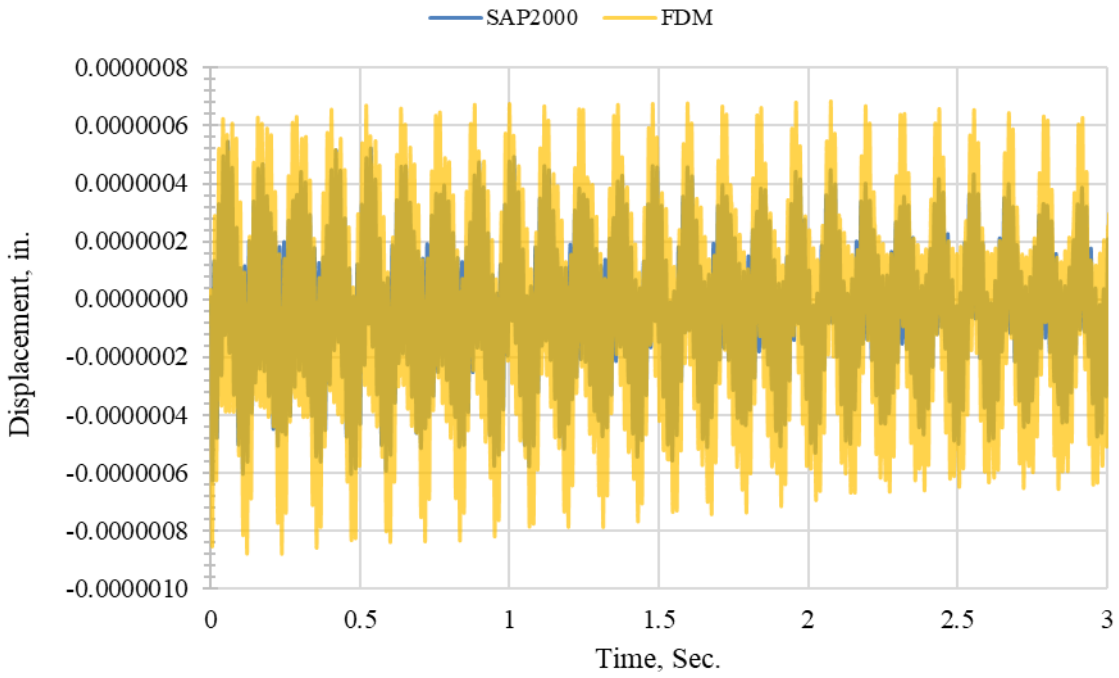

Figure 60. Displacement-time relations at mid-height, with c = 0.00029

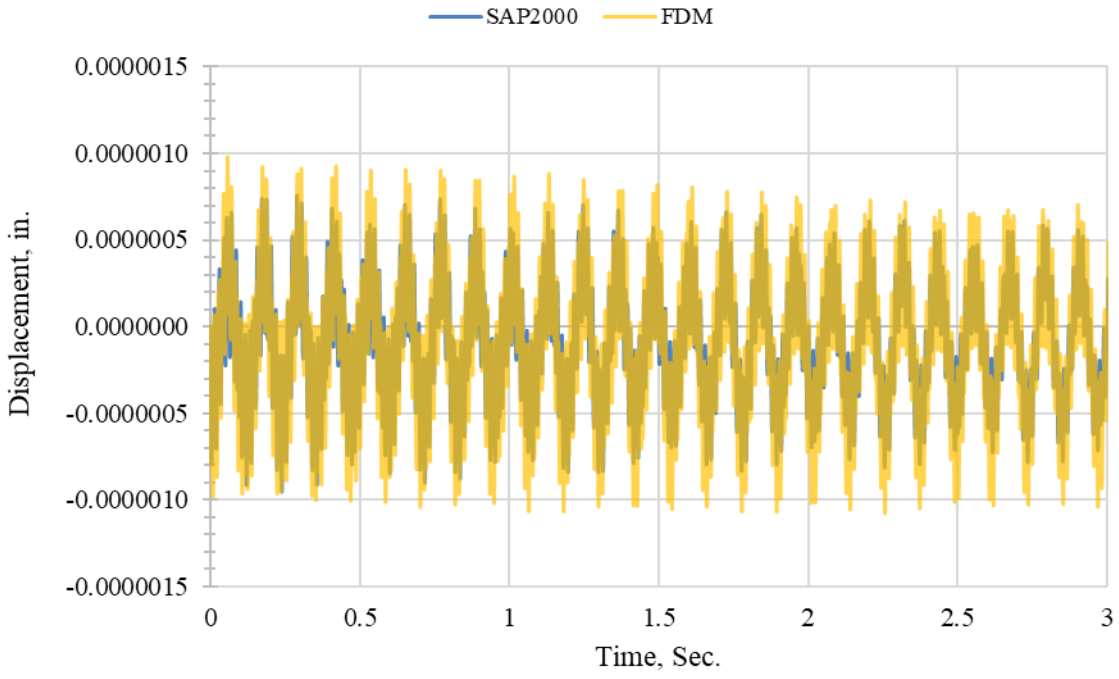

Figure 61. Displacement-time for top Column AB, with c = 0.00029

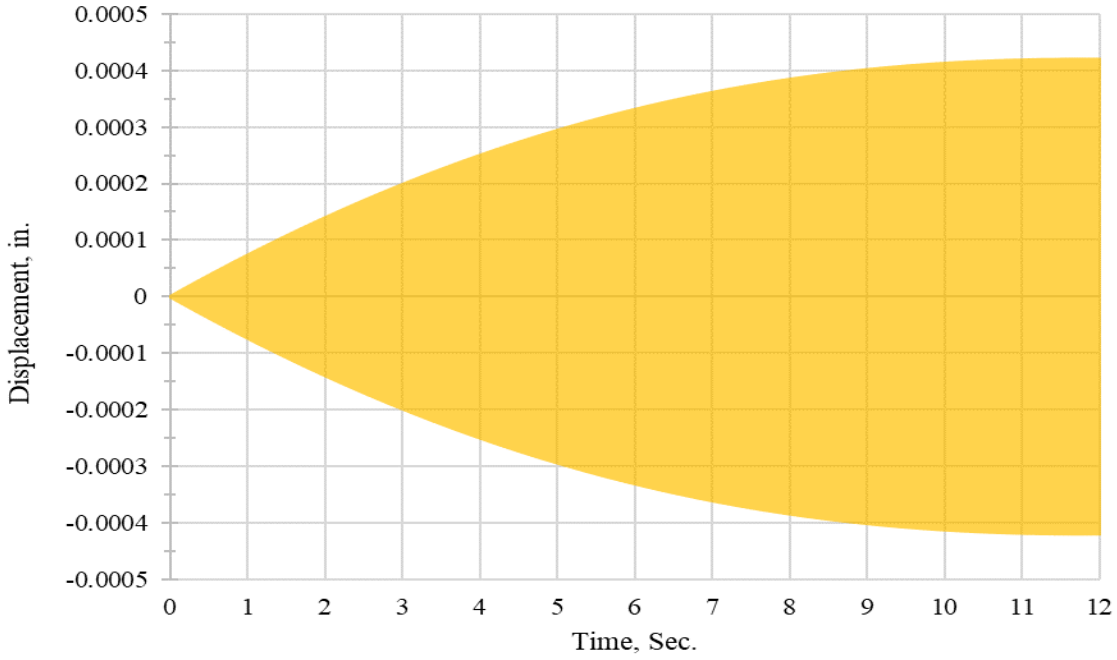

Figure 62. Displacement-time relation for Column AB mid-height, with c = 0.00029 and Ω = 432.8 rad/sec.

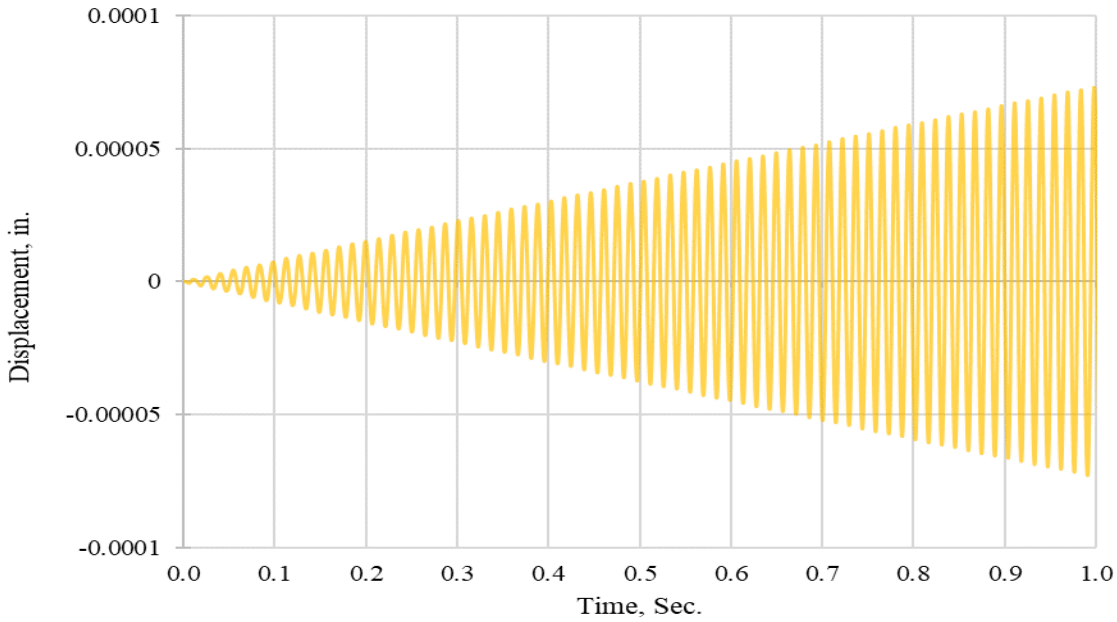

Figure 63. Displacement-time relation for Column AB mid-height, with c = 0.00029 and Ω = 432.8 rad/sec, 0<t<1 sec.

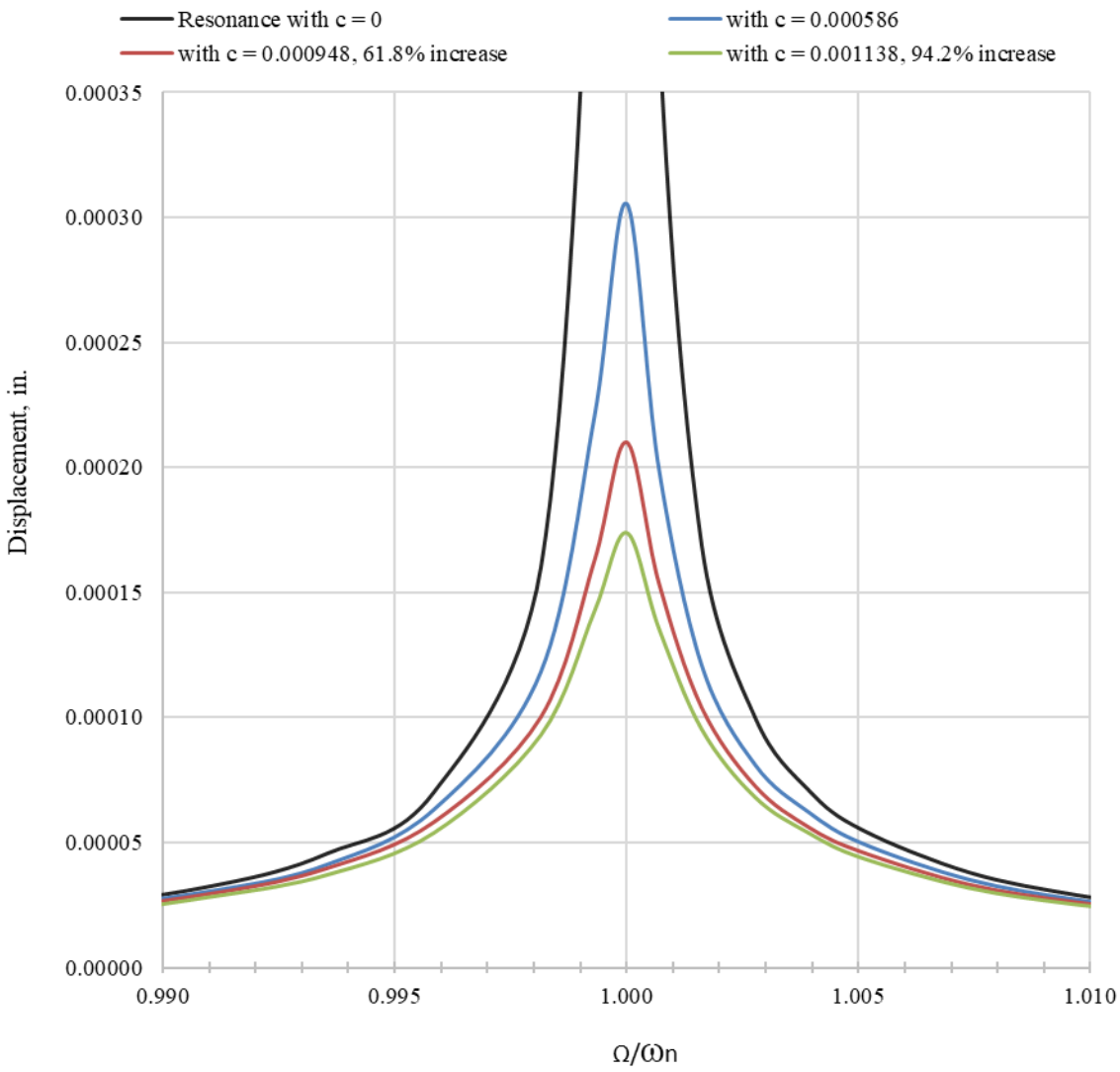

Figure 64. Ground-level top end displacement versus frequency ratio Ω/ω_n

Figures 65 and 66 show a comparison between the calculation results from FDM and SAP-2000 for the column analysis at the middle of column AB, Node 6, when the damping coefficient is 0, and 0.00029, respectively.

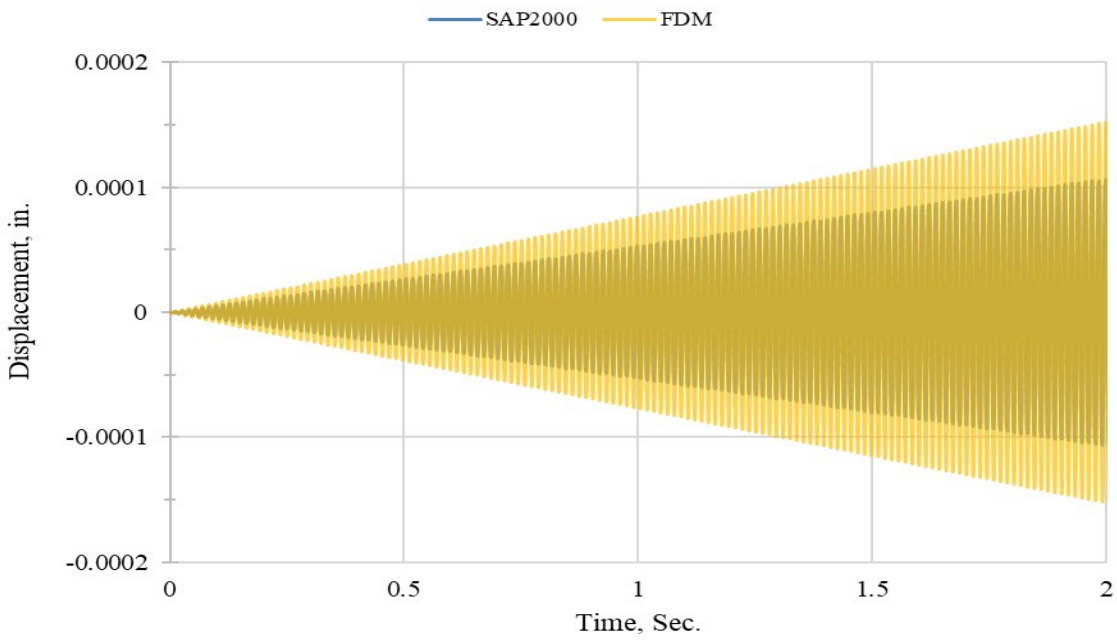

Figure 65. Displacement-time relations for Column AB mid-height, with c = 0 and Ω = 432.8 rad/sec

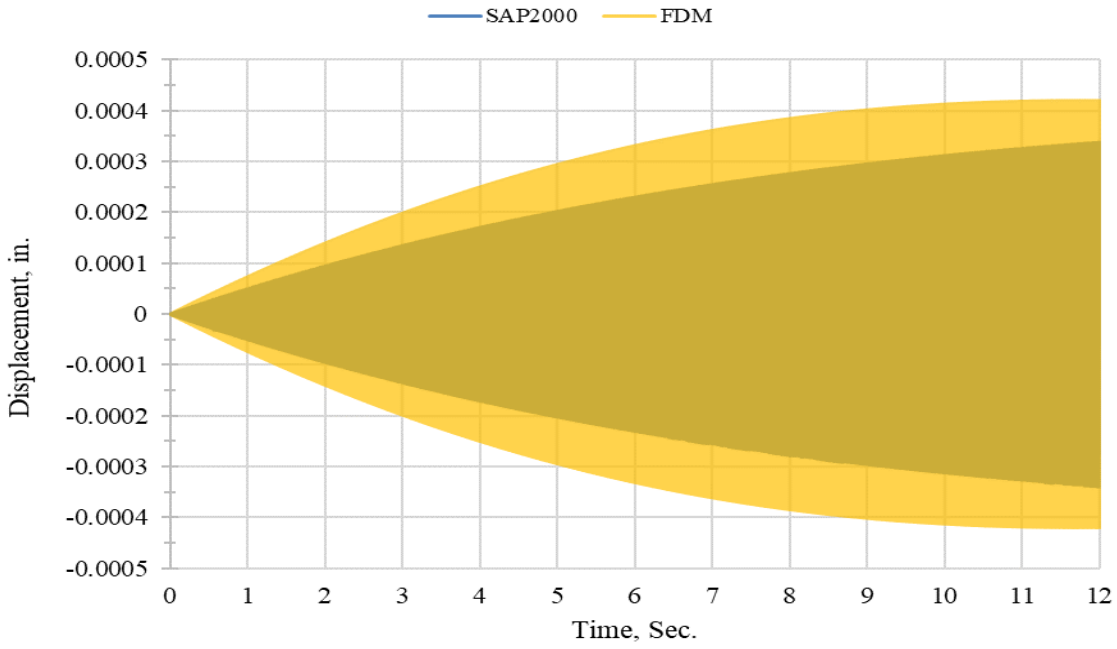

Figure 66. Displacement-time relations for Column AB mid-height, with c = 0.00029 and Ω = 432.8 rad/sec

3.2.5 Ground-Level Column Dynamic Response with Impact Load

In this section, dynamic stability of ground-column AB shown in Figure 67 is analyzed for both pulsating axial load and lateral impact load. The study includes the use of experimentally obtained lateral forcing function, Equation 2, and the calculated camping coefficient, in the equation of motion.

$$\mathrm{EI}\frac{\partial^4 v}{\partial z^4} + m\frac{\partial^2 v}{\partial t^2} + c\frac{\partial v}{\partial t} + \mathrm{P(t)}\frac{\partial^2 v^*}{\partial z^2} = F(\frac{L}{2}, t) \tag{60}$$

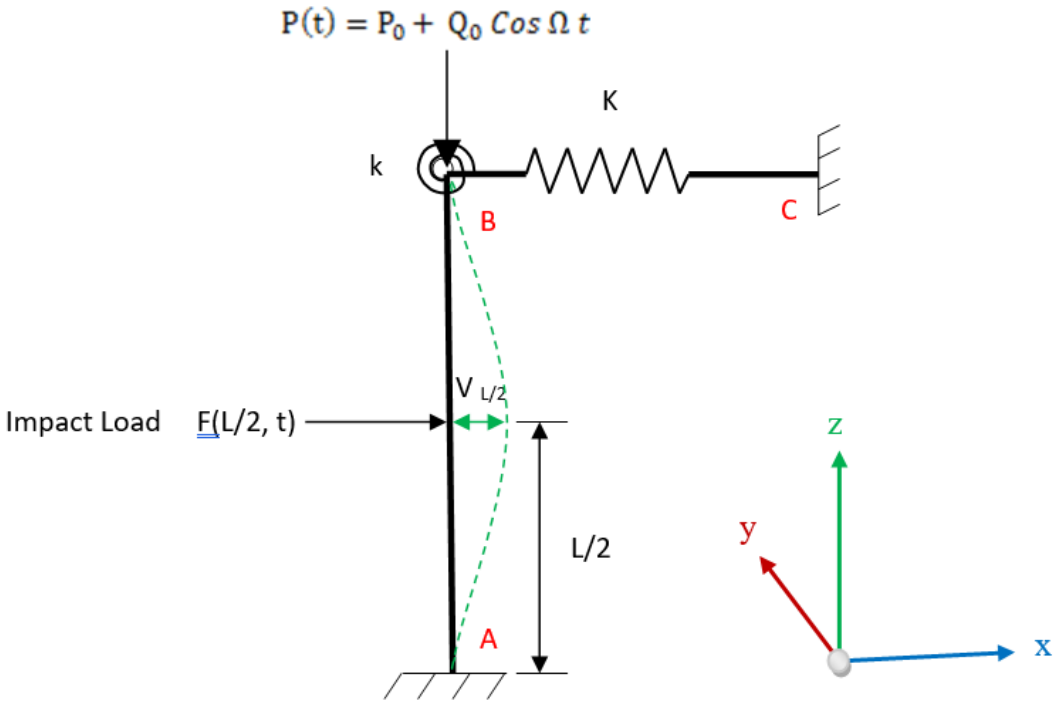

Figure 67. Column AB with pulsating vertical and lateral impact load

In order to account for imperfection in the column, Equation 48 is inserted into equation 60 after being differentiated twice:

$$\mathrm{EI}\frac{\partial^4 v}{\partial z^4} + m\frac{\partial^2 v}{\partial t^2} + c\frac{\partial v}{\partial t} + \mathrm{P(t)}\frac{\partial^2 v}{\partial z^2} = -\mathrm{P(t)}\left(-\left(\frac{\pi^2}{10{,}000\,L} Sin\ \left(\frac{\pi\, Z}{L}\right)\right)\right) + F(\frac{L}{2}, t) \tag{61}$$

After applying the finite-difference method to Equation 61, the equation of motion becomes;

$$\mathrm{EI}\frac{v_{i-2}^{k}-4v_{i-1}^{k}+6v_{i}^{k}-4v_{i+1}^{k}+v_{i+2}^{k}}{h^{4}}+m\frac{v_{i}^{k-1}-2v_{i}^{k}+V_{i}^{k+1}}{\Delta t^{2}}+c\frac{v_{i}^{k+1}-v_{i}^{k-1}}{2\Delta t}+\mathrm{P(t)}\frac{v_{i-1}^{k}-2v_{i}^{k}+v_{i+1}^{k}}{h^{2}}=$$
$$+\mathrm{P(t)}\left(\frac{\pi^{2}}{10{,}000\,L}Sin\left(\frac{\pi Z}{L}\right)\right)+F(\frac{L}{2},t) \quad (62)$$

Equation 62 is rearranged to calculate displacement at time $t+\Delta t$, i.e. at time $k+1$:

$$v_{i}^{k+1}=\Big\{\big[-\gamma \mathrm{v}_{\mathrm{i-2}}^{\mathrm{k}}-(-4\gamma+\lambda)\mathrm{v}_{\mathrm{i-1}}^{\mathrm{k}}-(6\gamma-2\beta-2\lambda)\mathrm{v}_{\mathrm{i}}^{\mathrm{k}}-(-4\gamma+\lambda)\mathrm{v}_{\mathrm{i+1}}^{\mathrm{k}}-\gamma \mathrm{v}_{\mathrm{i+2}}^{\mathrm{k}}-$$
$$(\beta-\alpha)\mathrm{v}_{\mathrm{i}}^{\mathrm{k-1}}\big]+\mathrm{P(t)}\left(\frac{\pi^{2}}{10{,}000\,L}Sin\left(\frac{\pi Z}{L}\right)\right)+F(\frac{L}{2},t)\Big\}/(\beta+\alpha) \quad (63)$$

In Equation 63, the subscript i represents nodal place along the column, and subscript k represents the time increment.

For the first time interval solution, as explained in the previous section, the shape function ($\varkappa$), Equation is merged with the first time interval for forwarding difference approximation [54]:

$$v_{i}^{1}=\varkappa_{i}+\frac{\Delta t^{2}}{2}\left(-\frac{EI}{mh^{4}}(\varkappa_{i-2}-4\varkappa_{i-1}+6\varkappa_{i}-4\varkappa_{i+1}+\varkappa_{i+2})-\frac{\mathrm{P(t)}}{mh^{2}}(\varkappa_{i-1}-2\varkappa_{i}+\right.$$
$$\left.\varkappa_{i+1})+\left(\frac{F\left(\frac{L}{2},0\right)}{m}\right)\right) \quad (64)$$

Initial displacement at the first time interval for each node is found using Equation 64. for each next time interval, Equation 63 is applied to each nodal location along the column after dividing the column into equal segments as shown in Figure 68.

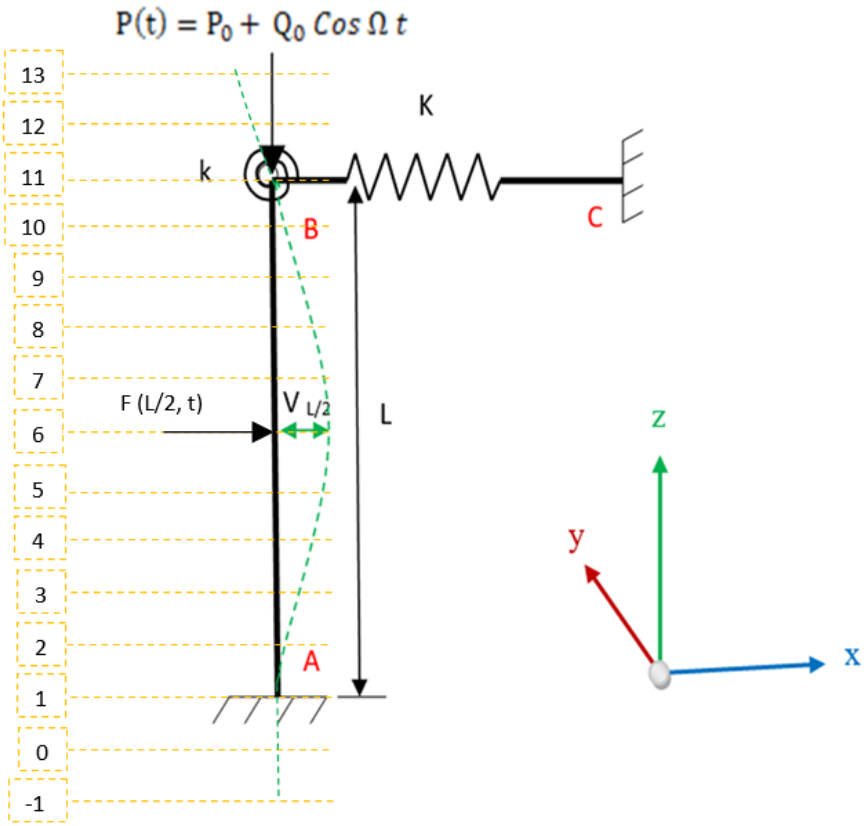

Figure 68. Ground-level Column AB under vertical pulsating and lateral impact loads

After solving for the first time-interval, $t+\Delta t$, the following equations are applied to each node. The boundary equations are embedded in the following nodal equations. The following nodal equations are run for each time interval, Δt. In order to have a stable calculation, Δt, must be equal or smaller than 0.0005 seconds. Also, the damping coefficient value, c_i^k= 0.00029.

1 $$v_1^{k+1} = \{[-\gamma v_{-1}^k - (-4\gamma + \lambda)v_0^k - (6\gamma - 2\beta - 2\lambda)v_1^k - (-4\gamma + \lambda)v_2^k - \gamma v_3^k -$$

$$(\beta-\alpha)v_1^{k-1}\,]+\mathrm{P(t)}\left(\frac{\pi^2}{10{,}000\,L}Sin\,\left(\frac{\pi\,Z}{L}\right)\right)\Big\}/(\beta+\alpha) \qquad \text{(65-a)}$$

2 $$v_2^{k+1}=\Big\{\big[-\gamma v_0^k-(-4\gamma+\lambda)v_1^k-(6\gamma-2\beta-2\lambda)v_2^k-(-4\gamma+\lambda)v_3^k-\gamma v_4^k-(\beta-\alpha)v_2^{k-1}\,\big]+\mathrm{P(t)}\left(\frac{\pi^2}{10{,}000\,L}Sin\,\left(\frac{\pi\,Z}{L}\right)\right)\Big\}/(\beta+\alpha)$$

$$v_2^{k+1}=\Big\{\big[-(7\gamma-2\beta-2\lambda)v_2^k-(-4\gamma+\lambda)v_3^k-\gamma v_4^k-(\beta-\alpha)v_2^{k-1}\,\big]+\mathrm{P(t)}\left(\frac{\pi^2}{10{,}000\,L}Sin\,\left(\frac{\pi\,Z}{L}\right)\right)\Big\}/(\beta+\alpha) \qquad \text{(65-b)}$$

3 $$v_3^{k+1}=\Big\{\big[-\gamma v_1^k-(-4\gamma+\lambda)v_2^k-(6\gamma-2\beta-2\lambda)v_3^k-(-4\gamma+\lambda)v_4^k-\gamma v_5^k-(\beta-\alpha)v_3^{k-1}\,\big]+\mathrm{P(t)}\left(\frac{\pi^2}{10{,}000\,L}Sin\,\left(\frac{\pi\,Z}{L}\right)\right)\Big\}/(\beta+\alpha)$$

$$v_3^{k+1}=\Big\{\big[-(-4\gamma+\lambda)v_2^k-(6\gamma-2\beta-2\lambda)v_3^k-(-4\gamma+\lambda)v_4^k-\gamma v_5^k-(\beta-\alpha)v_3^{k-1}\,\big]+\mathrm{P(t)}\left(\frac{\pi^2}{10{,}000\,L}Sin\,\left(\frac{\pi\,Z}{L}\right)\right)\Big\}/(\beta+\alpha) \qquad \text{(65-c)}$$

4 $$v_4^{k+1}=\Big\{\big[-\gamma v_2^k-(-4\gamma+\lambda)v_3^k-(6\gamma-2\beta-2\lambda)v_4^k-(-4\gamma+\lambda)v_5^k-\gamma v_6^k-(\beta-\alpha)v_4^{k-1}\,\big]+\mathrm{P(t)}\left(\frac{\pi^2}{10{,}000\,L}Sin\,\left(\frac{\pi\,Z}{L}\right)\right)\Big\}/(\beta+\alpha) \qquad \text{(65-d)}$$

5 $$v_5^{k+1}=\Big\{\big[-\gamma v_3^k-(-4\gamma+\lambda)v_4^k-(6\gamma-2\beta-2\lambda)v_5^k-(-4\gamma+\lambda)v_6^k-\gamma v_7^k-(\beta-\alpha)v_5^{k-1}\,\big]+\mathrm{P(t)}\left(\frac{\pi^2}{10{,}000\,L}Sin\,\left(\frac{\pi\,Z}{L}\right)\right)\Big\}/(\beta+\alpha) \qquad \text{(65-e)}$$

6 $$v_6^{k+1}=\Big\{\big[-\gamma v_4^k-(-4\gamma+\lambda)v_5^k-(6\gamma-2\beta-2\lambda)v_6^k-(-4\gamma+\lambda)v_7^k-\gamma v_8^k-(\beta-\alpha)v_6^{k-1}\,\big]+\mathrm{P(t)}\left(\frac{\pi^2}{10{,}000\,L}Sin\,\left(\frac{\pi\,Z}{L}\right)\right)+\,F\left(\frac{L}{2},t\right)\Big\}/(\beta+\alpha) \qquad \text{(65-f)}$$

7 $$v_7^{k+1}=\Big\{\big[-\gamma v_5^k-(-4\gamma+\lambda)v_6^k-(6\gamma-2\beta-2\lambda)v_7^k-(-4\gamma+\lambda)v_8^k-\gamma v_9^k-(\beta-\alpha)v_7^{k-1}\,\big]+\mathrm{P(t)}\left(\frac{\pi^2}{10{,}000\,L}Sin\,\left(\frac{\pi\,Z}{L}\right)\right)\Big\}/(\beta+\alpha) \qquad \text{(65-g)}$$

8 $$v_8^{k+1} = \left\{\left[-\gamma v_6^k - (-4\gamma+\lambda)v_7^k - (6\gamma-2\beta-2\lambda)v_8^k - (-4\gamma+\lambda)v_9^k - \gamma v_{10}^k - (\beta-\alpha)v_8^{k-1}\right] + \mathrm{P(t)}\left(\frac{\pi^2}{10{,}000\,L} Sin\left(\frac{\pi Z}{L}\right)\right)\right\}/(\beta+\alpha) \quad \text{(65-h)}$$

9 $$v_9^{k+1} = \left\{\left[-\gamma v_7^k - (-4\gamma+\lambda)v_8^k - (6\gamma-2\beta-2\lambda)v_9^k - (-4\gamma+\lambda)v_{10}^k - \gamma v_{11}^k - (\beta-\alpha)v_9^{k-1}\right] + \mathrm{P(t)}\left(\frac{\pi^2}{10{,}000\,L} Sin\left(\frac{\pi Z}{L}\right)\right)\right\}/(\beta+\alpha) \quad \text{(65-i)}$$

10 $$v_{10}^{k+1} = \left\{\left[-\gamma v_8^k - (-4\gamma+\lambda)v_9^k - (6\gamma-2\beta-2\lambda)v_{10}^k - (-4\gamma+\lambda)v_{11}^k - \gamma v_{12}^k - (\beta-\alpha)v_{10}^{k-1}\right] + \mathrm{P(t)}\left(\frac{\pi^2}{10{,}000\,L} Sin\left(\frac{\pi Z}{L}\right)\right)\right\}/(\beta+\alpha)$$

$$v_{10}^{k+1} = \left\{\left[-\gamma v_8^k - (-4\gamma+\lambda)v_9^k - ((6\gamma-2\beta-2\lambda) - \gamma(\tfrac{(\psi+\varphi)}{(\psi-\varphi)}))v_{10}^k - ((-4\gamma+\lambda)+2\gamma(\tfrac{\psi}{(\psi-\varphi)}))v_{11}^k - (\beta-\alpha)v_{10}^{k-1}\right] + \mathrm{P(t)}\left(\frac{\pi^2}{10{,}000\,L} Sin\left(\frac{\pi Z}{L}\right)\right)\right\}/(\beta+\alpha) \quad \text{(65-j)}$$

11 $$v_{11}^{k+1} = \left\{\left[-\gamma v_9^k - (-4\gamma+\lambda)v_{10}^k - (6\gamma-2\beta-2\lambda)v_{11}^k - (-4\gamma+\lambda)v_{12}^k - \gamma v_{13}^k - (\beta-\alpha)v_{11}^{k-1}\right] + \mathrm{P(t)}\left(\frac{\pi^2}{10{,}000\,L} Sin\left(\frac{\pi Z}{L}\right)\right)\right\}/(\beta+\alpha)$$

$$v_{11}^{k+1} = \left\{-2\gamma v_9^k + \left(6\gamma-\lambda-\gamma\check{S} + \left((\lambda-2\gamma-\gamma\check{S})\tfrac{(\psi+\varphi)}{(\psi-\varphi)}\right)\right)v_{10}^k + ((-6\gamma+2\beta+2\lambda-\gamma\varphi') + \left((4\gamma-2\lambda+2\gamma\check{S})\tfrac{(\psi)}{(\psi-\varphi)}\right))v_{11}^k - (\beta-\alpha)v_{11}^{k-1} + \mathrm{P(t)}\left(\frac{\pi^2}{10{,}000\,L} Sin\left(\frac{\pi Z}{L}\right)\right)\right\}/(\beta+\alpha) \quad \text{(65-k)}$$

For each Δt, starting from 0 seconds, displacement, v_6, at mid-height of the column is calculated at the presence of the pulsating axial load and the lateral impact load. Figures 69 shows the response of the column when the actual natural circular frequency of the cooling tower (Ω=52.88 Rad/Sec.) is used in the pulsating axial load with the damping, c=0.00029. The figure shows a comparison between the results from

the FDM and SAP-2000 for the displacement-time relations at the mid-height of the column.

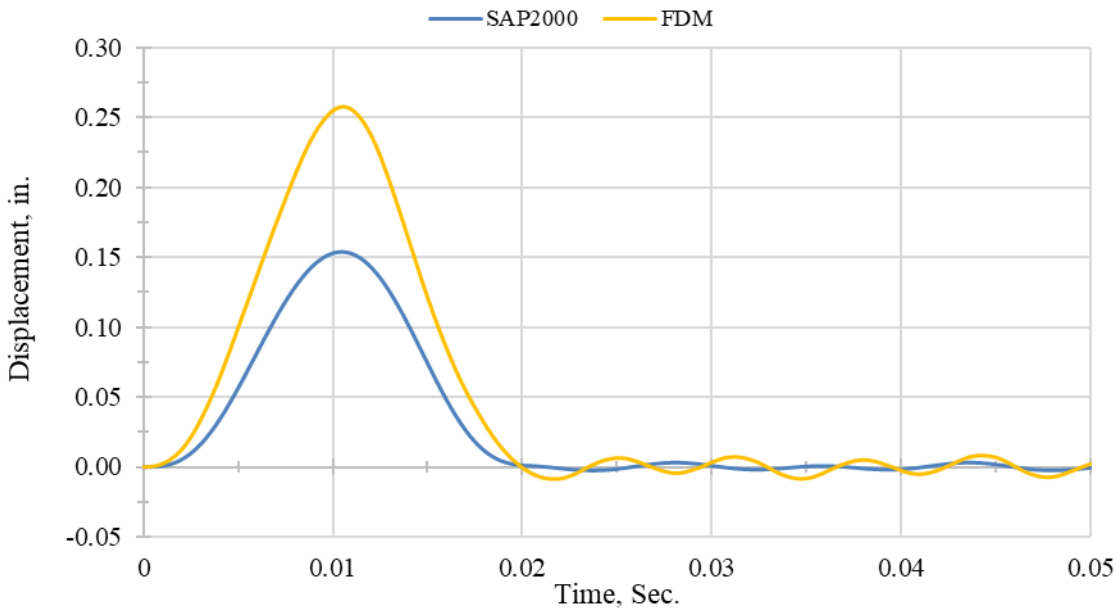

Figure 69. Displacement-time for Column AB mid-height, with pulsating axial load and lateral impact loads, with Ω=52.88 rad/sec.

3.3 Dynamic Response with or without Impact Load Using SAP-2000

The commercial computer program SAP-2000 is used to analyze the lab model and a full-scale building frame under vertical vibrating load from the HVAC system and the lateral applied impact load on the first floor's middle column.

3.3.1 Steel Building Frame Model Dynamic Response with and without Impact Load

The building frame model shown in Figure 70 is analyzed using SAP-2000 to observe the frame's response at the mid-height of the ground-level column, joint number 21, and the top floor, joint number 76. 10% of the HVAC system's load is applied to the top two middle joints, joint numbers 71 and 75, that pulsate simultaneously at the same

time. Also, the lateral impact load, F(L/2,t) is applied to the mid-span of the front middle column at joint number 21. From chapter 2; natural circular frequency of the frame model is ω_n= 135.55 rads/sec. and the calculated damping coefficient is 0.000586.

Figures 71 and 72 show the building frame's response at the mid-height of the ground-level column and the top floor, respectively. Figures 73 and 74 show the building's response when the frame model's damping coefficient is changed to the damping coefficient obtained from adding bolted damping panels to the system, c = 0.586.

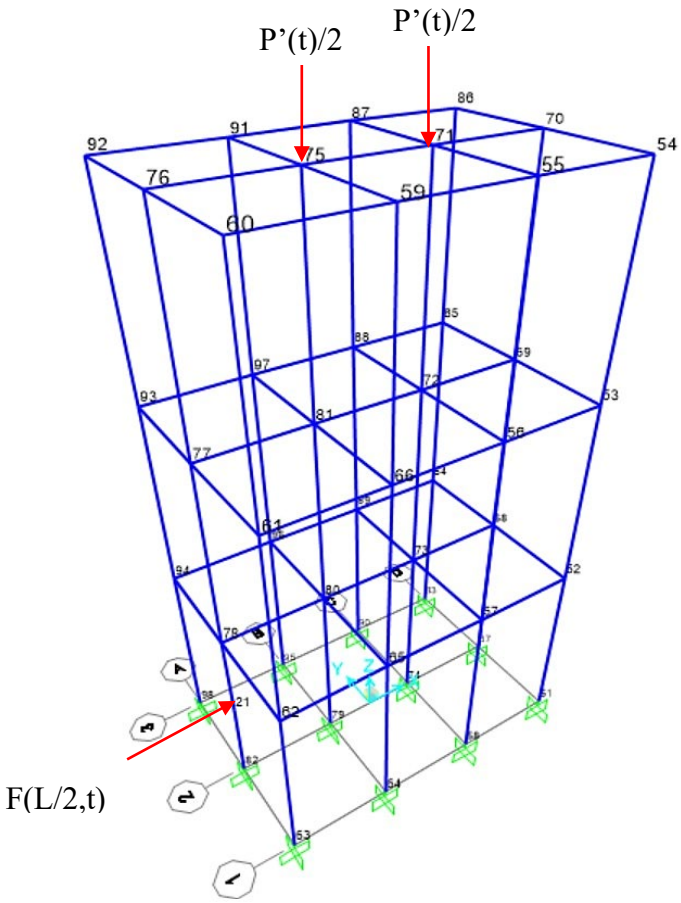

Figure 70. Building model with impact load on ground-level column and pulsating load on top

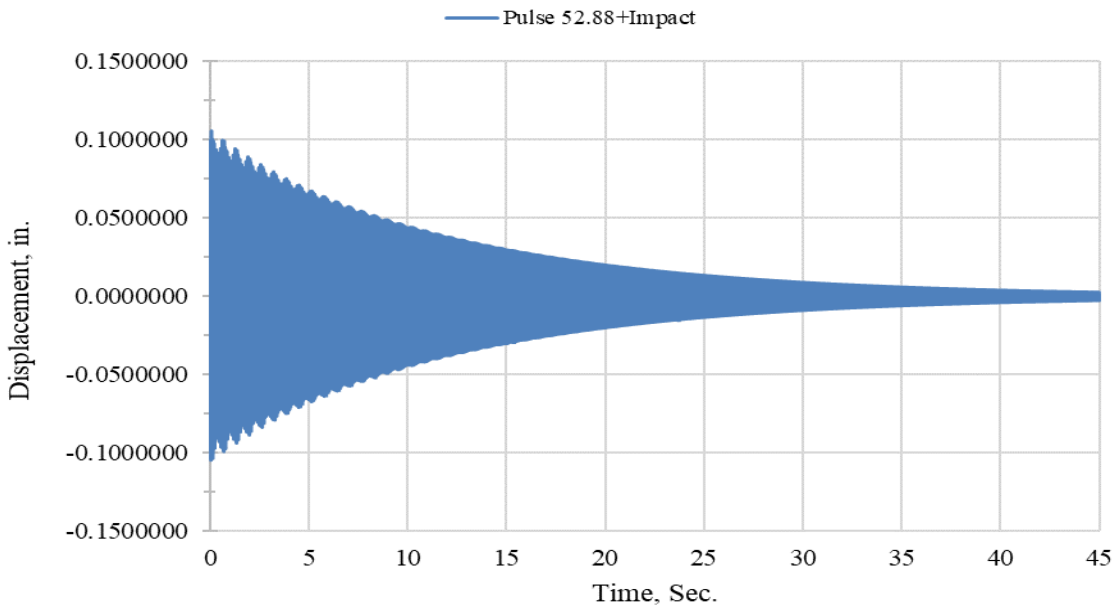

Figure 71. Displacement-time at top floor, Joint 76, with c = 0.00586

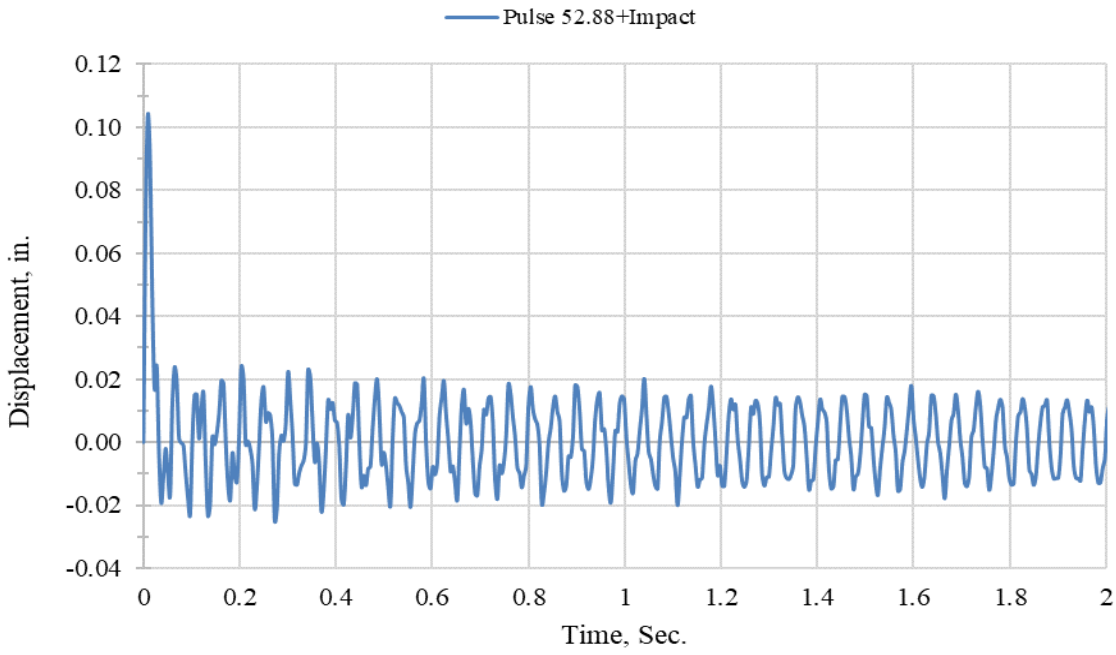

Figure 72. Displacement-time at ground-level column mid-height, Joint 21, with c = 0.00586

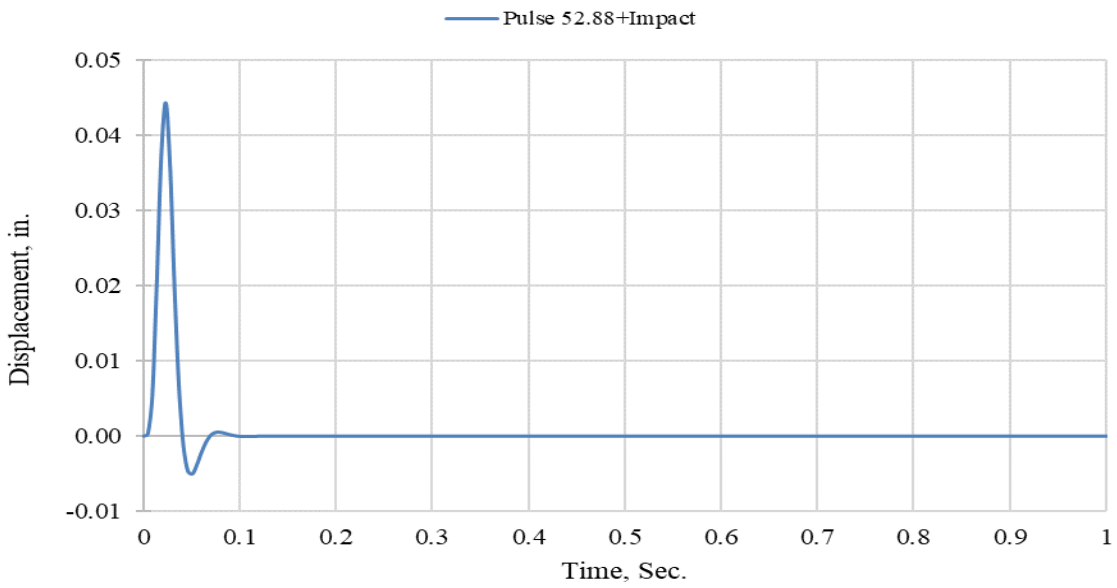

Figure 73. Displacement-time at top floor, Joint 76, with c = 0.586

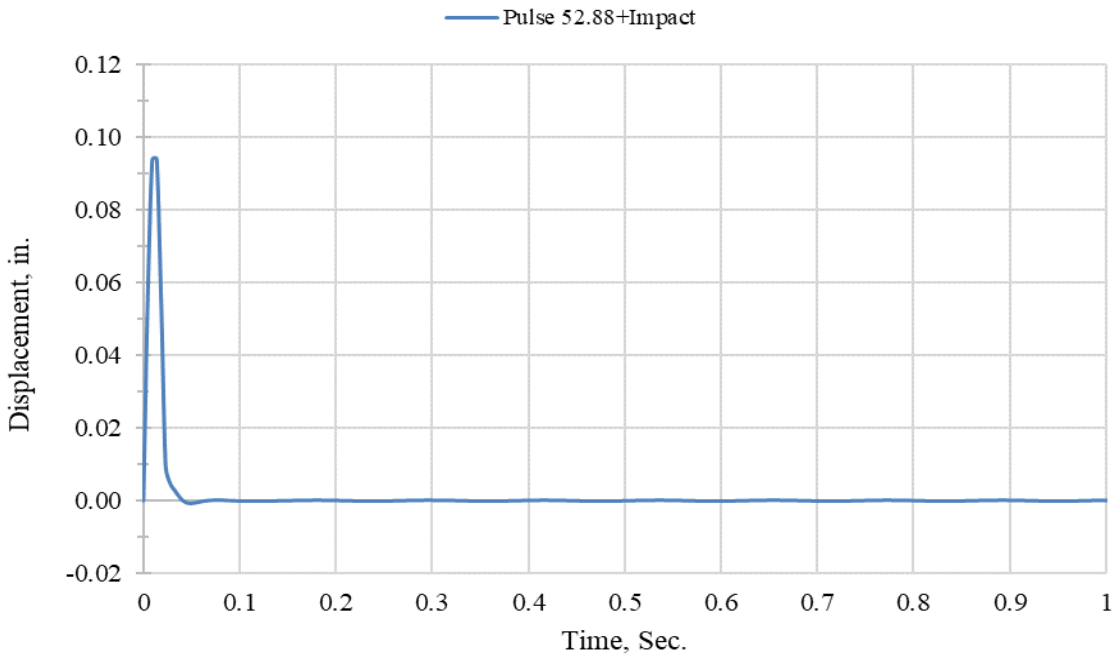

Figure 74. Displacement-time at ground-level column mid-height, Joint 21, with c = 0.586

3.3.2 Full-Scale Building Frame Dynamic Response with and without Impact Load

A full-scale steel frame structure is analyzed when the cooling tower is placed on the top floor to include the total operational load of the HVAC system (7780 bl) and a lateral impact load is applied to the ground-level column, simultaneously. The frame shown in Figure 75 is a three-story with two-bay by three-bay on the x-axis, the height of each floor is 15-ft and each bay is 20-ft. The building frame is analyzed with different loadings and various loading combinations. The steel frame shown in Figure 76 has HSS 8x8x1/4 for the beams and the columns. The square section steel has yielding stress of 46 ksi and Young's Modulus of elasticity of 29,000 ksi [53]. This tubular square section size is determined after designing the frame to the pulsating axial load, dead load, and the live load for both full load and checkered load shown in Figures 77, 78 and 79, simultaneously. The applied live load used in the calculations is 50 psf which is suggested for both office and lobby design calculations in ASCE 7-10 [57]. It is assumed that each beam is carrying half of the live load on each bay area, meaning, each beam is carrying 50 psf x 10 ft = 500 lb/ft = 41.67 lb/in. The load combination for the applied dead and live loads are based on the LRFD design load combination of ASCE 7-10 [57].

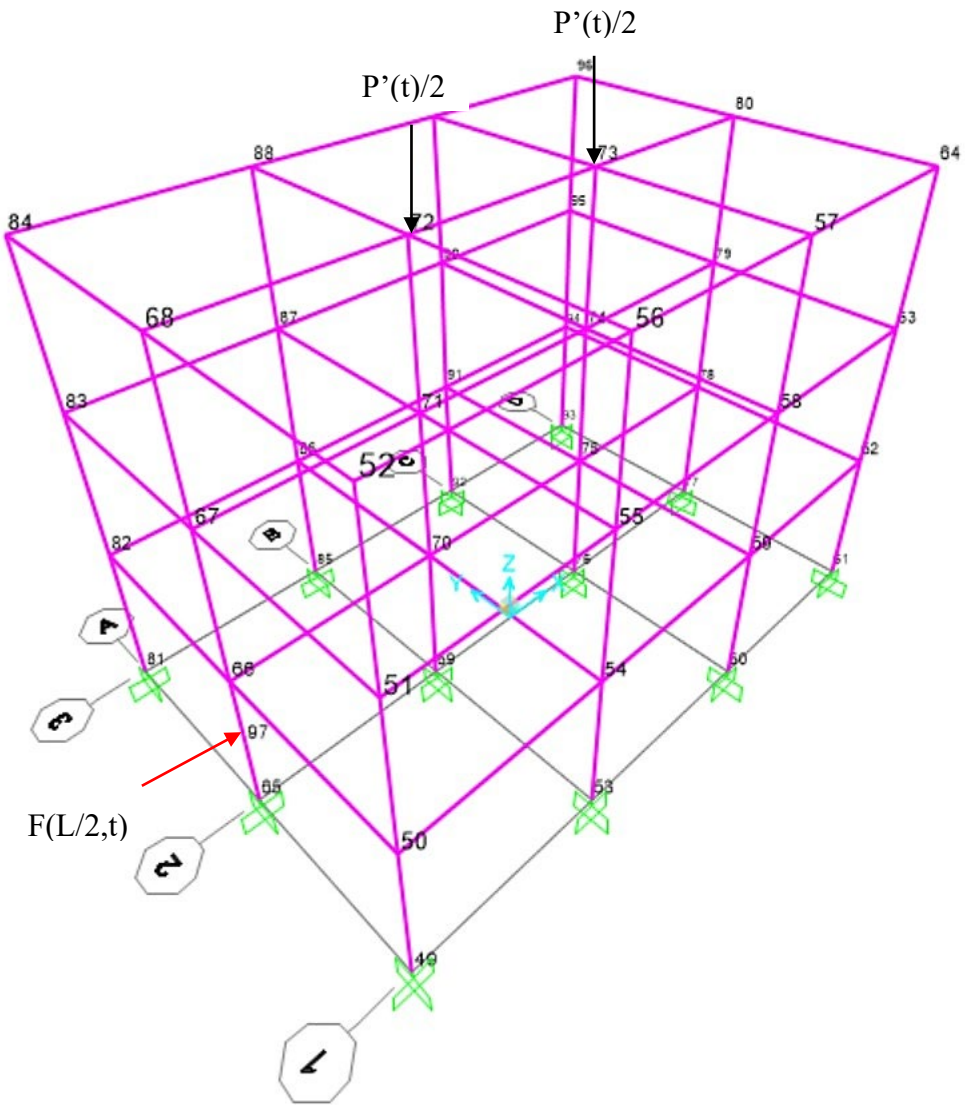

Figure 75. Building frame with impact load on ground-level column and pulsating vertical load on top

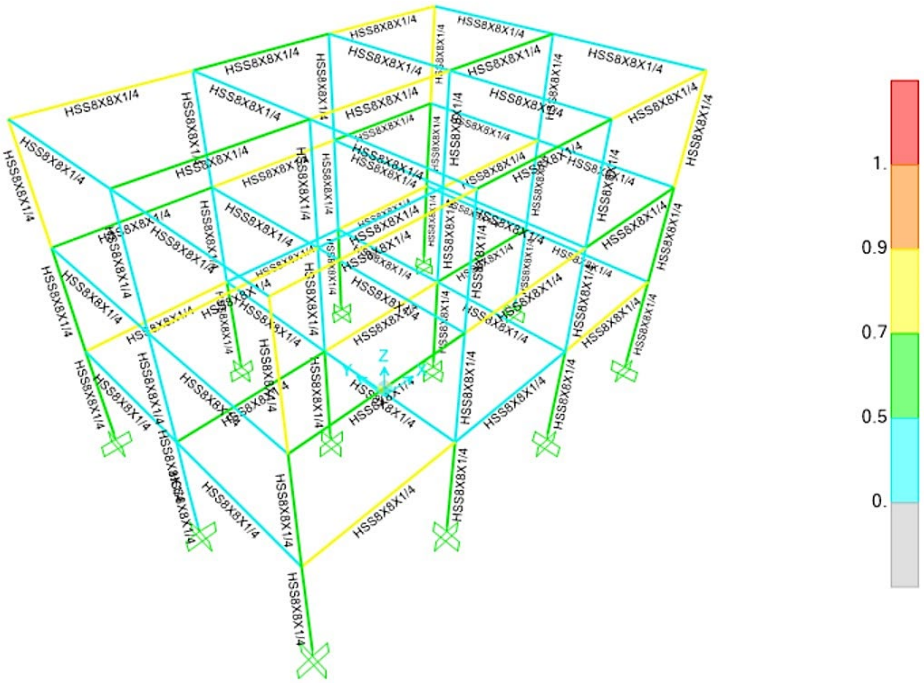

Figure 76. Building frame structural member sizes (HSS 8x8x1/4)

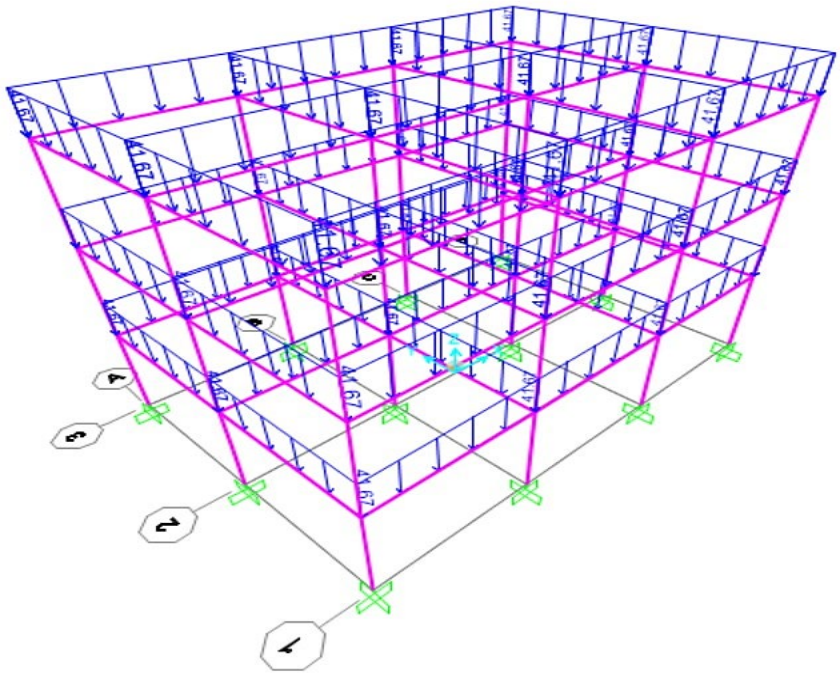

Figure 77. Building frame service loading

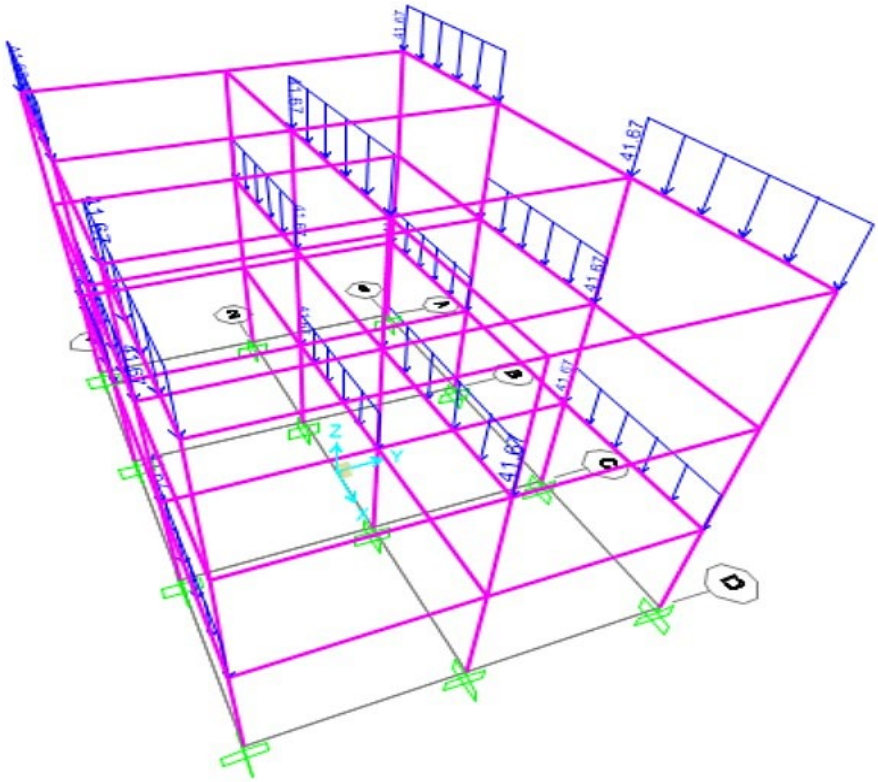

Figure 78. Building frame checkered-board service loading

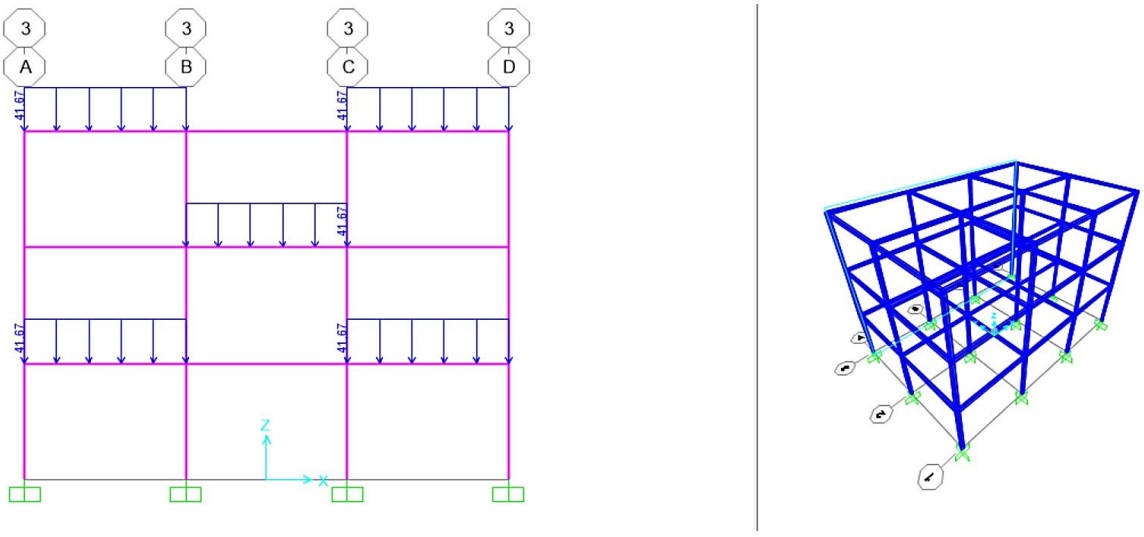

Figure 79. Building frame checkered-board service loading in XZ plane

The following loading combinations are adopted from ASCE 7-10 [57] and are used for determining the full-scale building frame:

1.4 DL,

1.2 DL+1.6LL,

1.2 DL+1.6LL_{check},

1.2DL+ P+LL, and

1.2DL+ P+LL_{check}

In the above load combinations, DL is dead load, LL is live load, LL_{check} is checkered live load applied to every other beam on the x-axis, and P is the pulsating axial load (P'(t)).

From SAP-2000, it is found that for the first mode of the full-scale frame, Time Period, T_n, is 0.559765 seconds. From that, the natural frequency is f = 1.78 Hz and ω_n = 11.22 rad/sec. Damping coefficient used in the analysis is c = 0.05. The lateral impact load applied to the ground-level column is shown in Figure 80.

The model is analyzed for service load combinations of DL+ P+LL_{check} and DL+ P+LL_{check} + Impact. The building frame's response at the top floor, joint 68, are shown in Figures 81 and 82, respectively. The lateral impact load formed three plastic hinges in the ground-level column as shown in Figure 83. Figures 84 and 85 show the building's response when the damping coefficient is increased by 94.2% from adding bolted damping panels to the frame. Increasing the damping coefficient eliminated one plastic hinge in the ground-level column as shown in Figure 86.

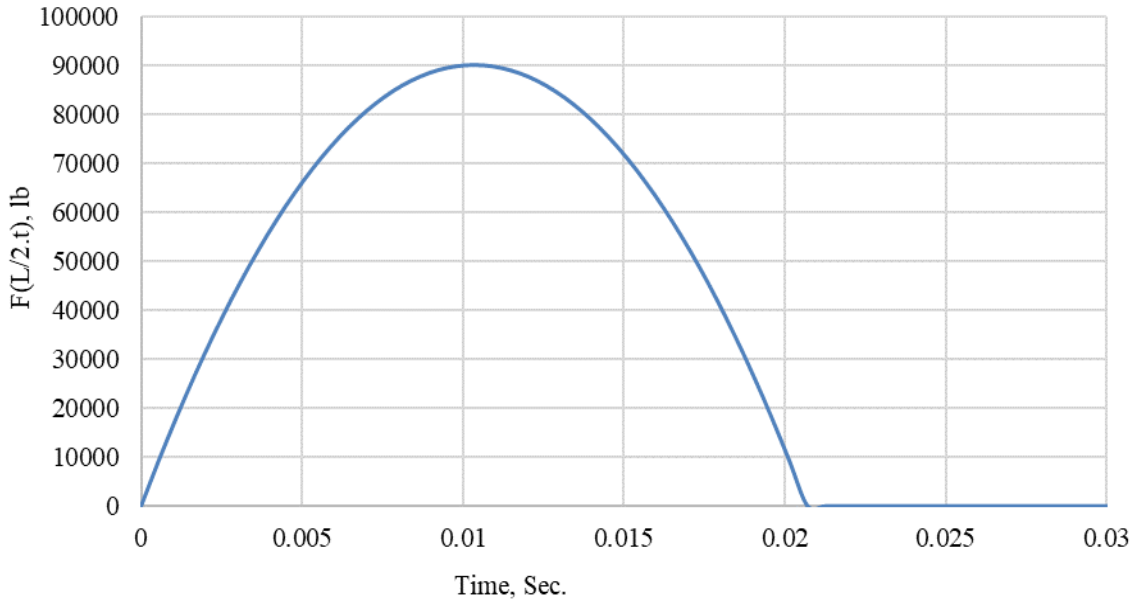

Figure 80. Applied forcing function

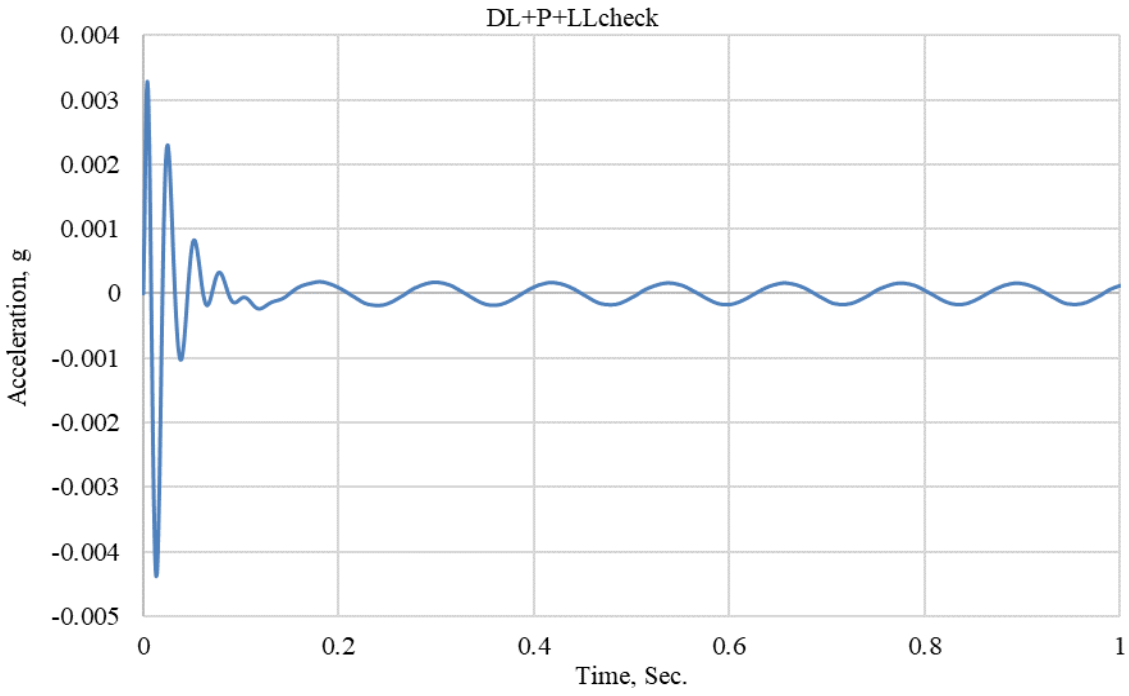

Figure 81. Acceleration-time relation at top-floor for DL+ P+LL_{check} with c = 0.05

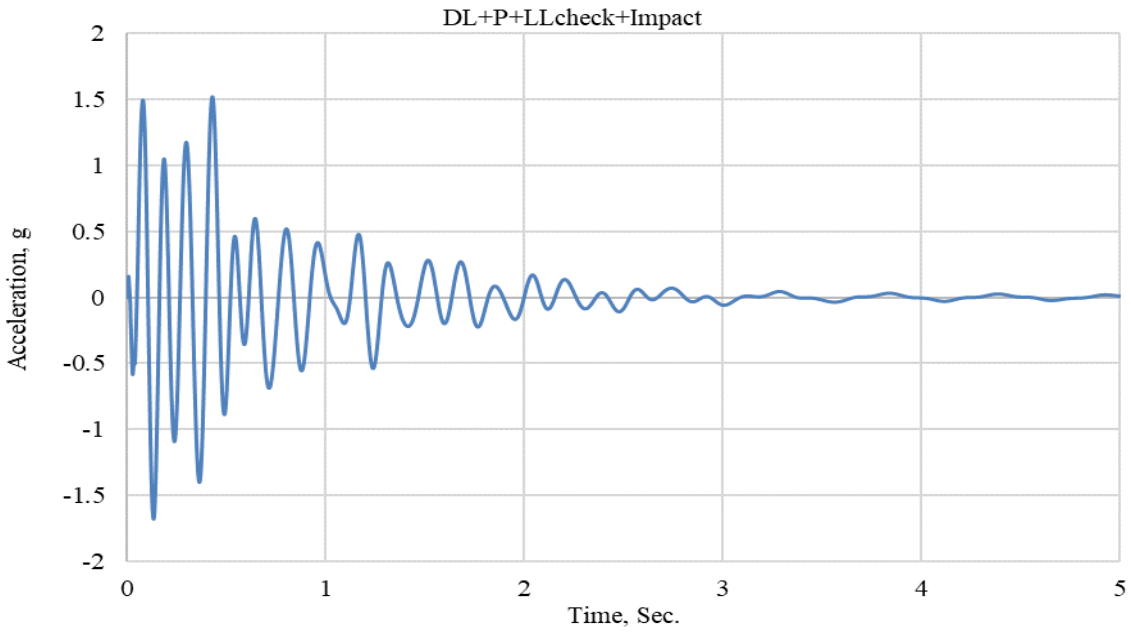

Figure 82. Acceleration-time relation at top-floor for DL+ P+LL$_{check}$ + Impact with c = 0.05

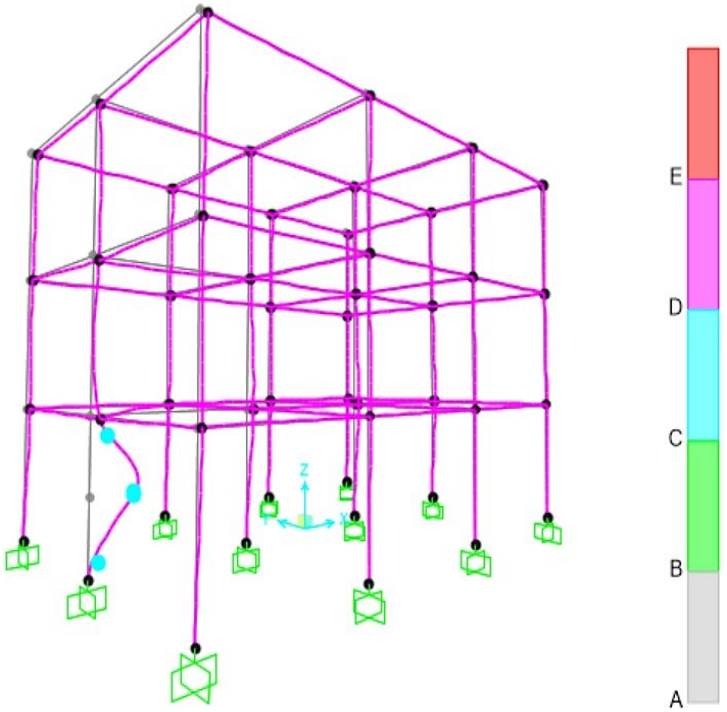

Figure 83. Location of three plastic hinges in ground-level column, c = 0.05

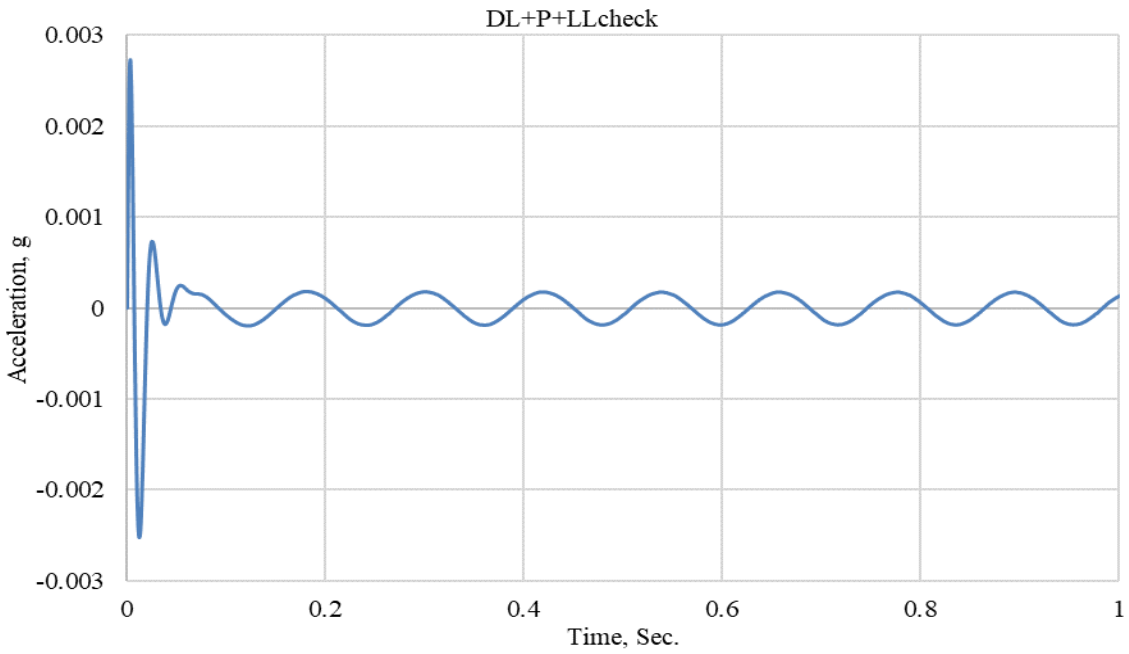

Figure 84. Acceleration-time relation at top-floor for DL+ P+LL_{check} with c = 0.097

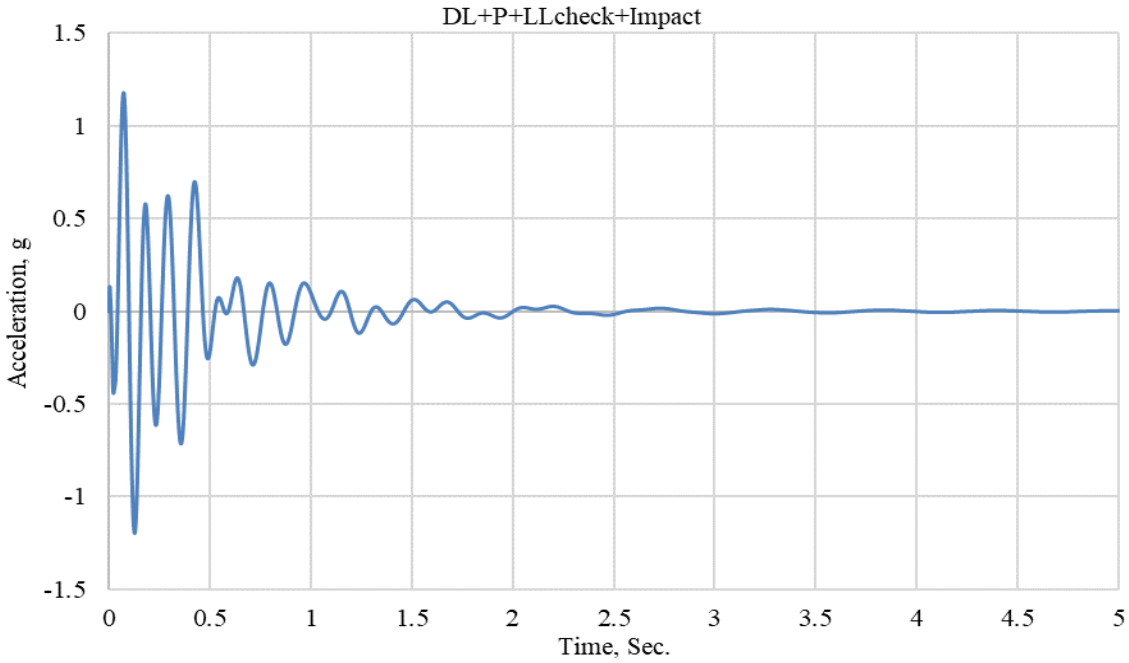

Figure 85. Acceleration-time relation at top-floor for DL+ P+LL_{check} + Impact with c = 0.097

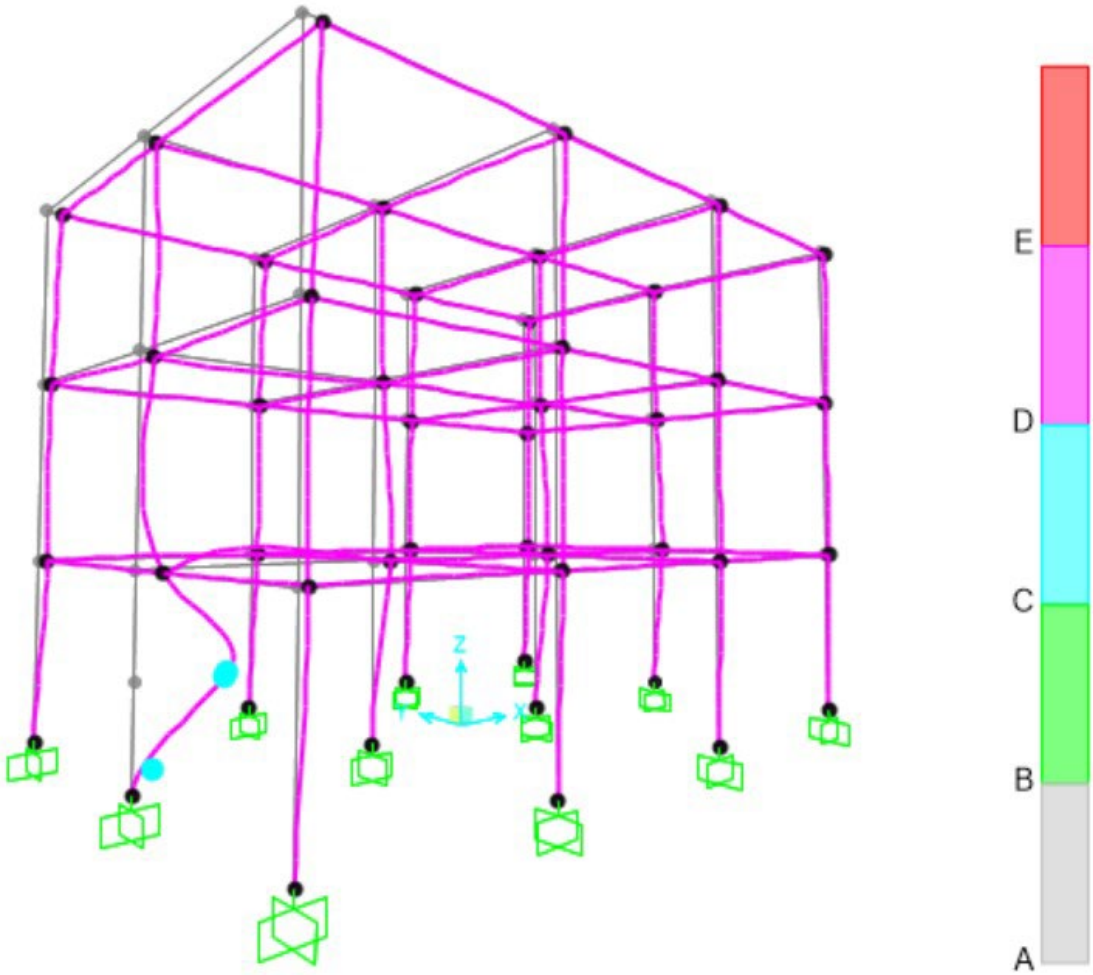

Figure 86. Location of two plastic hinges in ground-level column, with c = 0.097

3.4 Transient Dynamic Elastic-Plastic Behavior

Ground-column AB of the building frame is studied to investigate the plastic moment capacity of the building frame under applied impact load to the frame. For this purpose, the frame is experimentally impacted by three various impact loads to generate a plot for maximum force from each impact load vs the height of the pendulum to the

building's column (5, 7, and 9 inches). Figure 87 shows the pendulum, the frame, and the location of the three possible plastic hinges.

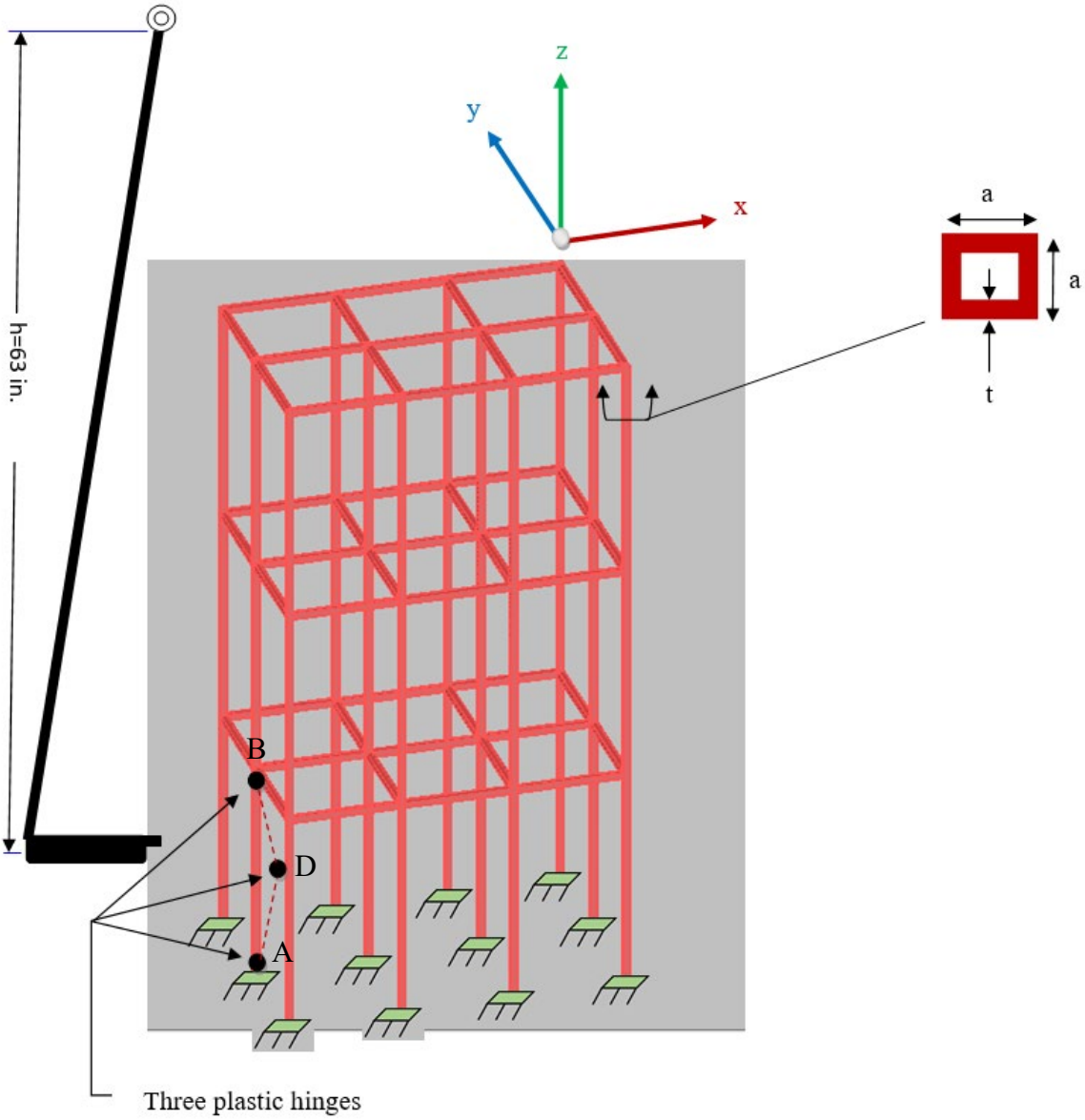

Figure 87. Plastic hinge formation in Column AB

Figure 88 shows each of the forcing functions applied to the ground-level column, separately, and Figure 89 shows the relationship between the maximum force of each impact load vs pendulum's distance, q. From the SAP-2000 analysis, maximum bending moments at locations A, B, and D for each impact load are found, respectively, as shown in Table 2. The average bending moment at each forcing function is taken to calculate the maximum pendulum's height that forms the three plastic hinges. Figure 90 shows the relation between the maximum force, F(t) max, obtained from Figure 88 versus the corresponding average internal bending moment, M_{avg}, obtained from the frame analysis.

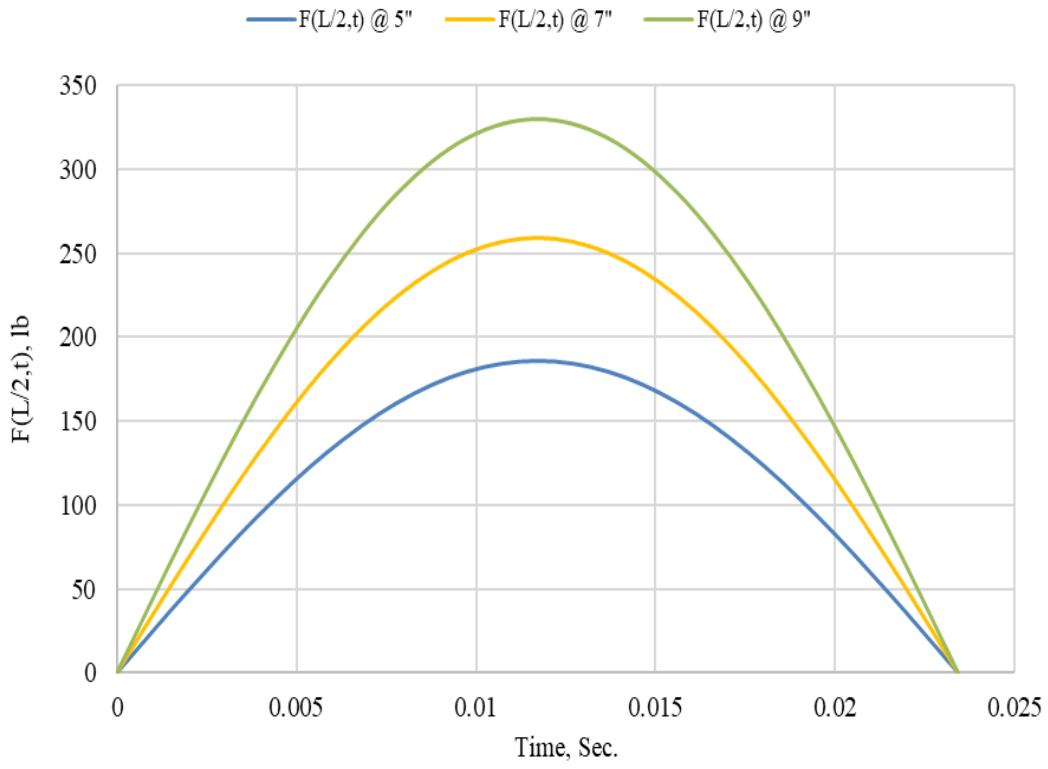

Figure 88. Forcing functions

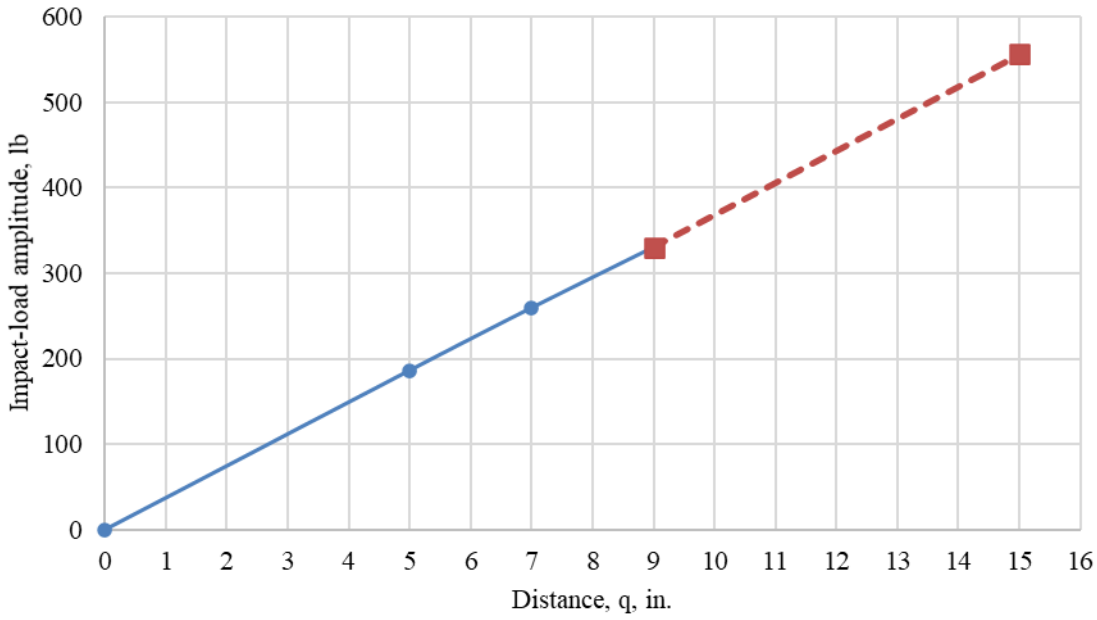

Figure 89. Impact load amplitude versus distance q

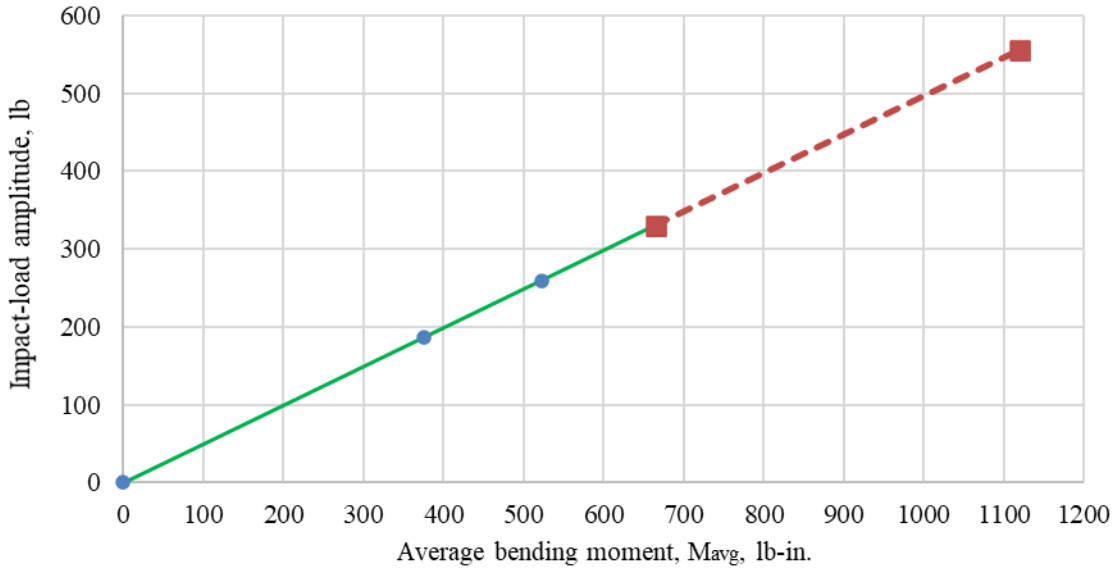

Figure 90. Impact load amplitude versus average bending moment at A,B, and D in Column AB at q = 5, 7, and 9 in.

Table 4. Impact load amplitude F_{max} at locations A, D, and B of Column AB, and M_{avg}

		M (lb-in)			M_{avg} (lb-in)
Distance, q (in)	F_{max} (lb)	A	D	B	(A+D+B)/3
0	0	0	0	0	0
5	186	483	404	239	375
7	259	673	562	333	523
9	330	857	715	423	665
15.00	556				1120

The plastic moment of the hollow section is calculated to be 1120 lb.in. ($M_P = \sigma y \times Z = 62{,}000 \times 0.018066406 = 1120\ lb.in.$). From Figure 90, it is found that at moment = 1120 lb.in. force is 556.1 lb. From Figure 89, at force = 556.1 lb, q is found to be 15 in. meaning; if the pendulum is pulled by 15 inches from the column, it generates enough forcing function that forms three plastic hinges at joints A, B, and D.

At the laboratory, the model frame is impacted by the pendulum when it was pulled by 16 inches, no permanent damage was observed in the column. This is because the forcing function at 16 inches did not generate the maximum required force, 556 lb, on the column. This is because the forcing functions duration at q = 15 inches vs the forcing function at q = 16 inches is much shorter and the forcing function is more intense as shown in Figure 91. The pendulum at q = 18 inches impact the column again, this time, it left a permanent deformation by 0.1 inches at the middle span in the column as shown in Figure 92. The forcing function at q = 18 inches was able to generate the force (581 lb), above the force needed (556 lb), to form the plastic hinges.

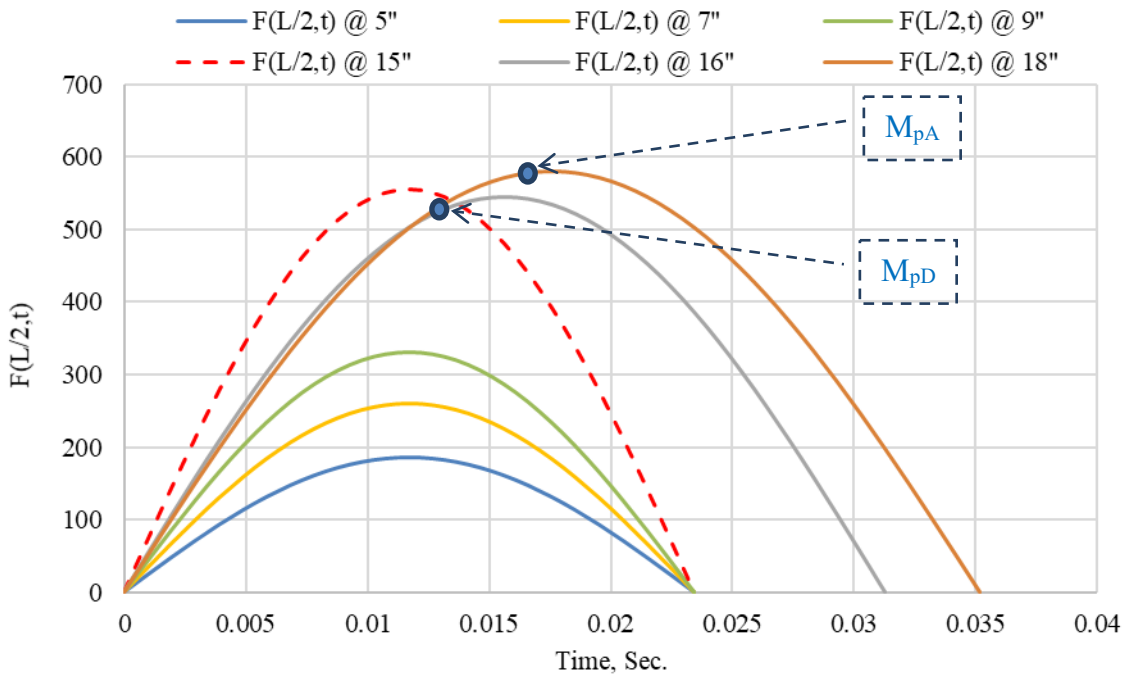

Figure 91. Forcing functions at q = 5, 7, 9, 15, 16, and 18 in.

The lab frame is analyzed using SAP-2000 to predict the times when each of the three plastic hinges form as well as the building's response at the top floor. Time History analysis showed only two plastic hinges formed, at A and D, as shown in Figure 93. The first plastic hinge was at location D, at time 0.013 seconds, and the second plastic hinge was at joint A, at time 0.017 seconds. Figure 94 shows a comparison between the lab data vs SAP-2000 for the top floor when the model frame is impacted at q = 18 in. to generate the plastic hinges. The comparison is in acceptable range, the difference refers to the errors during data collection, material behavior and the difference between the two approaches, real behaviors of the model at the lab and the lump-mass based calculation from SAP-2000.

Figure 92. Ground-level column of model frame after impact with q = 18 in.

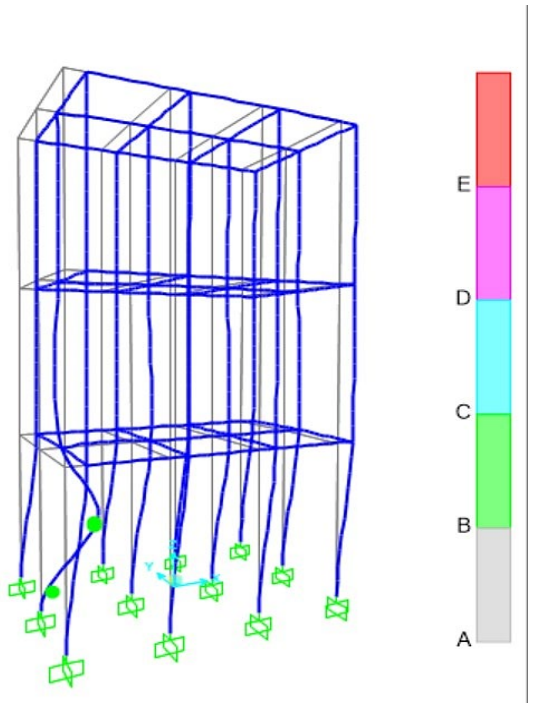

Figure 93. Location of two plastic hinges in Column AB of model frame

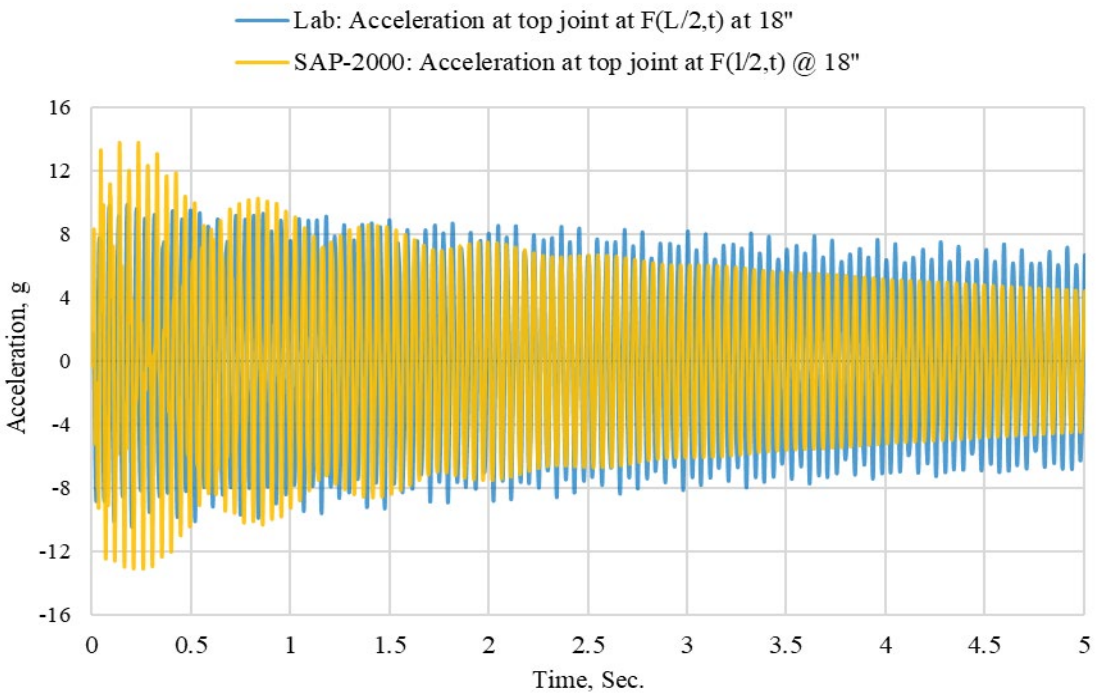

Figure 94. Comparison of acceleration-time relations at top floor for impact with q = 18 in.

The Time History analysis was run multiple time for various increased forcing function to predict the required forcing function that generates three plastic hinges in the column. The analysis showed that if the pendulum is pulled by around 25 inches to generated maximum applied force of 730 lb, the three plastic hinges form in the column. At the lab, the pendulum is pulled by 25 inches to impact the ground column with forcing function shown in Figure 95 to generate the three plastic hinges, as shown in Figure 96. Figure 97 shows a large permanent deformation in the ground column by 0.44 inches. The compared acceleration vs time relations at the top floor in Figure 98 show an acceptable difference between the collected data during the impact test versus the Time History analysis for the dame impact load intensity, the difference refers to real behaviors of the model at the lab and the lump-mass based calculation from SAP-2000.

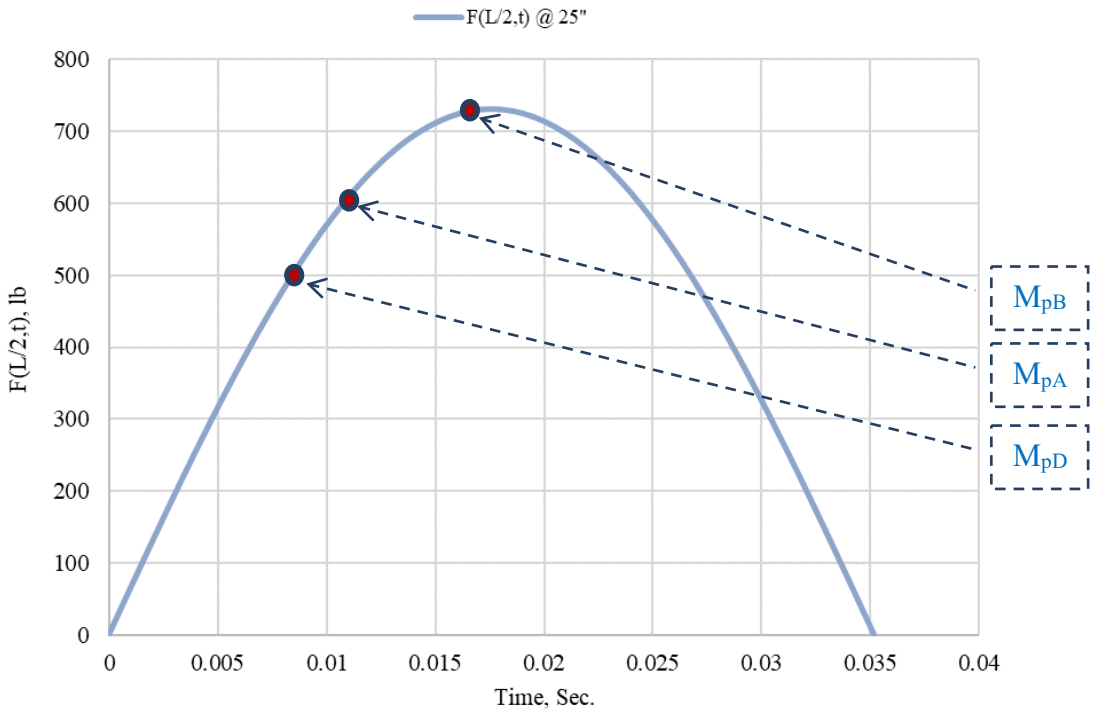

Figure 95. Applied forcing function versus time with q = 25 in.

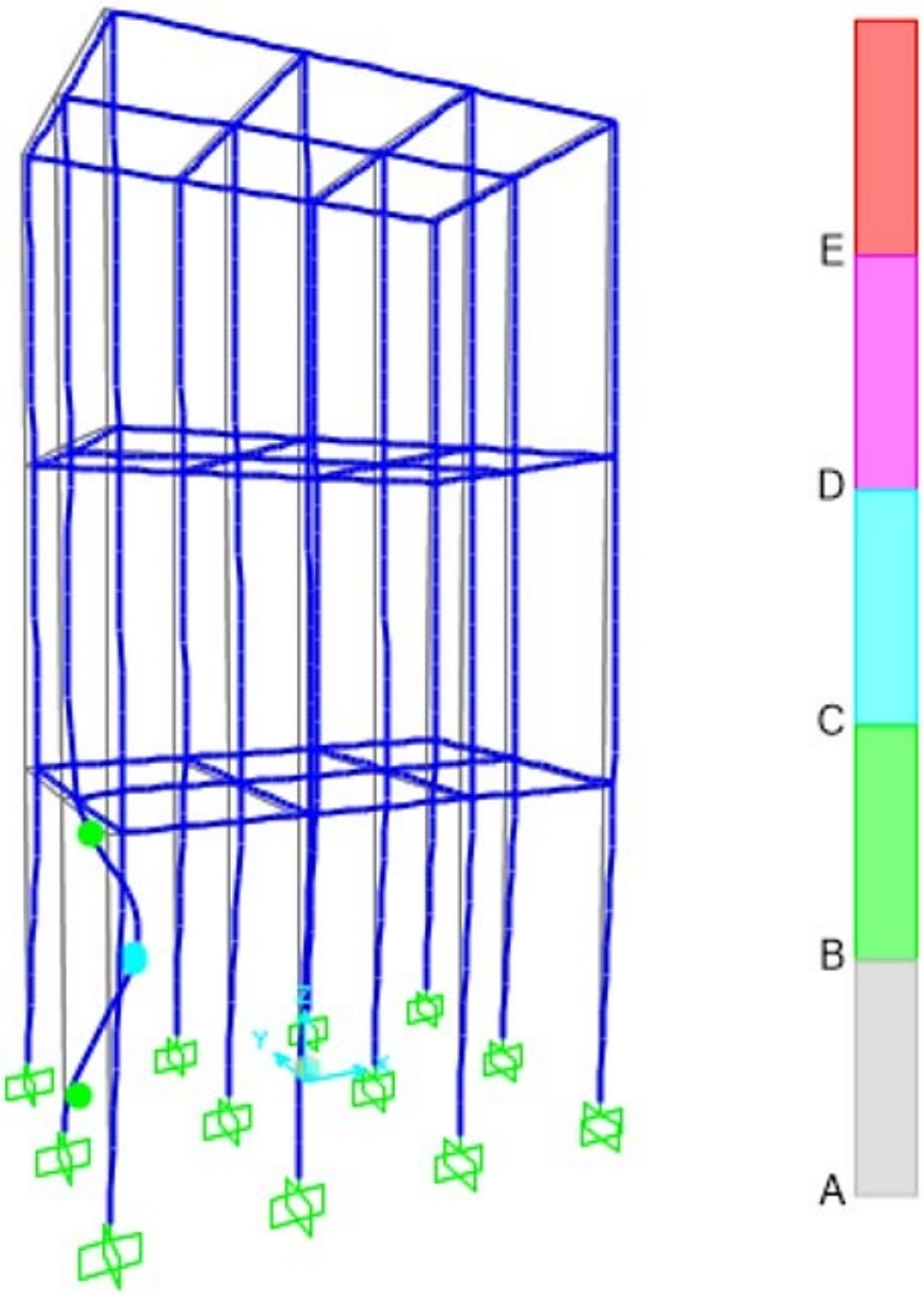

Figure 96. Location of three plastic hinges in Column AB of model frame

Figure 97. Ground-level column deformation of model impacted with q = 25 in.

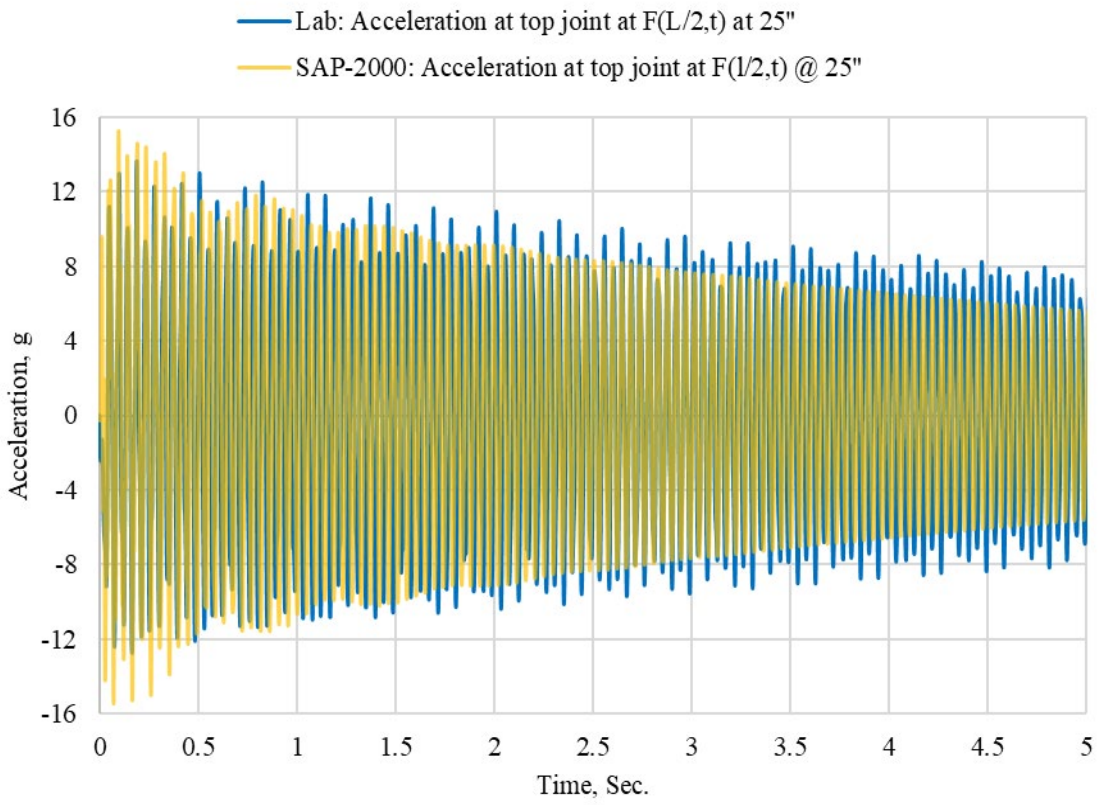

Figure 98. Comparison of acceleration-time relations at top floor of model frame for impact with q = 25 in.

From Figure 99, it is shown that the spikes in the theoretical run are higher than the collected data. However, in Figure 98, it is shown that with time, vibration in the theoretical model analysis fades quicker. This is because the damping coefficient used in the SAP-2000 (c=0.000586) is calculated for the entire building for mode 1, while in the reality, all the modes happen simultaneously, and the damping coefficient changes along the height of the frame and time.

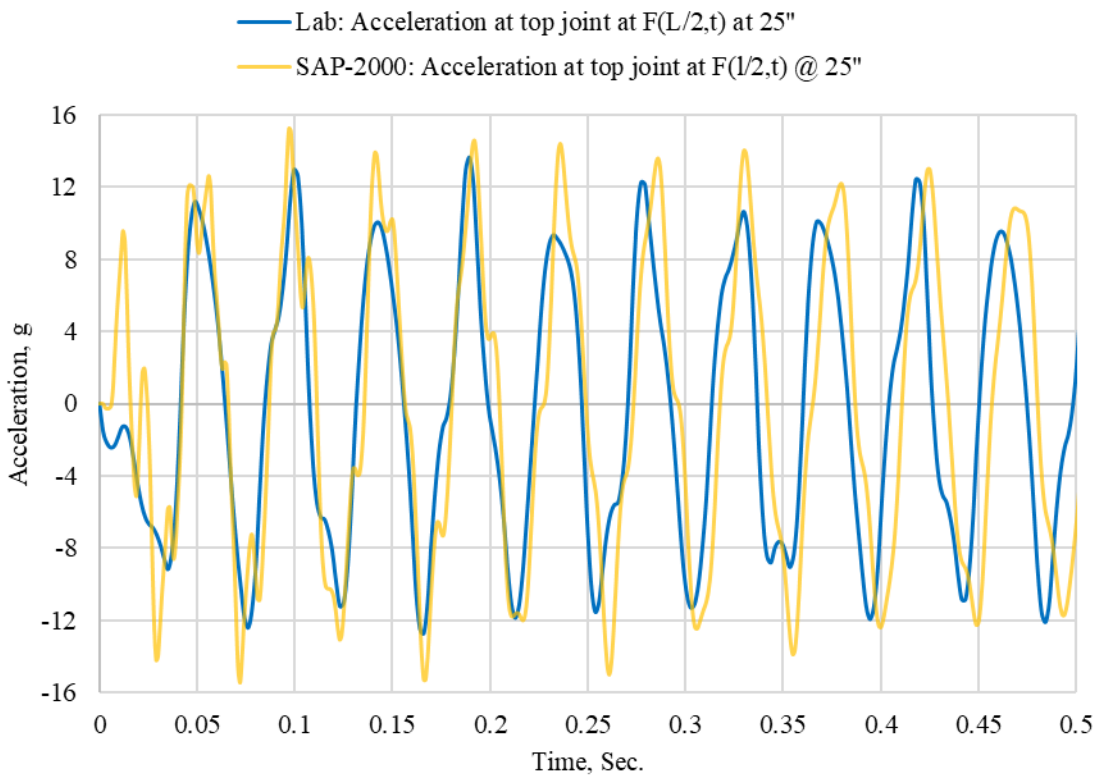

Figure 99. Comparison of acceleration-time relations at top floor of model frame for impact with q = 25 in., 0<t<0.5 sec.

Figures 100 shows the response of the ground-level column at its mid-height. The figure shows acceleration, velocity, and displacement versus time relations. The figure shows that right after the formation of the plastic hinges, drastic changes in the dynamic behavior occur. Table 5 shows the boundary conditions at the mid-height of the ground-column, D, during the time of each plastic hinge in the column. The table shows acceleration in g, velocity in in./sec., and displacement in in. at node D at time 0.0009 sec. when the first plastic hinge forms at D, and at time 0.011 sec. when the second plastic hinge forms at A, and at time 0.017 sec. when the third plastic hinge forms at B.

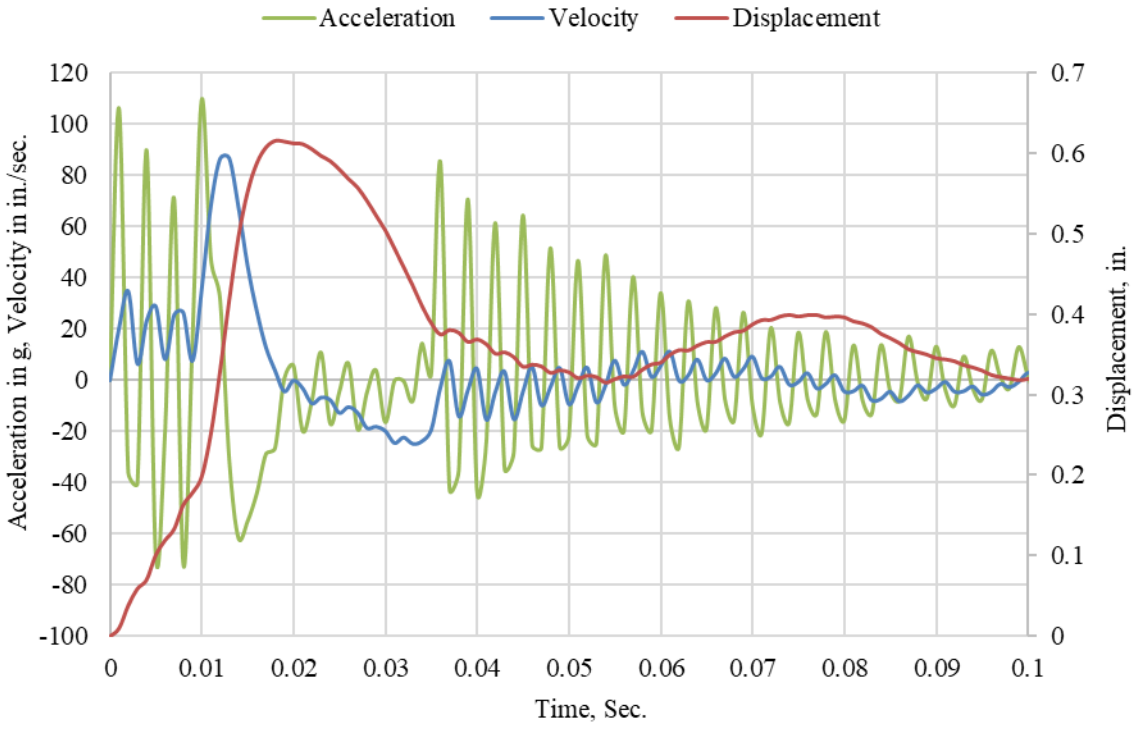

Figure 100. Acceleration, velocity, and displacement versus time for model frame at ground-level column mid-height with q = 25 in.

Table 5. Displacement, velocity, and acceleration values at times of plastic hinge development at ground-level column Nodes D, A, and B

Plastic hinges	Time (sec.)	Displacement (in.)	Velocity (in/sec.)	Acceleration (g)
D	0.0009	0.179	7.66	15.62
A	0.0110	0.252	68.24	47.49
B	0.0170	0.607	12.94	-28.91

The results from the lab tests to the SAP-2000 Time-History analysis show an acceptable agreement that the results are reliable and can be used for bigger scale.

CHAPTER IV

4. COMPARISON OF RESULTS AND DISCUSSION

A comparison of the results for the steel building frame model, the cantilever, and the full-scale building frame is presented in this chapter.

4.1 Steel Building Frame Model

Adding various lead damping systems to the steel building frame model showed a significant effect on decreasing vibration in the building model.

4.1.1 Suspended Lead Dampers

Figure 101 shows that adding lead dampers to the exterior columns showed significant impact on decreasing vibration and increasing damping in the building frame model. From Figure 101, at a time of 2.9173-3.2415 seconds, the frame has 3.09g acceleration in the absence of lead dampers in the building. When 12, 24, or 48 0.15-in. diameter lead dampers are installed in the exterior columns, simultaneously, acceleration is decreased to 2.20g, 1.95g, and 1.72g, respectively. Meaning, vibrations is decreased by 29% (((3.09g-2.20g)/3.09g)*100), 37%, and 44%, respectively. From the results, it is found that with increasing the number of lead dampers in the exterior columns, vibration decays faster.

At the time when the impact load impacts the frame, the lead dampers do not dampen anything as shown in Figure 102. Adding the lead dampers to the exterior columns does not help in decreasing the impact of the impact load on the building. However, right after the impact load impacts the building, the lead dampers start working

on decaying motion in the building from time 0.4 sec. as shown in Figure 103. With passing time, the lead dampers decay more and more motion. Right after 0.4 sec., the building with 48-lead dampers in the exterior columns decreases vibration by 22%.

The building frame is tested again to observe the response of the frame when it is impacted on the y-axis. From Figure 104, it is shown that on the y-axis at times 2.7552-2.8363 seconds, acceleration is decreased from 3.31g to 2.46g, i.e. vibrations is decreased by 25% when 48 0.15-in. lead dampers are added to the exterior columns.

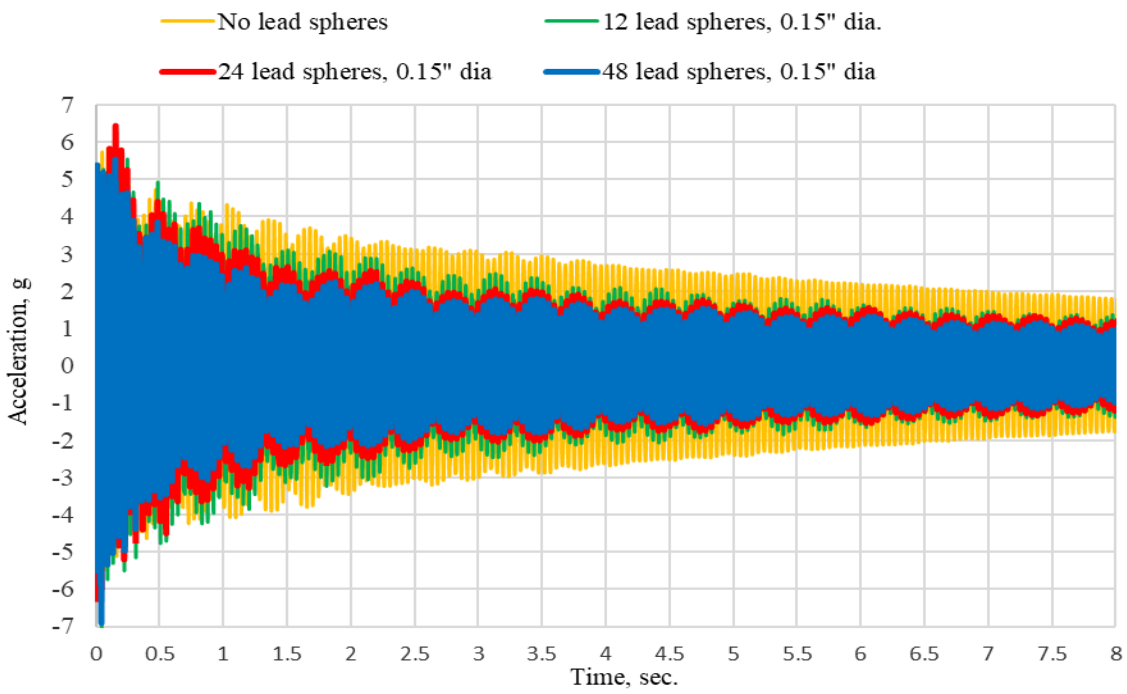

Figure 101. Node 3 acceleration-time relations of frame model along x-axis

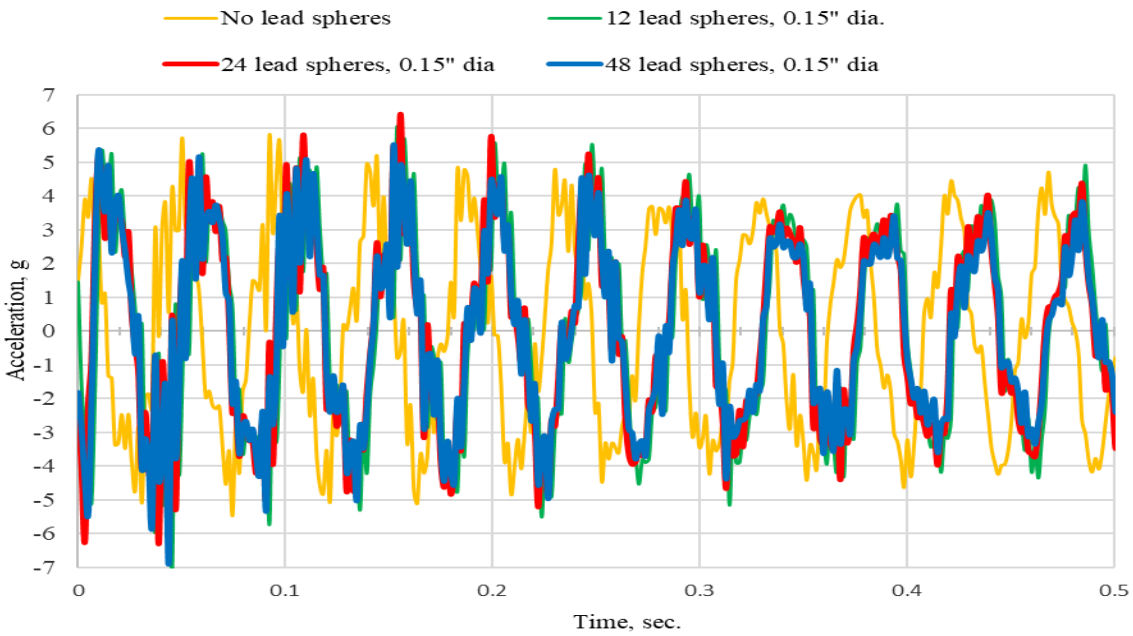

Figure 102. Node 3 acceleration-time relations of frame model along x-axis, 0<t<0.5 sec.

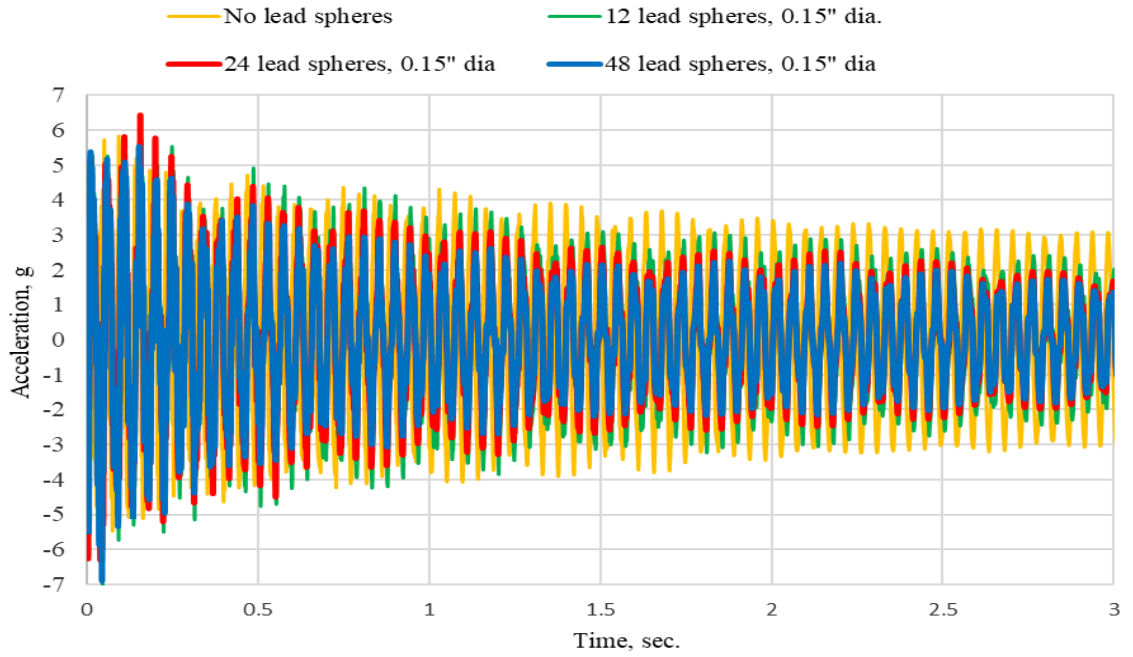

Figure 103. Node 3 acceleration-time relations of frame model along x-axis, 0<t<3 sec.

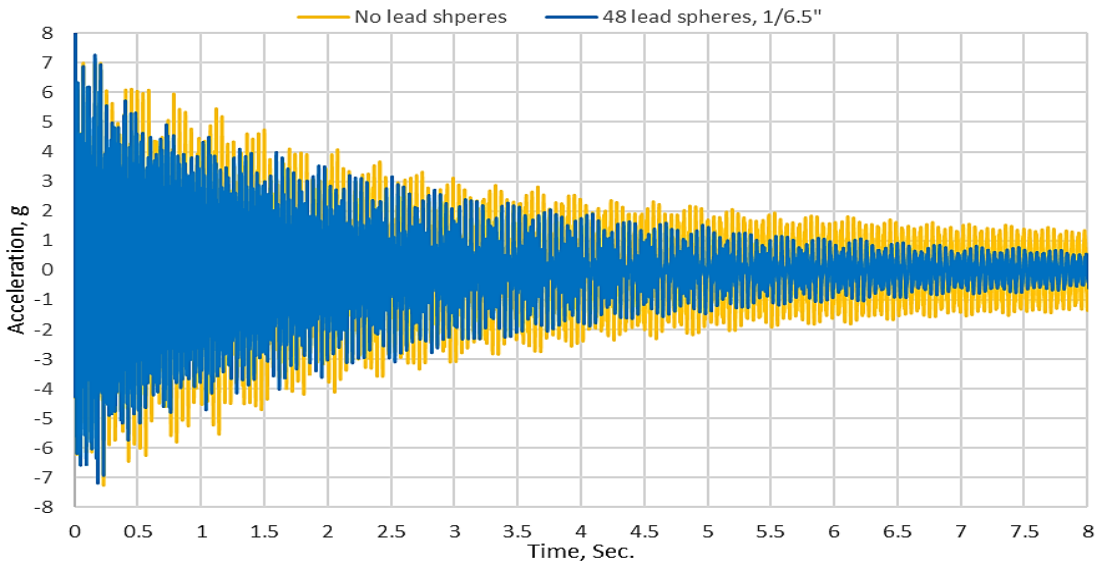

Figure 104. Acceleration-time relations of frame model at top floor along y-axis

4.1.2 Welded Damping Panel Along x-axis

Figures 105 and 106 show the building model's response to the applied impact load at the presence of welded dampers on x-axis with and without the presence of lead dampers in the damping panels, respectively. From the figures, from time 3.2577 seconds to 3.5008 seconds, it is observed that the empty welded panels were able to reduce acceleration at the top floor from 3.04g to 1.20g, and after adding 15 0.2-in. lead dampers to each panel column, acceleration is decreased to 1.00g. The graphs show that the empty panels and the panels with lead dampers in them were able to decrease vibration (acceleration) by 60% and 67%, respectively.

From Figure 107, it is observed that the welded panels do not show any impact during the impact load event. The system starts decaying motion right after the impact load impacts the frame at a time of 0.4 seconds. As shown in Figure 108, at time 0.4 sec., the damping system decreases vibration by 44%.

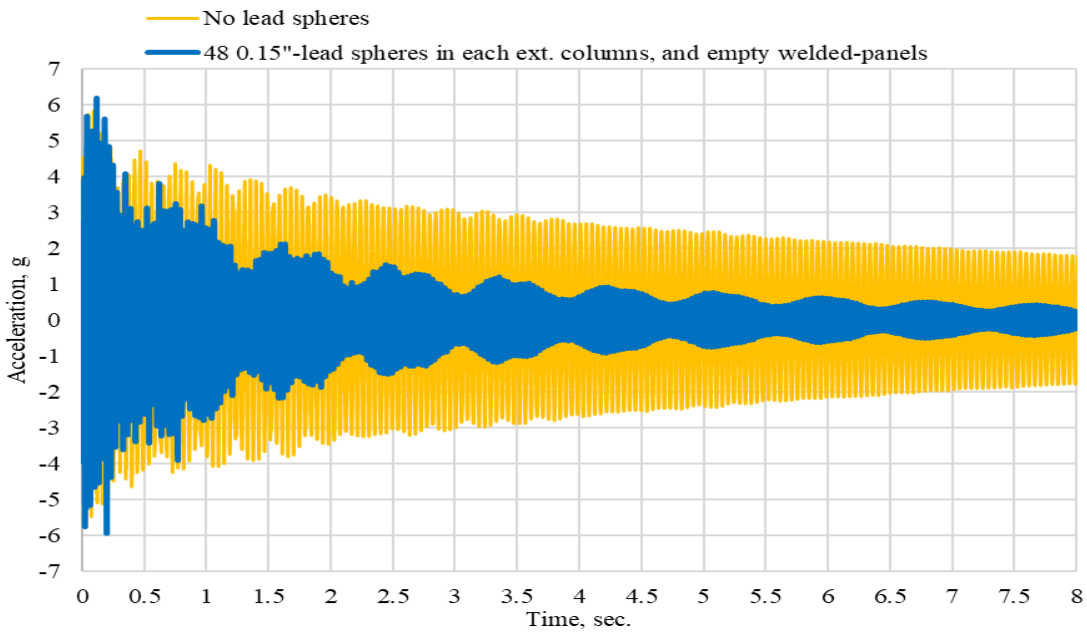

Figure 105. Acceleration-time relations of building frame with empty welded panels on the x-axis and 48 lead dampers in exterior columns

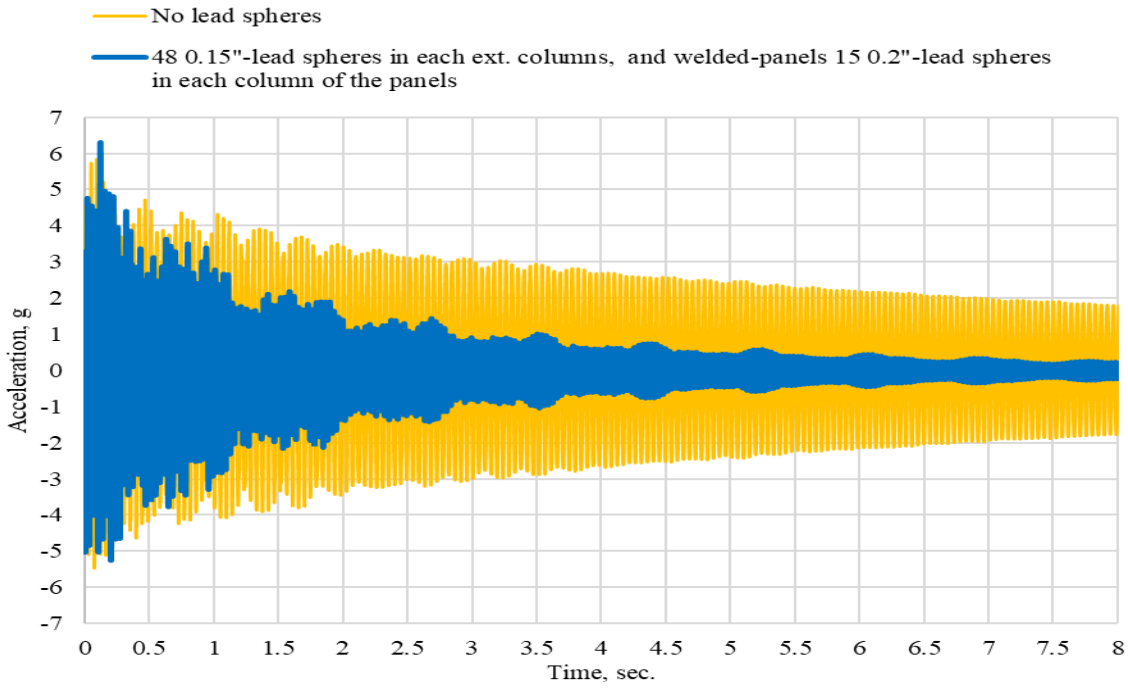

Figure 106. Acceleration-time relations of building frame with welded panels including 15 lead dampers on x-axis and 48 lead dampers in exterior columns

Figure 107. Acceleration-time relations of building frame with welded panels including 15 lead dampers on x-axis and 48 lead dampers in exterior columns, 0<t<0.5 sec.

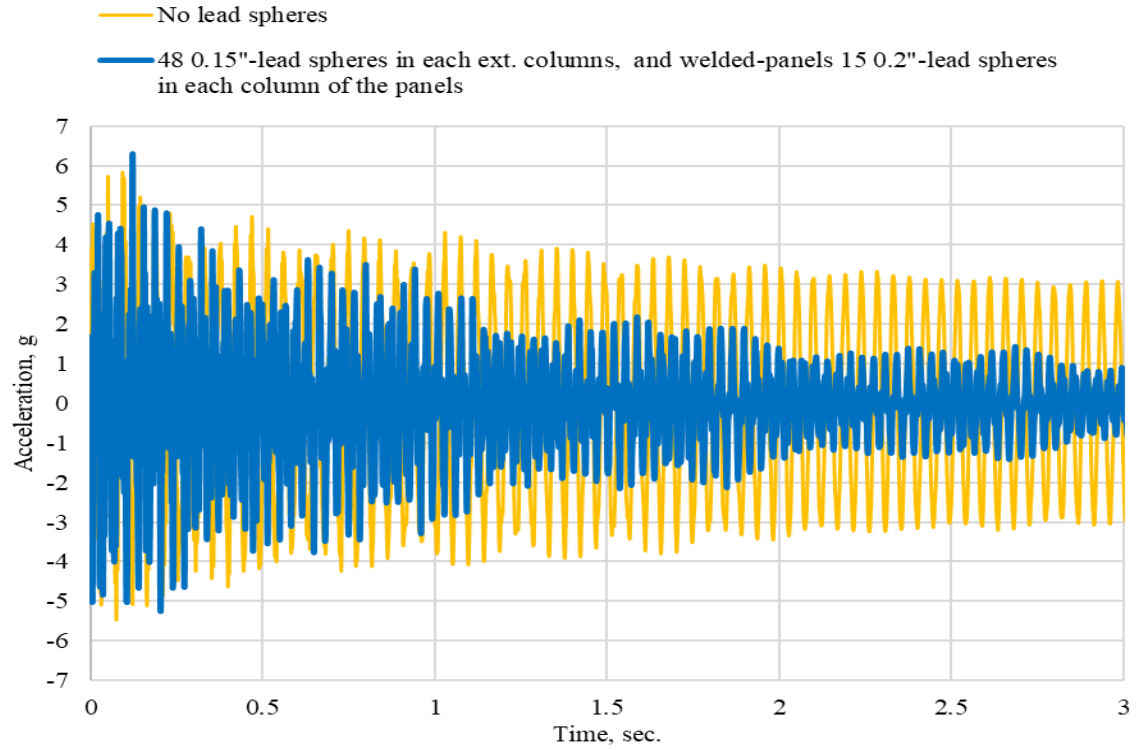

Figure 108. Acceleration-time relations of building frame with welded panels including 15 lead dampers on x-axis and 48 lead dampers in exterior columns, 0<t<3 sec.

4.1.3 Bolted Damping Panel Along x-axis

Figures 109 and 110 show the effect of mounting bolted damping panels on the building frame model's x-axis on decreasing vibration in the building model and decaying vibration faster. From the figures, it is determined that from the time around 1.1345 seconds, acceleration in the frame is close to zero. Meaning, both the empty bolted lead dampers and the bolted lead dampers with 14 0.2-in. diameter lead dampers decay acceleration in the building by almost 100%.

The bolted panels showed more impact on decaying vibration compared to both the lead dampers and the welded panels. The bolted panels have helped damping the system in the event of the impact load. At the time when the impact load excites the frame, the bolted panels act and help the structure in absorbing energy. As shown in Figure 111, the damping system has helped the frame to decrease acceleration in the frame by 20% at the time of the impact load hitting the frame, at 0.05 sec. Right after the impact load excites the frame, the bolted frame decays in motion drastically. At time 0.2 seconds, it drops acceleration from 4.8g to 1.62g, i.e., it decreases acceleration/vibration by 66%. At time 0.45 sec., it decreases vibration by 90%. The impressive effectiveness of the bolted panels refers to the friction between the bolts, the panels, and the beams during the excitement in absorbing energy. As shown in Figure 112, as time passes, the welded panels absorb even more energy, it stops the frame from vibrating as soon as the first second passes.

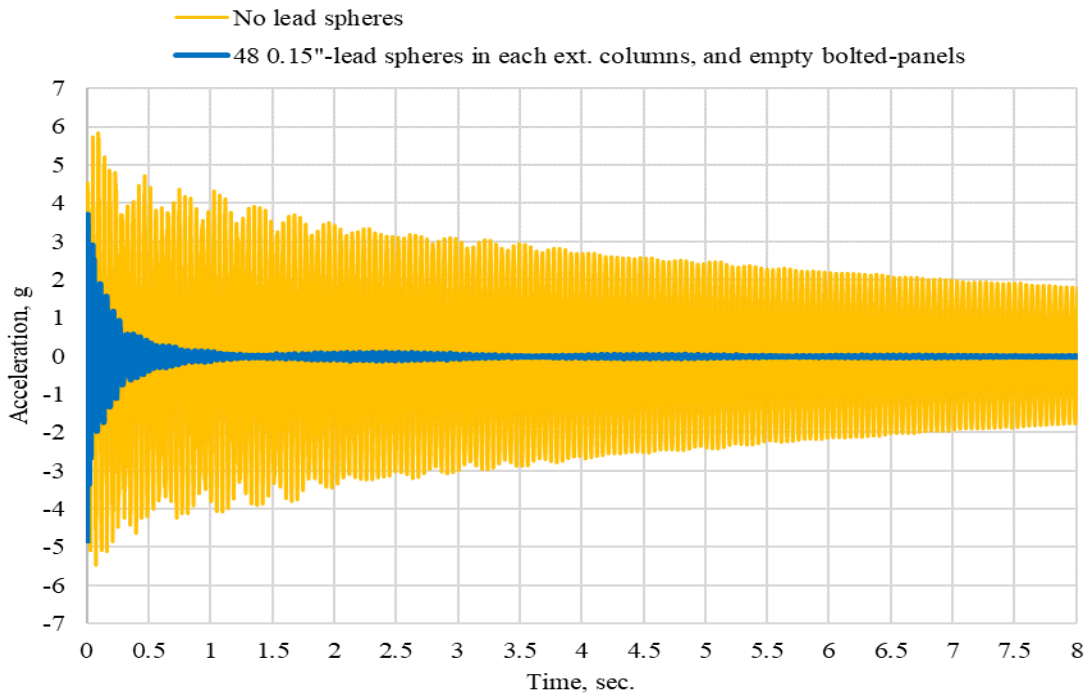

Figure 109. Acceleration-time relations for building frame with empty bolted panels on x-axis and 48 lead dampers in exterior columns

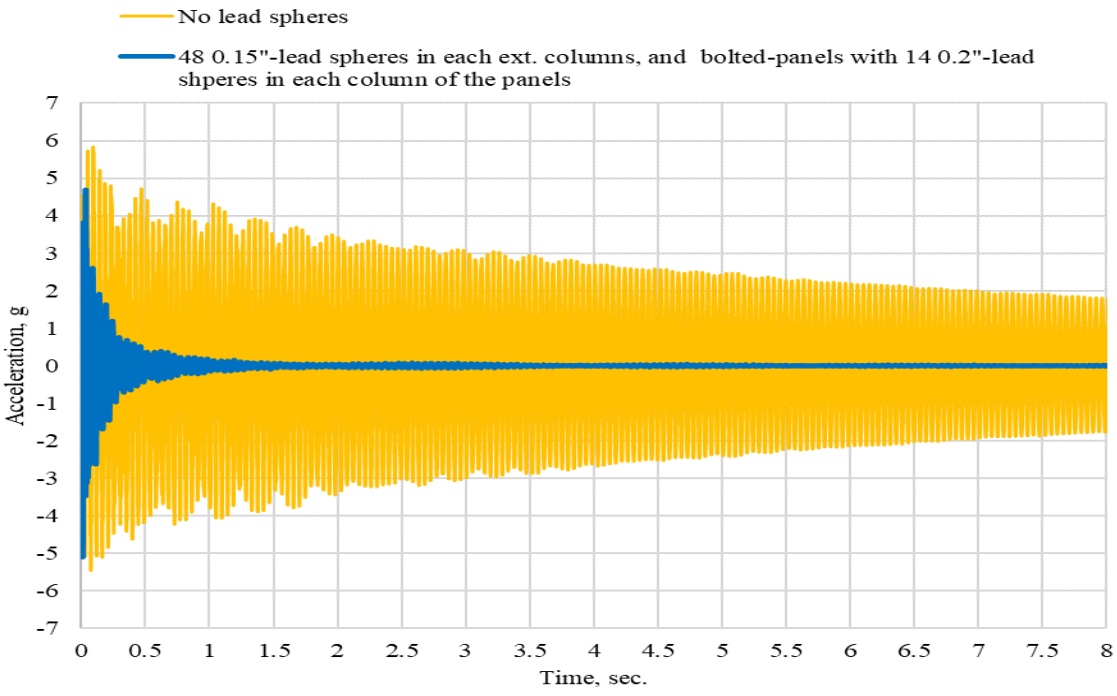

Figure 110. Acceleration-time relations for building frame with bolted panels including 14 lead dampers on x-axis and 48 lead dampers in exterior columns

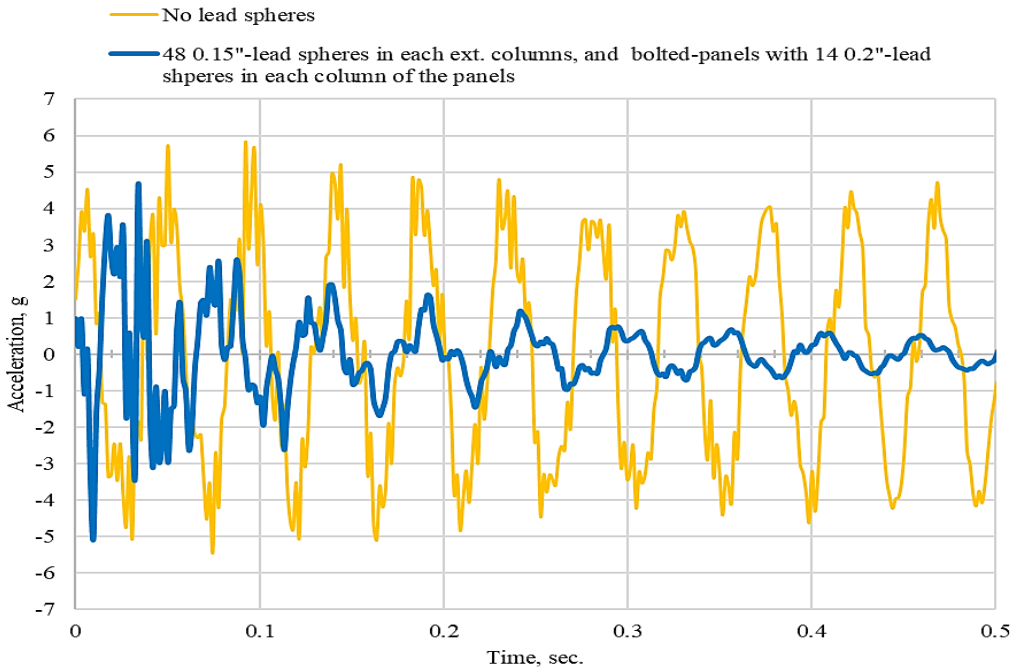

Figure 111. Acceleration-time relations of building frame with bolted panels including 14 lead dampers on x-axis and 48 lead dampers in exterior columns, 0<t<0.5 sec.

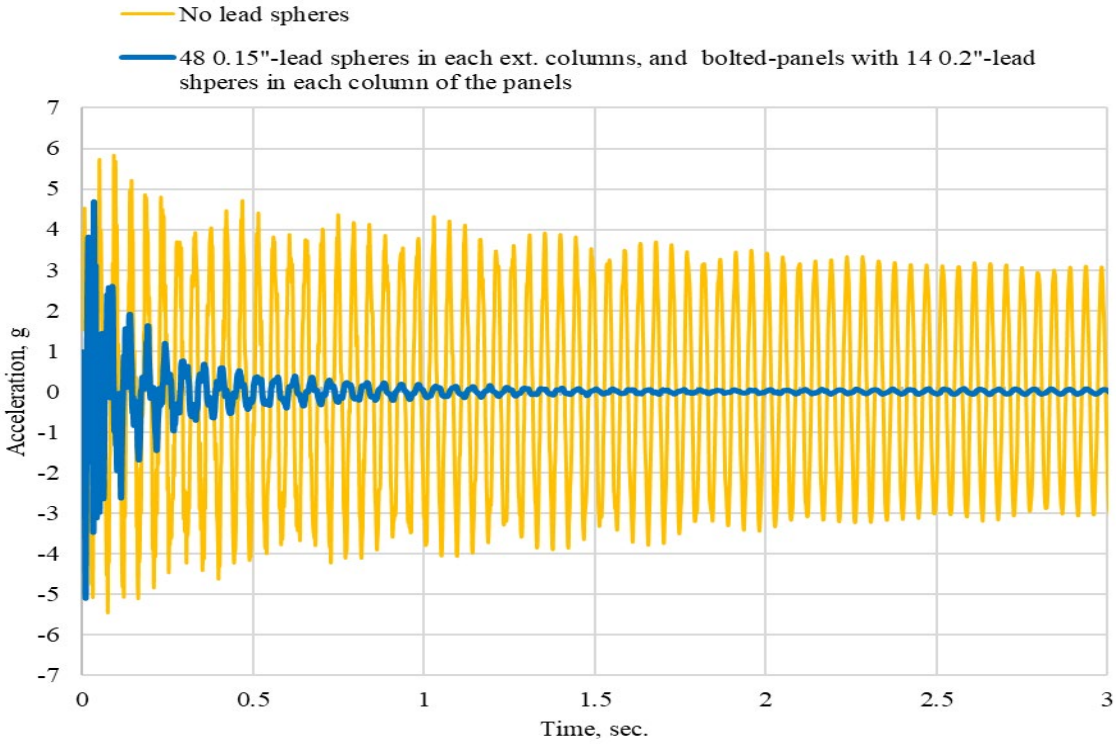

Figure 112. Acceleration-time relations of frame with bolted panels including 14 lead dampers on x-axis and 48 lead dampers in exterior columns, 0<t<3 sec.

4.1.4 Bolted Damping Panel Along y-axis

Figures 113 and 114 show the effect of mounting bolted damping panels on the building frame model's y-axis on decreasing vibration in the building model and decaying vibration faster. From the figures, it is determined that from the time around 1.2966 seconds, acceleration in the frame is close to zero. Meaning, both the empty bolted lead dampers and the bolted lead dampers with 14 0.2-in. diameter lead dampers decay acceleration in the building by close to 100%.

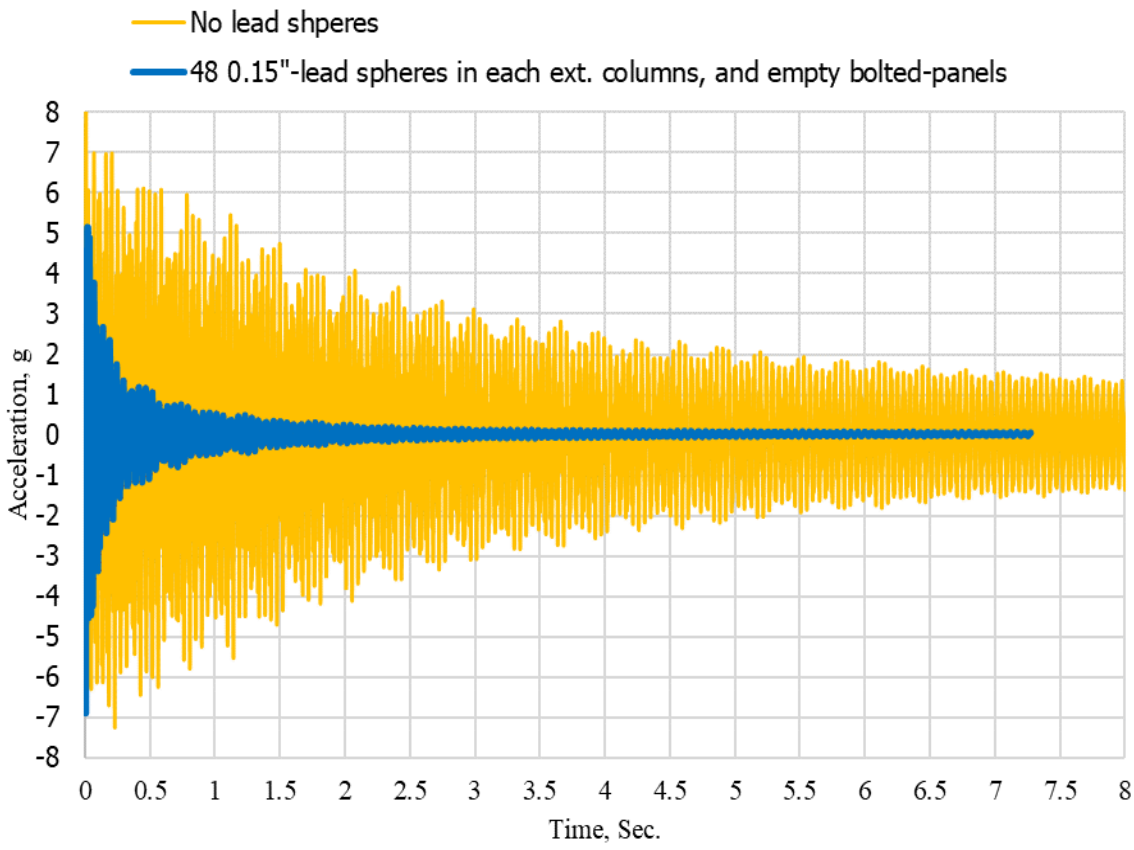

Figure 113. Acceleration-time relations of building frame with empty bolted panels on y-axis and 48 lead dampers in exterior columns

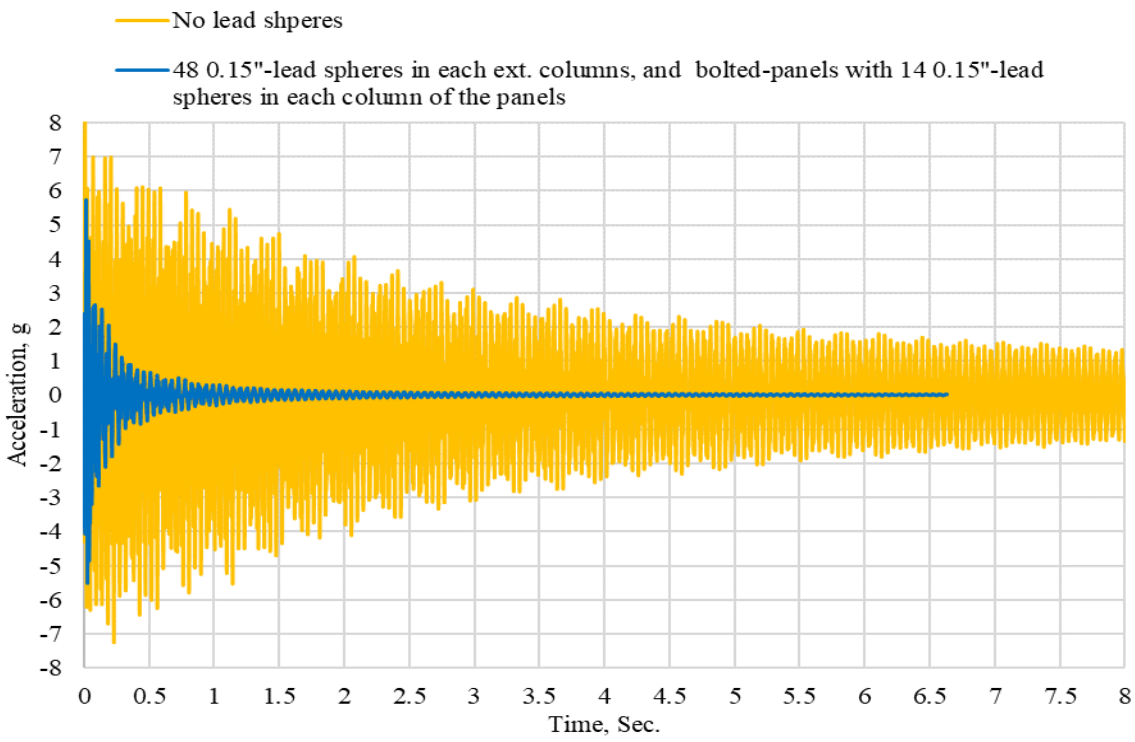

Figure 114. Acceleration-time relations of building frame with bolted panels including 14 lead dampers on y-axis and 48 lead dampers in exterior columns

4.2 Steel Cantilever with Lead dampers

Figures 115 and 116 show that with increasing the number of lead dampers of both sizes (0.5" and 0.6", respectively) in the cantilever, vibration decays much faster. At a time of 2.00-2.10 seconds, the frame has 4.28g acceleration in the absence of lead dampers in the building. When 27, or 53 lead dampers of each size are installed in the exterior columns, simultaneously, acceleration is decreased to 0.78g (27 0.5" lead dampers), 0.43g (53 0.5" lead dampers), 0.39g (27 0.6" lead dampers), and 0.23g (53 0.6" lead dampers), respectively, i.e. vibrations is decreased by 82% (((4.28g-0.78g)/4.28g)x100), 90%, 91%, and 95%, respectively. From Figures 117 and 118, it is shown that with time, increasing number of lead dampers become negligible.

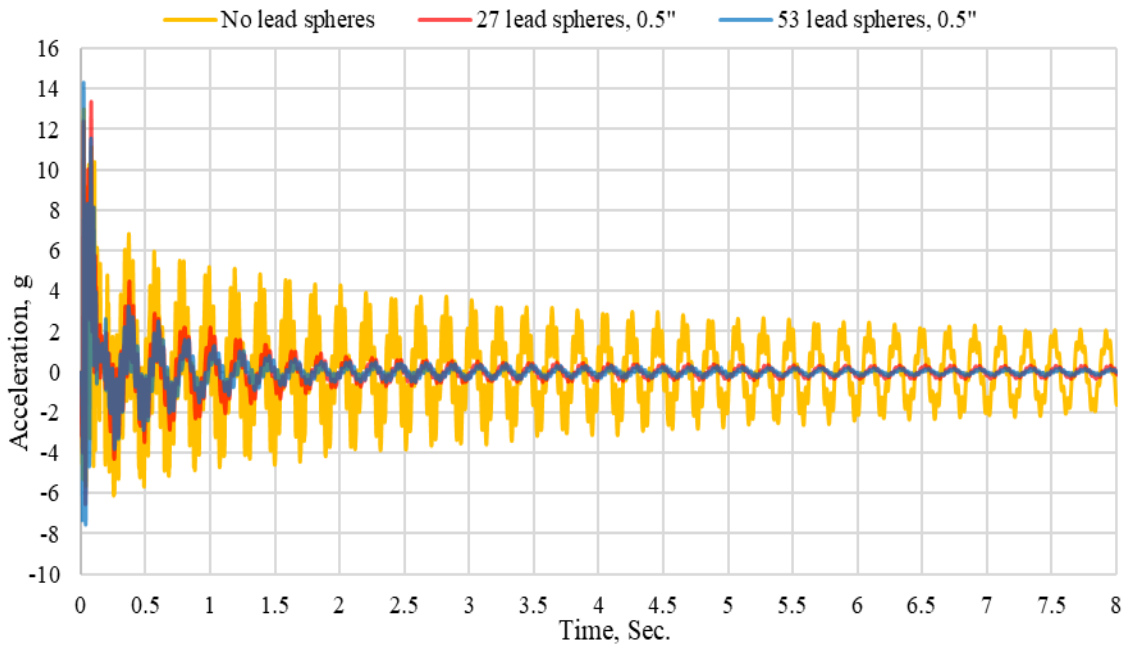

Figure 115. Cantilever acceleration-time relations with 0.5-in. lead dampers

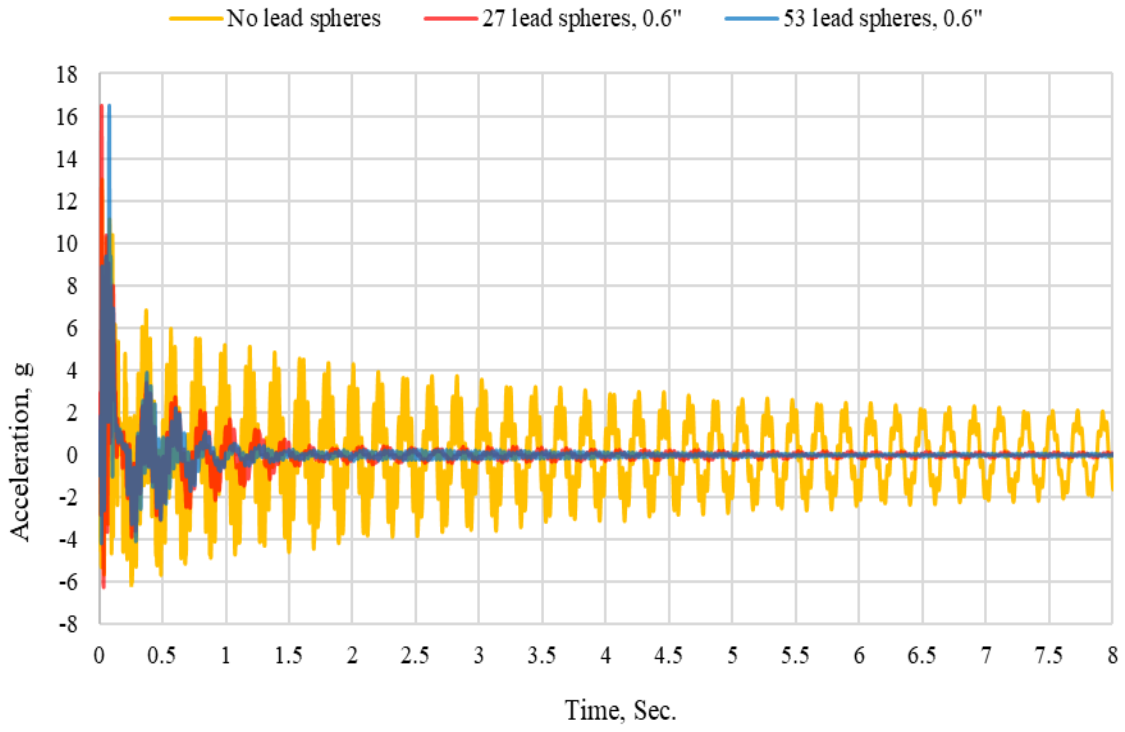

Figure 116. Cantilever acceleration-time relations with 0.6-in. lead dampers

At the time when the impact load excites the frame, from 0 sec. to 0.1 sec., shown in Figures 117 and 118 for lead dampers sizes 0.5” and 0.6”, respectively, the lead dampers do not damp anything. Adding the lead dampers to the cantilever does not help in decreasing the impact of the impact load on the structural member. However, right after the impact load excites the cantilever, the lead dampers start working on decaying motion in the building from time 0.1 sec. Right after 0.1 sec., the member with 53-lead dampers of 0.5” and 0.6”, get a decrease in vibration by 22% and 32%, respectively.

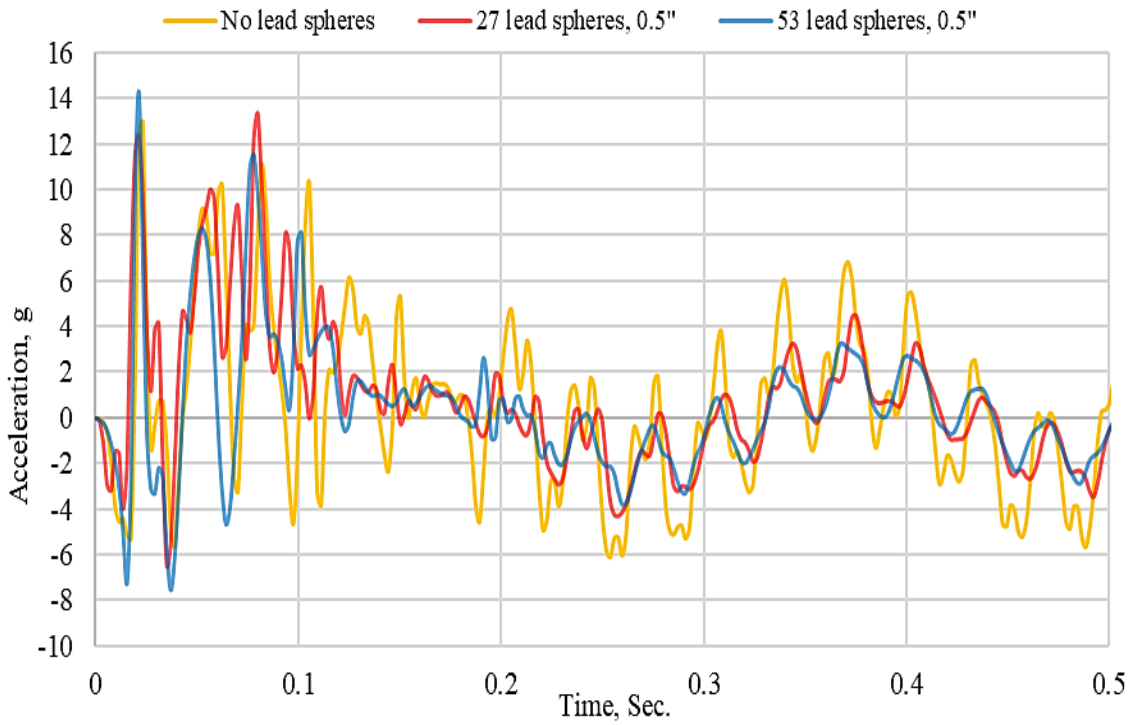

Figure 117. Cantilever acceleration-time relations with 0.5-in. lead dampers, 0<t<0.5 sec.

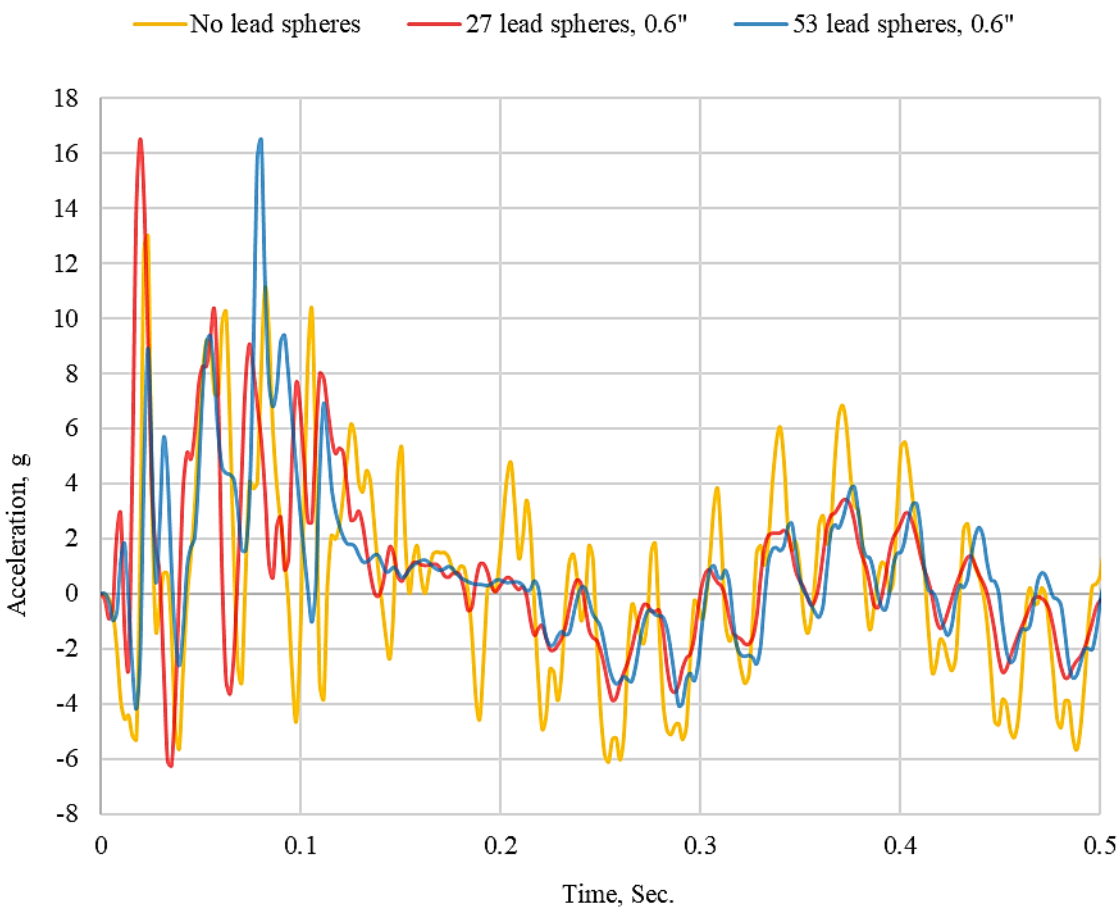

Figure 118. Cantilever acceleration-time relations with 0.6-in. lead dampers, 0<t<0.5 sec.

4.3 Full-Scale Steel Frame

The analytical results showed that with adding bolted damping panels to the full-scale steel frame, the top end plastic hinge was eliminated and the impacted ground-level column was prevented from collapse. Figure 119 shows the drastic reduction in vibration at the top floor of the building frame.

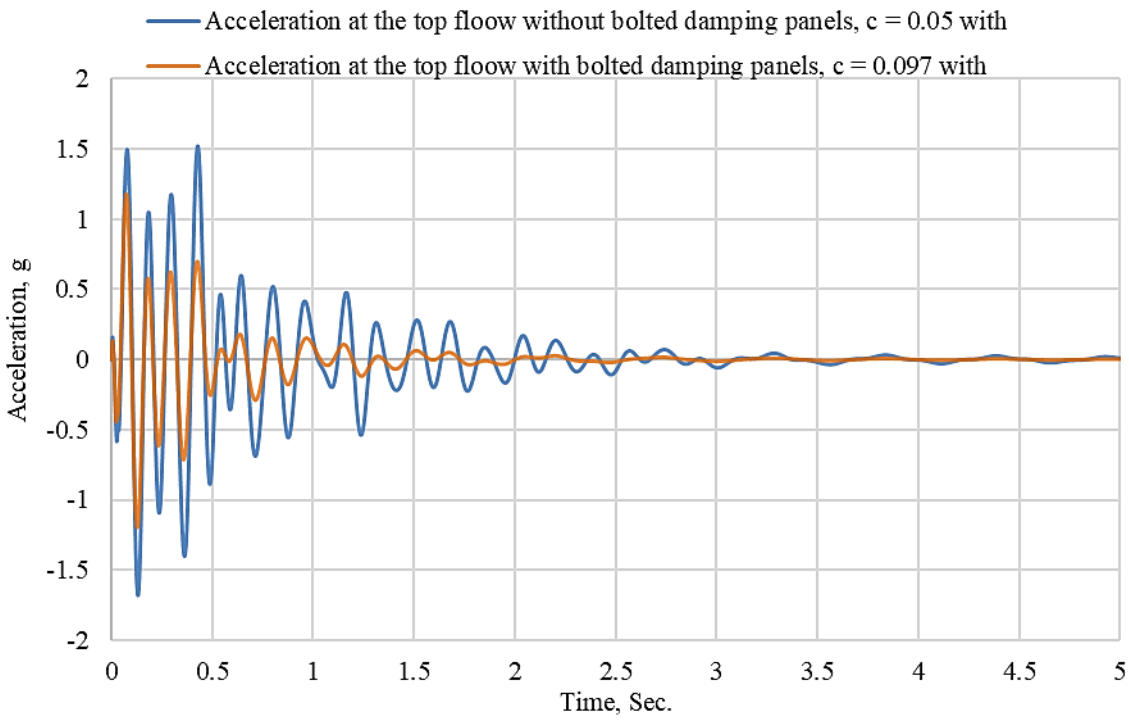

Figure 119. Full-scale building frame acceleration-time relations

In summary, the collected data show that with increasing number and or size of lead dampers, vibration decays more and faster. The results show that the lead dampers and damping panels have significant role in decreasing vibration in steel buildings.

CHAPTER V

5. CONCLUSIONS AND FUTURE RESEARCH

5.1 Conclusions

Based on the results of the experimental and the theoretical study conducted, the following conclusions are drawn:

1. In both steel building frame model as well as the full-scale building subjected to a localized column impact load, a very significant reduction in vibration occurs when suspended lead dampers are used.
2. Both the cantilever as well as the model frame tests show that the degree of the effectiveness of suspended lead dampers is related to the number of lead dampers.
3. Installation of welded or bolted steel panels with suspended lead dampers in the laboratory frame model showed a substantial reduction in vibration.
4. The numerical solution algorithm developed for solving the partial differential equation of dynamic equilibrium to account for both axial pulsating load and lateral impact load on a ground-level building column reveals a substantial reduction of vibration when suspended lead dampers are used.
5. The transient dynamic elastic-plastic analysis of both the model frame as well as the full-scale building shows that the ground-level column develops a plastic hinge first at the location of the impact load, followed by a plastic hinge at the column base, and finally at its top end.

6. The use of bolted damping panels eliminated the formation of the plastic hinge at the top end of the impacted ground-level column; however, in the absence of such damping panels, the impacted column develops three plastic hinges thereby turning into a collapse mechanism.
7. The bolted damping panel was more effective than the welded one; however, the welded damping panel performed better than the suspended lead dampers used only in the building columns.
8. The elastic-plastic transient dynamic analysis of the building model frame exhibits a drastic reduction in vibration after the formation of the three plastic hinges in the ground-level column under impact.

The study conducted shows that suspended lead dampers can significantly reduce vibration in steel buildings when subjected to a localized impact load both with and without an axial pulsating load.

5.2 Future Research

The transient dynamic elasto-plastic behavior of building frames subjected to simultaneous or sequentially applied impact loads on both the ground level columns, as well as, those in the upper stories of the frames should be studied in the future. Additional studies can include impact loads applied to the building beams and joints. Retrofitting schemes to strengthen existing buildings under impact or shock loads also need to be developed.

REFERENCES

[1] T. K. Datta, *Seismic analysis of structures*. John Wiley & Sons, 2010.

[2] A. Benavent-Climent, "A brace-type seismic damper based on yielding the walls of hollow structural sections," *Engineering Structures,* vol. 32, no. 4, pp. 1113-1122, 2010.

[3] K. Ghabraie, R. Chan, X. Huang, and Y. M. Xie, "Shape optimization of metallic yielding devices for passive mitigation of seismic energy," *Engineering Structures,* vol. 32, no. 8, pp. 2258-2267, 2010.

[4] R. W. Chan and F. Albermani, "Experimental study of steel slit damper for passive energy dissipation," *Engineering Structures,* vol. 30, no. 4, pp. 1058-1066, 2008.

[5] F. Mazza and A. Vulcano, "Displacement-based design procedure of damped braces for the seismic retrofitting of rc framed buildings," *Bulletin of Earthquake Engineering,* vol. 13, no. 7, pp. 2121-2143, 2015.

[6] Y. Xu and C. Ng, "Seismic protection of a building complex using variable friction damper: experimental investigation," *Journal of engineering mechanics,* vol. 134, no. 8, pp. 637-649, 2008.

[7] S. P. Ontiveros-Pérez, L. F. F. Miguel, and J. D. J. E. S. Riera, "Reliability-based optimum design of passive friction dampers in buildings in seismic regions," vol. 190, pp. 276-284, 2019.

[8] P. Ramaiah and G. Krishnaiah, "Modelling and design of friction damper used for the control of vibration in a gas-turbine blade-a microslip approach," *Proceedings of the Institution of Mechanical Engineers, Part C: Journal of Mechanical Engineering Science,* vol. 221, no. 8, pp. 887-895, 2007.

[9] A. Downey, L. Cao, S. Laflamme, D. Taylor, and J. J. E. S. Ricles, "High capacity variable friction damper based on band brake technology," vol. 113, pp. 287-298, 2016.

[10] M. Montgomery and C. Christopoulos, "Experimental validation of viscoelastic coupling dampers for enhanced dynamic performance of high-rise buildings," *Journal of Structural Engineering,* vol. 141, no. 5, p. 04014145, 2014.

[11] S. Gong, Y. Zhou, and P. Ge, "Seismic analysis for tall and irregular temple buildings: A case study of strong nonlinear viscoelastic dampers," *The Structural Design of Tall and Special Buildings,* vol. 26, no. 7, 2017.

[12] E. Tubaldi, "Dynamic behavior of adjacent buildings connected by linear viscous/viscoelastic dampers," *Structural Control and Health Monitoring,* vol. 22, no. 8, pp. 1086-1102, 2015.

[13] Z. Yang, S. Eddie, and S. Lam, "Dynamic responses of two buildings connected by viscoelastic dampers under bidirectional earthquake excitations," *Earthquake Engineering and Engineering Vibration,* vol. 13, no. 1, p. 137, 2014.

[14] R. J. Mcnamara and D. P. Taylor, "Fluid viscous dampers for high-rise buildings," *The structural design of tall and special buildings,* vol. 12, no. 2, pp. 145-154, 2003.

[15] F. R. Rofooei and S. Mohammadzadeh, "Improving the seismic torsional behavior of plan-asymmetric, single-storey, concrete moment resisting buildings with fluid

viscous dampers," *Earthquake Engineering and Engineering Vibration,* vol. 15, no. 1, pp. 61-78, 2016.

[16] S. Wang and S. A. Mahin, "Seismic retrofit of a high-rise steel moment-resisting frame using fluid viscous dampers," *The Structural Design of Tall and Special Buildings,* vol. 26, no. 10, 2017.

[17] A. Ras and N. Boumechra, "Seismic energy dissipation study of linear fluid viscous dampers in steel structure design," *Alexandria Engineering Journal,* vol. 55, no. 3, pp. 2821-2832, 2016.

[18] A. Lucchini, R. Greco, G. Marano, and G. Monti, "Robust design of tuned mass damper systems for seismic protection of multistory buildings," *Journal of Structural Engineering,* vol. 140, no. 8, p. A4014009, 2013.

[19] R. Latifi and R. Razani, "Vibration Mitigation of Shazand Railway Bridge Induced by Train Using Tuned Mass Damper (TMD)," *Periodica Polytechnica. Engineering. Mechanical Engineering,* vol. 59, no. 4, p. 189, 2015.

[20] J. G. Johnson, C. P. Pantelides, and L. D. Reaveley, "Nonlinear rooftop tuned mass damper frame for the seismic retrofit of buildings," *Earthquake Engineering & Structural Dynamics,* vol. 44, no. 2, pp. 299-316, 2015.

[21] A. Erdle, J. Weckendorf, A. Asiz, and I. Smith, "Effectiveness of distributed mass damper systems for lightweight superstructures," *Journal of Performance of Constructed Facilities,* vol. 28, no. 6, p. A4014005, 2013.

[22] A. J. C. w. e. Heysami, "Types of dampers and their seismic performance during an earthquake," vol. 10, no. Special-Issue1, pp. 1002-1015, 2015.

[23] K. L. Ryan and A. K. J. J. o. S. E. Chopra, "Estimation of seismic demands on isolators based on nonlinear analysis," vol. 130, no. 3, pp. 392-402, 2004.

[24] K. S. Arsava, Y. Kim, T. El-Korchi, and H. S. Park, "Nonlinear system identification of smart structures under high impact loads," *Smart materials and structures,* vol. 22, no. 5, p. 055008, 2013.

[25] L. Zhang, F. Ma, and J. Wang, "Study of control system of magnetorheological dampers under impact load," in *2009 Second International Conference on Intelligent Computation Technology and Automation*, 2009, vol. 1, pp. 894-897: IEEE.

[26] U. Maqbool, "Numerical assessment of friction dampers under quasi-static and impact loading," Universidade de Coimbra, 2018.

[27] W. H. Robinson, "Lead-rubber hysteretic bearings suitable for protecting structures during earthquakes," *Earthquake engineering & structural dynamics,* vol. 10, no. 4, pp. 593-604, 1982.

[28] W. Robinson, "Recent applications of high-damping hysteretic devices for the seismic isolation of buildings and bridges," *Journal of alloys and compounds,* vol. 211, pp. 592-595, 1994.

[29] W. Robinson, "Recent research and applications of seismic isolation in New Zealand," *Bulletin of the New Zealand Society for Earthquake Engineering,* vol. 28, no. 4, pp. 253-264, 1995.

[30] W. Robinson, "Passive control of structures, the New Zealand experience," *ISET Journal of Earthquake Technology,* vol. 35, no. 4, pp. 63-75, 1998.

[31] Y. Ribakov and J. Gluck, "Optimal design of ADAS damped MDOF structures," *Earthquake spectra,* vol. 15, no. 2, pp. 317-330, 1999.

[32] R. Jankowski, M. Kujawa, and C. Szymczak, "Reduction of steel chimney vibrations with a pendulum damper," *Task Quarterly,* vol. 8, no. 1, pp. 71-78, 2004.
[33] M. Nakashima, P. Pan, D. Zamfirescu, and R. Weitzmann, "Post-Kobe approach for design and construction of base-isolated buildngs," *Journal of Japan Association for Earthquake Engineering,* vol. 4, no. 3, pp. 259-264, 2004.
[34] R. Curadelli and J. Riera, "Design and testing of a lead damper for seismic applications," *Proceedings of the Institution of Mechanical Engineers, Part C: Journal of Mechanical Engineering Science,* vol. 221, no. 2, pp. 159-164, 2007.
[35] S. M. S. Alehashem, A. Keyhani, and H. Pourmohammad, "Behavior and performance of structures equipped with ADAS & TADAS dampers (a comparison with conventional structures)," in *The 14th World Conference on Earthquake Engineering*, 2008, pp. 12-17.
[36] M. Bayat and G. Abdollahzade, "Analysis of the steel braced frames equipped with ADAS devices under the far field records," *Latin American Journal of Solids and Structures,* vol. 8, no. 2, pp. 163-181, 2011.
[37] G. P. Warn and K. L. Ryan, "A review of seismic isolation for buildings: historical development and research needs," *Buildings,* vol. 2, no. 3, pp. 300-325, 2012.
[38] C. Soydan, E. Yuksel, and E. İrtem, "The behavior of a steel connection equipped with the lead extrusion damper," *Advances in Structural Engineering,* vol. 17, no. 1, pp. 25-39, 2014.
[39] Z. Razzaq, *Stability, Vibration and Passive Damping of Partially restrained imperfect columns*. 1983.
[40] Z. Razzaq, "Passive damping concepts for slender columns in space structures," 1985.
[41] Z. Razzaq and D. W. Mykins, "Experimental and theoretical investigation of passive damping concepts for member forced and free vibration," 1987.
[42] Z. Razzaq and B. Najjar, "Passive damping concepts for free and forced member and grillage vibration," 1988.
[43] Z. Razzaq and D. K. Muyundo, "Passive damping concepts for tubular beams with partial rotational and translational end restraints," 1991.
[44] Z. Razzaq and N. F. Aridi, "PASSIVE DAMPING DESIGN CONCEPTS FOR HOLLOW CANTILEVERS," in *Structural Stability And Dynamics: With CD-ROM (Volume 1)*: World Scientific, 2003, pp. 813-819.
[45] Z. Razzaq and B. S. Najjar, "Experimental Passive Damping Concepts for Space Structures with Tubular Members," 2016.
[46] C. ASTM, "ASTM standards," *Philadelphia: American Society for Testing Materials,* 1958.
[47] LORD. (2021, March 2021). Available: www.microstrain.com
[48] A. Chopra, "Dynamics of Structures 4th Edition, 2019," ed: Prentice Hall, New Jersey.
[49] H. Hussein and H. Hussein, "CFRP Sheets for Retrofitting Prestressed Concrete Bridge Girders," 2022.
[50] H. A. Hussein, "Effective CFRP Retrofitting Schemes for Prestressed Concrete Beams," Old Dominion University, 2014.

[51] H. A. Hussein and Z. Razzaq, "Prestressed Concrete Inverted Tee Beams With CFRP for Building Structures," *Global Journal of Research In Engineering,* 2017.
[52] H. A. Hussein and Z. Razzaq, "CFRP Retrofitting Schemes for Prestressed Concrete Box Beamsfor Highway Bridges," *Global Journal of Research In Engineering,* 2017.
[53] H. A. Hussein and Z. Razzaq, "Strengthening Prestressed Concrete Bridge Girders and Building Beams with Carbon Fiber Reinforced Polymer Sheets," *European Journal of Engineering and Technology Research,* vol. 6, no. 1, pp. 55-57, 2021.
[54] E. Popov and T. Balan, "Engineering mechanics of solids, 1999," ed: Prentice-Hall.
[55] Y. Yilmaz, Z. Girgin, and S. Evran, "Buckling analyses of axially functionally graded nonuniform columns with elastic restraint using a localized differential quadrature method," *Mathematical Problems in Engineering,* vol. 2013, 2013.
[56] B. AirCoil. (2021, Sep. 18, 2021). *Baltimore AirCoil*. Available: https://www.baltimoreaircoil.com/
[57] ASCE, "Minimum design loads for buildings and other structures," 2013: American Society of Civil Engineers.
[58] SAP2000, "Nonlinear analysis," 19 ed. Californaia: CSI,, 1975.

APPENDIX: COMPUTER PROGRAM SAP-2000

In dynamic analysis, the computer program SAP-2000 uses lumped mass. It automatically generates lumped masses at the joints of each element. “In a dynamic analysis, the mass of the structure is used to compute inertial forces. Normally, the mass is obtained from the elements using the mass density of the material and the volume of the element. This automatically produces lumped (uncoupled) masses at the joints. The element mass values are equal for each of the three translational degrees of freedom. No mass moments of inertia are produced for the rotational degrees of freedom. This approach is adequate for most analyses.” [58] [SAP-2000 analysis manual, page 40]. SAP-2000 always uses lumped masses, which means that at the joints, there no mass coupling between the degree of freedom.

“Inertial forces acting on the joints are related to the accelerations at the joints by a 6x6 matrix of mass values. These forces tend to oppose the accelerations. In a joint local coordinate system, the inertia forces and moments F1, F2, F3, M1, M2, and M3 at a joint are given by:

$$\begin{Bmatrix} F_1 \\ F_2 \\ F_3 \\ M_1 \\ M_2 \\ M_3 \end{Bmatrix} = - \begin{bmatrix} \mathbf{u1} & \mathbf{0} & \mathbf{0} & \mathbf{0} & \mathbf{0} & \mathbf{0} \\ & \mathbf{u2} & \mathbf{0} & \mathbf{0} & \mathbf{0} & \mathbf{0} \\ & & \mathbf{u3} & \mathbf{0} & \mathbf{0} & \mathbf{0} \\ & & & \mathbf{r1} & \mathbf{0} & \mathbf{0} \\ & \mathbf{sym.} & & & \mathbf{r2} & \mathbf{0} \\ & & & & & \mathbf{r3} \end{bmatrix} \begin{Bmatrix} \ddot{u}_1 \\ \ddot{u}_2 \\ \ddot{u}_3 \\ \ddot{r}_1 \\ \ddot{r}_2 \\ \ddot{r}_3 \end{Bmatrix}$$

Where $\ddot{u}_1$, $\ddot{u}_2$, $\ddot{u}_3$, $\ddot{r}_1$, $\ddot{r}_2$, and $\ddot{r}_3$ are the translational and rotational accelerations at the joint, and the terms u1, u2, u3, r1, r2, and r3 are the specified mass values.” [SAP-2000 analysis manual, page 40].

VITA

Herish Abdullah Hussein was born December 15, 1984 in Kurdistan (Northern part of Iraq). He received his BSc. in Civil-Geotechnical Engineering from University of Koya in Koya City in Kurdistan in July 2009. After graduation, he started working as a civil engineer with construction companies such as Falah Hassan, Nalia, and Nokan Company on different projects for two and a half years. Then he received a scholarship from the Kurdistan Regional Government to study abroad for Master of Science in Civil Engineering. After receiving his Master's degree majoring in structural engineering in December 2014 in Civil Engineering at Old Dominion University (ODU), he started is Ph.D. program at the same department. He began his Ph.D. program in Spring 2015 majoring in structural engineering. This dissertation, titled EFFECTIVENESS OF SUSPENDED LEAD DAMPERS IN STEEL BUILDINGS UNDER LOCALIZED LATERAL IMPACT AND VERTICAL PULSATING LOAD, was completed in December 2022 with Dr. Zia Razzaq as the adviser. Herish was/is teaching civil engineering classes at ODU as a part time from January 2014 to December 2022. Currently, he works for the city of Virginia Beach as a fulltime project manager at the Facilities Design and Construction division, Public Works department since February 2019.

The author's current address is:

1801 N Streamline Dr.

Virginia Beach, VA 23454

Phone: 757-646-8331

Email: hhuss001@odu.edu